IMPROVING REGIONAL AND GLOBAL AIR-SEA CO_2 FLUX ESTIMATES

YUANXU DONG

Ph.D.

2023

Improving regional and global air-sea CO_2 flux estimates

A thesis submitted to the School of Environmental Sciences of the University of East Anglia in partial fulfilment of the requirements for the degree of Doctor of Philosophy

By Yuanxu Dong

March 2023

“During your Ph.D., you can participate in cruises, you can learn how to interpret scientific data, you can publish papers, but Yuanxu, think about what is your research, what is YUANXU’s research? Ten or twenty years later, when people mention your name, what they will remember about you?” (Peter S. Liss on my probationary meeting in April 2020)

Abstract

The global oceans are a major carbon sink accounting for approximately a quarter of carbon dioxide (CO_2) emissions by human activities. Accurate quantification of ocean CO_2 uptake is critical to the assessment of the global carbon budget and to the projection of the future climate. The air-sea CO_2 flux is often estimated by the bulk method using sea surface CO_2 fugacity (fCO_{2w}) measurements combined with a wind speed-dependent gas transfer velocity (K_{660}). However, there are large uncertainties in bulk CO_2 flux estimates due to uncertainties in K_{660}, upper ocean gradients in fCO_{2w} and in temperature. In this thesis, I use direct air-sea CO_2 flux observations by the eddy covariance (EC) technique to improve CO_2 flux estimates over the high-latitude oceans. Upper ocean temperature gradients and their impact on CO_2 flux estimates are further assessed to update our understanding of global ocean CO_2 uptake.

Here I first make a comprehensive analysis of the uncertainties in ship-based EC air-sea CO_2 flux measurements to better understand the EC observations and to optimise the EC-based studies of K_{660}. Second, the impact of shallow stratification due to sea-ice melt is investigated using the EC CO_2 flux and fCO_{2w} measurements in the Arctic Ocean. Additional analysis of EC CO_2 fluxes from seven cruises in the Southern Ocean helps to improve our understanding of Southern Ocean CO_2 flux estimates. Finally, I reassess two temperature effects (the warm bias in the shipboard temperature dataset and the cool skin effect) and update their impact on global ocean CO_2 flux estimates.

My uncertainty analysis suggests that the state-of-the-art EC system is well suited for air-sea CO_2 flux measurements and that the EC flux can be considered a reference for evaluating indirect fluxes in strong flux signal regions. The Arctic study shows a clear underestimation of the bulk CO_2 flux in sea-ice melt regions estimated from subsurface fCO_{2w} observations (made on water from typically 5 m depth). The EC CO_2 flux indicates strong CO_2 uptake in the summertime Southern Ocean, which supports the shipboard fCO_{2w} observation (from SOCAT dataset)-based flux products after correcting for the temperature effects but suggests that the float observation (from SOCCOM dataset)-based CO_2 sink estimate is too weak. The impact of the temperature effects is even more significant for global ocean CO_2 flux estimates, increasing the global ocean CO_2 uptake by ~35% (0.6 Pg C yr^{-1}). The K_{660}–wind speed relationships based on EC observations agree well with the widely used K_{660} parameterisations, especially at intermediate wind speeds. In summary, this thesis advances our understanding of oceanic CO_2 uptake and contributes to reducing the uncertainties in air-sea CO_2 flux estimates.

Acknowledgements

I cannot be grateful enough for the support, encouragement, and inspiration from my supervisors Dorothee Bakker, Tom Bell, Peter Liss, and Mingxi Yang. I will always remember the weekly meetings with Dorothee and the beer time with Peter in the Alexandra pub. It is from your words and deeds, day by day, that I have been able to thrive with confidence and enthusiasm in academia. I also remember the thousands of email conversations with Ming and Tom and I appreciate your immense patience. These emails were the few things that gave me comfort and motivation during the pandemic. The exchange of ideas with you has been the most enjoyable part of my PhD. Pearls are everywhere but not the same as the eyes. How lucky I am for being recognised by four pairs of eyes, although I am just a stone.

I would like to thank my colleagues and peers at UEA, PML, and 95 Friends Road. I would like to first appreciate Vassilis Kitidis and Ian Brown from PML who made fCO_2 observations. I enjoyed the discussion with so many peers especially Elise Droste, Chata Seguro, and Charel Wohl. Also thank you to my Chinese friends in particular Qianyao, Xuewei, Shenjie, Yixi, and Qinbiao for their deep friendship during my darkest time. My housemate, Weici, Longji, Yanxin, and Chuanchuan, who makes me feel at home, thank you for your tireless patience, care, and encouragement. I wish all of you a bright future and we will meet again.

I also thank my collaborators and colleagues around the world. Particular thanks to Peter Landschützer for the always positive feedback and for teaching me to use a neural network technique, and to Judith Hauck for the informative discussion about the Southern Ocean CO_2 flux estimates. I would further like to thank all scientists with whom I had invaluable discussions at conferences and meetings, in particular Andy Watson, Jamie Shutler, Chris Merchant, and Haifeng Zhang with whom I had fruitful discussions about the upper ocean temperature structures, as well as Bernd Jähne, Christa Marandino, David Woolf, and Rik Wanninkhof, who inspired me to understand gas exchange at high wind speeds. I also acknowledge my PhD funder, the China Scholarship Council, as without the funding, I could not have begun this journey.

I am grateful to my parents for providing love and belief. You are the only persons in the world whenever I have needed you, you have been there. Also, particular thanks to my granduncle, your mental and economic support has been important for me to complete this degree. Finally, my girlfriend, Rui, your companionship is the most valuable gift I have ever received. I am so excited about our journey together.

Contents

List of tables

List of figures

Chapter 1

1 Background

> "Don't compare to your supervisors, we have experience, but you have time."
>
> (Dorothee C. E. Bakker, January 2020)

Abstract: This thesis aims to improve air-sea carbon dioxide (CO_2) flux estimates by using direct flux measurements including considerations of refined upper ocean temperature structures. This chapter provides a general introduction to the relevance of the topic. Anthropogenic CO_2 emissions and the global carbon budget are first reviewed to indicate the importance of the global ocean in slowing down the increase of the atmospheric CO_2 mole fraction and the capacity of the oceans to accommodate anthropogenic CO_2. The bulk equation for CO_2 flux estimates is derived employing a film model with an illustration of the air-sea CO_2 exchange processes. The sea surface CO_2 fugacity and gas transfer velocity are two key parameters for estimating CO_2 flux. The way to measure CO_2 fugacity and progress in parameterising the gas transfer velocity is described. At the end of the chapter, I indicate current knowledge gaps in estimating regional and global air-sea CO_2 fluxes and point out key questions this PhD thesis will focus on.

1.1 CO_2 and climate change

1.1.1 Increasing atmospheric CO_2 mole fraction

Just before the Industrial Revolution, the CO_2 mole fraction of the atmosphere remained relatively constant at ~278 parts per million (ppm, i.e., in every million molecules of dry air there are on average 278 CO_2 molecules, equal to μmol mol^{-1}) (Gulev et al., 2021), which means that uptake of CO_2 balanced its emissions (Broecker & Peng, 1993). But from the late 18th century onwards, anthropogenic CO_2 emissions from human activities, such as fossil fuel burning and land-use change, have remarkably broken this balance (Friedlingstein et al., 2022). In the late 1950s, Charles David Keeling started to record the CO_2 concentration of the atmosphere at the Mauna Loa Observatory (Keeling, 1960) and the records provide direct evidence for the increase in atmospheric CO_2 (https://gml.noaa.gov/ccgg/trends/mlo.html). The curve showing the increasing CO_2 mole fraction of the atmosphere is known as the 'Keeling Curve'. The atmospheric CO_2 content has risen steeply (Figure 1.1) and reached ~420 ppm in 2023 (Dlugokencky & Tans, 2023), more than 50% above the pre-industrial level.

Carbon dioxide is a strong absorber of thermal infrared energy radiated by the Earth's surface. With the atmospheric CO_2 concentration increasing due to anthropogenic emissions, more thermal energy is kept in the Earth's lower atmosphere, which is deemed to be the major contributor to global warming (Lashof & Ahuja, 1990).

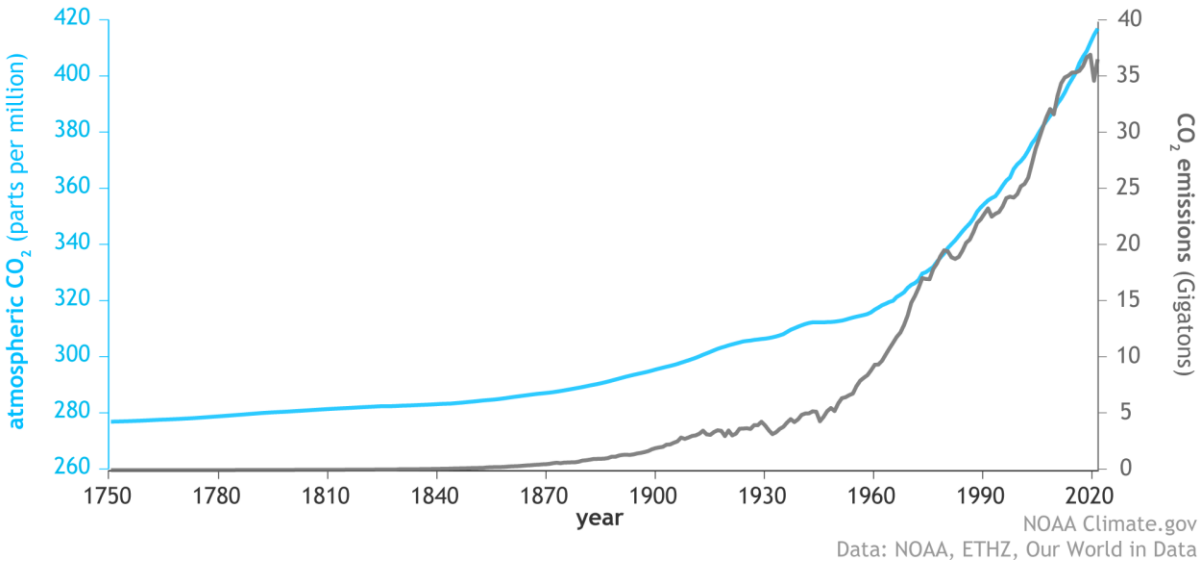

Figure 1.1 The mole fraction of atmospheric CO_2 (blue line) has increased along with human CO_2 emissions (grey line) since the start of the Industrial Revolution in 1750. Atmospheric CO_2 data are from NOAA (https://www.esrl.noaa.gov/gmd/ccgg/trends/data.html) and ETHZ (https://iac.ethz.ch/). CO_2 emissions data from Our World in Data (https://ourworldindata.org/co2-and-other-greenhouse-gas-emissions#how-have-global-co2-emissions-changed-over-time) and the Global Carbon Project (https://www.globalcarbonproject.org/). This figure is from the NOAA Climate.gov graph (https://www.climate.gov/news-features/understanding-climate/climate-change-atmospheric-carbon-dioxide).

1.1.2 The global carbon budget

Although the atmosphere's CO_2 mole fraction is rising, the rate of increase is slower than would have been the case without the storage of CO_2 in the land and ocean reservoirs. As assessed by the 17th version of the global carbon budget (a budget for CO_2 emitted into the atmosphere by human activities) (Friedlingstein et al., 2022), only about half of the anthropogenic CO_2 emissions remain in the atmosphere.

An understanding of the global carbon budget over different time scales is essential to understand climate change, which is the main aim of the Global Carbon Project (GCP). Since 2005, the GCP has coordinated with the global carbon community to publish the global carbon budgets (GCB) annually. The GCB is reported as five main components with independent estimates (Friedlingstein et al., 2022):

1) CO_2 emissions from fossil fuel burning and oxidation including cement production (CO_2 sources due to fossil CO_2 emissions, E_{FOS}). The estimate is based on energy

statistics and cement production data.

2) CO_2 emissions due to deliberate human activities on land, mainly deforestation (CO_2 emission sources due to land use change, E_{LUC}). The estimate is based on land use and land-use change data and bookkeeping models.

3) The growth rate of atmospheric CO_2 mole fraction (the atmospheric CO_2 sink, G_{ATM}). The estimate is based on the measured atmospheric CO_2 mole fraction.

4) Uptake of anthropogenic CO_2 by the global oceans (the ocean CO_2 sink, S_{OCEAN}). Estimated with global ocean biogeochemistry models and observation-based data products.

5) Uptake of CO_2 by land (the terrestrial CO_2 sink, S_{LAND}); Estimated with dynamic global vegetation models.

The two CO_2 emission sources (1, 2) are in balance with the three CO_2 sinks (3, 4, 5) in the real world averaged globally. However, due to the uncertainty in the CO_2 budget estimates, these five components do not add up to zero. Thus, the sixth component, the mismatch between the source estimates and the sink estimates is additionally introduced (budget imbalance, B_{IM}):

$$B_{IM} = (E_{FOS} + E_{LUC}) - (G_{ATM} + S_{OCEAN} + S_{LAND}) \quad (1.1)$$

where all the components are in units of petagrams of carbon every year (Pg C yr^{-1}, 1 Pg C = 10^{15} g C) or gigatonnes of carbon every year (Gt C yr^{-1}, 1 Pg C = 1 Gt C).

The latest released GCB (Global Carbon Budget 2022, Friedlingstein et al., 2022) reported the global annual average (± 1 standard deviation) CO_2 budget for the last decade (i.e., 2012–2021, in Pg C yr^{-1}, Figure 1.2) as: E_{FOS} = 9.6 ± 0.5 (89% of total CO_2 emissions); E_{LUC} = 1.2 ± 0.7 (11% of total CO_2 emissions); G_{ATM} = 5.2 ± 0.02 (48% of total CO_2 emissions); S_{OCEAN} = 2.9 ± 0.4(26% of total CO_2 emissions); S_{LAND} = 3.1 ± 0.6 (29% of total CO_2 emissions); B_{IM} = -0.3 (-3% of total CO_2 emissions, the total estimated sinks were too high or sources were too low).

Among the five main component estimates, the land-use change emission estimate has the largest uncertainty persistently in the history of the released GCB, while the atmospheric CO_2 sink estimate is the most accurate one. The land CO_2 sink estimate in the northern extratropics has a low agreement between different methods, while models and observation-based data

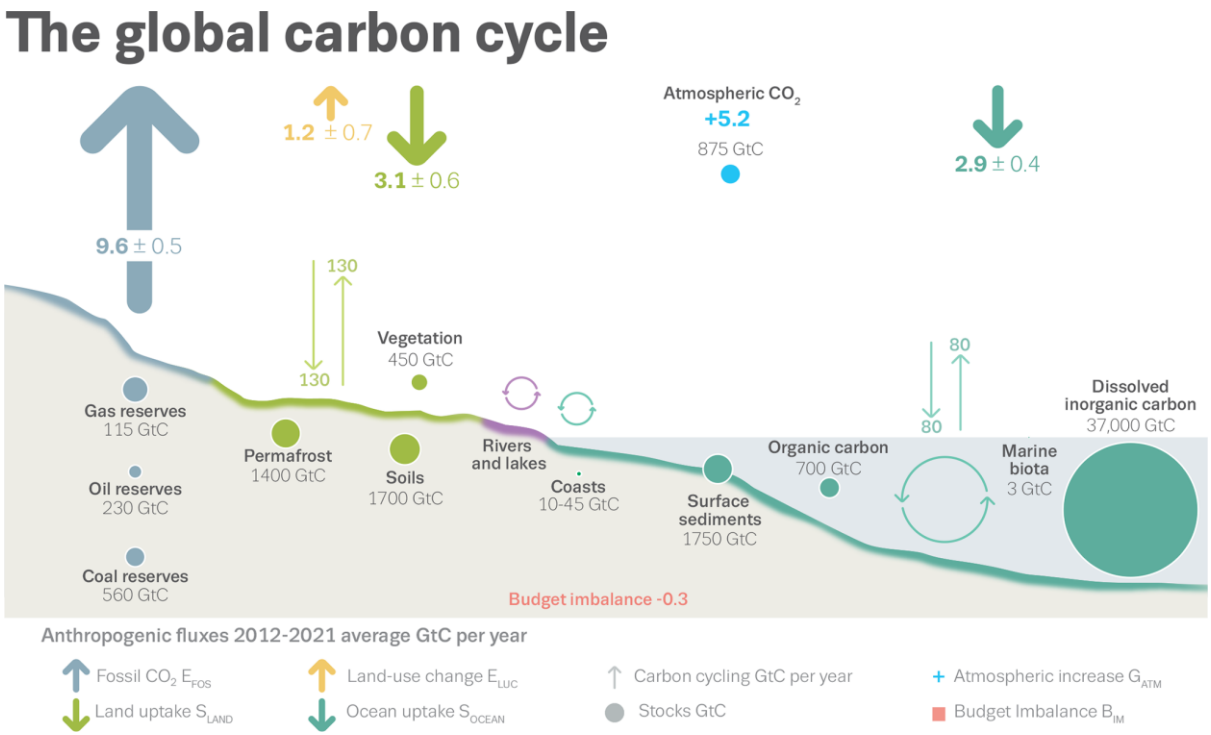

Figure 1.2 Schematic representation of the global carbon budget averaged globally for the decade 2012–2021 from Friedlingstein et al. (2022).

products have a large discrepancy in the trend of ocean CO_2 uptake over the last decade (Friedlingstein et al., 2022).

1.1.3 Ocean CO_2 uptake

The oceans are a major CO_2 sink, currently taking up approximately a quarter of anthropogenic emissions and ~40% of all anthropogenic CO_2 released since the Industrial Revolution (Friedlingstein et al., 2022; Gruber et al., 2019; Sabine et al., 2004).

Most of the CO_2 in the atmosphere-ocean system is dissolved in seawater (98%, Zeebe & Wolf-Gladrow, 2001) by reacting with water (H_2O) to form dissolved CO_2 and carbonic acid (aqueous CO_2 plus H_2CO_3), bicarbonate (HCO_3^-), carbonate ions (CO_3^{2-}) and hydrogen ions (H^+) (Figure 1.3). These species (aqueous CO_2, H_2CO_3, HCO_3^-, and CO_3^{2-}) comprise the dissolved inorganic carbon (DIC) in seawater. In surface seawater, HCO_3^- (~90%) and CO_3^{2-} (~9%) dominate the DIC, and only about 1% exists in the form of aqueous CO_2 and undissociated H_2CO_3. The special properties of the carbonate system result in the unique behaviour of the ocean in response to CO_2 perturbation. For the fluctuation of the mole fraction of abundant gases in the earth's atmosphere such as nitrogen, the re-equilibration between the

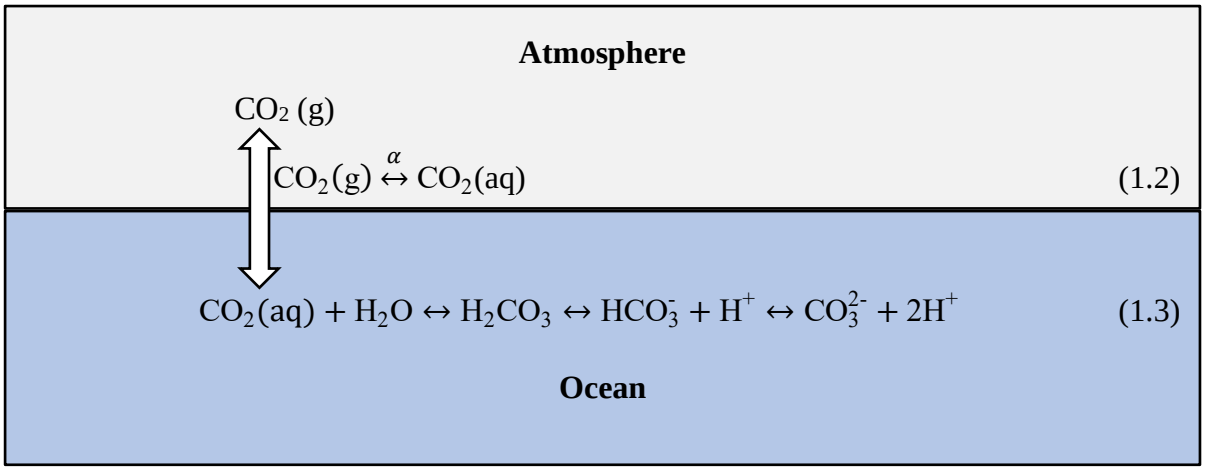

Figure 1.3 A schematic of two equilibrium processes of CO_2 in the atmosphere-ocean system

surface ocean and the atmosphere only requires the thermodynamic equilibrium process (Equation 1.2) mediated first by the solubility (α) and then physical mixing to full ocean depth. However, CO_2 not only needs to equilibrate between the gaseous CO_2 in the atmosphere and the aqueous CO_2 in the ocean, but also with all carbonate species constituting DIC (Equation 1.3, carbonate system equilibrium).The abundance of HCO_3^- and CO_3^{2-} in the seawater results in a strong oceanic CO_2 uptake capacity (aqueous CO_2 reacts with CO_3^{2-} and H_2O to form two HCO_3) in response to the increase in atmospheric CO_2 mole fraction. The ocean will take up and accommodate about 80% of the anthropogenic CO_2 emissions when atmospheric CO_2 eventually equilibrates with the entire ocean (Bakker et al., 2014).

However, this final equilibration is based on a long time scale because of the slow vertical transport of the ocean (Broecker & Peng, 1993). The air-sea CO_2 exchange occurs in the upper ocean. In response to the increasing atmospheric CO_2 mole fraction, the invaded CO_2 first accumulates in the surface ocean layer, which is renewed by vertical mixing and thus maintains the uptake capacity of the surface seawater. The mixing process transports the anthropogenic CO_2 from the surface to the deep ocean, by which the ocean eventually plays its role in carbon sequestration. But this vertical transport of the ocean is much slower than the CO_2 uptake from the atmosphere. This means that the anthropogenic CO_2 emissions result in a quick increase of the atmospheric CO_2 mole fraction, but that the ocean CO_2 uptake cannot respond as rapidly as expected. Therefore, Broecker & Peng (1993) stated that only a relatively small percentage of the ocean CO_2 uptake potential is being utilised at the moment.

Globally, the oceans take up CO_2, corresponding to a negative value of the air-sea CO_2 flux, but there is seasonal and regional variability. These variations are often characterised by the

temperature effect and the biological effect. Both lowering the temperature and increasing biological utilisation of CO_2 enhance the CO_2 uptake ability of seawater. Based on surface ocean observations, Takahashi et al. (2002) estimated the global air-sea CO_2 flux and revealed that a zone between 40° and 60° latitude in both hemispheres is the major sink for atmospheric CO_2 because of the cold, nutrient-rich waters and the high wind speeds in these areas. In particular, the Southern Ocean (< 35°S) covers only ~20% of the global ocean surface area, but accounts for ~40% of the oceanic uptake of anthropogenic CO_2 emissions (e.g., DeVries, 2014). The equatorial Pacific (14°N–14°S) is the major source of atmospheric CO_2 due to the high temperature of the surface seawater and the upwelling process. Seasonal changes in seawater temperature and biological processes regulate the seasonal amplitude of the CO_2 flux. The seasonality of the air-sea CO_2 fluxes in equatorial and subpolar to polar oceans is controlled by biological processes, whereas that in the temperate gyre areas is dominated by the temperature effect (Takahashi et al., 2002). The biological effect is about 6 months out of phase with the temperature effect and the magnitude of the combined effects is a diminution of the seasonality. The global ocean air-sea CO_2 flux also has interannual and decadal variations in response to factors such as increases in atmospheric CO_2 due to the anthropogenic CO_2 emissions and the El Nino–Southern Oscillation in the equatorial Pacific (McKinley et al., 2017; Takahashi et al., 2009).

1.2 Air-sea gas exchange

In Section 1.1.3, I explained why the oceans have a huge potential for the storage of anthropogenic CO_2. In this section, I will describe how CO_2 is exchanged across the air-sea interface and how the exchange flux is quantified.

1.2.1 Air-sea gas exchange processes

Gas transfer across the sea surface is a complex process and several models have been developed to describe it (see reviews in Liss & Merlivat, 1986; Wanninkhof et al., 2009). The most widely used model is the stagnant film model (Liss & Slater, 1974; Figure 1.4). This model assumes that there are mass boundary layers above and beneath the air-sea interface, respectively, and that the main body of the atmosphere and ocean outside of these two layers is well mixed by turbulent transfer. The main resistance to gas transfer comes from these two interface layers because gases can only transfer across the gas-liquid interface by slow molecular diffusion. The total exchange resistance is the sum of the resistance of the gas and liquid phases. For less soluble gases such as CO_2, the resistance mainly comes from the water-

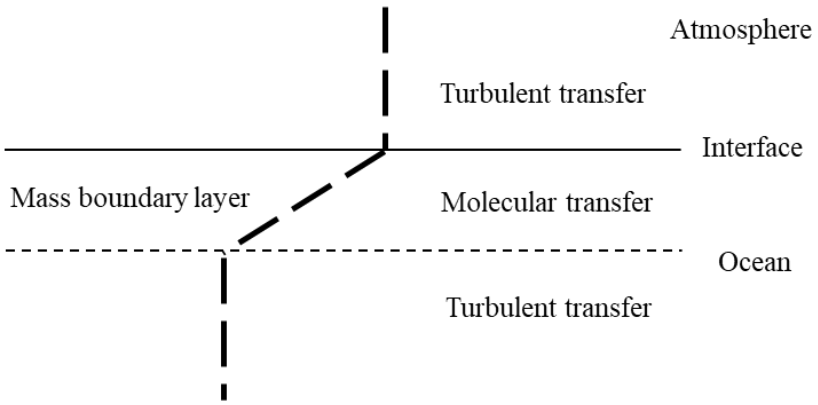

Figure 1.4 The stagnant film model of the exchange of less soluble gases across the air-sea interface. The solid dashed line represents the concentration profile of the gas in the case of ocean uptake. Figure developed from Liss & Slater (1974).

side mass boundary layer while air-side resistance dominates for gases with high solubility (e.g., water vapour and methanol). The gas exchange of moderately soluble gases like acetone is controlled by both interface layers.

1.2.2 Bulk algorithm of CO_2 flux across the sea surface

Figure 1.4 visualises the air-sea CO_2 exchange process by the stagnant film model. The water-side mass boundary layer is very thin with a thickness of ~10–100 µatm. The CO_2 transport flux across the air-sea interface (F, e.g., in mol m^{-2} s^{-1}) by molecular diffusion can be described by Fick's first law (Fick, 1855):

$$F = -D\,\partial c/\partial z \tag{1.4}$$

where D is the coefficient of molecular diffusion (m^2 s^{-1}) of the gas in the mass boundary layer; c is the gas concentration (mol m^{-3}), and z is the layer thickness (m). Equation 1.4 can be further written as:

$$F = (c_w - c_i)\,D/z \tag{1.5}$$

where $c_w - c_i$ is the CO_2 concentration difference between the bottom of the water-side mass boundary layer (c_w) and the interface (c_i). Equation 1.5 can be simplified as:

$$F = K(c_w - c_i) \tag{1.6}$$

where K is called the (total) gas transfer velocity (m s^{-1}) and is equal to D / z ; it is a measure of the CO_2 flux per unit concentration gradient (see Section 1.2.4 for discussions of K). K is proportional to D and also forced by the interfacial turbulence. To study the relationship

between *K* and the turbulence and concert *K* for one gas to the equivalent value for another gas, we typically normalise the gas transfer velocity by the dimensionless Schmidt number (*Sc*) for CO_2 in seawater at 20°C to eliminate the impact of *D* on *K*:

$$K_{660} = K(660/Sc)^n \tag{1.7}$$

where *Sc* is defined as the ratio of the kinematic viscosity of water (ν, $m^2\ s^{-1}$) and the coefficient of the molecular diffusion:

$$Sc = \nu/D \tag{1.8}$$

Schmidt number for a specific gas is temperature and salinity dependent and can be estimated by a polynomial fit of *Sc* for seawater (35‰ salinity) at temperatures from -2°C to 40°C (Wanninkhof, 2014):

$$Sc = \mathrm{A} + \mathrm{B}T_\mathrm{w} + \mathrm{C}T_\mathrm{w}^{\,2} + \mathrm{D}T_\mathrm{w}^{\,3} + \mathrm{E}T_\mathrm{w}^{\,4} \tag{1.9}$$

Here, T_w is the seawater temperature in degrees Celsius. The coefficients A to E for CO_2 in this fit are given by 2116.8, -136.25, 4.7353, -0.092307 and 0.0007555. At 20°C and 35‰ salinity seawater, *Sc* is calculated as ~660 for CO_2 and the gas transfer velocity is thus often normalised to K_{660} (Equation 1.7).

According to the stagnant film model, the Schmidt number exponent *n* in Equation 1.7 only would be -1. However, the wave-tank experiment indicated that the value of *n* varies and is higher than -1 (e.g., Jähne et al., 1987). These experimental results support the surface renewal model, which envisions that the surface ocean layer is dynamic and mixes with the bulk frequently (Danckwerts, 1951). The renewal model predicates that gas transfer velocity changes from -2/3 to -1/2 with the occurrence of waves on the sea surface (i.e., -2/3 for calm sea state and -1/2 for wavy sea state). In practice, we often use -1/2 for the flux calculation.

Using Equation 1.6 to calculate the air-sea CO_2 flux requires the measurements of c_w and c_i, but c_i cannot be measured directly and we often make measurements of the fugacity of CO_2 (fCO_2, µatm) in seawater (fCO_{2w}) and atmosphere (fCO_{2a}) (see Section 1.2.3 for the description of fCO_2 measurements). The CO_2 concentration and the fugacity can be related by the solubility (α, $mol\ m^{-3}\ atm^{-1}$):

$$c = \alpha f\mathrm{CO}_2 \tag{1.10}$$

The solubility α is related to seawater temperature, salinity and gas properties, and can be

estimated with the equation (Weiss, 1974):

$$\ln(\alpha) = A_1 + A_2(100/T_w) + A_3\ln(T_w/100) + S[B_1 + B_2(T_w/100) + B_3(T_w/100)^2 \quad (1.11)$$

The solubility calculated from Equation 1.11 is expressed in mol L^{-1} atm^{-1}. Here the temperature T_w is in Kelvin and salinity S is in ‰. For CO_2, the constants A_1 to A_3 are -58.0931, 90.5069 and 22.2940. B_1 to B_3 are 0.027766, -0.025888 and 0.0050578.

By combing Equations 1.6, 1.7, and 1.10, the air-sea CO_2 flux can be re-written as :

$$F = K_{660}(Sc/660)^{-1/2}(\alpha_w f\mathrm{CO_{2w}} - \alpha_i f\mathrm{CO_{2a}}) \quad (1.12)$$

where α_w and α_i are the CO_2 solubility at the bottom of the water-side mass boundary layer and at the air-sea interface, respectively (Figure 1.4).

1.2.3 Air-sea CO_2 fugacity

The seawater CO_2 fugacity ($f\mathrm{CO_{2w}}$) is often measured with a showerhead equilibrator using the ship's underway system. The $f\mathrm{CO_2}$ measurement system typically consists of an equilibrator and an infrared CO_2 analyser (Pierrot et al., 2009). The dry CO_2 mole fraction in the seawater ($\chi\mathrm{CO_{2w}}$, in ppm) (from the ship's seawater supply which is pumped from the surface layer at ~5 m depth) is first measured by a non-dispersive infrared detector (e.g., LI-COR, LI-6262) following 'vented-showerhead' equilibration of the pumped seawater. The $\chi\mathrm{CO_{2w}}$ is then converted into CO_2 partial pressure ($p\mathrm{CO_{2w\_eq}}$, in µatm) using the water temperature (T_{eq}, in K), salinity and air pressure in the equilibrator (P_{eq}, in atm):

$$p\mathrm{CO_{2w\_eq}} = \chi\mathrm{CO_{2w}}\left[P_{eq} - p\mathrm{H_2O_{eq}}\right] \quad (1.13)$$

where $p\mathrm{H_2O_{eq}}$ (atm) is the water vapour pressure at the sea surface salinity and the temperature of the equilibrator. The equilibrator CO_2 fugacity $p\mathrm{CO_{2w\_eq}}$ is then corrected to the sea surface temperature (T_w, in K) via the empirical temperature relationship of Takahashi et al. (1993):

$$p\mathrm{CO_{2w}} = p\mathrm{CO_{2w\_eq}}\exp\left[0.0423\left(T_w - T_{eq}\right)\right] \quad (1.14)$$

where $p\mathrm{CO_{2w}}$ is the CO_2 partial pressure in the seawater. The temperature dependence of 4.23 ± 0.02% $°C^{-1}$ has been determined from the North Atlantic surface water (Takahashi et al., 1993). Recent measurements for 21 cruises sampling the major ocean basins from 1992 to 2020 indicate a temperature dependence of 4.13 ± 0.01% $°C^{-1}$ (Wanninkhof et al., 2022), which is in good agreement with the Takahashi et al. (1993) empirical estimate. Thus, in this study, we use the 4.23% temperature dependence for the $p\mathrm{CO_{2w}}$ correction.

The dry CO_2 mole fraction in the atmosphere (χCO_{2a}, in ppm) (from air samples collected from near the sea surface at ~10–20 m above mean sea level) is also measured by the infrared detector. The χCO_2 measurements alternate between atmosphere samples and seawater samples. The CO_2 partial pressure in the atmosphere (pCO_{2a}) is converted from the χCO_{2a}:

$$pCO_{2a} = \chi CO_{2a}[P_a - pH_2O_a] \quad (1.15)$$

where P_a (in atm) is the atmospheric pressure and the water pressure pH_2O_a is estimated using the sea surface temperature and seawater salinity.

The partial pressure (pCO_2) can be further converted into fugacity (fCO_2) by correcting for any non-ideal behaviour of the gas with the equation (Pierrot et al., 2009):

$$fCO_2 = pCO_2 \exp\{[B + 2(1 - \chi CO_2)^2 \delta CO_2]P_{atm}/RT_w\} \quad (1.16)$$

Here, R = 82.0578 is the ideal gas constant converted to units of atm mol^{-1} cm^{-3} K^{-1}. P_{atm} is the atmospheric pressure (atm) and T_w is the sea surface temperature in K. B is the second virial coefficient in cm^3 mol^{-1} given by (Weiss, 1974):

$$B = -1636.75 + 12.0408T_w - 3.27957 \times 10^{-2}{T_w}^2 + 3.16528 \times 10^{-5}{T_w}^3 \quad (1.17)$$

and δCO_2 (cm^3 mol^{-1}):

$$\delta CO_2 = 57.7 - 0.118T_w \quad (1.18)$$

In practice, the CO_2 fugacity is quite close to the CO_2 partial pressure, the difference being less than 0.5% in seawater (Weiss, 1974).

In summary, for the seawater CO_2 measurements, the χCO_{2w} in the pumped seawater is first equilibrated with the air in the headspace of the equilibrator and the air in equilibrium is measured by an infrared CO_2 detector. To go from χCO_{2w} to fCO_{2w} requires three conversions: $\chi CO_{2w} \rightarrow pCO_{2w\_eq} \rightarrow pCO_{2w} \rightarrow fCO_{2w}$. For the atmospheric CO_2 measurements, the χCO_{2a} is directly analysed (without the equilibration step) by the infrared CO_2 detector from the sampled air, and to go from χCO_{2a} to fCO_{2a} requires two conversions: $\chi CO_{2a} \rightarrow pCO_{2a} \rightarrow fCO_{2a}$. It is worth noting that sea surface temperature is a key parameter for the conversion processes (Equations 1.13 to 1.18).

Since fCO_{2w} is essential for the air-sea CO_2 flux estimates, much effort has gone into measurements of fCO_{2w} during the last several decades. The Lamont-Doherty Earth Observatory (LDEO) provided the first fCO_{2w} dataset on a global scale, which enabled studies

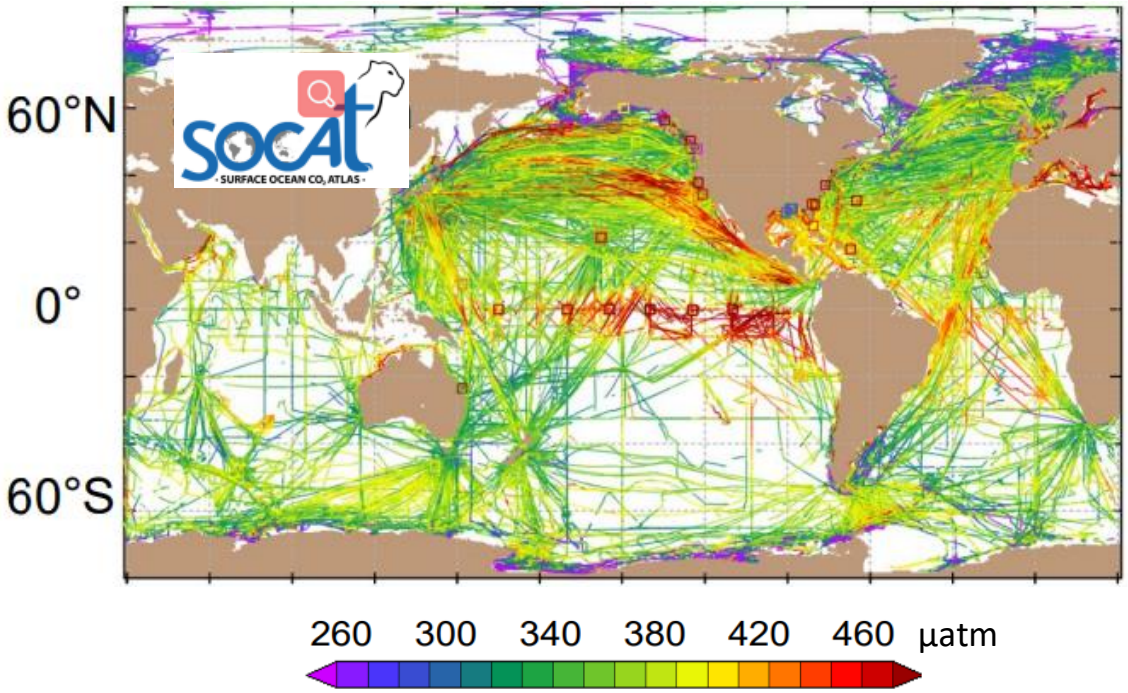

Figure 1.5 *In-situ* surface ocean fCO_2 values (colour coded, µatm) with an estimated accuracy of < 5 µatm in SOCAT version 2022 (Bakker et al., 2022). Squares indicate moorings, lines represent ship tracks.

of global air-sea CO_2 flux and surface ocean CO_2 cycle on different time scales (Takahashi et al., 1997, 2002, 2009). More recently, further effort by the ocean carbon community has led to the largest fCO_{2w} database with uniform quality control and regular updates: The Surface Ocean CO_2 ATlas (SOCAT, https://www.socat.info/). These measurements are usually based on research vessels or voluntary observing ships, with an underway measurement system which mainly includes an air-water equilibrator and an infrared analyser (Bakker et al., 2016). In addition, measurements are increasingly made by instruments and sensors on moorings, drifters, and autonomous surface vehicles. The latest SOCAT version (version 2022) contains 33.7 million observations with an accuracy of better than 5µatm from 1957 to 2021 for the global oceans and coastal seas (Figure 1.5). The SOCAT products have been widely used for global and regional ocean carbon cycle studies and quantification of the ocean carbon sink in the global carbon budget (Bakker et al., 2016; Friedlingstein et al., 2022).

The distribution of fCO_{2w} measurements in SOCAT is highly heterogenous in time and space (Figure 1.5). To estimate the global ocean CO_2 flux from these surface observations, the SOCAT fCO_{2w} dataset needs to be interpolated to reconstruct a global gap-free fCO_{2w} product.

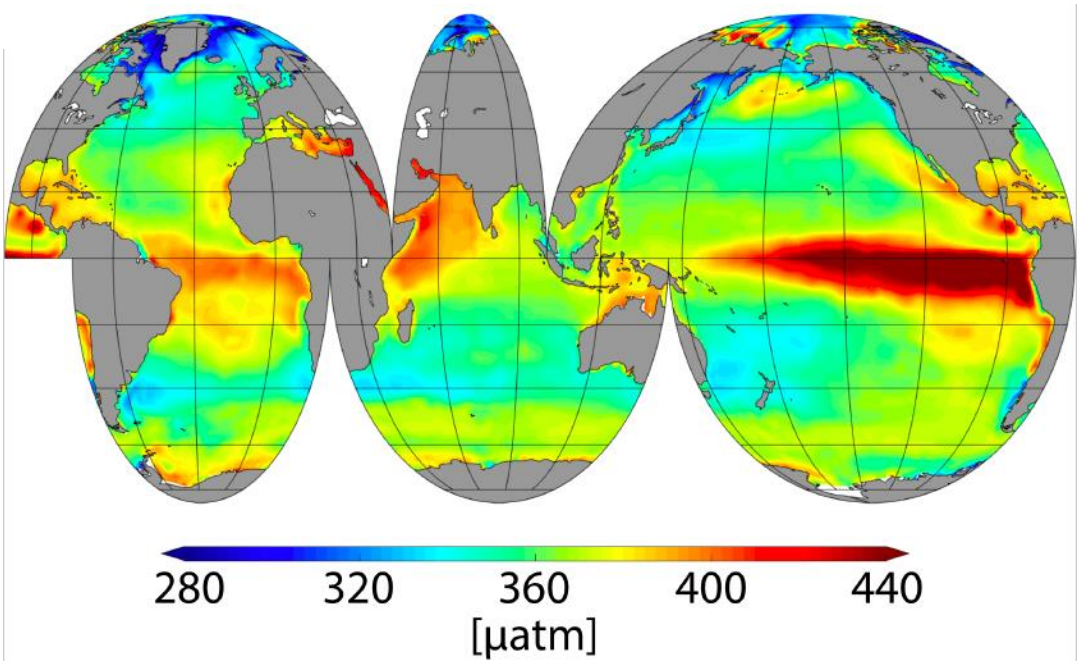

Figure 1.6 The climatological mean fCO_{2w} of the global ocean based on the SOCAT synthesis dataset and a neural network technique (Landschützer et al., 2020).

A widely used approach for this mapping process is establishing the relationships between the observed fCO_{2w} and the potential drivers (readily available globally) such as sea surface temperature, salinity, chlorophyll, and mixed layer depth either by multiple linear regression (e.g., Rödenbeck et al., 2015) or by using a neural network approach (e.g., Landschützer et al., 2013). Figure 1.6 shows an example of a reconstructed fCO_{2w} product based on the SOCAT dataset (Figure 1.5) and a neural network technique (Landschützer et al., 2016, 2020).

1.2.4 Gas transfer velocity

The current advances in understanding gas transfer and the remaining challenges are comprehensively reviewed in a book chapter by Garbe et al. (2014) and a journal paper by Wanninkhof et al. (2009). Here, I summarise the basic principles and advancements in gas transfer velocity studies.

Molecular diffusion and turbulent transport are direct controlling factors of gas transfer (Jähne et al., 1987). Molecular diffusion is related to the properties of the gas and chemical and biological enhancement, while turbulent transport represents the environmental forcing which includes physical (e.g. wind, waves, bubbles, rain), chemical and biological processes (surfactants) in the atmosphere and seawater interface (Garbe et al., 2014).

Molecular diffusion: The molecular diffusion effect on K is characterized by the Schmidt number dependence (Equation 1.7) and after being normalised to K_{660}, the gas transfer velocity is mainly controlled by the degree of the turbulence on both sides of the air-sea interface.

Chemical enhancement: The chemical reactions (Equation 1.3) in the mass boundary layer also possibly contribute to the CO_2 flux, which is known as the chemical enhancement effect. Typically, the timescale of the chemical equilibrium is longer than the molecular diffusion across the air-sea interface in the open ocean except for two conditions. 1) At the low wind speed of the tropics (with high sea surface temperature), the mass boundary layer is thicker, and the timescale of the chemical reactions is comparable to that of the molecular diffusion (Boutin et al., 1999; Wanninkhof & Knox, 1996); 2) At regions rich in carbonic anhydrase, which can catalyse chemical reactions between the carbon species and substantially shorten the equilibrium time (Matthews, 1999; Mustaffa et al., 2017).

Wind speed: Among all the turbulence-related factors, wind speed plays a dominant role over the global ocean, because wind strongly influences most of the air-sea interface physical processes (Wanninkhof, 2014). Wind can drive surface turbulence, generate ocean waves and bubbles, and disperse surfactants.

Ocean waves: Waves can affect the air-sea gas exchange significantly, especially breaking waves. Since CO_2 is a water-side controlled gas, turbulence at the sea surface strongly affects gas exchange. Breaking waves contribute significantly to turbulence at the sea surface and enhance the mixing of the surface layer (Jähne et al., 1987). However, due to the complexity of the properties of the waves and the difficulty of turbulence measurements, the contribution of the waves to the enhancement of air-sea gas exchange is difficult to quantify (Garbe et al., 2014). Zhao et al. (2003) argued that air-sea gas exchange depends not only on wind speed but also on the wind-wave state. Kitaigorodskii (2011) presented a wave-age dependent gas transfer velocity based on consideration of dissipation caused by the breaking waves. But due to the lack of *in-situ* observations, these models have not been verified in detail.

Bubbles: Bubbles enhance air-sea gas exchange via an additional exchange pathway. Bubble-mediated gas exchange is more complex than direct exchange across the sea surface. Firstly, solubility is a controlling factor in bubble-mediated exchange, with a greater enhancement for low-solubility gases compared with higher-solubility gases (Memery & Merlivat, 1985). Secondly, bubble-mediated exchange is asymmetric with bubble-driven gas fluxes for invasion being higher than for evasion (Woolf, 1997). The effect of bubbles has been argued to scale

with the fraction of whitecap cover which is often scaled with the cube of the wind speed (Monahan & Spillane, 1984).

Surfactants: Surfactants can suppress air-sea gas exchange by modifying the hydrodynamic properties of the sea surface and hence turbulent energy transfer (Garbe et al., 2014). Surfactants can be produced by phytoplankton (Frew et al., 1990) and enriched at the sea surface via bubble scavenging (Asher et al., 1996). Recent research found that the Atlantic Ocean CO_2 sink in 2014 was reduced by 9% due to surfactants (Pereira et al., 2018). But the effect of surfactants is probably more significant at low to moderate wind speeds (Yang et al., 2021) because high winds and waves can disperse surfactants.

Sea ice: Sea ice is a barrier between the atmosphere and seawater which strongly reduces air-sea gas exchange. The effect of sea-ice cover on air-sea gas exchange has been found that the CO_2 gas transfer velocity at an area decreases in proportion to the percentage of sea-ice cover (Butterworth & Miller, 2016; Prytherch et al., 2017; Takahashi et al., 2009). Other studies suggest that the gas transfer velocity is higher than the linear scaling with sea ice cover, which indicates that the K_{660} appears to be driven by other kinetics than wind speed in the ice-covered zone (Loose et al., 2009, 2017). Sea ice is not an inert medium and can hold tracers such as CO_2.

Among all the driving factors described above, wind speed is the major driver of gas transfer and the global wind speed data is also readily available, and thus K_{660} is often parameterised with the 10-meter wind speed (U_{10}). The wind speed dependence of K_{660} can be constrained by theoretical considerations, the global bomb-^{14}C inventory, local dual-tracer results, and local eddy covariance observations.

Theoretical considerations: Based on the gas exchange theory and wind-wave tank results, Liss & Merlivat (1986) identified three regimes where different physical processes appear to be controlling gas exchange: the smooth surface regime, the rough surface regime, and the breaking wave (bubble) regime. They proposed three linear segments of K_{660} with U_{10} adjusted to a lake environment (Wanninkhof et al., 1985):

$$K_{660} = 0.16U_{10} \quad (U_{10} \leq 3.6 \text{ m s}^{-1}) \tag{1.19}$$

$$K_{660} = 2.72U_{10} - 9.2 \quad (3.6 < U_{10} \leq 13 \text{ m s}^{-1}) \tag{1.20}$$

$$K_{660} = 5.63U_{10} - 47 \quad (U_{10} > 13 \text{ m s}^{-1}) \tag{1.21}$$

The bomb-^{14}C inventory: In the early 1960s, a large amount of bomb-^{14}C was released into the atmosphere due to atomic bomb testing. The global inventory of bomb-^{14}C in the ocean provides a global constraint on the air-sea exchange rate of gases such as CO_2. The ^{14}C gas exchange data was first established by Broecker et al. (1985, 1986). Wanninkhof (1992) employed this ^{14}C exchange data assumed a quadratic relationship between K_{660} and wind speed based on wind-wave tank studies (Wanninkhof and Bliven, 1991), and proposed an widely used K_{660}–wind speed parameterisation for steady or short-term winds:

$$K_{660} = 0.31{U_{10}}^2 \tag{1.22}$$

A reassessment of the bomb-^{14}C inventory (Naegler, 2009; Sweeney et al., 2007) in the ocean suggested a lower global mean gas transfer velocity (16.5 ± 3.2 cm h^{-1}) compared to the previous estimate (21.9 ± 3.3 cm h^{-1}, Broecker et al., 1985). The global wind speed product was also improved by remote sensing observations. Using the updated bomb-^{14}C inventory dataset and a improved wind speed product (CCMP, Atlas et al., 2011), Wanninkhof (2014) revised the parameterisation of Equation 1.22 into:

$$K_{660} = 0.25{U_{10}}^2 \tag{1.23}$$

The coefficient (here 0.25) changes with different wind speed products (Fay et al., 2021). Global ocean CO_2 flux estimates often scale K to match a global mean transfer velocity of 16.5 cm h^{-1} (Naegler, 2009). Note that the Liss & Merlivat (1986) parametrisation yields a significantly smaller mean global gas transfer velocity than the constraint by the bomb-^{14}C inventory (Figure 1.7), and this parameterisation is thus not recommended for global ocean CO_2 flux estimates. Equation 1.23 is derived from large spatial (the global ocean) and time (half-century) scales. Its application to local and short-time CO_2 flux estimates needs to be confirmed by further regional studies.

Dual-tracer experiments: The local dual-tracer studies provide strong regional evidence to support the quadratic wind speed dependence of the gas transfer velocity in Equations 1.22 and 1.23. The gases ^{3}He and SF_6 have different molecular diffusion coefficients. When they are released into the ocean deliberately, the loss of the gas for the water due to gas exchange will be different. The gas transfer velocity can be derived by successive ^{3}He and SF_6 concentration measurements (Watson et al., 1991). Based on the dual-tracer experiments in the North Sea (a coastal sea), Nightingale et al. (2000) proposed another popular parameterisation of K_{660}:

$$K_{660} = 0.32U_{10} + 0.21{U_{10}}^2 \tag{1.24}$$

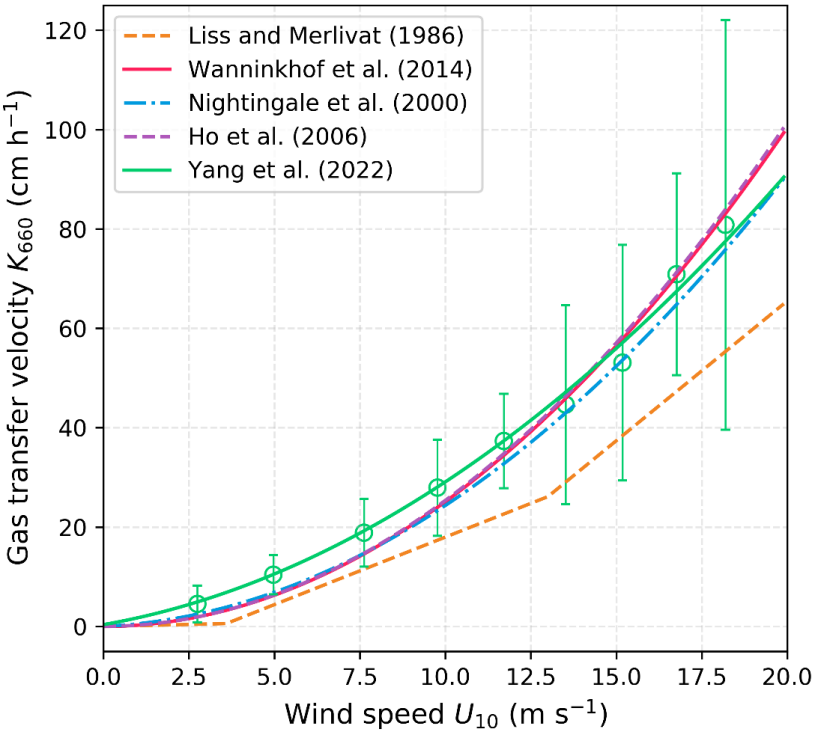

Figure 1.7 The normalised gas transfer velocity (K_{660}) versus 10-meter wind speed (U_{10}) for different parameterisation schemes. The orange, red, blue, purple, and green lines represent the gas transfer velocity parameterisation based on theoretical considerations (Equation 1.19 to 1.21; Liss & Merlivat, 1986), the updated bom-^{14}C inventory (Equation 1.23; Wanninkhof, 2014), the North Sea dual-tracer observations (Nightingale et al., 2000), the Southern Ocean dual-tracer measurements (Ho et al., 2006), and a global synthesis of eddy covariance observations (Yang et al., 2022), respectively. The green circles are the grand (ensemble) average of eddy covariance K_{660} measurements in different ocean regions with the error bars indicating the standard deviation (Yang et al., 2022).

More recently, Ho et al. (2006) performed a dual-tracer experiment in the Southern Ocean (open ocean) with wind speeds up to 16 m s^{-1}. This led to a K_{660}–U_{10} parameterisation similar to Equations 1.23 and 1.24 (Figure 1.7). Therefore, Equations 1.23 and 1.24 and the parametrisation of Ho et al. (2006) are widely used for local air-sea CO_2 flux estimates.

The temporal scale of the dual-tracer observations (days) is shorter than that of the bomb-^{14}C constraint, but it is still much longer than the timescale of the air-sea gas exchange (seconds, Jähne, 2019). In addition, based on the existing open-ocean dual-tracer observations, only 1 and 3 values for K_{660} are available at the low (smooth) and high (breaking) wind speed regimes, respectively (Ho et al., 2011).

Eddy covariance technique: The eddy covariance (EC) technique provides small-scale

(hourly) gas transfer velocity observations. The EC technique can be used to measure air-sea CO_2 fluxes directly, and by combining the EC CO_2 flux with air-sea fugacity difference measurements, the K can be derived. With advances in the EC system setup and the data processing procedures, the EC technique has been successfully used to measure K in different ocean regions, which were then used to study mechanisms of air-sea CO_2 exchange (Bell et al., 2017; Blomquist et al., 2017; Butterworth & Miller, 2016; Dong et al., 2021b; Fairall et al., 2022; Landwehr et al., 2018; Miller et al., 2009; Prytherch & Yelland, 2021; Yang et al., 2021; Zavarsky et al., 2018). In supplement S1, I summarise and assess the progress of gas transfer velocity measurements made using the EC technique over the last quarter of the century. Yang et al. (2022) synthesised eight EC datasets (from 11 research cruises) and proposed a new parameterisation of K_{660} for CO_2 based on the grand average of these EC K_{660} datasets:

$$K_{660} = 0.36 + 1.20U_{10} + 0.17{U_{10}}^2 \quad (1.25)$$

Compared to Equations 1.23 and 1.24, this small-scale EC-based parameterisation has a constant term and higher K_{660} values at low wind speeds (Figure 1.7), which might be due to the chemical enhancement of CO_2 exchange. The K_{660}–U_{10} relationship from EC observations on different cruises suggests apparent regional variation (see Yang et al., 2022 for details; error bars in Figure 1.7 represent standard deviations of the K_{660} from different cruises), which can be attributed to the impact of driving factors other than the wind speed. Therefore, only using wind speed to estimate K_{660} is insufficiency. The mechanistic understanding of the air-sea gas exchange process is key to improving the parameterisation of K_{660} and to reducing the uncertainty associated with the K_{660} in global and regional air-sea CO_2 flux estimates.

1.3 Current knowledge gaps

Although scientists worldwide have made efforts to advance our understanding of ocean CO_2 uptake, many knowledge gaps still exist and the uncertainties in regional and global ocean CO_2 flux estimates are significant notably for the polar oceans. In this section, I summarise the main challenges which I focus on in this thesis.

Uncertainties in the gas transfer velocity: For surface observation-based global air-sea CO_2 flux estimates, the main uncertainty is considered to be the uncertainty in the parameterisation of the gas transfer velocity (Woolf et al., 2019). As reviewed in section 1.2.4, wind speed is the major but not the only driver for air-sea CO_2 exchange, but the widely used parametrisation schemes all relate K_{660} with wind speed only (Figure 1.7). The mechanism studies of air-sea gas exchange based on the EC technique (Table S1.1) indicated that using wind speed only is

insufficient to describe K_{660}. The EC technique is a powerful tool in improving the parameterisation of K_{660}, but the inherent uncertainties in EC air-sea CO_2 flux measurements have not been well quantified, which may confound analyses of EC fluxes and EC-derived K_{660}. A better understanding of the uncertainties in ship-based EC CO_2 fluxes can enhance our confidence in using EC measurements to explore mechanisms of the gas exchange and to validate the indirect bulk flux estimates. The main aim of Chapter 2 is to thoroughly analyse the uncertainties in ship-based EC air-sea CO_2 flux measurements.

Challenges of the well-mixing assumption: The CO_2 fugacity measurements are typically made at ~5 meter depth and then employed to estimate air-sea CO_2 fluxes by the bulk equation (Equation 1.12). This estimate includes an implicit assumption that the seawater in the upper ocean layer (e.g., 1 mm –10 m depth) is well mixed, and that the fCO_{2w} at 5 m depth is identical to that at the bottom of the mass boundary layer (Figure 1.4). However, summertime sea-ice melt results in near-surface stratification and the fCO_{2w} at 5 m might differ from that close to the sea surface (e.g., 20 cm, Miller et al., 2019). In this case, using fCO_{2w} taken from a ship's seawater inlet at ~5 m depth will bias the air-sea CO_2 flux. In Chapter 3, I show the impact of shallow stratification due to sea-ice melt on Arctic air-sea CO_2 flux estimates.

Challenges of the Southern Ocean CO_2 flux estimates: As shown in Figure 1.5, the Southern Ocean has the lowest surface ocean CO_2 measurement density in SOCAT compared to other ocean basins, leading to high uncertainty in Southern Ocean CO_2 flux estimates (Gruber et al., 2019). The novel pH observations by biogeochemical floats (SOCCOM, Southern Ocean Carbon and Climate Observations and Modelling) provide an opportunity to fill the data gap. However, SOCCOM-based CO_2 flux estimates substantially disagree with SOCAT-based CO_2 flux estimates (Bushinsky et al., 2019; Gray et al., 2018). In Chapter 4, I employ independent novel CO_2 flux measurements by eddy covariance in the Southern Ocean to validate the current CO_2 flux estimates, and provide insights on how to improve the Southern Ocean CO_2 sink estimates.

Questionable temperature treatments: Sea surface temperature (SST) is not an explicit variable in the bulk equation (Equation 1.12), but as indicated by Equations 1.13 to 1.18, SST is a key variable for air-sea CO_2 flux estimates. A small bias in SST (e.g., 0.1 K) may not be important for local air-sea CO_2 estimates in regions with large flux signals, but is significant for estimating the global air-sea CO_2 flux because the absolute value of the air-sea CO_2 fugacity difference (ΔfCO_2) is on average only ~10 µatm globally from 1982 to 2021 (Fay et al., 2021).

According to the Takahashi et al. (1993) temperature normalisation (Equation 1.14), with a mean seawater CO_2 fugacity of ~400 µatm for the global ocean, a 0.1 K bias in SST will result in ~1.7 µatm or ~17% change in the global mean ΔfCO_2 and thus the global air-sea CO_2 flux. The ship SST in the SOCAT dataset is typically used for the conversion process of fCO_{2w}, but the SST measured by ships is well known by the SST community to have a warm bias (Kennedy et al., 2019). In addition, as shown by Equations 1.11, 1.12 and Figure 1.4, the CO_2 solubility is temperature dependent and the temperature very close to the sea surface (e.g., the skin temperature) should be used to calculate the interface solubility (α_i). However, the subskin (e.g., at 20 cm depth) or the subsurface (e.g., at ~5 m depth) temperature is often used for the calculation of α_i. The skin temperature is generally lower than the subskin temperature because of the cool skin effect (Donlon et al., 2002; Fairall et al., 1996; Robertson & Watson, 1992). By considering these two temperature effects (warm bias in the SOCAT SST and the cool skin effect), Watson et al. (2020) estimated that the net global ocean CO_2 uptake increases by ~0.9 Pg C yr^{-1} (~50%) on average from 1982 to 2019. I revisit these two temperature effects and provide an updated temperature correction for global air-sea CO_2 flux estimates.

Chapter 2

2 Methods

"Research is not about RIGHT or WRONG, it is about improving the understanding."

(Mingxi Yang, September 2020)

The results presented in the following chapter have been published in:

Uncertainties in eddy covariance air-sea CO_2 flux measurements and implications for gas transfer velocity parameterisations

Yuanxu Dong[1,2], Mingxi Yang[2], Dorothee C. E. Bakker[1], Vassilis Kitidis[2] and Thomas G. Bell[2]

[1]Centre for Ocean and Atmospheric Sciences, School of Environmental Sciences, University of East Anglia, Norwich, UK
[2]Plymouth Marine Laboratory, Prospect Place, Plymouth, UK

Atmospheric Chemistry and Physics, 2021, 21, 8089–8110.
https://doi.org/10.5194/acp-218089-2021

The work and analysis presented in this chapter was led by Y. Dong. Co-authors on this publication collected the data, provided guidance and suggestions regarding the analysis and the results to help and address the interests of the wider scientific community.

Abstract: Air-sea carbon dioxide (CO_2) flux is often indirectly estimated by the bulk method using the air-sea difference in CO_2 fugacity (ΔfCO_2) and a parameterisation of the gas transfer velocity (K). Direct flux measurements by eddy covariance (EC) provide an independent reference for bulk flux estimates and are often used to study processes that drive K. However, inherent uncertainties in EC air-sea CO_2 flux measurements from ships have not been well quantified and may confound analyses of K. This paper evaluates the uncertainties in EC CO_2 fluxes from four cruises. Fluxes were measured with two state-of-the-art closed-path CO_2 analysers on two ships. The mean bias in the EC CO_2 flux is low but the random error is relatively large over short time scales. The uncertainty (1 standard deviation) in hourly averaged EC air-sea CO_2 fluxes (cruise-mean) ranges from 1.4 to 3.2 mmol m^{-2} day^{-1}. This corresponds to a relative uncertainty of ~20% during two Arctic cruises that observed large CO_2 flux magnitude. The relative uncertainty was greater (~50%) when the CO_2 flux magnitude was small during two Atlantic cruises. Random uncertainty in the EC CO_2 flux is mostly caused by sampling error. Instrument noise is relatively unimportant. Random uncertainty in EC CO_2 fluxes can be reduced by averaging for longer. However, averaging for too long will result in the inclusion of more natural variability. Auto-covariance analysis of CO_2 fluxes suggests that the optimal timescale for averaging EC CO_2 flux measurements ranges from 1–3 hours, which increases the mean signal-to-noise ratio of the four cruises to higher than 3. Applying an appropriate averaging timescale and suitable ΔfCO_2 threshold (20 µatm) to EC flux data enables an optimal analysis of K.

2.1 Introduction

Since the Industrial Revolution, atmospheric CO_2 levels have risen steeply due to human activities (Broecker & Peng, 1993). The ocean plays a key role in the global carbon cycle, having taken up roughly one--quarter of anthropogenic CO_2 emissions over the last decade (Friedlingstein et al., 2020). Accurate estimates of air-sea CO_2 flux are vital to forecast climate change and to quantify the effects of ocean CO_2 uptake on the marine biosphere.

Air-sea CO_2 flux (F, e.g., in mmol m^{-2} day^{-1}) is typically estimated indirectly by the bulk equation:

$$F = K_{660}(Sc/660)^{-0.5}\,\alpha\left(fCO_{2w} - fCO_{2a}\right) \quad (2.1)$$

Where K_{660} (in cm h^{-1}) is the gas transfer velocity, usually parameterised as a function of wind speed (e.g., Nightingale et al., 2000), *Sc* (dimensionless) is the Schmidt number (Wanninkhof, 2014) and α (mol L^{-1} atm^{-1}) is the solubility (Weiss, 1974). *Sc* is equal to 660 for CO_2 at 20°C and 35‰ salt water (Wanninkhof et al., 2009). fCO_{2w} and fCO_{2a} are the CO_2 fugacity (in µatm) at the sea surface and in the overlying atmosphere, respectively, with $fCO_{2w} - fCO_{2a}$ the air-sea CO_2 fugacity difference (ΔfCO_2). Uncertainties in the K_{660} parameterisation and limited coverage of fCO_{2w} measurements result in considerable uncertainties in global bulk flux estimates (Takahashi et al., 2009; Woolf et al., 2019). Note that the impact of the cool skin effect on CO_2 flux estimates is not considered in this chapter.

Eddy covariance (EC) is the most direct method for measuring the air-sea CO_2 flux *F*:

$$F = \rho \overline{w'c'} \tag{2.2}$$

where ρ is the mean mole density of dry air (e.g., in mole m^{-3}). The dry CO_2 mixing ratio *c* (in ppm or µmol mol^{-1}) is measured by a fast-response gas analyser and the vertical wind velocity *w* (in m s^{-1}) is often measured by a sonic anemometer. The prime denotes the fluctuations from the mean, while the overbar indicates the time average. Equation 2.2 does not rely on ΔfCO_2 measurements nor empirical parameters and assumptions of the gas properties (Wanninkhof, 2014). EC flux measurements can therefore be considered useful as an independent reference (i.e., direct real flux measurements) for bulk air-sea CO_2 flux estimates. Furthermore, the typical temporal and spatial scales of EC flux measurements are ca. hourly and 1–10 km^2. These scales are much smaller than the temporal and spatial scales of alternative techniques for measuring gas transfer, e.g., by dual tracer methods (daily and 1000 km^2) (Nightingale et al., 2000; Ho et al., 2006). EC measurements are thus potentially better-suited to capture variations in gas exchange due to small-scale processes at the air-sea interface (Garbe et al., 2014).

The EC CO_2 flux method has developed and improved over time. Before 1990, EC was successfully used to measure air-sea momentum and heat fluxes. EC air-sea CO_2 flux measurements made during those times were unreasonably high (Jones & Smith, 1977; Wesely et al., 1982; Smith & Jones, 1985; Broecker et al., 1986). After 1990, with the development of the infrared gas analyser, EC became routinely used for terrestrial carbon cycle research (Baldocchi et al., 2001). Development of the EC method was accompanied by improvements in the flux uncertainty analysis, which was generally based on momentum, heat and land-atmosphere gas flux measurements (Lenschow & Kristensen, 1985; Businger, 1986; Lenschow et al., 1994; Wienhold et al., 1995; Mahrt, 1998; Finkelstein & Sims, 2001; Loescher et al.,

2006; Rannik et al., 2009, 2016; Billesbach, 2011; Mauder et al., 2013; Langford et al., 2015; Post et al., 2015).

In the late 1990s, the advancement in motion correction of wind measurements (Edson et al., 1998; Yelland et al., 1998) facilitated ship-based EC CO_2 flux measurements from a moving platform (McGillis et al., 2001; 2004). After 2000, a commercial open-path infrared gas analyser LI-7500 (LICOR Inc. USA) became widely used for air-sea CO_2 flux measurements (Weiss et al., 2007; Kondo & Tsukamoto, 2007; Prytherch et al., 2010a; Edson et al., 2011; Else et al., 2011; Lauvset et al., 2011). The LI-7500 generated extremely large and highly variable CO_2 fluxes in comparison to expected fluxes (Kondo & Tsukamoto, 2007; Prytherch et al., 2010a; Edson et al., 2011; Else et al., 2011; Lauvset et al., 2011). This problem is generally considered to be an artefact caused by water vapour cross-sensitivity (Kohsiek, 2000; Prytherch et al., 2010a; Edson et al., 2011; Landwehr et al., 2014). Mathematical corrections proposed to address this artefact (Edson et al., 2011; Prytherch et al., 2010a) were later shown to be unsatisfactory (Else et al., 2011; Ikawa et al., 2013; Blomquist et al., 2014; Tsukamoto et al., 2014) or incorrect (Landwehr et al., 2014).

The most reliable method for measuring EC air-sea CO_2 fluxes involves the physical removal of water vapour fluctuations from the sampled air. The simplest approach is to combine a closed-path gas analyser with a physical dryer to eliminate most of the water vapour fluctuation (Miller et al., 2010; Blomquist et al., 2014; Landwehr et al., 2014; Yang et al., 2016a; Nilsson et al., 2018). The tuneable-diode-laser-based cavity ring-down spectrometer (CRDS) made by Picarro Inc. (Santa Clara, California, USA) is the most precise closed-path analyser currently available (Blomquist et al., 2014). The closed-path infrared gas analyser LI-7200 (LICOR Biosciences, Lincoln, Nebraska, USA) is another popular choice.

The advancements in instrumentation and in motion correction methods have significantly improved the quality of air-sea EC CO_2 flux observations but, despite these changes, the flux uncertainties have not been well-quantified. The aims of this study are to: 1) analyse uncertainties in EC air-sea CO_2 flux measurements; 2) propose practical methods to reduce the systematic and random flux uncertainty; and 3) investigate how the EC flux uncertainty influences our ability to estimate and parameterise K_{660}.

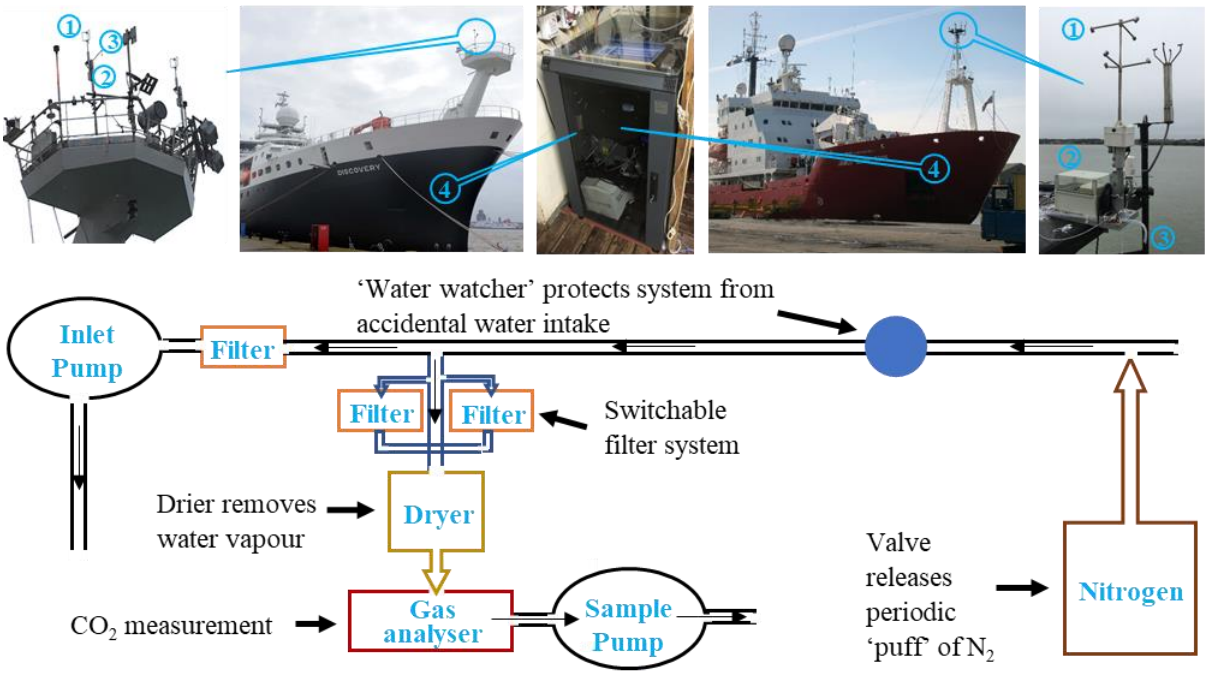

Figure 2.1 EC system (upper panel) and a diagram of system setup (bottom panel). EC instruments: 1) Sonic anemometer, 2) Motion sensor, 3) Air sample inlet for gas analyser, 4) Datalogger/gas analyser. Arctic and Atlantic data from 2018 were collected on the RRS *James Clark Ross* (JCR, upper right) using a Picarro G2311-f, and Atlantic data from 2019 were collected using a LI-7200 on the RRS *Discovery* (upper left).

2.2 Experiment and methods

2.2.1 Experimental setup

The basic information of the four cruises is summarised in Table 2.1. Appendix A2 shows the four cruise tracks (Figure A2.1, A2.2). Data from the Atlantic cruises (AMT28 and AMT29) are limited to 3°N–20°S in order to focus specifically on the performance of two different gas analysers in the same region with low flux signal (tropical zone).

The CO_2 flux and data logging systems installed on the JCR and Discovery were operated autonomously. The EC systems were approximately 20 m above mean sea level on both ships (at the top of the foremasts, Figure 2.1) to minimise flow distortion and exposure to sea spray. Computational fluid dynamics (CFD) simulation indicates that the airflow distortion at the top of the JCR foremast is small (~1% of the free stream wind speed when the ship is head to wind, Moat & Yelland, 2015). The hull structure of RRS *Discovery* is nearly identical to that of RRS *James Cook*. CFD simulation of the *James Cook* indicates that the airflow at the top foremast

is distorted by ~2% for bow-on flows (Moat et al., 2006). The deflection of the streamline from horizontal and its effects on the vertical wind component is accounted for by the double rotation (motion correction processes, see Section 2.2.2) prior to the EC flux calculation for both ships.

Table 2.1 Basic information for all four cruises on the RRS *James Clark Ross* (JCR) and RRS *Discovery* that measured air-sea EC CO_2 fluxes.

Cruise	**JR18006**	**JR18007**	**AMT28**	**AMT29**
Data period	30 June–1 August 2019	5 August–29 September 2019	9 October–16 October 2018	4 November–11 November 2019
Visited region	Arctic Ocean (Barents Sea)	Arctic Ocean (Fram Strait)	Tropical Atlantic Ocean	Tropical Atlantic Ocean
Research vessel	JCR	JCR	JCR	Discovery
Gas analyser	Picarro G2311-f	Picarro G2311-f	Picarro G2311-f	LI-7200

The EC system on the JCR consists of a three-dimensional sonic anemometer (Metek Inc., Sonic-3 Scientific), a motion sensor (initially Systron Donner Motionpak II, which compared favourably with and was then replaced by a Life Performance-Research LPMS-RS232AL2 in April 2019), and a Picarro G2311-f gas analyser. All instruments sampled at a frequency of 10 Hz or greater and the data were logged at 10 Hz with a datalogger (CR6, Campbell Scientific, Inc.), similar to the setup by Butterworth & Miller (2016). Air is pulled through a long tube (30 m, 0.95 cm inner diameter, Reynolds number 5957) with a dry vane pump at a flow rate of ~40 L min^{-1} (Gast 1023 series). The Picarro gas analyser subsamples from this tube through a particle filter (Swagelok 2 µm) and a dryer (Nafion PD-200T-24M) at a flow of ~5 L min^{-1} (Figure 2.1). The dryer is setup in the 're-flux' configuration and uses the lower-pressure Picarro exhaust to dry the sample air. This method removes ~80% of the water vapour and essentially all of the humidity fluctuations (Yang et al., 2016a). The Picarro internal calculation accounts for the detected residual water vapour and yields a dry CO_2 mixing ratio that is used in the flux calculations. A valve controlled by the Picarro instrument injects a 'puff' of nitrogen (N_2) into the tip of the inlet tube for 30 s every 6 hours. This enables estimates of the time delay and high-frequency signal attenuation (Section 2.2.2).

The EC system on RRS *Discovery* consists of a Gill R3-50 sonic anemometer, an LPMS motion sensor package, and a LI-7200 gas analyser. The LI-7200 gas analyser was mounted within the enclosed staircase, directly underneath the meteorological platform and close to the inlet (inlet

length 7.5 m, inner diameter 0.95 cm, Reynolds number 1042). A single pump (Gast 1023) was sufficient to pull air through a particle filter (Swagelok 2 µm), a dryer (Nafion PD-200T-24M), and the LI-7200 at a flow of ~7 L min^{-1}. There was no N_2 puff system setup on Discovery but equivalent lab tests confirmed that the delay time was less than on the JCR because of the shorter inlet line. The dryer on the Discovery is setup in the same 're-flux' configuration as the JCR and uses the lower pressure at the LI-7200 exhaust (limited by an additional 0.08 cm diameter critical orifice) to dry the sample air. This setup removes ~60–70% of the water vapour and essentially all of the humidity fluctuations. The dry CO_2 mixing ratio, computed by accounting for the LI-7200 temperature, pressure, and residual water vapour measurements, is used in the flux calculations.

2.2.2 Flux processing

The EC air-sea CO_2 flux calculation steps using the raw data are outlined with a flow chart (Figure 2.2) and detailed below. The raw high-frequency wind and CO_2 data are processed first, yielding fluxes in 20 min averaging time interval and related statistics. These statistics are then used for quality control of the fluxes. Further averaging of the quality-controlled 20 min fluxes to hourly or longer time scales is then used to reduce random error (Section 2.4.1). Linear detrending was used to identify the turbulent fluctuations (i.e., w' and c') throughout the analyses.

To correct the wind data for ship motion, we first generated hourly data files containing the measurements from the sonic anemometer (three-dimensional wind speed components: u, v and w and sonic temperature Ts), motion sensor (three-axis accelerations: accel_x, accel_y, accel_z; and rotation angles: rot_x, rot_y, rot_z), the ship heading over ground (HDG, from the gyro compass) and ship speed over ground (SOG, from Global Position System). Spikes larger than 4 standard deviations (SDs) from the median were removed. Secondly, a complementary filtering method using Euler angles (see Edson et al., 1998) was applied to the hourly data files to remove apparent winds generated by the ship movements. The motion-corrected winds were further decorrelated against ship motion to remove any residual motion-sensitivity (Miller et al., 2010; Yang et al., 2013). The motion-corrected winds were double-rotated to account for the wind streamline over the ship, yielding the vertical wind velocity (w) required in Equation 2.2. Inspection of frequency spectra showed that the spectral peak at the ship motion frequencies (approximately 0.1–0.3 Hz) had disappeared after the motion correction (Figure S2.1, Supplement S2). This indicates that the majority of ship motion had

been removed from the measured wind speed. The last step in the wind data processing was the calculation of 20 min average friction velocity, sensible heat flux and other key variables used for data quality control (Table S2.1, Supplement S2).

The CO_2 data were de-spiked (by removing values > 4 SDs from the median). The Picarro CO_2 mixing ratio was further decorrelated against analyser cell pressure and temperature to remove CO_2 variations due to the ship's motion. The LI-7200 CO_2 mixing ratio was further decorrelated against the LI-7200 H_2O mixing ratio and temperature to remove residual air density fluctuations, following Landwehr et al. (2018). CO_2 data were also decorrelated against the ship's heave and accelerations because these can produce spurious CO_2 variability (Miller et al., 2010; Blomquist et al., 2014).

A lag between CO_2 data acquisition and the wind data is created because of the time taken for sample air to travel through the inlet tube. On the JCR, we use the 'puff' system where the lag time is the time difference between the N_2 'puff' start (when the on/off valve is switched) and the time when the diluted signal is sensed by the gas analyser. The lag time can also be estimated by the maximum covariance method, calculated by shifting the time base of the CO_2 signal and finding the shift that achieves maximum covariance between the vertical wind velocity (w) signal and the shifted CO_2 signal. The lag times estimated by the maximum covariance method agree well with the estimates of the 'puff' procedure (Figure S2.2, Supplement S2). These estimates indicate a lag time of 3.3–3.4 s for the Arctic cruises and 3.3 s for cruise AMT28 on the JCR. The maximum covariance method estimated lag time on Discovery (AMT29) was 2.6 s, consistent with laboratory test results prior to the cruise.

The inlet tube, particle filter and dryer cause high-frequency CO_2 flux signal attenuation. The N_2 'puff' was also used to assess the response time by considering the e-folding time in the CO_2 signal change (similar approaches have been used by Bariteau et al., 2010; Blomquist et al., 2014, Bell et al., 2015). The response time is 0.35 s for the EC system on JCR and 0.25 s for the EC system on Discovery (estimated in the laboratory prior to the cruise). These response times were combined with the relative wind speed-dependent, theoretical shapes of the cospectra (Kaimal et al., 1972) to estimate the percentage flux loss due to the inlet attenuation (Yang et al., 2013). The mean attenuation percentage is less than 10% with a relative wind speed dependence (Figure S2.3, Supplement S2). The attenuation percentage value was applied to the computed flux to compensate for the flux loss due to the high-frequency signal attenuation. Finally, horizontal CO_2 fluxes and other statistics such as CO_2 range and CO_2 trend

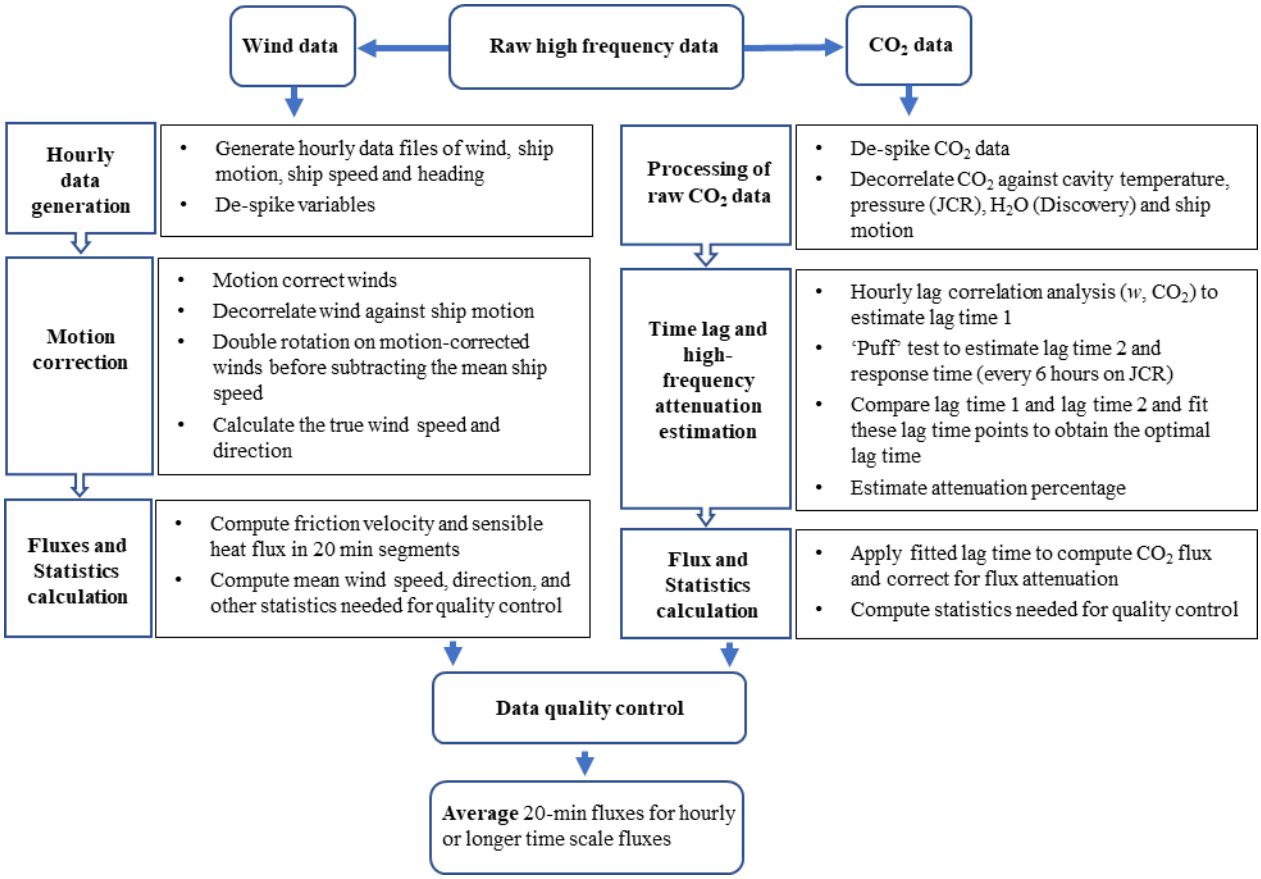

Figure 2.2 Flow chart of EC data processing. The raw high frequency (10 Hz) wind and CO_2 data were initially processed separately and then combined to calculate fluxes. CO_2 fluxes were filtered by a series of data quality control criteria. The 20-min flux intervals were averaged to longer time scales (hourly or more). The data processing is detailed in the text.

were computed for quality control purposes (Table S2.1, Supplement S2).

The computed 20-min fluxes were filtered for non-ideal ship manoeuvres or violations of the homogeneity/stationary requirement of EC (see Supplement S2 for the quality control criteria).

2.2.3 Uncertainty analysis methods

Uncertainty components: Uncertainty contains two components: systematic error (δF_S) and random error (δF_R). According to the propagation of uncertainty theory (JCGM, 2008), the total uncertainty in EC CO_2 fluxes (from random and systematic errors) can be expressed as:

$$\delta F = \sqrt{{\delta F_R}^2 + {\delta F_S}^2} \quad (2.3)$$

Systematic errors will cause bias in the flux. They thus should be eliminated/minimised with appropriate system setup and, if needed, effective numerical corrections. The random error results in imprecision (but not bias) and can be reduced by averaging repeated measurements. Errors due to insufficient sampling and instrument noise are generally considered the most important in EC flux measurements (Lenschow & Kristensen, 1985; Businger 1986; Mauder et al., 2013; Rannik et al., 2016).

Sampling error is an inherent issue for EC flux measurements and is typically the main source of CO_2 flux uncertainty (Mauder et al., 2013). The sampling error is caused by the difference between the ensemble average and the time average. The calculation of EC flux (Equation 2.2) requires the separation between the mean and fluctuating components, which can be represented fully for CO_2 mixing ratio c as:

$$c(x,t) = \bar{c}(x,t) + c'(x,t) \tag{2.4}$$

The mean component $\bar{c}$ represents ensemble average over time (t) and space (x) and does not contribute to the flux. The time average of a stationary turbulent signal and space average of a homogenous turbulent signal theoretically converge on the ensemble average when the averaging time approaches infinity, i.e., $T \to \infty$ (Wyngaard, 2010). In practice, Reynolds averaging over a much shorter time interval (10 min to an hour) is typically used for EC flux measurements from a fixed point or from a slow-moving platform such as a ship. This is because the atmospheric boundary layer is only quasi-stationary for a few hours. Non-stationarity (e.g., diurnal variability and synoptic conditions) is an inherent property of the atmospheric boundary layer (Wyngaard, 2010). EC flux observations thus inevitably contain some random error due to insufficient sampling time, and this error is greater at shorter averaging times.

Random error due to instrument noise comes mainly from the white noise of the gas analyser, as the noise from the sonic anemometer is relatively unimportant (Blomquist et al., 2010; Fairall et al., 2000; Mauder et al., 2013). Blomquist et al. (2014) show 'pink' noise with a weak spectral slope for their CRDS gas analyser (G1301-f), but the gas analysers on JCR (G2311-f) and Discovery (LI-7200) demonstrate white noise with a constant variance at high frequency (Figure B2.2, Appendix B2).

Systematic error: Table 2.2 details the measures taken during instrument setup and data processing that help eliminate most sources of systematic error in EC CO_2 fluxes.

Table 2.2 Potential sources of bias in our EC air-sea CO_2 flux measurements and the methods used to minimise them.

Potential source of bias	**Methods used to minimise the bias**	**Flux uncertainty**
$\boldsymbol{\delta F_{S,1}}$ **Water vapour cross-sensitivity**	Closed-path gas analyser with a dryer removes essentially all of the water vapour fluctuation (Blomquist et al., 2014; Yang et al., 2016a). The residual H_2O signal is measured by the gas analyser and used in the calculation of dry CO_2 mixing ratio, which removes water cross-sensitivity.	Negligible
$\boldsymbol{\delta F_{S,2}}$ **Ship motion**	Flux uncertainty from an earlier version of the motion correction procedure (less rigorous than the one used by ourselves) is estimated to be 10–20% (Edson et al. 1998). The more recently-adopted decorrelation of vertical winds and CO_2 against platform motion (Miller et al., 2010; Yang et al., 2013) reduces this uncertainty. Flügge et al. (2016) compare EC momentum fluxes measured from a moving platform (buoy) with fluxes measured from a nearby fixed tower. Flux estimates from these two platforms agree well (relative flux bias due to the motion correction ≤ 6%).	≤ 6%
$\boldsymbol{\delta F_{S,3}}$ **Airflow distortion**	The EC flux system is deployed as far forward and as high as possible on the ship (top of the foremast), which minimises the impacts of flow distortion. Subsequent distortion correction using the CFD simulation (Moat et al., 2006; Moat & Yelland, 2015) along with a relative wind direction restriction further reduces the impact of flow distortion on the fluxes. Measured EC friction velocities and friction velocities from the COARE3.5 model (Edson et al., 2013) agree well (e.g., R^2 = 0.95, slope = 0.97) for data collected during cruise JR18006. A good comparison between observed and COARE3.5 friction velocity estimates indicates that we have fully accounted for flow distortion effects.	Negligible
$\boldsymbol{\delta F_{S,4}}$	High-frequency flux signal attenuation (in the inlet tube, particle filter and dryer) is evaluated by the CO_2 signal	< 2% for the vast

Inlet effects (high-frequency flux attenuation and CO_2 sampling delay)	response to a puff of N_2 gas. Flux attenuation is calculated from the 'inlet puff' response and applied as a correction (< 10%, see Section 2.2.2). The uncertainty in the attenuation correction is about 1% for unstable/neutral atmospheric conditions, which is generally the case over the ocean (e.g., 93% of the time for Atlantic cruises, 80% of the time for Arctic cruises). During stable conditions, the attenuation correction is larger (Landwehr et al., 2018) and the uncertainty is also greater (~20%). The lag time adjustment prior to the flux calculation aligns the CO_2 and wind signals. Two methods are used to estimate the optimal lag time: puff injection and maximum covariance. The two lag estimates are in good agreement (Section 2.2.2). Random adjustment of ± 0.2 s (1 σ of the puff test result) to the optimal lag time impacts the CO_2 flux by < 1%.	majority of the cruises
$\delta F_{S,5}$ **Spatial separation between the sonic anemometer and the gas inlet**	The CO_2 inlet is ~70 cm directly below the centre volume of the sonic anemometer. This distance is small relative to the size of the dominant flux-carrying eddies encountered by the EC measurement system height above sea level. The excellent agreement between the lag time determined by the puff system and by the optimal covariance method further confirms that the distance between the CO_2 inlet and anemometer is sufficiently small.	Negligible
$\delta F_{S,6}$ **Imperfect calibration of the sensors**	The potential flux bias resulting from instrument calibration (gas analyser, anemometer and meteorological sensors required to calculate air density: air temperature, relative humidity and pressure) is up to 4% for the JCR setup. The largest instrument calibration uncertainty derives from the wind sensor accuracy (± 0.15 m s^{-1} at 4 m s^{-1} winds according to the Metek uSonic instrument specification). This bias is even lower (< 2%) for the Discovery setup because the Gill R3 sonic anemometer is more accurate.	≤ 4%
Propagated bias	Estimated from the individual bias estimates above ($\delta F_{S,1}, \delta F_{S,2}$, etc.) using $\delta F_S = \sqrt{\sum_1^n \delta F_{S,n}^2}$	< 7.5%

In addition to bias sources related to the instrument setup (Table 2.2), insufficient sampling time (an inherent issue of EC fluxes) may also generate a systematic error. We use a theoretical method to estimate this systematic error in EC CO_2 flux (Lenschow et al., 1994):

$$|\delta F_S| \leq 2\sigma_w \sigma_{c_a} \frac{\sqrt{\tau_w \tau_c}}{T} \tag{2.5}$$

where σ_w (m s^{-1}) and σ_{c_a} (ppm) are the standard deviations of the vertical wind velocity and the CO_2 mixing ratio due to atmospheric processes, respectively. T is the averaging time interval (s), and τ_w and τ_c are integral time scales (s) for vertical wind velocity and CO_2 signal, respectively. The definition and estimation of the integral time scale are shown in Appendix B2. The sign of δF_S could be positive or negative (i.e., under or over-estimation) because of the poor statistics in capturing low-frequency eddies within the flux averaging period (Lenschow et al., 1993). The mean hourly relative systematic error due to insufficient sampling time for four cruises estimated by Equation 2.5 is < 5%. According to the propagation of uncertainty theory (JCGM, 2008), the total systematic error is less than 9% ($= \sqrt{7.5\%^2 + 5\%^2}$).

Random error: Five approaches used to estimate the total random error (A–C) and the random error component due to instrument noise (C–E) in EC CO_2 fluxes are discussed below. The random error assessments are empirical (A and D) or theoretical (B, C and E).

A. An empirical approach to estimate total random error involves shifting the *w* data relative to the CO_2 data (or vice versa) by a large, unrealistic time shift and then computing the 'null fluxes' from the time-desynchronized CO_2 and *w* time series (Rannik et al., 2016). The shift removes any real correlation between CO_2 and *w* due to vertical exchange. The standard deviation of the resultant 'null' fluxes represents the random flux uncertainty (Wienhold et al., 1995). We applied a series of time shifts of $\sim 20 - 60 \times \tau_w$ (i.e., using time shifts ranging from -300 to -100 and 100 to 300 s, Rannik et al., 2016). This empirical estimation of total random flux uncertainty will hereafter be referred to as $\delta F_{R,\text{Wienhold}}$.

B. Lenschow & Kristensen (1985) derived a rigorous theoretical equation for total random error estimation, which contains both the auto-covariance and cross-covariance functions. The theoretical equation has been numerically approximated by Finkelstein & Sims (2001):

$$\delta F_{R,\text{ Finkelstein}} = \left\{ \frac{1}{n} \left[\sum_{p=-m}^{m} r_{ww}(p) r_{cc}(p) + \sum_{p=-m}^{m} r_{wc}(p)\, r_{cw}(p) \right] \right\}^{1/2} \tag{2.6}$$

where n is the number of data points within an averaging time interval, p is the number of shifting points. The maximum shifting point m can be chosen subjectively ($< n$). We found that the random error for m between 1000 and 2000 data points was similar, so for this study, we use $m = 1500$ (150 s shift time). The first term in the brackets represents the auto-covariance component and the second term is the cross-covariance component. r_{ww} and r_{cc} are the auto-covariance functions for vertical wind velocity (w) and CO_2 mixing ratio (c), respectively. r_{wc} and r_{cw} are the cross-covariance functions for w and c. Here r_{wc} represents shifting w data relative to CO_2 data, while r_{cw} represents shifting CO_2 data relative to w data.

C. Blomquist et al. (2010) attributed the sources of CO_2 variance σ_c^2 to atmospheric processes ($\sigma_{c_a}^2$) and white noise ($\sigma_{c_n}^2$). The sources of variance are considered to be independent of each other and the sonic anemometer is assumed to be relatively noise-free. According to the propagation of uncertainty theory (JCGM, 2008), the total random flux error can be defined as:

$$\delta F_{R,\,\text{Blomquist}} \leq \frac{a\sigma_w}{\sqrt{T}}\left(\sigma_{c_a}^2 \tau_{wc} + \sigma_{c_n}^2 \tau_{c_n}\right)^{1/2} \tag{2.7}$$

where the constant a varies from $\sqrt{2}$ to 2, depending on the relationship between the covariance of the two variables (w and CO_2) and the product of their auto-correlations (Lenschow & Kristensen, 1985). Here, τ_{wc} is equal to the shorter of τ_w and τ_c, which is typically τ_w (Blomquist et al., 2010), and τ_{c_n} is the integral time scale of white noise in the CO_2 signal. The CO_2 variance due to atmospheric processes ($\sigma_{c_a}^2$) includes two components: variance due to vertical flux (i.e., air-sea CO_2 flux) $\sigma_{c_{av}}^2$, and variance due to other atmospheric processes $\sigma_{c_{ao}}^2$ (Fairall et al., 2000). The variance in CO_2 due to vertical flux ($\sigma_{c_{av}}^2$) depends on atmospheric stability. $\sigma_{c_{av}}^2$ can be estimated with Monin-Obukhov similarity theory (Blomquist et al., 2010; Blomquist et al., 2014; Fairall et al., 2000):

$$\sigma_{c_{av}}^2 = \left[3\frac{\overline{w'c'}}{u_*} f_c(z/L)\right]^2 \tag{2.8}$$

where u_* is the friction velocity (m s^{-1}) and the similarity function (f_c) depends on the stability parameter z/L, where z is the observational height (m) and L is the Obukhov length (m). The expression of f_c can be found in Blomquist et al. (2010).

Equation 2.7 can be used to assess the random error due to instrument noise by setting $\sigma_{c_a}^2 = 0$, referred to hereafter as $\delta F_{RN,\,\text{Blomquist}}$. We use the CO_2 variance spectra to directly estimate the white noise term $\sigma_{c_n}^2 \tau_{c_n}$ in Equation 2.7. The variance is fairly constant at high frequencies

(1–5 Hz; Figure B2.2, Appendix B2), which is often referred to as band-limited white noise. The relationship between $\sigma_{c_n}^2 \tau_{c_n}$ and the band-limited noise spectral value φ_{c_n}, is expressed in Blomquist et al. (2010) as:

$$\sigma_{c_n}^2 \tau_{c_n} = \frac{\varphi_{c_n}}{4} \tag{2.9}$$

D. Billesbach (2011) developed an empirical method to estimate the random error due to instrument noise alone (referred to as $\Delta F_{RN,\,\text{Billesbach}}$). This involves random shuffling of the CO_2 time series within an averaging interval and then calculating the covariance of *w* and CO_2. The correlation between *w* and CO_2 is minimised by the shuffling, and any remaining correlation between *w* and CO_2 is due to the unintentional correlations contributed by instrument noise.

E. Mauder et al. (2013) describe another theoretical approach to estimate the random flux error due to instrument noise:

$$\delta F_{RN,\,\text{Mauder}} = \frac{\sigma_w \sigma_{c_n}}{\sqrt{n}} \tag{2.10}$$

White noise correlates with itself but is uncorrelated with atmospheric turbulence. Thus, the white noise-induced CO_2 variance (σ_{c_n}) only contributes to the total variance. The value of σ_{c_n} can be estimated from the difference between the zero-shift auto-covariance value (CO_2 variance σ_c^2) and the noise-free variance extrapolated to a time shift of zero (Lenschow et al., 2000):

$$\sigma_{c_n}^2 = \sigma_c^2 - \sigma^2(t \to 0) \tag{2.11}$$

where $\sigma^2(t \to 0)$ represents the extrapolation of auto-covariance to a zero shift, which is considered equal to variance due to atmospheric processes ($\sigma_{c_a}^2$). Figure 2.3 shows the normalised auto-covariance function curves of *w* and CO_2 as measured by the Picarro G2311-f and the LI-7200. There is a sharp decrease in the CO_2 auto-covariance when shifting from 0 s shift to 0.1 s shift for both the Picarro G2311-f and LI-7200 gas analyser. The same sharp decrease is not seen in the vertical wind velocity (*w*) auto-covariance. The relative difference

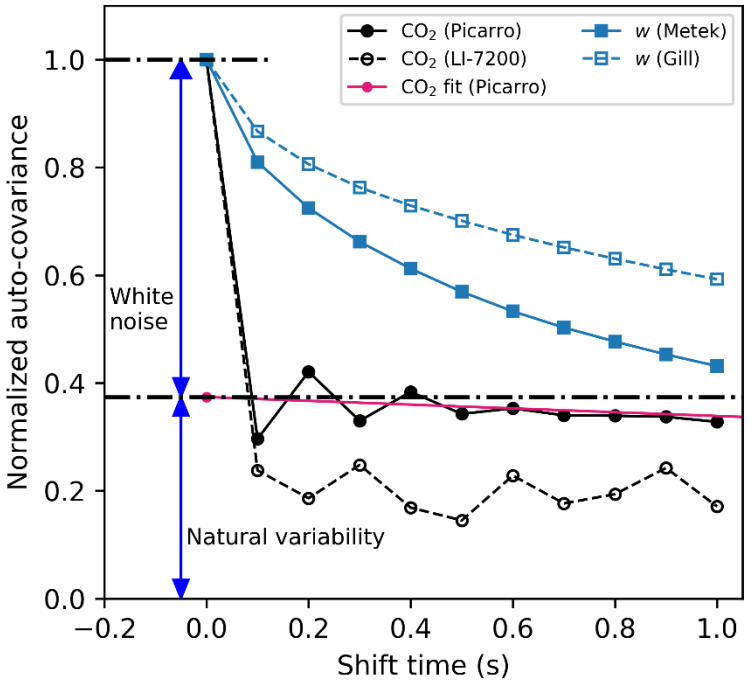

Figure 2.3 Mean normalised auto-covariance functions of CO_2 and vertical wind velocity (w) by four different instruments. The magenta line represents a fit to the noise-free auto-covariance function of CO_2 (measured by Picarro) extrapolated back to a zero time shift. An example of the white noise and natural variability contributions to the total CO_2 (measured by Picarro) variance is indicated by two blue arrows. The sharp decrease of the CO_2 auto-covariance between the zero shift and the initial 0.1 s shift corresponds to the large contribution of white noise from the gas analysers. The LI-7200 is the noisier instrument. The noise contributions from the anemometer are relatively small (< 10%).

in the change in normalised auto-covariance shows that white noise makes a much larger relative contribution to the CO_2 variance than to the vertical wind velocity variance.

2.3 Results

Measurements from AMT28 and AMT29 set the scene for our uncertainty analysis. These two Atlantic cruises transited across the same tropical region (Figure A2.2, Appendix A2) in October 2018 and September 2019 with different eddy covariance systems (Section 2.2.1). AMT28 and AMT29 show broadly similar latitudinal patterns (Figure 2.4a). An obvious question of interest is whether the measured fluxes were the same for the two years. To answer this question, the measurement uncertainties must be quantified. The total random uncertainties in CO_2 flux ($\delta F_{R,\,\text{Finkelstein}}$) are comparable for the two cruises even though the random error component due to instrument noise ($\delta F_{RN,\,\text{Mauder}}$) is about 3 times higher during AMT29 using LI-7200 than during AMT28 using Picarro G2311-f (Figure 2.4b; Figure D2.1, Appendix D2).

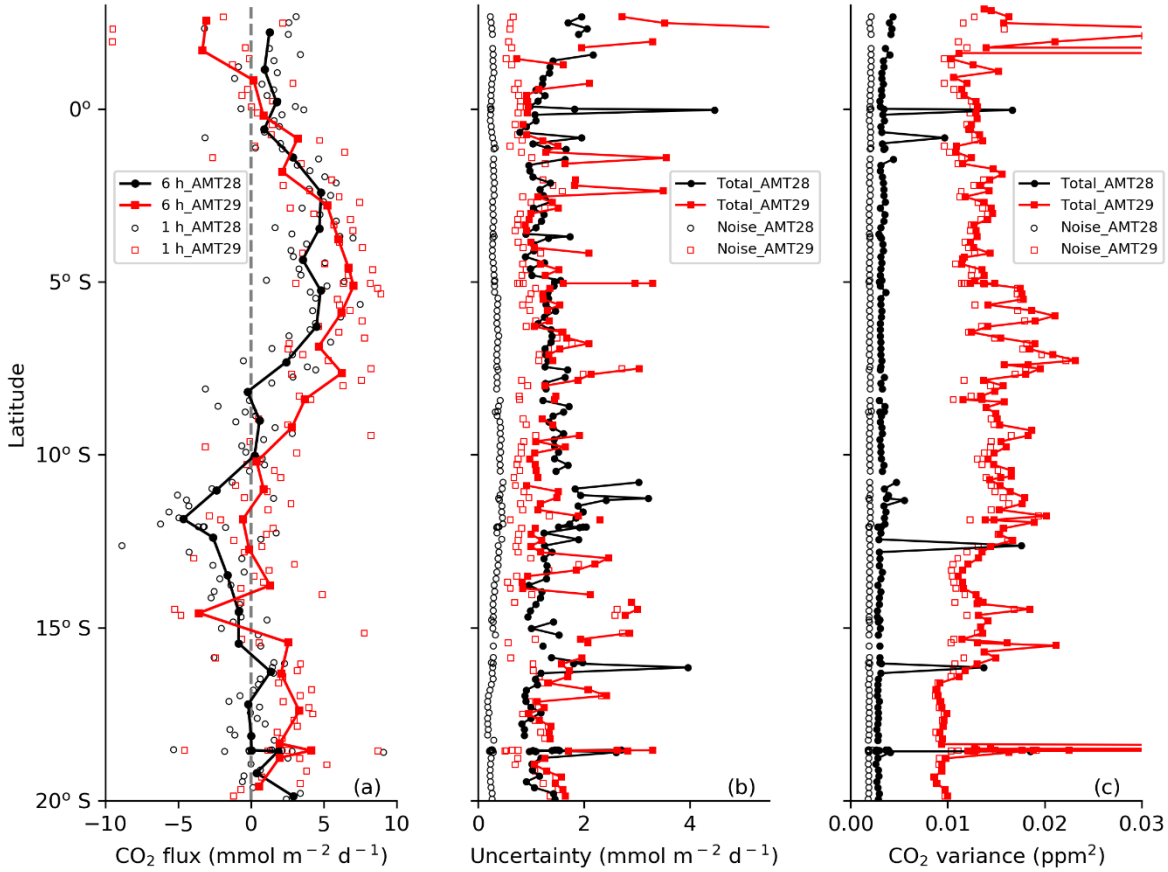

Figure 2.4 (a) Air-sea CO_2 fluxes (hourly and 6-h averages), (b) random uncertainty in flux (total and due to instrument noise only), and (c) variance in CO_2 mixing ratio (total and due to instrument noise only) for two Atlantic cruises.

The similar total random uncertainty in the AMT28 and AMT29 fluxes shows that both gas analysers are equally suitable for air-sea EC CO_2 flux measurements. The variance budgets of the atmospheric CO_2 mixing ratio (used to estimate random flux uncertainty, see Section 2.3.1) are shown in Figure 2.4c. Total variance in CO_2 mixing ratio is dominated by instrument noise on both cruises. CO_2 mixing ratio variance (total and instrument noise) was substantially higher during AMT29.

2.3.1 Random uncertainty

Theoretical derivation of flux uncertainty ($\delta F_{RN,\,\text{Blomquist}}$, Equation 2.7) requires knowledge of the contributions to CO_2 mixing ratio variance. Total CO_2 variance is made up of instrument noise ($\sigma_{c_n}^2$) and atmospheric processes ($\sigma_{c_a}^2$). Atmospheric processes include vertical flux ($\sigma_{c_{av}}^2$) and other atmospheric processes ($\sigma_{c_{ao}}^2$). The variance budgets of CO_2 mixing ratio for the four cruises are listed in Table 2.3. Atmospheric processes contribute a larger CO_2 variance in the

Arctic (where flux magnitudes are greater) compared to the Atlantic. Vertical flux accounts for ~10% of the variance in CO_2 mixing ratio in the Arctic and ~1% of the CO_2 variance in the Atlantic. Previous results demonstrate that horizontal transport is a major source of $\sigma_{c_{ao}}^2$ for long-lived greenhouse gases (Blomquist et al., 2012). Small changes in CO_2 mixing ratio transported horizontally can yield variance that greatly exceeds the variance from vertical flux.

Table 2.3 Variance in the CO_2 mixing ratio estimated using Equation 2.8 and 2.11 for the Arctic (JR18006/7, Picarro G2311-f) and Atlantic cruises (AMT28, Picarro G2311-f; AMT29, LI-7200). Total CO_2 variance (σ_c^2) consists of white noise ($\sigma_{c_n}^2$) and atmospheric processes ($\sigma_{c_a}^2$). The latter can be further broken down to the CO_2 variance due to vertical flux ($\sigma_{c_{av}}^2$) and due to other processes ($\sigma_{c_{ao}}^2$) (i.e., $\sigma_{c_{ao}}^2 = \sigma_{c_a}^2 - \sigma_{c_{av}}^2$).

CO_2 variance ($\times 10^{-3}$ ppm^2)	**JR18006**	**JR18007**	**AMT28**	**AMT29**
Total, σ_c^2	9.9	8.6	3.6	13.9
Due to instrument white noise, $\sigma_{c_n}^2$	5.8	5.4	2.0	12.6
Due to atmospheric processes, $\sigma_{c_a}^2$	4.1	3.3	1.6	1.3
- Due to vertical flux, $\sigma_{c_{av}}^2$	1.3	0.8	0.03	0.08
- Due to other atmospheric processes, $\sigma_{c_{ao}}^2$	2.8	2.5	1.6	1.2

Three quasi-independent methods were used to estimate random uncertainty in EC air-sea CO_2 fluxes caused by instrument noise (δF_{RN}, Methods C–E, Section 2.2.3). Good agreement was found between all three estimates (Figure C2.2, Appendix C2) when $\sqrt{2}$ is used as the constant in Equation 2.7 (a). The $\Delta F_{RN,\,\text{Billesbach}}$ estimates have more scatter and are slightly higher than the theoretical results, possibly because the random shuffling of data fails to fully exclude the contribution from atmospheric turbulence (Rannik et al., 2016). For the remainder of this study, we use the $\delta F_{RN,\,\text{Mauder}}$ method to estimate δF_{RN}.

We used three methods to estimate the total random uncertainty (δF_R, Methods A–C, Section 2.2.3) in the hourly-averaged air-sea CO_2 fluxes. There is good agreement among the three estimates ($r > 0.88$; Figure C2.1, Appendix C2). Again, the constant in Equation 2.7 (a) is set to $\sqrt{2}$, as informed by the instrument noise uncertainty analysis above. We use $\delta F_{R,\,\text{Finkelstein}}$ (Equation 2.6) to estimate the total random flux uncertainty hereafter. Our decision is based on

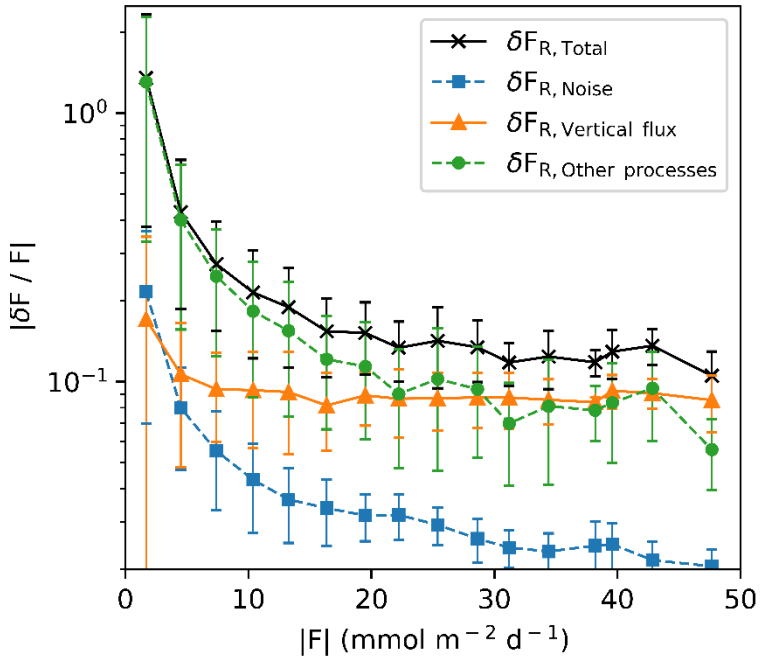

Figure 2.5 Relative random uncertainty in hourly CO_2 flux and its contribution from noise, vertical flux, and other processes during two Arctic cruises. Relative random uncertainty data are binned into 3 mmol m^{-2} day^{-1} flux magnitude bins (error bars represent 1 standard deviation).

$\delta F_{R,\,\text{Finkelstein}}$ not requiring the integral time scale (unlike $\delta F_{R,\,\text{Blomquist}}$) and showing less scatter than $\delta F_{R,\,\text{Wienhold}}$.

Figure 2.5 shows the different relative contributions to the random flux uncertainty for the Arctic cruises (hourly average). Here the uncertainty is normalised by the flux magnitude and then averaged into flux magnitude bins. When the flux magnitude is sufficiently large (> 20 mmol m^{-2} day^{-1}), the total relative random uncertainty in flux asymptotes to about 15% and is driven by variance associated with both vertical flux and other atmospheric processes. This estimate is similar to uncertainties in air-sea fluxes of other well-resolved (i.e., high signal-to-noise ratio) variables (Fairall et al., 2000). At a lower flux magnitude, uncertainty due to atmospheric processes other than vertical flux dominates the total random uncertainty. Uncertainty due to the white noise from the Picarro G2311-f gas analyser is small.

2.3.2 Summary of systematic and random uncertainties

The total uncertainty δF in the hourly average EC CO_2 flux (estimated using Equation 2.3) ranges from 1.4 to 3.2 mmol m^{-2} day^{-1} in the mean for the four cruises (Table 2.4). Our EC flux system setup was optimal and subsequent corrections have minimised any bias to < 9%

(Section 2.2.3). The systematic error is on average much lower than the random error (Table 2.4). This means the accuracy of the EC CO_2 flux measurements is very high, but the precision of hourly averaged EC CO_2 air-sea flux measurements is relatively low. In Section 2.4.1, we discuss how the precision can be improved by averaging the observed fluxes for longer.

Table 2.4 Summary of hourly average EC CO_2 fluxes and associated uncertainties in the mean for the four cruises (mmol m^{-2} day^{-1}). Shown are the mean CO_2 flux magnitude ($\overline{|F|}$, mmol m^{-2} day^{-1}), upper limitation of the total uncertainty (δF, Equation 2.3), upper limitation of the absolute systematic error ($|\delta F_S|$, propagated from Table 2.2 and Equation 2.5), and random error (δF_R, Equation 2.6). The random error components are white noise (δF_{RN} , Equation 2.10), vertical flux (δF_{RV}, Equation 2.7 and 2.8) and other atmospheric processes ($\delta F_{RO} = \sqrt{\delta F_R^2 - \delta F_{RN}^2 - \delta F_{RV}^2}$). The total uncertainty is also expressed as a % of the mean flux magnitude ($\delta F/|F| \times 100\%$).

Cruises	**JR18006**	**JR18007**	**AMT28**	**AMT29**
$\overline{|\mathbf{CO2\ flux}|}$, $\overline{|F|}$	10.1	16.3	2.5	3.5
Total uncertainty, δF	2.3	3.2	1.4	1.7
($\delta F/|F| \times 100\%$)	(23%)	(20%)	(58%)	(49%)
Systematic error, $|\delta F_S|$	0.8	1.2	0.3	0.3
Total random error, δF_R	2.2	2.9	1.4	1.7
Random error due to white noise, δF_{RN}	0.5	0.6	0.3	1.0
Random error due to vertical flux, δF_{RV}	1.1	1.4	0.2	0.4
Random error due to other atmospheric processes, δF_{RO}	1.5	2.4	1.4	1.5

The theoretical uncertainty estimates above can be compared with a portion of the AMT28 cruise data (15°–20°S, ~25°W; Figure 2.4), when the ship encountered sea surface CO_2 fugacity close to equilibrium with the atmosphere (i.e., ΔfCO_2 ~0, Figure A2.2, Appendix A2). The data from this region is useful for assessing the random and systematic flux uncertainties. The standard deviation of the EC CO_2 flux during cruise AMT28 when ΔfCO_2 ~0 is 1.6 mmol m^{-2} day^{-1}, which compares well with the theoretical random flux uncertainty in this region (1.4 mmol m^{-2} day^{-1}). The mean EC CO_2 flux from this region was 0.5 mmol m^{-2} day^{-1}, which is indistinguishable from zero considering the random uncertainty. This further confirms the minimal bias in our flux observations.

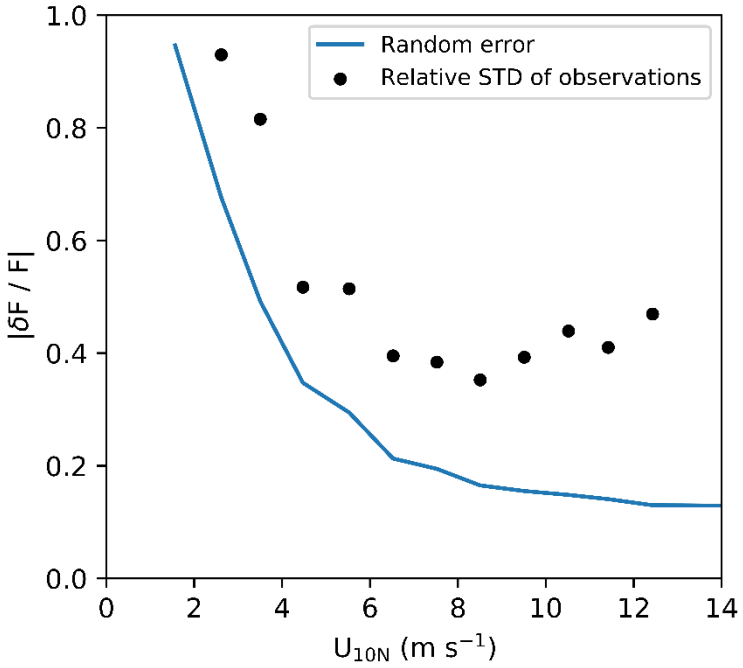

Figure 2.6 Comparison of relative random uncertainty in hourly CO_2 flux and relative standard deviation (RSTD, standard deviation/|flux mean|) of the EC CO_2 flux from two Arctic cruises. These results are binned in 1 m s^{-1} wind speed bins.

Figure 2.6 shows a comparison between the relative uncertainty and the relative standard deviation (RSTD) in the hourly CO_2 flux for the two Arctic cruises. Results have been binned into 1 m s^{-1} wind speed bins. Wind speed was converted to 10-meter neutral wind speed (U_{10N}) using the COARE3.5 model (Edson et al., 2013). The relative random error decreases with increasing wind speed. This is partly because the fluxes tend to be larger at higher wind speeds and so the signal-to-noise ratio in the flux is greater. In addition, at higher wind speeds, a greater number of high-frequency turbulent eddies are sampled by the EC system, providing better statistics of turbulent eddies, and lower sampling error.

The RSTD of the flux is greater in magnitude than the estimated flux uncertainty because it also contains environmental variability. The CO_2 flux auto-covariance analysis (Section 2.4.1) shows that random error in hourly flux explains ~20% of the flux variance on average for the two Arctic cruises. This implies that the remaining variability in the EC flux (~80%) is due to natural phenomena (e.g., changes in ΔfCO_2, wind speed, etc). Similarly, substantial variability is typical in EC-derived CO_2 gas transfer velocity at a given wind speed (e.g., Edson et al., 2011; Butterworth & Miller, 2016). K_{660} is derived from (EC CO2 flux) / ΔfCO_2, and thus an

understanding of EC flux uncertainty can help understand and explain the variability in EC-derived gas transfer velocity estimates (Section 2.4.2).

2.4 Discussion

2.4.1 Impact of averaging time scale on flux uncertainty

The random error in flux decreases with increasing averaging time interval T or the number of sampling points n (Equations 2.6, 2.7 and 2.10). This is because a longer averaging time interval results in better statistics of the turbulent eddies. However, averaging for too long is also not ideal since the atmosphere is less likely to maintain stationarity. The typical averaging time interval is thus typically between 10 min and 60 min for air-sea flux measurements (20 min intervals were used in this study). The timeseries of quality controlled 20 min flux intervals can be further averaged over a longer time scale to reduce the random uncertainty. Averaging the 20 min flux intervals assumes that the flux interval data are essentially repeated measurements within a chosen averaging time scale. If the 20 min flux intervals are averaged, one can ask: What is the optimal averaging time scale for interpreting air-sea EC CO_2 fluxes?

We use an auto-covariance method to determine the optimal averaging time scale. The observed variance in CO_2 flux consists of random uncertainty (random noise) as well as natural variability. The random noise component should only contribute to the CO_2 flux variance when the data are zero-shifted. After the CO_2 flux data are shifted, the noise will not contribute to the auto-covariance function. Figure 2.7 shows the auto-covariance function of the air-sea CO_2 flux with different averaging time scales for Arctic cruise JR18007. For the 20-min fluxes (Figure 2.7a), the auto-covariance decreases rapidly between the zero shift and the initial time shift, which indicates that a large fraction of the 20-min flux variance is due to random noise.

The random noise in the CO_2 fluxes decreases with a longer averaging time scale, with the greatest effect observed from 20 min to 1 hour (Figure 2.7b). A fit to the noise-free auto-covariance function extrapolated back to a zero time shift gives us an estimate of the non-noise variability in the natural CO_2 flux. Subtracting the extrapolated natural flux variability from the total variance in CO_2 flux provides an estimate of the random noise in the flux for each averaging timescale (Figure 2.7a). All four cruises consistently demonstrate a non-linear reduction in the noise contribution to the flux measurements when the averaging timescale increases (Figure 2.8). The random noise in flux can be expressed relative to the natural variance in flux representing the inverse of the signal-to-noise ratio (i.e., random noise in flux

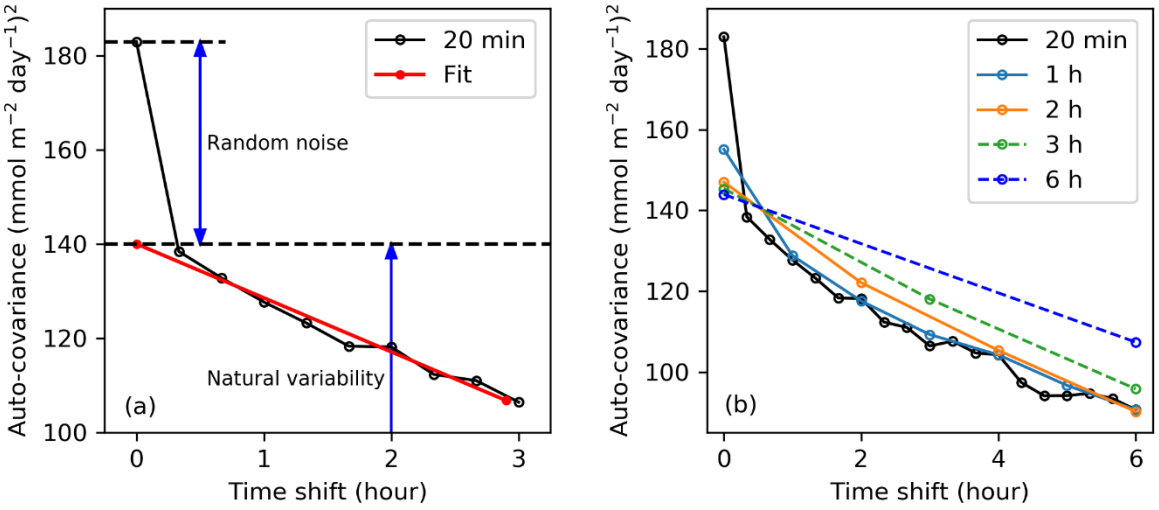

Figure 2.7 (a) Auto-covariance of the original 20-min fluxes (cruise JR18007) and a fit to the noise-free auto-covariance function extrapolated back to a zero time shift. (b) CO_2 flux auto-covariance functions with different averaging time scales. The black line represents the auto-covariance of the original 20-min fluxes. The 20-min fluxes are further averaged at different time scales (1, 2, 3 and 6 hour) and the corresponding auto-covariance functions are shown with different colours (dark blue, orange, green and light blue).

/ natural flux variability , hereafter referred to as noise:signal). The noise:signal also facilitates comparison of all four cruises (Figure 2.8) and demonstrates the consistent effect that increasing the averaging timescale has on noise:signal. Consistent with Table 2.4, the Arctic cruises show much lower noise:signal because the flux magnitudes are much larger. Typical detection limits in analytical science are often defined by a 1:3 noise:signal ratio. A 1:3 noise:signal is achieved with a 1 h averaging timescale for the Arctic cruises. The Atlantic cruises encountered much lower air-sea CO_2 fluxes and an averaging timescale of at least 3 h is required to achieve the same 1:3 noise:signal ratio.

The flux measurement uncertainty at a 6-h averaging timescale for the AMT cruises is ~0.6 mmol m^{-2} day^{-1}. The analysis presented above permits an answer to the question posed at the beginning of the Results section. The mean difference between the 6-h averaged EC CO_2 flux observations on AMT29 and AMT28 (1.3 mmol m^{-2} day^{-1}, Figure 2.4a) is much greater than the measurement uncertainty. This significant difference was likely because of the interannual variability in AMT CO_2 flux due to changes in the natural environment (e.g., ΔfCO_2, sea surface temperature, and physical drivers of interfacial turbulence such as wind speed) during the two cruises.

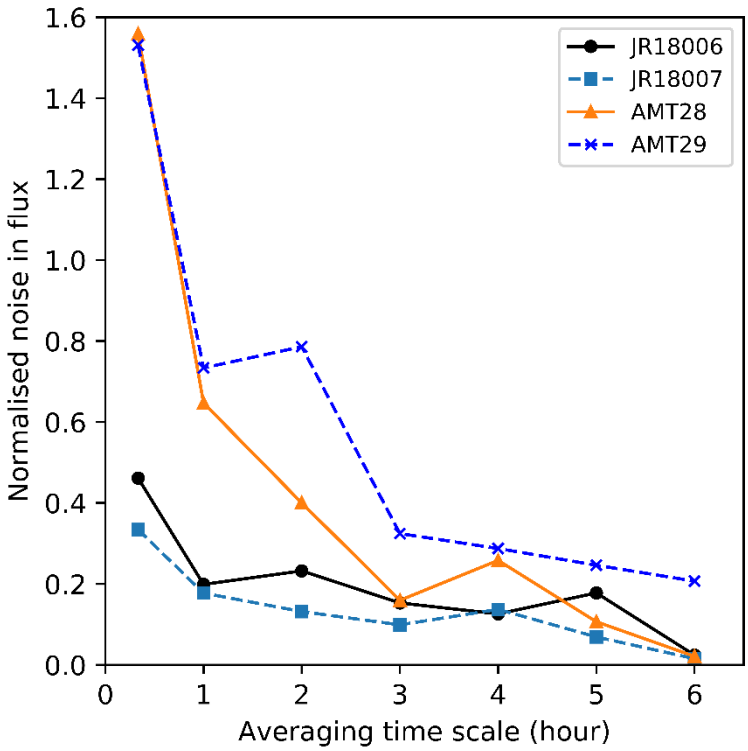

Figure 2.8 Effect of the averaging timescale on the noise:signal (random noise in flux / natural flux variability) for EC air-sea CO_2 flux measurements during four cruises.

At a typical research ship speed of ~10 knots, the AMT cruises cover ~110 km in 6 h, which is equivalent to ~1° latitude. Averaging for longer than 6 h is likely to cause a substantial loss of real information about the natural variations in air-sea CO_2 flux and the drivers of flux variability. For example, the mean flux between 0–20°S during cruise AMT28 is 0.9 mmol m^{-2} day^{-1}. However, the 6 h average EC measurements show that the flux varied between +5 mmol m^{-2} day^{-1} (~2–6°S) and -5 mmol m^{-2} day^{-1} (~11–13°S, Figure 2.4a).

2.4.2 Effect of CO_2 flux uncertainty on the gas transfer velocity *K*

The uncertainties in the EC CO_2 air-sea flux measurement will influence the uncertainty that translates to EC-based estimates of the gas transfer velocity, *K*. For illustration, *K* is computed for Arctic cruise JR18007, which had a high flux signal:noise ratio of ~5 (Figure 2.8). Any data potentially influenced by ice and sea ice melt were excluded using a sea surface salinity filter (data excluded when salinity < 32‰). Equation 2.1 is rearranged and used with concurrent measurements of CO_2 flux (*F*), ΔfCO_2, and sea surface temperature (SST) to obtain *K* adjusted for the effect of temperature (K_{660}).

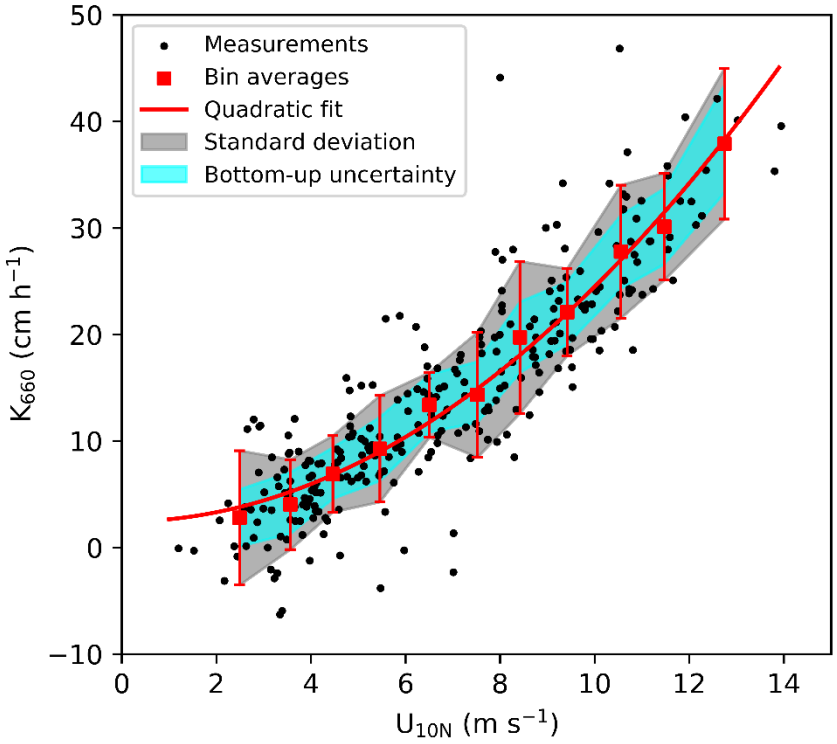

Figure 2.9 Gas transfer velocity (K_{660}) measured on Arctic cruise JR18007 (hourly average, signal:noise ~5) versus 10-m neutral wind speed (U_{10N}). Red squares represent 1 m s^{-1} bin averages with error bars representing one standard deviation (SD). The red curve represents a quadratic fit using the bin averages: $K_{660} = 0.22U_{10N}^2 + 2.46$ ($R^2 = 0.76$). The grey shaded area represents the standard deviation calculated for each wind speed bin ($K_{660} \pm 1SD$). The cyan region represents the upper and lower bounds in K_{660} uncertainty computed from the EC flux uncertainty ($K_{660} \pm \delta K_{660}$, see text for detail).

The determination coefficient (R^2) of the quadratic fit between wind speed (U_{10N}) and EC-derived K_{660} (Figure 2.9) demonstrates that wind speed explains 76% of the K_{660} variance during Arctic cruise JR18007. How much of the remaining 24% can be attributed to uncertainties in EC CO_2 fluxes?

Variability in K_{660} within each 1 m s^{-1} wind speed bin can be considered to have minimal wind speed influence. It is thus useful to compare the variability within each wind speed bin ($K_{660} \pm$ 1SD) with the upper and lower uncertainty bounds derived from the EC flux measurements. Uncertainty in EC flux-derived K_{660} (δK_{660}) is calculated from the uncertainty in hourly EC flux (δF) by rearranging Equation 2.1 (bulk flux equation) and replacing F with δF. The resultant δK_{660} is then averaged in wind speed bins. The shaded cyan band in Figure 2.9 ($K_{660} \pm \delta K_{660}$) is consistently narrower than the grey shaded band ($K_{660} \pm$ 1SD). On average, EC

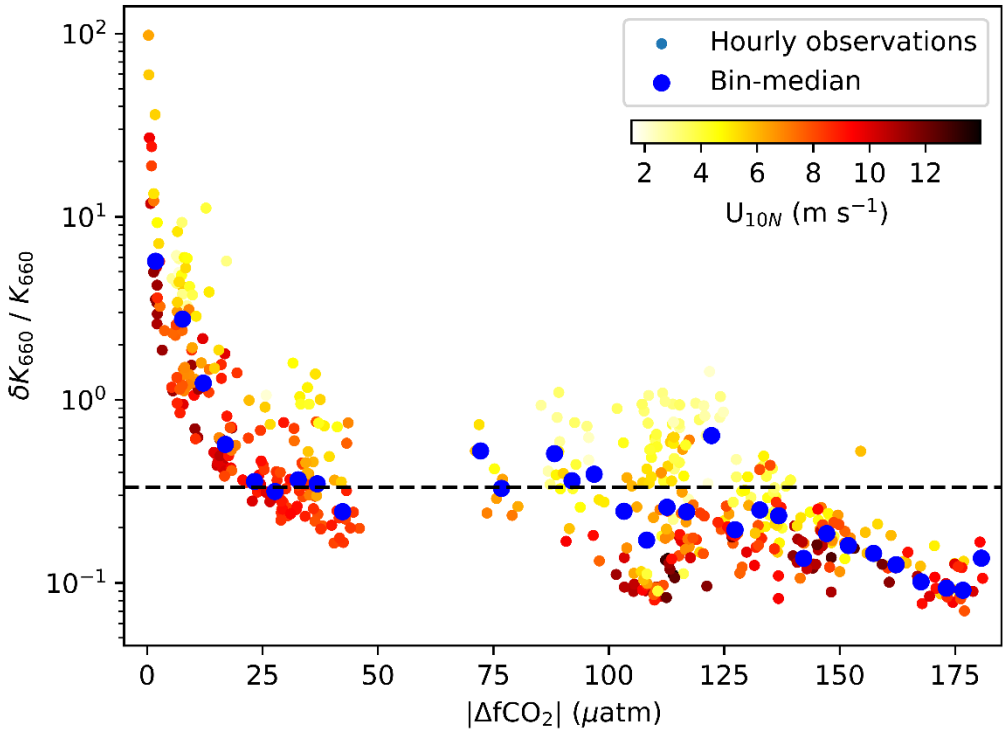

Figure 2.10 Relative uncertainty in EC-estimated hourly K_{660} (δK_{660} / K_{660}) versus the magnitude of the air-sea CO_2 fugacity difference ($|\Delta fCO_2|$) during Arctic cruise JR18007 and Atlantic cruises AMT28 and AMT29 (no ΔfCO_2 data were collected on JR18006). The data points are colour-coded by wind speed. Blue points are medians of δK_{660} / K_{660} in 5 µatm bins. Here we use the parameterised K_{660} (= $0.22U_{10N}^2 + 2.46$) to normalise the uncertainty in K_{660}. The dashed line represents the 3:1 signal:noise ratio ((δK_{660} / K_{660} = 1/3).

flux-derived uncertainty in K_{660} can only account for a quarter of the K_{660} variance within each wind speed bin and the remaining variance is most likely due to the non-wind speed factors that influence gas exchange (e.g., breaking waves, surfactants).

The analysis above can be extended to assess how EC flux-derived uncertainty affects our ability to parameterise K_{660} (e.g., as a function of wind speed). To do so, a set of synthetic K_{660} data is generated (same U_{10N} as the K_{660} measurements in Figure 2.9). The synthetic K_{660} data are initialised using a quadratic wind speed dependence that matches JR18007 (i.e., K_{660} = $0.22U_{10N}^2 + 2.46$). Random Gaussian noise is then added to the synthetic K_{660} data, with the relative noise level corresponding to the relative flux uncertainty values taken from JR18007 (mean of 20%, Table 2.4). The relative uncertainty in K_{660} due to EC flux uncertainty (δK_{660} / K_{660}) shows a wind speed dependence (Figure S2.4a, Supplement S2), and the artificially-generated Gaussian noise incorporates this wind speed dependence (Figure S2.4b, Supplement

S2). The R^2 of the quadratic fit to the synthetic data as a function of U_{10N} is 0.90 (the rest of the variance is due to uncertainty in K_{660}). Since wind speed explains 76% of the variance in the observed K_{660}, it can be inferred that non-wind speed factors can account for 14% (i.e., (100-76)% - (100-90)%) of the total variance in K_{660} from this Arctic cruise. If the synthetic K_{660} data is assigned a relative flux uncertainty of 50% (reflective of a region with low fluxes, e.g., AMT28/29), the R^2 of the wind speed dependence in the synthetic data decreases to 0.60.

The relative uncertainty in EC flux-derived K_{660} (δK_{660} / K_{660}) is large when $|\Delta fCO_2|$ is small (Figure 2.10). Previous EC studies have filtered EC flux data to remove fluxes when the $|\Delta fCO_2|$ falls below a specified threshold (e.g., 20 µatm, Blomquist et al. (2017); 40 µatm, Miller et al. (2010), Landwehr et al. (2014), Butterworth & Miller (2016), Prytherch et al. (2017); 50 µatm, Landwehr et al. (2018)). Analysis of the data presented here suggests that a $|\Delta fCO_2|$ threshold of at least 20 µatm is reasonable for hourly K_{660} measurements, leading to δK_{660} of ~10 cm h^{-1} (δK_{660} / K_{660} ~1/3) or less on average. At very large $|\Delta fCO_2|$ of over 100 µatm, δK_{660} is reduced to only a few cm h^{-1} (δK_{660} / K_{660} ~1/5). At longer flux averaging time scales, it may be possible to relax the minimal $|\Delta fCO_2|$ threshold.

2.5 Conclusions

This study uses data from four cruises with a range in air-sea CO_2 flux magnitude to comprehensively assess the sources of uncertainty in EC air-sea CO_2 flux measurements. Data from two ships and two different state-of-the-art CO_2 analysers (Picarro G2311-f and LI-7200, both fitted with a dryer) are analysed using multiple methods (Section 2.2.3). Random error accounts for the majority of the flux uncertainty, while the systematic error (bias) is small (Table 2.4). Random flux uncertainty is primarily caused by variance in CO_2 mixing ratio due to atmospheric processes. The random error due to instrument noise for the Picarro G2311-f is threefold smaller than for LI-7200 (Table 2.4 and Figure D2.1, Appendix D2). However, the contribution of the instrument noise to the total random uncertainty is much smaller than the contribution of atmospheric processes such that both gas analysers are well suited for air-sea CO_2 flux measurements.

The mean uncertainty in hourly EC flux is estimated to be 1.4–3.2 mmol m^{-2} day^{-1}, which equates to a relative uncertainty of ~20% in high CO_2 flux regions and ~50% in low CO_2 flux regions. Lengthening the averaging timescale can improve the signal:noise ratio in EC CO_2 flux through the reduction of random uncertainty. Auto-covariance analysis of CO_2 flux is used to quantify the optimal averaging timescale (Figure 2.7 and 2.8, Section 2.4.1). The optimal

averaging timescale varies between 1 hour for regions of large CO_2 flux (the Arctic in our analysis) and at least 3 hours for regions of low CO_2 flux (tropical/sub-tropical Atlantic in our analysis).

The measurement uncertainty in EC CO_2 flux contributes directly to scatter in the derived gas transfer velocity, K_{660}. Flux uncertainties determined in this paper are applied to a synthetic K_{660} dataset. This enables partitioning of the variance in measured K_{660} that is due to EC CO_2 flux uncertainty, wind speed, and other processes (10%, 76%, 14% for Arctic cruise JR18007). At a given averaging timescale, a $|\Delta fCO_2|$ threshold helps to reduce the scatter in K_{660}. A minimum $|\Delta fCO_2|$ filter of 20 µatm is needed for interpreting hourly K_{660} data, with the signal:noise ratio in K_{660} improving further at higher $|\Delta fCO_2|$.

Chapter 3

3 Arctic Ocean CO_2 flux estimates

> "PhD is a kind of training process. Doing a PhD is a big job and getting a PhD gives you a lot of confidence to develop your own ideas.
>
> (Peter S. Liss, January 2021)

The results presented in the following chapter have been published in:

Near-surface stratification due to ice melt biases Arctic air-sea CO_2 flux estimates

Yuanxu Dong[1,2], Mingxi Yang[2], Dorothee C. E. Bakker[1], Peter S. Liss[1], Vassilis Kitidis[2], Ian Brown[2], Melissa Chierici[3,4], Agneta Fransson[5] and Thomas G. Bell[2]

[1]Centre for Ocean and Atmospheric Sciences, School of Environmental Sciences, University of East Anglia, Norwich, UK
[2]Plymouth Marine Laboratory, Prospect Place, Plymouth, UK
[3]Institute of Marine Research, Fram Centre, Tromsø, Norway
[4]Department of Arctic Geophysics, University Centre in Svalbard, Longyearbyen, Norway
[5]Norwegian Polar Institute, Fram Centre, Tromsø, Norway

Geophysical Research Letters, 2021, 48, e2021GL095266.
https://doi.org/10.1029/2021GL09 5266

The work and analysis presented in this chapter was led by Y. Dong. Co-authors on this publication collected the data, provided guidance and suggestions regarding the analysis and the results to help and address the interests of the wider scientific community.

Abstract: Air-sea carbon dioxide (CO_2) flux is generally estimated by the bulk method using upper ocean CO_2 fugacity measurements. In the summertime Arctic, sea-ice melt results in stratification within the upper ocean (top ~10 m), which can bias bulk CO_2 flux estimates when the seawater CO_2 fugacity is taken from a ship's seawater inlet at ~6 m depth (fCO_{2w_bulk}). Direct flux measurements by eddy covariance are unaffected by near-surface stratification. We use eddy covariance CO_2 flux measurements to infer sea surface CO_2 fugacity ($fCO_{2w\_surface}$) in the Arctic Ocean. In sea-ice melt regions, $fCO_{2w\_surface}$ values are consistently lower than fCO_{2w_bulk} by an average of 39 µatm. Lower $fCO_{2w\_surface}$ can be partially accounted for by fresher (≥ 27%) and colder (17%) melt waters. A back-of-the-envelope calculation shows that neglecting the summertime sea-ice melt could lead to a 6–17% underestimate of the annual Arctic Ocean CO_2 uptake.

Plain language summary: The Arctic Ocean is considered to be a strong sink for atmospheric CO_2. The air-sea CO_2 flux is almost always estimated indirectly using bulk seawater CO_2 fugacity measured from the ship's seawater inlet at typically ~6 m depth. However, sea-ice melt results in near-surface stratification and can cause a bias in air-sea CO_2 flux estimates if the bulk water CO_2 fugacity is used. The micrometeorological eddy covariance flux technique is not affected by stratification. Here for the first time, we employ eddy covariance measurements to assess the impact of sea-ice melt on Arctic Ocean CO_2 uptake estimates. The results show that the summertime near-surface stratification due to sea-ice melt could lead to an ~10% (with high uncertainty) underestimation of the annual Arctic Ocean CO_2 uptake.

3.1 Introduction

The Arctic Ocean is a strong sink of atmospheric CO_2 due to the active biological production and high CO_2 solubility in cold waters (Anderson et al., 1998; Takahashi et al., 2009). While only accounting for 4% of the world's ocean by area and seasonally covered by sea ice, the Arctic Ocean contributes 5–14% (66–199 Tg C yr^{-1}, Bates & Mathis, 2009; Yasunaka et al., 2018) of mean global atmospheric CO_2 removal every year (~1400 Tg C yr^{-1}, Takahashi et al., 2009; Landschützer et al., 2014). However, this Arctic carbon sink is rapidly changing due to climate change. The Arctic warming rate has been more than twice as fast as the global average over the past 5 decades (Romanovsky et al., 2017). The sea-ice extent in the Arctic Ocean in September decreased at a rate of 13.1% $decade^{-1}$ during 1979–2020 relative to the 1981–2010

average (Perovich et al., 2020). Sea-ice loss reinforces upper ocean warming due to reduced surface albedo and increased shortwave penetration, which in turn inhibits sea-ice formation in winter and allows for the acceleration of summertime sea-ice loss (Perovich et al., 2007). The reduction in sea-ice coverage in polar regions is expected to increase CO_2 uptake due to larger sea-ice free area, longer sea-ice free period, more freshwater at the surface and greater biological primary production (Bates & Mathis, 2009; Arrigo & van Dijken, 2015; McPhee et al., 2009; Perovich et al., 2020). However, sea-ice melt also causes near-surface stratification and suppresses water mixing between the surface and sub-surface, which likely generates upper-ocean gradients in temperature, salinity, dissolved inorganic carbon (DIC), total alkalinity (TA) and thus seawater CO_2 fugacity (Rysgaard et al., 2007; Li et al., 2009; Yamamoto-Kawai et al., 2009; Fransson et al., 2009, 2013; Cai et al., 2010; Else et al., 2013; Calleja et al., 2013; Miller et al., 2019; Ahmed et al., 2020).

The air-sea CO_2 flux (F_{CO_2}, mmol m^{-2} day^{-1}) is generally estimated indirectly by the bulk equation as the product of the gas transfer velocity and the air-sea gas concentration difference. Accounting for near-surface temperature gradients, Woolf et al. (2016) recommended:

$$F_{CO_2} = K_{660}(Sc/660)^{-0.5}\left(\alpha_w f\mathrm{CO}_{2\mathrm{w}} - \alpha_i f\mathrm{CO}_{2\mathrm{a}}\right) \quad (3.1)$$

where K_{660} (cm h^{-1}) is the gas transfer velocity at a Schmidt number (Sc) of 660 (Wanninkhof et al., 2009). K_{660} is usually parameterized as a function of wind speed (e.g., Nightingale et al., 2000). α_w and α_i are the CO_2 solubility (mol L^{-1} atm^{-1}, Weiss, 1974) in the subskin and skin seawater, respectively (Woolf et al., 2016). fCO_{2w} and fCO_{2a} are the CO_2 fugacity (µatm) near the sea surface and in the overlying atmosphere, respectively. Similarly, the air-sea sensible heat flux can be estimated by the bulk method using a parameterized sensible heat transfer velocity and the sea-air temperature difference (Supplement S3, Text S3.1).

Air-sea exchange of sparingly soluble gases (e.g., CO_2) is limited mostly by transport within the waterside molecular diffusive layer (MDL, 20–200 µm depth; Jähne, 2009) just beneath the water surface (Liss & Slater, 1974). Thus, fCO_{2w} represents the CO_2 fugacity at the base of MDL ($fCO_{2w\_surface}$). In practice, fCO_{2w} measurements are generally made on bulk seawater from the ship's underway inlet (~6 m depth, fCO_{2w_bulk}). For convenience, the upper several meters of the ocean are assumed to be homogeneous in bulk flux calculations (i.e., fCO_{2w} = $fCO_{2w\_surface}$ = fCO_{2w_bulk}).

However, incidences of near-surface stratification call into question the vertical homogeneity assumption. In the Arctic, three sea-ice-related mechanisms likely drive near-surface vertical gradients in CO_2: 1) Brine drainage. When sea ice forms, carbonate species and salt are ejected into the water under the sea ice as part of brine drainage (e.g., Fransson et al., 2013), which depletes the CO_2 within the sea ice. The salty, dense water sinks and is eventually sequestered in the deep ocean (Rudels et al., 2005). 2) Surface photosynthesis. Phytoplankton is often found in the bottom ice or beneath the Arctic sea ice and their photosynthetic activity further reduces the CO_2 concentration within the sea ice (Assmy et al., 2017; Fransson et al., 2013, 2017). 3) Ikaite dissolution. Dissolution of sea-ice-derived ikaite will consume CO_2 in Arctic surface waters (Fransson et al., 2017; Chierici et al., 2019). The latest measurements in the Arctic coastal waters show significant vertical fCO_{2w} gradients in the upper ocean (Ahmed et al., 2020; Miller et al., 2019). Miller et al. (2019) show both positive and negative fCO_{2w} gradients without separating the contributions of sea-ice melt and river runoff. Ahmed et al. (2020) show consistently negative gradients (i.e., $fCO_{2w\_surface} < fCO_{2w\ bulk}$) in the sea-ice melt regions. Vertical gradients, if left unaccounted for, will result in a bias in bulk air-sea CO_2 flux estimates.

The micrometeorological eddy covariance (EC) method derives CO_2 fluxes directly and represents an alternative approach for understanding Arctic air-sea CO_2 exchange. EC does not rely on seawater measurements (S3, Text S3.2), and thus EC fluxes are not affected by near-surface vertical variation in seawater properties. However, polar oceans are a hostile environment and reliable direct CO_2 flux measurements by EC are scarce (Butterworth & Miller, 2016; Prytherch et al., 2017; Butterworth & Else, 2018; Prytherch & Yelland, 2021). This paper presents EC CO_2 and sensible heat flux data from two Changing Arctic Ocean Programme cruises. Directly measured fluxes were used to compute the implied sea surface fCO_{2w} and water temperature ($fCO_{2w\_surface}$, $T_{w\_surface}$). Comparisons of implied surface values with bulk measurements enable us to assess the impact of vertical gradients on bulk air-sea CO_2 flux estimates. We further speculate on the influence of near-surface stratification on bulk air-sea CO_2 flux estimates for the entire Arctic Ocean.

3.2 Methods

3.2.1 Description of cruises

Cruise tracks of JR18006 and JR18007 (on RRS *James Clark Ross*, JCR) and FS2019 (on RV *Kronprins Haakon*) are shown in Figure S3.1 (Supplement S3). JR18006 visited the Barents Sea between 28 June and 1 August 2019. JR18007 targeted the Fram Strait region within the

Greenland Sea between 4 and 30 August 2019. DIC and TA were not measured during JR18006 and JR18007. Measurements taken between 2 and 5 September 2019 (between 0°W and 10°W) on cruise FS2019 were used to constrain the upper ocean carbonate system. Methods for DIC and TA measurements can be found in Chierici et al. (2019). The EC system on JCR, processing and quality control of fluxes, underway measurements and the meteorological observations are detailed elsewhere (Dong et al., 2021a) and are briefly described in the supporting information (S3, Text S3.3). fCO_{2w} measurements were only available during ice-free periods of JR18007.

3.2.2 Implied surface variables from eddy covariance fluxes

We use Brunt–Väisälä frequency (N^2) threshold to identify stratified waters. N^2 at ~6 m depth is calculated from the CTD (conductivity, temperature, depth) profiles ($N^2 = -g(\rho_{7m} - \rho_{5m})/(2 * \rho_{7m})$ with gravitational acceleration g and seawater density ρ). Fischer et al. (2019) used $N^2 \geq 10^{-4}$ s^{-2} in upwelling waters, but we expect the threshold for near-surface stratification to be more evident in regions with sea-ice melt, so use a more robust threshold of $N^2 \geq 10^{-3}$ s^{-2}. Measurements in waters without a CTD cast and salinity below 34.5‰ are marked as having an 'unknown' stratification status.

The derivations of EC air-sea CO_2 flux (FCO_{2_EC}) and sensible heat flux (H_{S_EC}) are detailed in the supporting information (S3, Text S3.2). The gas transfer velocity (hourly) is computed by replacing the bulk flux with the hourly EC flux in a rearrangement of Equation 3.1:

$$K_{660} = \frac{F_{CO_2\_EC}}{(Sc/660)^{-0.5}\left(\alpha_w fCO_{2w\_bulk} - \alpha_i fCO_{2a}\right)} \quad (3.2)$$

In regions with near-surface stratification, fCO_{2w_bulk} may not be representative of the surface (i.e., $fCO_{2w\_bulk} \neq fCO_{2w\_surface}$). Therefore, to derive a wind speed (U_{10N}) dependent parametrization of K_{660} from this project (K_{660_u}), only data from non-stratified waters are considered. K_{660_u} and the EC CO_2 flux observations are then used to compute the implied $fCO_{2w\_surface}$ for all water types (non-stratified and stratified):

$$fCO_{2w\_surface} = \frac{F_{CO_2\_EC}}{K_{660\_u}(Sc/660)^{-0.5}\,\alpha_w} + \frac{\alpha_i}{\alpha_w} fCO_{2a} \quad (3.3)$$

A similar approach is used to derive sensible heat transfer velocity (K_H) and compute the implied surface seawater temperature ($T_{w\_surface}$):

$$K_H = \frac{H_{S\_EC}}{\rho_a c_{pa}(T_{w\_bulk} - dT - T_a)} \quad (3.4)$$

$$T_{\mathrm{w\_surface}} = \frac{H_{\mathrm{S\_EC}}}{\rho_{\mathrm{a}} c_{\mathrm{pa}} K_{\mathrm{H\_u}}} + T_{\mathrm{a}} \quad (3.5)$$

where K_{H} (cm h^{-1}) is parametrized with $U_{10\mathrm{N}}$ ($K_{\mathrm{H\_u}}$) using data from non-stratified waters (S3, Figure S3.2). Here, ρ_{a} (kg m^{-3}) is the mean density of dry air, c_{pa} (J kg^{-1} K^{-1}) is the heat capacity of air and T_{a} (K) is the air temperature. The temperature offset due to the cool skin effect, dT (K), is estimated using the COARE 3.5 model (Edson et al., 2013; Fairall et al., 1996).

3.3 Results and discussion

3.3.1 CO_2 flux time series

The time series of hourly averaged EC and bulk fluxes for CO_2 and heat are shown for cruise JR18007 (Figure 3.1). The bulk CO_2 flux is calculated from $f\mathrm{CO_{2w\_bulk}}$, $f\mathrm{CO_{2a}}$ and $T_{\mathrm{w\_bulk}}$ measurements using the gas transfer velocity parametrisation from Nightingale et al. (2000). The bulk sensible heat flux is computed using the COARE 3.5 model (Edson et al., 2013). The sea ice concentration (Figure 3.1d) is derived from the Advanced Microwave Scanning Radiometer-Earth Observing System (AMSR-E, daily and 3.125 km resolution; Spreen et al., 2008).

Stratified areas were located at the edge of or within the sea ice (S3, Figure S3.1), with relatively low near-surface salinity and temperature (Figure 3.1) suggesting that sea-ice melt is the principal reason for near-surface stratification. Terrestrial runoff as a source of freshwater is unlikely because the ship was far from land (> 50 km) in the stratified stations (S3, Figure S3.1). Furthermore, there were no significant precipitation events during the cruise, ruling out surface freshening due to precipitation.

The relatively good agreement between EC fluxes and bulk air-sea CO_2 fluxes in non-stratified regions (Figure 3.1a and S3.3) suggests that the data (EC fluxes and underway $f\mathrm{CO_{2w\_bulk}}$) are reliable and that the Nightingale et al. (2000) gas transfer velocity parameterisation is reasonable for this study region. In areas with near-surface stratification (stations 6 and 16), bulk CO_2 fluxes are consistently less negative (lower in magnitude) than EC CO_2 fluxes (Figure 3.1a). Meanwhile, bulk sensible heat fluxes are slightly higher than EC fluxes in stratified regions.

Another intriguing feature is that EC sensible heat fluxes were close to zero during sea ice stations 8 and 9, but EC CO_2 fluxes were still significant. The sea ice concentration data (Figure 3.1d) show that the sea surface was not fully ice-covered in this region. One possible reason

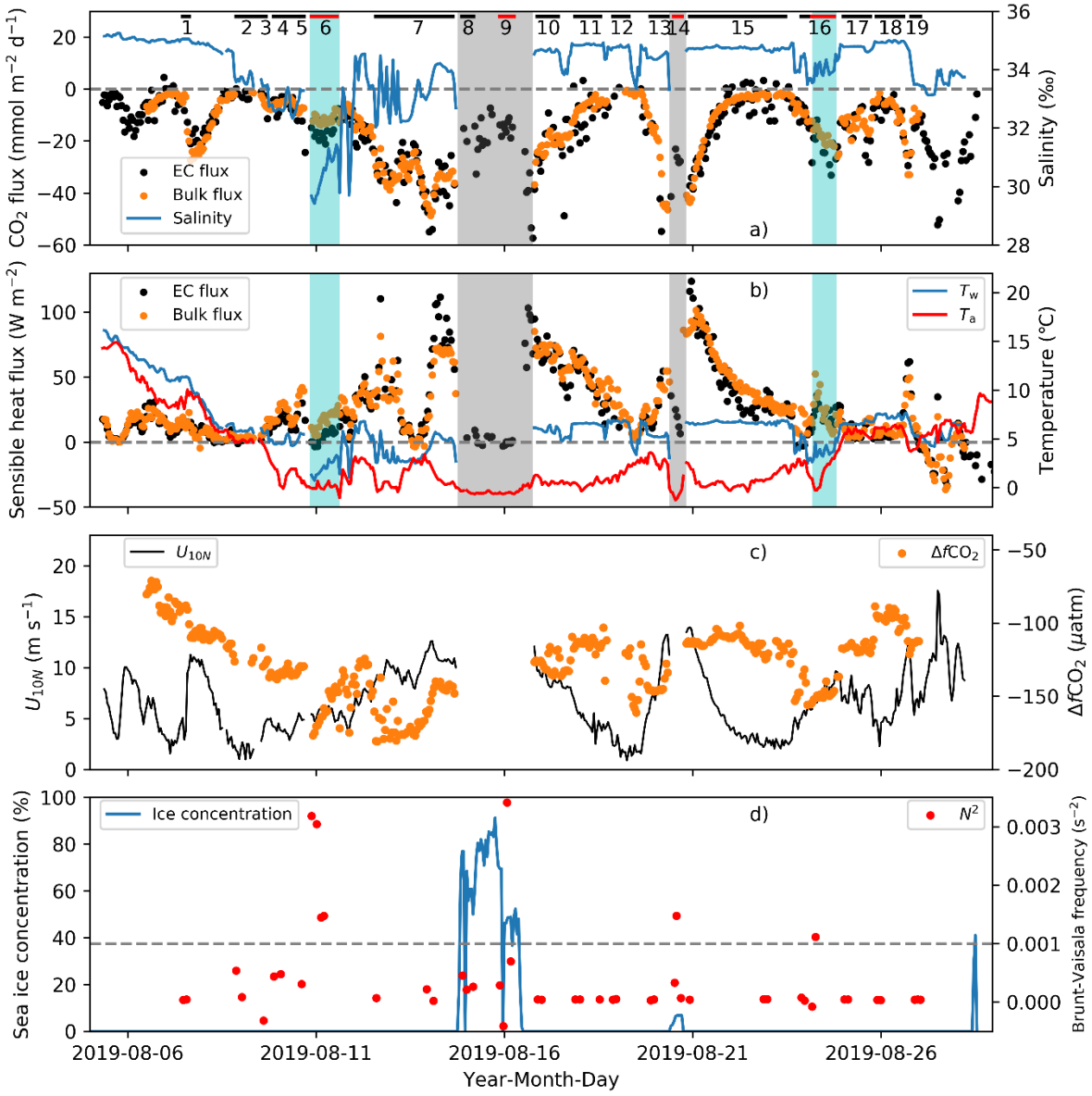

Figure 3.1 Time series of hourly fluxes and environmental variables on JR18007. Negative (positive) fluxes represent ocean sinks (sources): a) EC and bulk air-sea CO_2 fluxes, and salinity at 6 m depth. Light blue shading shows near-surface stratification (identified from CTD profiles). Grey shading indicates ice-covered waters where the underway seawater system was shut off. Dashes on the top axis correspond to CTD stations. Stations with near-surface stratification are in red. Dash length represents the duration on station; b) EC and bulk sensible heat flux, seawater temperature (T_w) at 6 m depth and air temperature (T_a); c) 10-m neutral wind speed and air-sea CO_2 fugacity difference ($\Delta fCO_2 = fCO_{2w\_bulk} - fCO_{2a}$); d) Sea ice concentration (Spreen et al., 2008) and Brunt–Väisälä frequency (N^2) at 6 m depth.

for near-zero sensible heat flux but detectable CO_2 flux is that the surface (seawater or sea ice) temperature was close to the air temperature, while a fCO_2 gradient existed across the sea

surface. Also, air-sea CO_2 exchange is mainly controlled by waterside processes (Liss & Slater, 1974), whereas air-sea heat exchange is controlled by airside processes (Yang et al., 2016c). It is possible that the impact of sea ice on waterside-controlled gases (e.g., CO_2) is different to the impact on airside-controlled gases and heat.

3.3.2 Gas transfer velocity

Dong et al. (2021a) show that the hourly EC air-sea CO_2 flux relative uncertainty is ~20% on average during JR18007. The ΔfCO_2 (= $fCO_{2w\_bulk} - fCO_{2a}$) ranges from -181 to -71 µatm (-130 µatm on average, Figure 3.1c) during JR18007. The relatively low flux uncertainty and large ΔfCO_2 values enable us to estimate the gas transfer velocity (K_{660}) with high accuracy. Figure 3.2 shows K_{660} derived from quality-controlled EC CO_2 fluxes and ΔfCO_2 observations, plotted against 10-m neutral wind speed (U_{10N}); the latter is determined from measurements of wind speed adjusted to U_{10N} using the COARE 3.5 model (Edson et al., 2013). There are 298 hourly averaged K_{660} values. 239 hourly K_{660} values from non-stratified waters are binned in wind speed intervals of 1 m s^{-1} and the bin averages (red squares) are used to derive a least square quadratic fit. The fit ($K_{660\_u} = 0.220\ U_{10N}^2 + 2.213$) agrees fairly well with a widely-used K_{660} parameterisation based on dual tracer results (Nightingale et al., 2000) and a more recent parameterisation derived from EC air-sea CO_2 flux measurements (Butterworth & Miller, 2016).

The K_{660} data in stratified waters (21 hourly K_{660}) are consistently higher than the parameterized K_{660_u} curve. Including data from stratified waters and waters with unknown stratification status (38 hourly K_{660}) decreases the strength of the quadratic fit between hourly K_{660} and U_{10N} from $R^2 = 0.801$ to $R^2 = 0.777$ (S3, Table S3.1). This is most likely due to a vertical gradient in fCO_{2w}, where fCO_{2w_bulk} systematically exceeds $fCO_{2w\_surface}$ (see Section 3.3.3).

3.3.3 Implied sea surface CO_2 fugacity and temperature

The K_{660} parameterisation in Figure 3.2 and the K_H parameterisations (S3, Figure S3.2) are used for estimating $fCO_{2w\_surface}$ (Equation 3.3) and $T_{w\_surface}$ (Equation 3.5). Data at low wind speeds ($U_{10N} < 4$ m s^{-1}) are excluded from these calculations because of the low signal-to-noise ratios of EC fluxes and larger relative uncertainties in transfer velocities during calm conditions (Dong et al., 2021a).

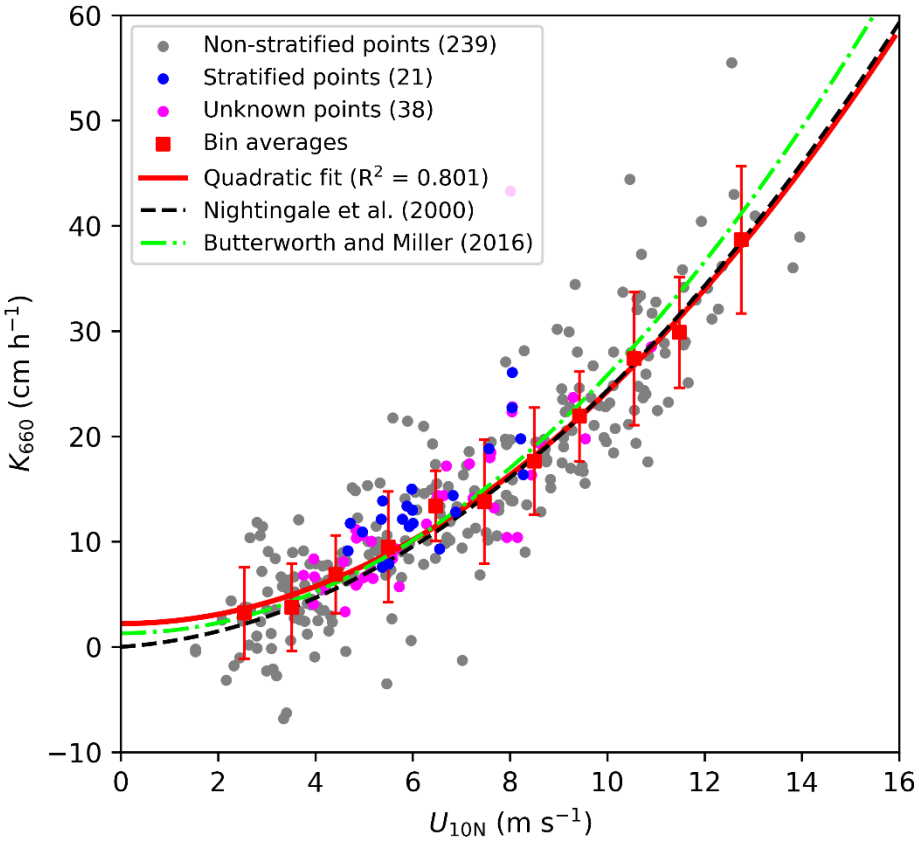

Figure 3.2 Relationship between the CO_2 gas transfer velocity (K_{660}, derived from hourly EC air-sea CO_2 flux measurements) and wind speed (U_{10N}) during JR18007. Grey dots represent K_{660} in non-stratified waters, blue dots correspond to K_{660} in stratified waters, and magenta dots indicate data with unknown stratification status. Red squares are 1 m s^{-1} bin averages of the non-stratified values, with error bars representing 1 standard deviation. The red curve is a quadratic parameterization (K_{660_u} = 0.220 U_{10N}^2 + 2.213; R^2 = 0.801). The K_{660} parameterizations of Nightingale et al. (2000) (black dashed) and Butterworth & Miller (2016) (green dot dashed) are also shown.

Figure 3.3 shows the comparison between hourly averages of the bulk seawater measurements (fCO_{2w_bulk} and, in the case of temperature, adjusted for the cool skin: T_w – dT) and the implied surface values ($fCO_{2w\_surface}$ and $T_{w\_surface}$). In non-stratified waters (grey dots in Figure 3.3a), the means of the two fCO_{2w} values compare reasonably well, even though the $fCO_{2w\_surface}$ values have a larger range than fCO_{2w_bulk} due to variability in the EC CO_2 flux observations and the uncertainty in the K_{660} parameterisation. In stratified waters (blue dots in Figure 3.3a), the implied $fCO_{2w\_surface}$ values are consistently lower than fCO_{2w_bulk}, indicating that bulk measurements are not representative of the surface. Similarly, EC implied $T_{w\_surface}$ values are consistently lower than the bulk water temperature in low salinity areas (≤ 32‰, Figure 3.3b).

These data corroborate the CTD profiles from JR18007 (S3, Figure S3.4) and suggest that the surface water is colder and fresher than bulk water in regions with sea ice melt.

Within the stratified areas during JR18007, $fCO_{2w\_surface}$ (mean = 208 µatm) is on average 39 ± 39 µatm lower than fCO_{2w_bulk} (mean = 247 µatm), while $T_{w\_surface}$ is on average 0.7 ± 0.8 °C below $T_{w\_bulk} - dT$. A temperature change of 0.7 °C should reduce fCO_{2w} by 7 µatm according to the Takahashi et al. (1993) empirical temperature relationship (S3, Equation S3.5), suggesting that the temperature effect accounts for 18% of the vertical fCO_{2w} gradient within the stratified area.

Although the top 4 m depth CTD data have been removed due to ship interferences and rough sea state, CTD profiles still indicate that seawater at 4 m depth is fresher than the 5–10 m water at the stratified stations (S3, Figure S3.4). The shapes of near-surface salinity profiles generally mirror those of temperature profiles (i.e., the vertical salinity gradient is nearly the same as the temperature gradient in magnitude; S3, Figure S3.4). Here we crudely assume that the salinity difference between the sea surface and 6 m depth is 0.7 (i.e., corresponding to the temperature difference of 0.7 °C). Variations in near-surface salinity alter carbonate chemistry and influence fCO_{2w}. We use bulk water (~6 m depth) DIC and TA measurements (S3, Table S3.2) collected a month later from 9 stations in the nearby Fram Strait (S3, Figure S3.1, the sea ice concentration had decreased from ~50% to ~0% during a previous week of the cruise) to estimate the influence of salinity change on the vertical fCO_{2w} gradient. The average DIC, TA and salinity were 1974 ± 19 µmol kg^{-1}, 2100 ± 22 µmol kg^{-1}, and 30.6 ± 0.6‰, respectively.

Bulk water DIC and TA are corrected to sea surface salinity by dividing by bulk salinity and multiplying by surface salinity (= bulk salinity − 0.7‰). The calculated surface and measured bulk water DIC and TA are used to estimate the sensitivity of fCO_{2w} to salinity change (Lewis & Wallace, 1998; Van Heuven et al., 2011). We estimate that the vertical salinity gradient can explain a fCO_{2w} gradient of on average 10.6 ± 1.1 µatm. This salinity-related decrease in fCO_{2w} accounts for 27% of the near-surface vertical fCO_{2w} gradient. Considering that the surface seawater is expected to be rapidly warmed by solar radiation, whereas salinity is less affected by surface warming, the temperature effect will be more transitory than the salinity effect. Thus, the estimated salinity effect is likely conservative, i.e., greater than 27%.

Sea-ice-related plankton metabolism might be another reason for lower fCO_{2w} in the surface stratified layer. The CTD oxygen profiles show that the oxygen concentration increases close

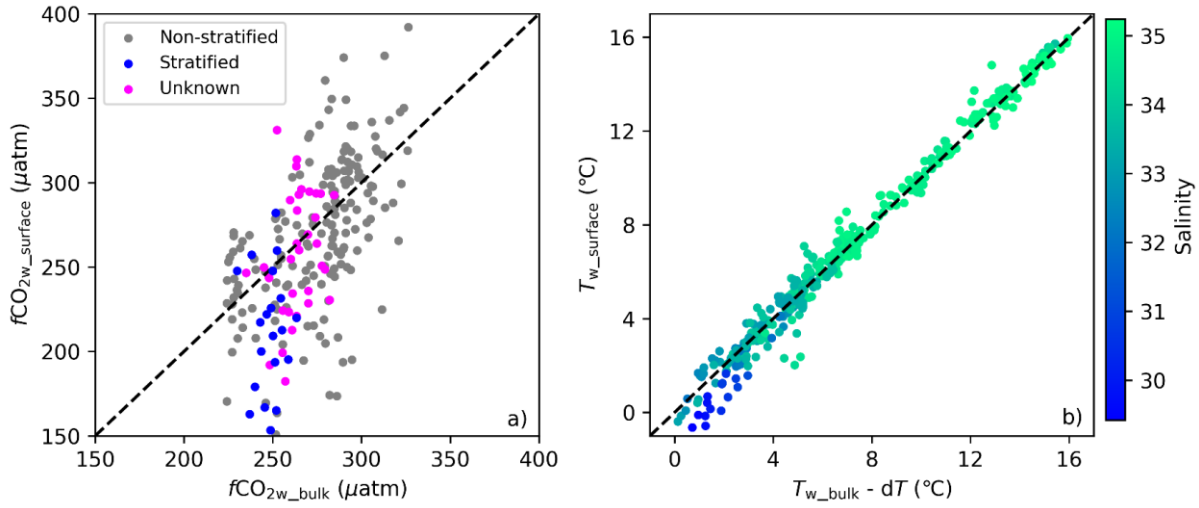

Figure 3.3 Measurements at 6 m depth of seawater CO_2 fugacity (fCO_{2w_bulk}) and temperature (corrected for the cool skin effect, i.e., T_{w_bulk} − dT) versus eddy covariance implied sea surface CO_2 fugacity ($fCO_{2w\_surface}$) and temperature ($T_{w\_surface}$): a) fCO_2 values from cruise JR18007. Grey dots are values in non-stratified waters, blue dots are in stratified waters and magenta dots are in waters for which the stratification status could not be determined; b) Seawater temperature for JR18006 and JR18007 with the dots colour-coded by salinity at 6 m depth.

to the surface in the stratified stations (S3, Figure S3.4). Chierici et al. (2019) observed meltwater-induced phytoplankton production in the marginal ice zone near Fram Strait in May 2019, which continued until the end of August. Photosynthesis in the upper few meters of the water column could reduce fCO_{2w}.

Air-sea gas exchange cannot be the cause of the lower surface fCO_{2w} observed in stratified waters because the influx of CO_2 would have not help to explain the observations, increasing fCO_{2w} at the surface. The results presented here demonstrate that near-surface stratification due to sea-ice melt generates a strong near-surface fCO_{2w} gradient ($fCO_{2w\_surface}$ < fCO_{2w_bulk}), which causes a bias in bulk air-sea CO_2 flux estimates when fCO_{2w_bulk} from ~6 m depth is used. In the next section, we estimate the impact of such a bias would have on CO_2 uptake by the entire Arctic Ocean.

3.3.4 Potential impact on Arctic Ocean CO_2 uptake estimates

Here we speculate on the potential impact of near-surface stratification due to summertime sea-ice melt on estimates of CO_2 uptake for the entire Arctic Ocean.

We make the following crude assumptions: 1) bulk fCO_{2w} measurements overestimate the surface fCO_{2w} in all regions with sea-ice melt; 2) the fCO_{2w} overestimation (-fCO_{2w} offset, µatm) decreases with wind speed for U_{10N} > 3 m s^{-1} (fCO_{2w} offset $= -408\,U_{10N}^{-1} + 27$, S3, Figure S3.5) (Fischer et al., 2019; Miller et al., 2019; Ahmed et al., 2020) and is assumed to be constant (109 µatm) at $U_{10N} \leq 3$ m s^{-1}; 3) surface seawater temperature and salinity are 2°C and 31‰ within the stratified areas, respectively (average of the EC implied $T_{w\_surface}$ and surface salinity in the stratified waters during JR18007).

The 6-hour Cross-Calibrated Multi-Platform (CCMP) Wind Vector Analysis (Atlas et al., 2011) at a height of 10 m above mean sea level is used to calculate K_{660} and to estimate the fCO_{2w} offset. The flux offset is calculated with Equation 3.1 (replacing ΔfCO_2 with fCO_{2w} offset), and the result from each grid cell is linearly scaled using the sea ice concentration. The AMSR-E (Spreen et al., 2008) daily sea ice concentration (SIC) data (3.125 km grid resolution) are used to determine the extent of stratified areas. There are two scenarios when a grid cell is deemed to contain near-surface stratified water: 1) the ice-free proportion of the grid cell is considered to be stratified when SIC is between 0% and 100%; 2) SIC of a grid cell has declined to 0% during the last 10 days (assuming that near-surface stratification lasts for 10 days, within the indicated duration time indicated by Ahmed et al., 2020), the whole cell is considered to be stratified.

We focus on the summertime (June to August inclusive) Arctic Ocean in 2019. The result shows that the largest area with near-surface stratification and the greatest underestimation of CO_2 uptake occur in July (S3, Figure S3.6). K_{660} increases with the wind speed, while the magnitude of fCO_{2w} offset decreases with wind speed, so the wind speed effect on the variability of the flux offset is almost cancelled out and the estimated bulk flux variability is mainly related to the size of the stratified area. The integrated summertime underestimation of Arctic Ocean CO_2 uptake due to sea-ice melt is estimated to be 11 Tg C, which is comparable with the back-of-the-envelope calculation (9.3 Tg C yr^{-1}) of Ahmed et al. (2020).

The above estimate is based on assumptions that the fCO_{2w} offset is wind speed dependent and the shallow stratification lasts for 10 days. High wind speed enhances the near-surface seawater mixing and weakens the shallow stratification. We do not have a robust relationship between fCO_{2w} offset and wind speed because our measurements in stratified waters only span a small range of wind speeds (6 ± 1 m s^{-1}) and the data are quite scattered (S3, Figure S3.5). If we do not consider the influence of wind speed on the fCO_{2w} gradient and assume a constant fCO_{2w}

offset of -39 µatm in the sea ice melt region, then the underestimation of Arctic Ocean CO_2 uptake is reduced to 6 Tg C. Another major uncertainty is inherent in our assumption that near-surface stratification lasts for 10 days. If we assume that the near-surface stratification lasts 7 days or 14 days, the underestimation of Arctic Ocean CO_2 uptake is 10 Tg C and 13 Tg C, respectively (using the wind speed-dependent fCO_{2w} offset).

The underestimation of 11 Tg C in 2019 corresponds to 6–17% of annual Arctic Ocean carbon uptake (66–199 Tg C yr^{-1}, Bates & Mathis, 2009). Note that the CO_2 sink estimate by Bates & Mathis (2009) was a decade ago, so the percentage of this underestimate may have slightly changed.

3.4 Conclusions

This study reports direct and indirect estimates of air-sea CO_2 and sensible heat fluxes from shipboard campaigns in the summertime Arctic Ocean. Direct fluxes by eddy covariance are used to compute the implied sea surface fCO_{2w} and T_w. Comparisons of implied surface values with bulk water measurements at 6 m depth help to identify possible vertical fCO_{2w} gradients in the upper ocean. Implied surface fCO_{2w} is on average 39 µatm lower than bulk fCO_{2w} in regions with near-surface stratification due to sea ice melt. EC-derived gas transfer velocities (K_{660}) using bulk seawater measurements in non-stratified regions agree well with previous parameterisations. However, in stratified regions, EC-derived K_{660} is higher at a given wind speed because of the near-surface fCO_{2w} gradient.

Cooling and freshening due to sea-ice melt in the Arctic summer accounts for 18% and at least 27% of the near-surface fCO_{2w} gradient during cruise JR18007, respectively. Enhanced photosynthesis in the stratified layer may also have contributed to the near-surface fCO_{2w} gradient.

The Arctic Ocean is an important CO_2 sink, but this ocean carbon uptake may have been underestimated previously due to near-surface fCO_{2w} gradients induced by sea-ice melt. A simple calculation for the summertime Arctic Ocean suggests that near-surface stratification due to sea-ice melt could lead to an ~10 Tg C underestimation of CO_2 uptake but there is considerable uncertainty in the validity of such an extrapolation. Continuing loss of Arctic sea ice is expected to increase CO_2 uptake in summer, and may further increase the uncertainty in Arctic air-sea CO_2 flux estimates if near-surface stratification is not considered.

This is the first time to our knowledge that direct measurements by EC have been used to quantify the potential bias in bulk flux estimates due to near-surface stratification in the Arctic Ocean. A similar underestimation in CO_2 flux related to sea-ice melt may also occur in the Southern Ocean. Detailed studies of upper ocean (0–10 m) gradients in fCO_{2w}, temperature, salinity, DIC, TA and biological rates along with EC flux measurements, are required to improve understanding of sea-ice melt impacts and near-surface stratification on air-sea exchange.

Chapter 4

4 Southern Ocean CO_2 flux estimates

> "You are now working hard to do details, but it is about the big picture which ultimately you will contribute. You should think about your ideas and how to enter the big picture."
>
> (Peter S. Liss, January 2021)

The results presented in the following chapter are ready for submitting to a scientific journal:

Strong summertime Southern Ocean CO_2 uptake from direct flux observations

Yuanxu Dong[1,2], Dorothee C. E. Bakker[1], Thomas G. Bell[2], Judith Hauck[3], Peter Landschützer[4], Peter S. Liss[1], and Mingxi Yang[2]

[1]Centre for Ocean and Atmospheric Sciences, School of Environmental Sciences, University of East Anglia, Norwich, UK

[2]Plymouth Marine Laboratory, Prospect Place, Plymouth, UK

[3]Alfred-Wegener-Institut, Helmholtz-Zentrum für Polar- und Meeresforschung, Bremerhaven, Germany

[4]Flamish Marine Research Institute, Ostend, Belgium

The work and analysis presented in this chapter is led by Y. Dong. Co-authors on this publication collected the data, provided guidance and suggestions regarding the analysis and the results to help and address the interests of the wider scientific community.

Abstract: The Southern Ocean is a major sink of anthropogenic carbon dioxide (CO_2) and regulates variations of the global ocean CO_2 uptake. However, sparse observations and the complex physical environments lead to the CO_2 sink of the Southern Ocean being poorly understood at different temporal and spatial scales. In this study, we provide independent validations of current CO_2 flux estimates by employing direct air-sea CO_2 flux measurements by the eddy covariance (EC) technique from seven cruises in the summertime Southern Ocean. We subsampled the CO_2 flux from ship-based, float-based, and ship plus float-based flux products at the times and locations of each EC observation. We find that EC flux measurements support the ship-based CO_2 fluxes after considering the temperature corrections, but indicate much stronger CO_2 uptake than the float-based CO_2 fluxes during the Austral summer. The EC observations also provide a good constraint for the gas transfer velocity from low to high wind speeds in the Southern Ocean environment, which agree fairly well with the widely used parameterisation schemes.

4.1 Introduction

The global ocean is a major carbon dioxide (CO_2) sink, accounting for ~25% (2.8 ± 0.4 Pg C yr^{-1}) of CO_2 emissions by human activities for the last decade and playing a key role in mitigating climate change (Friedlingstein et al., 2022). A substantial fraction (~40%) of the oceanic uptake of anthropogenic CO_2 occurs in the Southern Ocean (< 35°S) according to the estimate from ocean carbon inventory (eg., Devries, 2014). However, carbon-related observations in the Southern Ocean do not match its importance in CO_2 uptake. Measurements of sea surface CO_2 fugacity (fCO_{2w}) combining a wind speed-dependent gas transfer velocity (K_{660}) are often used for air-sea CO_2 flux estimates. The Southern Ocean is one of the most under-sampled regions with regard to fCO_{2w} from the Surface Ocean CO_2 Atlas (SOCAT, Bakker et al., 2016) dataset. This results in high uncertainties in SOCAT-based CO_2 flux estimates in the Southern Ocean (Gloege et al., 2021; Landschützer et al., 2015; Lenton et al., 2013; Monteiro et al., 2015). The latest release of the Global Carbon Budget highlights the large divergence between the model and observation-based CO_2 flux estimates in the Southern Ocean in both annual mean and flux trends in the last decade (Friedlingstein et al., 2022).

The SOCAT data are shipboard measurements, indicating the scarcity of winter observations because the extreme environments in the winter Southern Ocean prohibit ship-based sampling. Novel autonomous pH observations from biogeochemical floats (SOCCOM, Southern Ocean

Carbon and Climate Observations and Modeling) have been starting to fill this data gap since 2014. However, floats do not measure fCO_{2w} directly but estimate fCO_{2w} from pH observations and empirically estimated total alkalinity (Williams et al., 2017). The uncertainty in these estimated float fCO_{2w} (± 11.4 µatm at 400 µatm, Williams et al., 2017) is much higher than in the shipboard fCO_{2w} observations (± 2 µatm, Bakker et al., 2016). Additionally, there is likely an on average +4 µatm bias in these float fCO_{2w} data. The float data (i.e., SOCCOM)-based flux estimate shows a much weaker CO_2 uptake of the Southern Ocean (-0.35 Pg C yr^{-1}, negative values signify ocean CO_2 uptake in this study) compared to the ship (i.e., SOCAT)-based flux estimate (-1.14 Pg C yr^{-1}) (Bushinsky et al., 2019). The discrepancy in these two flux estimates is largest in austral winter (define as May to October in this study) but originates from all months. The wintertime disagreement may be attributed to the lack of ship fCO_{2w} observations. But SOCAT contains many highly accurate fCO_{2w} observations in summer (define as November to April in this study, Figure 4.1A), which should provide a good constraint of the summertime CO_2 flux of the Southern Ocean. A SOCAT-based flux product (Landschützer et al., 2021) estimates a significantly stronger (on average by a factor of ~1.6 from 2015 to 2020) CO_2 uptake than a SOCCOM-based flux estimate, especially in the Antarctic Circumpolar Current (ACC) zone (Figures 4.1C and 4.1D). Therefore, whether the novel float measurements advanced our understanding of the Southern Ocean CO_2 flux remains in debate.

Recent independent fCO_{2w} measurements in the Southern Ocean from an autonomous platform (Saildrone Inc. Uncrewed Surface Vehicles) yield a more similar CO_2 flux to the SOCAT-based flux product than the SOCCOM-based flux estimate in both winter and summer observation periods (Sutton et al., 2021). Mackay et al. (2022) produced an estimated wintertime surface fCO_{2w} using subsurface summertime carbon-related observations in the Southern Ocean, and including these estimated fCO_{2w} in the flux estimation results in an < 8% reduction in the SOCAT-based CO_2 sink estimates.

Furthermore, the Southern Ocean airborne campaigns provide a new CO_2 flux constraint from the airside observations and indicate consistent CO_2 flux with the ship-based flux products in winter (Long et al., 2021). Large outgassing signatures during winter and less uptake in summer suggested by the float data are not evident in any of the nine Southern Ocean aircraft campaigns. On the other hand, the aircraft observations indicate more significant (~50% higher) summertime CO_2 uptake in the south of 45°S than the flux estimate based on the SOCAT dataset (Long et al., 2021).

These disagreements between the different observation-based fluxes illustrate the large uncertainties in the current Southern Ocean CO_2 flux estimates. In addition to the uncertainty from the surface observations, the parameterisation of K_{660} is another major uncertainty source for the air-sea CO_2 flux estimates (Woolf et al., 2019). A quadratic wind speed-dependent K_{660} (Wanninkhof, 2014) constrained by the global bomb-^{14}C inventory (Naegler, 2009) is indistinctively applied to the global ocean CO_2 flux estimates without considering the regional variation of the wind speed dependence. A recent study shows notable regional variability of the K_{660}−wind speed relationships (Yang et al., 2022), which highlights the necessity of using specific K_{660} parameterisations for regional ocean CO_2 flux quantifications. Furthermore, the upper ocean temperature gradients likely introduce another uncertainty in the CO_2 flux estimate, in particular, increasing the Southern Ocean CO_2 uptake by 15−30% (Dong et al., 2022; Watson et al., 2020).

Novel direct air-sea CO_2 flux measurements by the eddy covariance (EC) method (e.g., Dong et al., 2021a) reported in this study provide an independent validation for the current Southern Ocean CO_2 flux estimates. The EC CO_2 fluxes are measured directly in the atmosphere and do not rely on K_{660} as well as unaffected by the upper ocean temperature effects, which provide unique reference material for the Southern Ocean CO_2 flux estimates. The EC measurements also enables an investigation of the K_{660}-wind speed relationship in the Southern Ocean. From 2019 to 2020, we collected high-quality ship-based EC air-sea CO_2 flux measurements from seven cruises in the summertime Southern Ocean (Figure 4.1E, 4.1F and supplement S4, hereafter S4). In this study, we employ these EC fluxes to compare with the ship-based and float-based CO_2 flux estimates, and to derive a new wind speed-dependent K_{660} parameterisation tailored for the Southern Ocean.

4.2 Results

4.2.1 Flux time series

To compare the current CO_2 flux estimates with the EC flux observations in the Southern Ocean, we subsample a neural network-based (Landschützer et al., 2013) SOCAT, SOCCOM, and SOCAT plus SOCCOM CO_2 flux product at the location and month of each hourly EC CO_2 flux measurement (see Materials and Methods, hereafter MM) and average the CO_2 fluxes over 1-day periods. We also subsample the variables used for the flux product estimates (ERA5 wind speed product, the three neural network-based fCO_{2w} products, and the OISST v2) in the same way as the flux subsampling. The EC measurements show a typical negative CO_2 flux

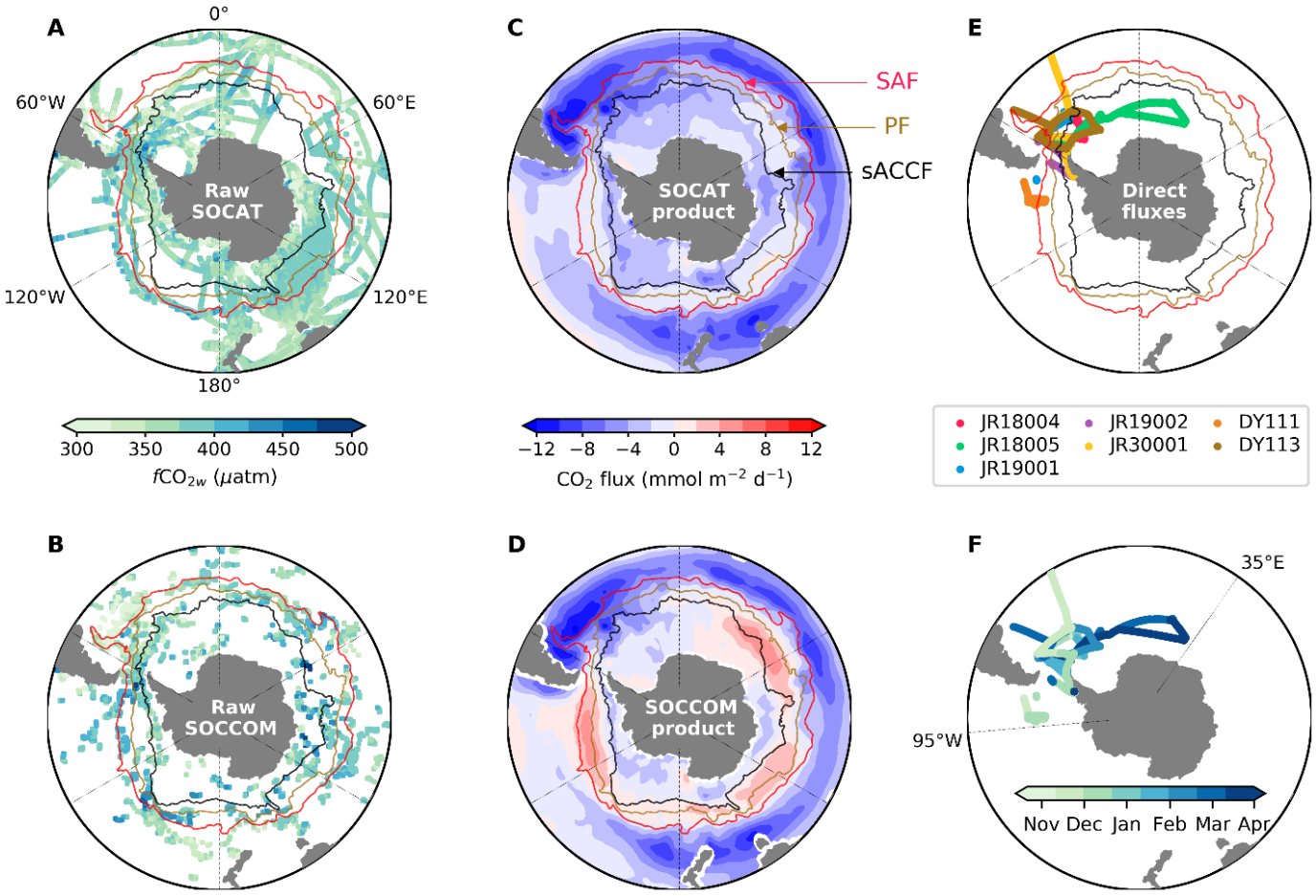

Figure 4.1 Maps of the surface ocean CO_2 fugacity (fCO_{2w}) observations, CO_2 flux estimates, and direct air-sea CO_2 flux measurements in the summertime Southern Ocean. (A and B) shipboard (SOCAT) and float (SOCCOM) sampling distributions. Colours represent the fCO_{2w} values. (C and D) CO_2 flux estimates based on the SOCAT dataset and SOCCOM dataset, respectively with a neural-network interpolation technique (Landschützer et al., 2013). (E and F) Cruises with eddy covariance air-sea CO_2 flux observations (see S4). The cruise tracks in Figure 1F are colour-coded by observation months. Fronts constructed from the satellite altimetry data (Park et al., 2019) shown as the red, brown, and black curves are as follows: the Subantarctic Front (SAF), the Polar Front (PF), and the southern Antarctic Circumpolar Current (sACCF) .

with short-lived outgassing events. The subsampled fluxes largely follow the variation of the EC fluxes (except for cruise JR19001), but with a smaller amplitude and a less negative flux on average. The smaller variability in the subsampled fluxes is partially due to the less variation in the 1° × 1°, monthly wind speed product (Figure 4.2B). The subsampled high resolution (0.25° × 0.25°, hourly) wind speed product shows a fairly good agreement to the *in-situ* wind observations during all the cruises (Figure 4.2B).

Several notable divergences between EC fluxes and subsampled flux products are because the products underestimate the magnitude of the fCO_{2w} such as a strong outgassing event during the early period of cruise JR18005 and strong uptake events during the second half of the cruise JR19001 (Figure 4.2A and 4.2C). Although the fCO_{2w} is sensitive to sea surface temperature (SST), these discrepancy in fCO_{2w} between observations and subsampled products cannot be attributed to the temperature effects since the *in-situ* SST nearly identical to the subsampled OISST v2 (Figure 4.2D). In addition, all the subsamples including the CO_2 flux, wind speed, and SST disagree with the *in-situ* observation during the first half of cruise JR19001 when the research vessel was on stations which are ~100 km far away from the coastline of the South Georgia and the South Sandwich Islands. Both SOCAT and SOCCOM products demonstrate that the regions nearby these Islands are strong CO_2 sinks (Figure 4.1C and 4.1D), but our EC measurements suggest neutral to a slight CO_2 outgassing.

The subsampled SOCCOM flux product shows a strong outgassing period during the cruise JR18005, which is not seen in the subsampled SOCAT and SOCAT plus SOCCOM flux products. The EC flux measurements only suggest short-lived outgassing events during this period and the average over this period does not lead to outgassing (shown uptake by EC measurements) as strong as the SOCCOM flux product. This short-lived outgassing phenomenon is also indicated by a previous study using high resolution observations. The short-lived outgassing event over hours to days occurs ubiquitously during all of our cruises (Figure 4.2A), but does not dominate the CO_2 flux direction (i.e., sink or source) over a longer period and a larger spital scale. This phenomenon can be well-captured by such as the continuous and mobile shipboard observations (Bakker et al., 2016), but may be biasedly sampled by the local SOCCOM float at a 10-day sampling frequency. Based on the high-resolution Saildrone-based fCO_{2w} measurements, research suggests a 23% positive CO_2 flux bias (more outgassing) when sampling the hourly dataset at all possible 10-day sampling frequency (Sutton et al., 2021). Another research employing hourly glider-based fCO_{2w} measurements, indicates a ± 5% uncertainty at the daily resolution, but ± 50% uncertainty at the 10-day sampling period of the mean air-sea CO_2 flux (Monteiro et al., 2015). Therefore, the current SOCCOM observations are likely a poor representative of the entire Southern Ocean. Interpolation of the not fully representative float fCO_{2w} dataset may overemphasize the short-lived, local effects.

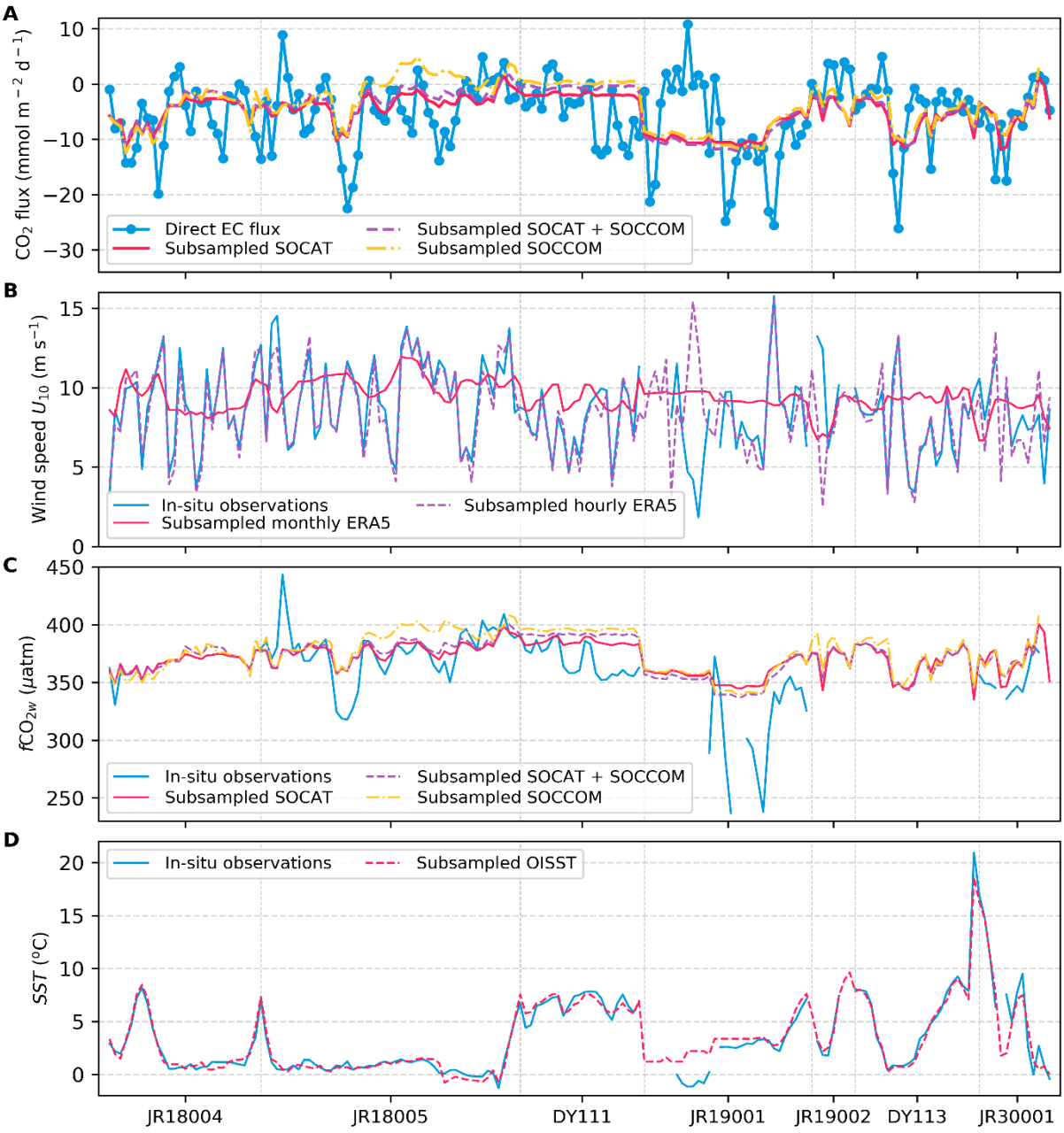

Figure 4.2 Time series of air-sea CO_2 fluxes, 10-meter wind speeds (U_{10}), fCO_{2w}, and sea surface temperature (SST) measured during cruises and subsampled from products at the *in-situ* observation locations and times. (A) EC air-sea CO_2 flux measurements (blue) and fluxes subsampled from three neural network-based products (red, SOCAT product; purple, SOCAT plus SOCCOM product; yellow, SOCCOM product). (B) Shipboard wind speed observations (blue) during the cruises and subsampled wind speed from a high resolution (red, 0.25° × 0.25°, hourly) and a low resolution (purple, average the square of the high resolution wind speed to 1° × 1°, monthly resolution) ERA5 product, respectively. (C) Shipboard fCO_{2w} flux measurements (blue) and fCO_{2w} subsampled from three neural network-based products (red, SOCAT product; purple, SOCAT plus SOCCOM product; yellow, SOCCOM product). (D) Shipboard SST observations (blue) and SST subsampled from a product named OISST v2. See Materials and Methods for details.

4.2.2 Monthly and regional variations of the CO_2 flux

The summertime accounts for ~60–80% of the annual CO_2 uptake in the Southern Ocean. Although the CO_2 flux divergence between the SOCAT product and the SOCOOM product is more evident in the wintertime, the summertime disagreement is also significant. The neural network-based SOCAT product yields a consistently stronger CO_2 uptake than the neural network-based SOCAT plus SOCCOM and SOCCOM product by a factor of 1.2 and 1.6, respectively in the summertime Southern Ocean on average from 2015 to 2020 (SM, S4.1). The subsampled SOCAT, SOCAT plus SOCCOM, and SOCCOM flux products with a monthly average show a typical decreasing trend of the CO_2 flux from January to April forced primarily by the biological processes (e.g., Merlivat et al., 2015; Takahashi et al., 2002; SM, S4), in line with the monthly variation of the EC flux observations (Figure 4.3A) during this period. But EC observations suggest a more negative monthly flux from December to March than all three subsampled flux products. The weaker EC flux in November is mainly due to the outgassing events in November 2019 during cruise JR19001.

The disagreement between the SOCAT flux product and the SOCCOM flux product is inhomogeneous and prominent in the Antarctic Circumpolar Current (ACC) regions between ~65°S to 55°S (S4.1). Fortunately, most of our EC observations were within this latitude band. Figure 4.3B shows that the EC fluxes (2°-latitude average) are consistently more negative than all three subsampled products, but agree best with the subsampled SOCAT product among the three products, especially at latitudes ~60°S. In addition, in the ACC regions between 10°E and 30°E, the SOCCOM flux product shows outgassing fluxes, while the SOCAT flux product suggests CO_2 uptake in this region (Figure 4.1C, 4.1D and S4.1). The EC flux measurements indicate even stronger CO_2 uptake than the resampled SOCAT flux product in this region (i.e., 10–30°E, Figure 4.3C). Similarly, in the region of cruise DY111 (~ 90°W), the SOCCOM product suggests slight CO_2 outgassing, but the SOCAT product and EC measurements show a sink and a strong sink of CO_2, respectively.

4.3 Discussion

The results above shows that the subsampled SOCCOM product flux considerably underestimates the CO_2 uptake measured by EC. The subsampled SOCAT flux product agrees best with the EC flux among these three flux products, but still yields significantly less negative

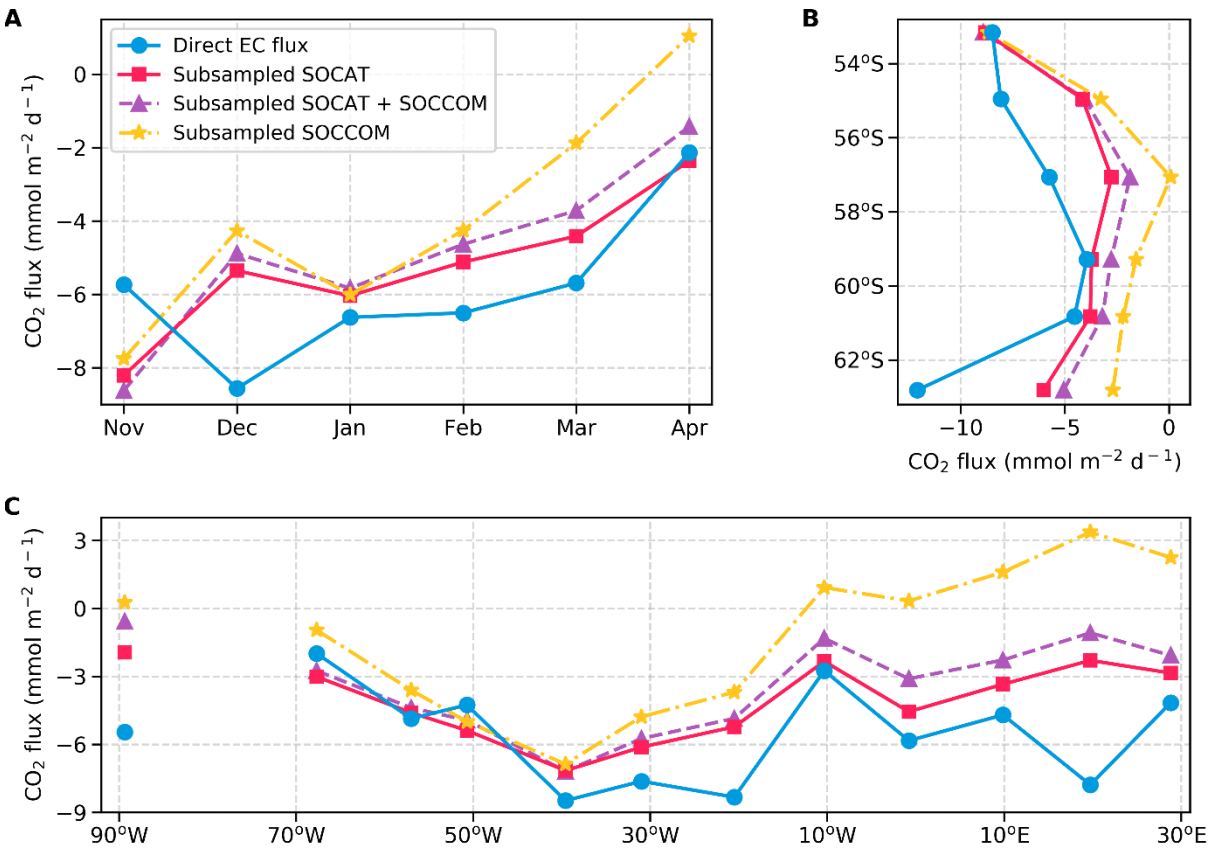

Figure 4.3 Monthly, latitudinal, and longitudinal variations of the air-sea CO_2 flux. The four lines with different colour in each figure represent the direct EC flux measurements (blue), subsampled SOCAT flux product (red), subsampled SOCAT plus SOCCOM flux product (purple), and subsampled SOCCOM flux product (yellow). (A) Monthly mean of the CO_2 fluxes. (B) 2° latitude mean of the CO_2 fluxes. (C) 10° latitude mean of the CO_2 fluxes.

fluxes (~30% on average) compared to the EC observations. What is the reason of this disagreement?

4.3.1 Gas transfer velocity

One possible reason for the disagreement between the subsampled SOCAT flux product and the EC flux is the uncertainty in the K_{660} used for SOCAT flux product estimates. The widely used K_{660} parameterisations are either based on the global bomb-^{14}C inventory (e.g., Wanninkhof, 2014) or based on the dual-tracer observations (e.g., Ho et al., 2006; Nightingale et al., 2000). However, the global bomb-^{14}C inventory only provides a mean gas transfer velocity (18.2 ± 3.6 cm hr^{-1}, Naegler, 2009) for the global ocean over a long timescale (half-century), while the dual-tracer method can investigate the local gas exchange but the observed

gas transfer rate still has a relatively long-term timescale (~10-day). The short-term (e.g., hourly) gas exchange at relatively high and low wind speeds will be averaged to have an intermediate wind speed over a long-term timescale (e.g., 10-day). Therefore, both the bomb-^{14}C inventory-based and the dual-tracer-based K_{660} parameterisations at low (< 5 m s^{-1}) and high wind speeds (> 13 m s^{-1}) are interpolated from the gas transfer at intermediate wind speed conditions by assuming a quadratic K_{660}-wind speed relationship. For the neural network-based flux products studied in this research, K_{660} is scaled to match the global mean transfer velocity of 18.2 cm hr^{-1} (Naegler, 2009) using the ERA5 wind speed product (Hersbach et al., 2020). However, recent EC-based studies (e.g., Yang et al., 2022) suggested regional variations of the K_{660}-wind speed relationship, which is understandable given wind speed is not the only driver for air-sea CO_2 exchange, others such as ocean waves, surfactants, and chemical enhancement can also affect K_{660}.

The small-scale (several km^2, hourly) EC air-sea CO_2 flux observations combining the CO_2 fugacity observations provide a good opportunity to constrain the K_{660} from low to high wind speeds for the Southern Ocean environment (see MM and Figure 4.4). Unsurprisingly, the EC-derived K_{660} agrees well with the ^{14}C-based and the dual-tracer-based parameterisations at the well-constrained intermediate wind speed, but disagrees at the poorly constrained low and high wind speeds (Figure 4.4). The EC-derived K_{660} is on average slightly higher at low wind speeds (< 7 m s^{-1}), but lower at high wind speeds (> 12 m s^{-1}) than K_{660} estimates from two widely used parameterisations (Wanninkhof, 2014; Ho et al., 2006). Intriguingly, the new K_{660} parameterisation based on these Southern Ocean observations is nearly identical to a K_{660}-wind speed formulation based on an Arctic cruise at low to intermediate wind speeds (Dong et al., 2021b). The Arctic K_{660} were derived from high-quality EC observations (relative uncertainty was small) at a very high flux signal (air-sea CO_2 fugacity difference between -181 and -71 µatm) environment (see Chapter 3 and Dong et al., 2021b) The non-zero K_{660} at low wind speed is most likely due to the chemical enhancement (only significant at low wind speed) of the air-sea CO_2 exchange, which is not included in the ^{14}C-based parameterisation (e.g., Wanninkhof, 2014) and cannot be sensed by the dual-tracer observations (e.g., Ho et al., 2006). But the chemical enhancement can be captured by EC observations and is contained in the EC-based K_{660} parameterisation (e.g., Dong et al., 2021b and this study). The chemical enhancement is SST dependent, and the similar SST at these two high-latitude ocean environments leads to a nearly identical K_{660} at low wind speeds. In addition, ocean waves and bubbles may play an important role in the air-sea CO_2 exchange at high wind speed (e.g., Bell et al., 2017; Blomquist

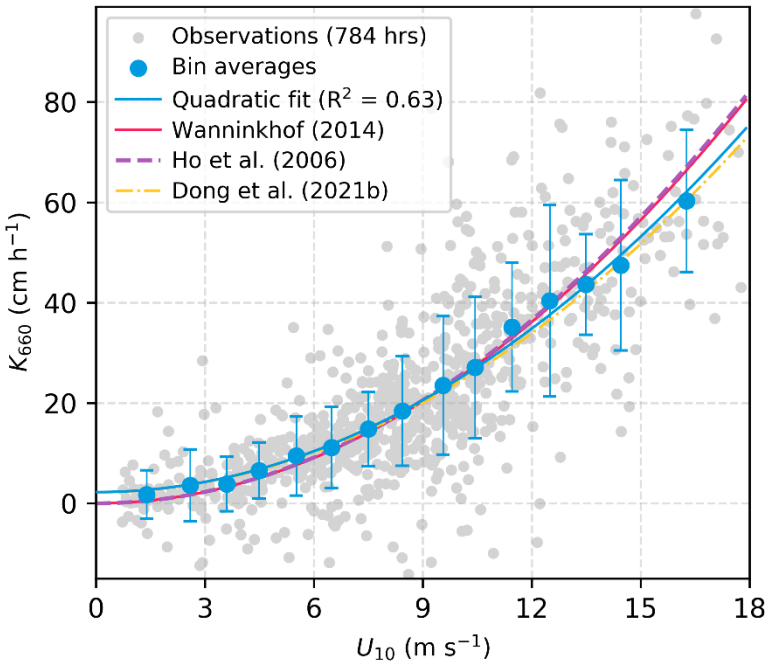

Figure 4.4 Gas transfer velocities (K_{660}) derived from EC air-sea CO_2 flux observations on Southern Ocean cruises vs. 10 m neutral wind speed (U_{10})**.** Gray dots are hourly EC-derived K_{660} and blue squares represent 1m s^{-1} bin averages, with error bars indicating 1 standard deviation. The blue curve represents a quadratic fit using the bin averages: $K_{660} = 0.23U_{10}^2 + 2.23$ ($R^2 = 0.63$). The red and purple and yellow lines correspond to the K_{660} parameterisations constrained by the global bomb-^{14}C inventory (Wanninkhof, 2014), based on the dual-tracer observations in an open ocean (Ho et al., 2006) and determined by the EC observations from an Arctic cruise in a very high flux signal region (Dong et al., 2021b), respectively.

et al., 2017). Therefore, different sea state is likely responsible for the divergence of K_{660} in different regions at high wind speed.

Although there are discrepancies between the EC-derived K_{660} and the ^{14}C and dual-tracer-based parameterisations at low and high wind speeds, the disagreement is insignificant. In addition, the intermediate wind speed (7–12 m s^{-1}) conditions dominate our observations (Figure 4.2B). Using the new K_{660}–wind speed relationship proposed in Figure 4.4 to recalculate the CO_2 flux based on the subsampled SOCAT fCO_{2w} product and the hourly ERA5 wind product only increases the CO_2 uptake by ~2.5% compared with using the ^{14}C or dual-tracer-based parameterisation (Wanninkhof, 2014; Ho et al., 2006) for the flux calculation. The enhanced flux at low wind speed is offset by the damped flux at high wind speed. Therefore, the divergence between the subsampled SOCAT flux product and the EC flux observations cannot be explained by the uncertainty in the parameterisation of K_{660}. These comparisons give

us confidence in using these previously proposed K_{660}-wind speed relationships for the CO_2 flux estimate in the summertime Southern Ocean, but we should keep in mind that the wintertime gas transfer might be enhanced by the bubble-mediated transfer at a rougher ocean environment (e.g., Blomquist et al., 2017).

In addition to the K_{660} parametrization scheme, the difference between the wind speed from *in-situ* observations and subsampled from the ERA5 product can also lead to flux disagreements. However, the mean square of the *in-situ* wind speed observations during these Southern Ocean cruises (90.9 m^2 s^{-2}) agrees with the mean square of the subsampled monthly ERA5 wind product (91.4 m^2 s^{-2}). Therefore, the flux difference is unlikely to result from the wind speed.

4.3.2 Warm bias and cool skin effect

The second possibility to account for the flux difference between the EC and subsampled SOCAT flux product is the warm bias (ship warming) and the cool skin effect. The SOCAT flux products are surface ocean observation-based flux estimates and are thus influenced by the warm bias and the cool skin effect while the EC flux observations are made in the atmosphere and are thus unaffected by these two temperature effects. Two recent research suggested a ~15–30% (0.22–0.35 Pg C yr^{-1}) increase in the SOCAT-based CO_2 uptake estimate of the Southern Ocean (Watson et al., 2020; Dong et al., 2022), which is in the same order as the mean flux difference between the EC and the subsampled SOCAT product in this study (~30%).

We collected 1580 hours with EC CO_2 flux and concurrent fCO_2 observations during the Southern Ocean cruises. The EC CO_2 flux was on average ~15% more negative than the fCO_2-based flux (using the Wanninkhof (2014) K_{660} parameterisation) without considering the cool skin effect. Applying the cool skin effect estimated by an empirical formulation (Zhang et al., 2020) to the fCO_2-based flux calculation could increase the flux estimate by ~10% (more uptake) and reduce the EC flux and fCO_2-based flux difference to ~5%. Similarly, a recalculation of the subsampled SOCAT-based flux indicates a 12% CO_2 sink estimate

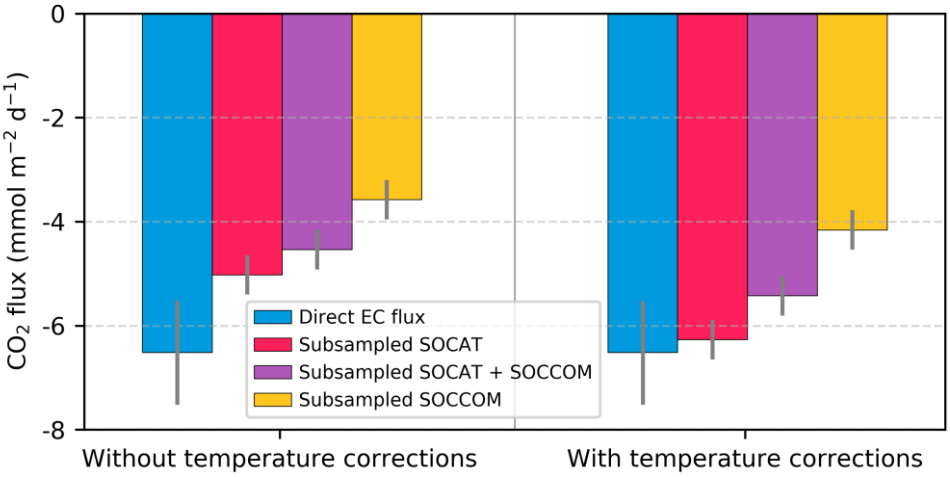

Figure 4.5 Mean air-sea CO_2 flux for a Southern Ocean region without (left) and with (right) the temperature corrections. The blue bar represents the EC air-sea CO_2 flux observations with error bars indicating a typical 1 mmol m^{-2} day^{-1} uncertainty for the daily (at least 4 hours) averaged EC CO_2 flux (Dong et al., 2021a). Red, purple, and yellow bars represent subsampled SOCAT, SOCAT plus SOCCOM, and SOCCOM flux products, respectively. Error bars represent ± 0.38 mmol m^{-2} day^{-1} (i.e., ± 0.15 Pg C yr^{-1} for the whole Southern Ocean) uncertainties associated with the neural network-based CO_2 flux estimates (Bushinsky et al., 2019). Two temperature corrections (warm bias and cool skin effect) are applied to the subsampled SOCAT flux product, while only the cool skin correction is applied to the subsampled SOCCOM flux product. The entire cool skin correction and half of the warm bias correction is applied to the subsampled SOCAT plus SOCCOM flux product.

enhancement by considering the cool skin effect. The potential warm bias in the shipboard SST dataset was less likely to impact our Southern Ocean observations because our data were collected on research vessels and the SST observations were frequently calibrated. However, the shipboard SST in the SOCAT dataset likely contains a small warm bias (on the order of 0.1K; Dong et al., 2022). Correcting for this warm bias increases the SOCAT-based CO_2 flux at a similar order to the cool skin flux correction (Dong et al., 2022) in the Southern Ocean. Therefore, considering the warm bias and the cool skin effect will increase the resampled SOCAT product flux by ~25%, which fills the mean flux gap between the EC observations and resampled SOCAT product within the uncertainty range (Figure 4.5). The SOCCOM-based flux estimate is affected by the cool skin effect, but undisturbed by the warm bias issue because the data were collected by float (e.g., without the warming process by such as the ship's engine). Applying the cool skin correction cannot bridge the flux gap between the EC flux and the subsampled SOCCOM flux products. The mean EC flux is ~60% more negative than the subsampled temperature-corrected SOCCOM product (Figure 4.5). Considering the SOCAT

plus SOCCOM product is based on both the shipboard and float datasets, we applied the entire cool skin correction and a half warm bias correction to the resampled SOCAT plus SOCCOM product. But the temperature-corrected SOCAT plus SOCCOM flux still indicates an on average ~20% underestimation of the EC CO_2 flux observations.

4.4 Conclusions

This study reports direct air-sea CO_2 flux measurements by the EC technique in the Southern Ocean from seven cruises. The neural network-based SOCAT (shipboard dataset), SOCCOM (float dataset), and SOCAT plus SOCCOM flux products are subsampled at the location and month of the EC observations. By comparing the EC flux observations to the subsampled flux products, we conclude:

All three subsampled flux products can largely reproduce the variation of the EC flux measurements but with a smaller amplitude. The EC flux show ubiquitous short-lived (hour-to-day) outgassing events, but the average of the EC flux over a long-term (i.e., 10-day) does not yield a strong outgassing flux suggested by the SOCCOM product. The EC observations suggest a generally stronger CO_2 uptake than the resampled flux product at the monthly and regional (latitudinal and longitudinal) scales with the order: EC observations > subsampled SOCAT product > subsampled SOCAT plus SOCCOM product > subsampled SOCCOM product. The EC flux observations are on average 30% more negative (more CO_2 uptake) than the subsampled SOCAT flux product.

A new K_{660}–wind speed relationship is proposed based on the EC CO_2 flux observations from very low (0.5 m s^{-1}) to high wind speeds (18 m s^{-1}) in the summertime Southern Ocean. This K_{660} tailored for the Southern Ocean shows good agreement with the widely used K_{660} parameterisations, which means the flux difference between the EC observation and the subsampled SOCAT product is not due to the uncertainty in the parameterisation scheme of K_{660}. The 30% mean flux difference can be bridged by considering the impact of the warm bias and the cool skin effect on the shipboard fCO_{2w}-based flux estimates. Although the temperature correction helps to improve the agreement between the EC flux and the subsampled flux products, but the corrected SOCCOM flux product still significantly underestimates the ocean CO_2 uptake by ~60% in the observed Southern Ocean regions.

4.5 Materials and methods

4.5.1 Direct flux measurements by eddy covariance

The air-sea CO_2 flux F can be measured directly by the EC technique:

$$F = \rho\overline{w'c'} \tag{4.1}$$

where ρ is the mean mole density of dry air (e.g., in mole m^{-3}). The dry CO_2 mixing ratio c (in ppm or μmol mol^{-1}) is measured by a fast-response gas analyser and the vertical wind velocity w (in m s^{-1}) is often measured by a sonic anemometer. The prime denotes the fluctuations from the mean, while the overbar indicates the time average with a typical time interval of 10 minutes to 1 hour (20 minutes in this study).

Seven research cruises (Figure 4.1E and 4.1F) were conducted in the Southern Ocean on two UK ships in the summertime of 2019 and 2020. The cruises DY111 and DY113 were on the RRS *Discovery* and the remaining five cruises (JR18004, JR18005, JR19001, JR19002, and JR30001) were on the RRS *James Clark Ross*. Air-sea CO_2 fluxes were measured using the state-of-the-art closed-path EC system with a dryer to eliminate the impact of water vapour fluctuations on the CO_2 flux measurements during all of these cruises (Dong et al., 2021a). The EC data are processed and filtered to meet the stationary requirement of the EC method (see Dong et al., 2021a). EC flux measurements in regions with sea-ice coverage and coastal oceans (distance from land < 30 km) are further removed to avoid the impact of sea ice on air-sea CO_2 exchange. In total, we present 2567 hours (minimum of 40 minutes required per hour) corresponding to 175 days (at least 4 hours required per day) of quality-controlled EC air-sea CO_2 flux measurements in the Southern Ocean. Detailed descriptions of these cruises and the EC system are given in S4.

4.5.2 Ship-based and float-based product flux subsampling

Air-sea CO_2 flux can be indirectly estimated by the bulk equation:

$$F = K_{660}(Sc/660)^{-0.5}\left(\alpha_w f\mathrm{CO}_{2\mathrm{w}} - \alpha_i f\mathrm{CO}_{2\mathrm{a}}\right) \tag{4.2}$$

where K_{660} (cm h^{-1}) is the normalised gas transfer velocity at a Schmidt number (Sc) of 660 (Wanninkhof et al., 2009). α_w and α_i are the CO_2 solubility (mol L^{-1} atm^{-1}, Weiss, 1974) in the subskin and skin layers in seawater while considering the cool skin effect, respectively (Woolf et al., 2016). $f\mathrm{CO}_{2\mathrm{a}}$ is the atmospheric CO_2 fugacity (μatm). The current global air-sea CO_2 flux estimates (e.g., the three neural network-based CO_2 flux products used in this study) generally

neglect the cool skin correction by assuming that α_w is equal to α_i and use the same seawater temperature to calculate α_w and α_i (see Chapter 5 for details).

To estimate the global ocean CO_2 flux by Equation 4.2, a wind speed-dependent K_{660} and a global wind speed product, a global sea surface temperature and salinity product used for *Sc* and solubility calculations, a global distribution of fCO_{2a} and a global ocean map of fCO_{2w} are required. Mapping of fCO_{2w} is a key step of the flux estimate and requires a sophisticated interpolation method. A novel neural network technique (Landschützer et al., 2013) was successfully applied to reconstruct the map of global ocean surface CO_2 fugacity based on the observations. Three neural network-based global ocean fCO_{2w} products are produced, namely, SOCAT product, SOCCOM product, and SOCAT plus SOCCOM product by using corresponding fCO_{2w} dataset as inputs to the mapping process (Bushinsky et al., 2019; Landschützer et al., 2016). Accordingly, three flux products are yielded at a 1° × 1°, monthly resolution. Except for the difference of the fCO_{2w} product, identical K_{660}−wind speed relationship, wind speed product (ERA5, Hersbach et al., 2020), sea surface temperature (OISST v2, Reynolds et al., 2007) and salinity products, and global fCO_{2a} product are used in the generation of these three flux products (see Landschützer et al., 2016). We subsample CO_2 fluxes from the three flux products to the month and location of the hourly EC flux measurements.

4.5.3 Gas transfer velocity derived from eddy covariance fluxes

Gas transfer velocities can be derived from the EC CO_2 flux observations combing the air-sea CO_2 fugacity measurements:

$$K_{660} = \rho\overline{w'c'}/[(\alpha_w fCO_{2w} - \alpha_i fCO_{2a})(Sc/660)^{-0.5}] \quad (4.3)$$

We measured fCO_{2w} and fCO_{2a} with a showerhead equilibrator using the ship's underway system during the seven cruises in the Southern Ocean. In total, we collected 2468 hours of fCO_2 with 1580 hours containing both quality-controlled EC CO_2 flux and fCO_2 observations. To reduce the relative uncertainty in the EC air-sea CO_2 flux and enable an optimal analysis, we filter the derived K_{660} by a minimum 20 µatm threshold of the $|fCO_{2w} - fCO_{2a}|$. 784 hours of high-quality K_{660} are finally used for analysis in this study.

Chapter 5

5 Global ocean CO_2 flux estimates

> "Everyone is different. You should find your own style, what is suitable for you."
>
> (Dorothee C. E. Bakker, May 2021)

The results presented in the following chapter have been published in:

Update on the temperature corrections of global air-sea CO_2 flux estimates

Yuanxu Dong[1,2], Dorothee C. E. Bakker[1], Thomas G. Bell[2], Boyin Huang[3], Peter Landschützer[4], Peter S. Liss[1], Mingxi Yang[2]

[1]Centre for Ocean and Atmospheric Sciences, School of Environmental Sciences, University of East Anglia, Norwich, UK

[2]Plymouth Marine Laboratory, Prospect Place, Plymouth, UK

[3]National Centers for Environmental Information, National Oceanic and Atmospheric Administration, Asheville, NC, USA

[4]Max Planck Institute for Meteorology, Hamburg, Germany

Global Biogeochemical Cycles, 2022, 36, e2022GB007360. https://doi.org/10.1029/2022GB007360

The work and analysis presented in this chapter was led by Y. Dong. Co-authors on this publication collected the data, provided guidance and suggestions regarding the analysis and the results to help and address the interests of the wider scientific community.

Abstract: The oceans are a major carbon sink. Sea surface temperature (SST) is a crucial variable in the calculation of the air-sea carbon dioxide (CO_2) flux from surface observations. Any bias in the SST or any upper ocean vertical temperature gradient (e.g., the cool skin effect) potentially generates a bias in the CO_2 flux estimates. A recent study suggested a substantial increase (~50% or ~0.9 Pg C yr^{-1}) in the global ocean CO_2 uptake due to this temperature effect. Here, we use a gold standard buoy SST dataset as the reference to assess the accuracy of *in-situ* SST used for flux calculation. A physical model is then used to estimate the cool skin effect, which varies with latitude. The bias-corrected SST (assessed by buoy SST) coupled with the physics-based cool skin correction increases the average ocean CO_2 uptake by ~35% (0.6 Pg C yr^{-1}) for 1982 to 2020, which is substantially smaller than the previous correction. After these temperature considerations, we estimate an average net ocean CO_2 uptake of 2.2 ± 0.4 Pg C yr^{-1} for 1994 to 2007 based on an ensemble of surface observation-based flux estimates, in line with the independent interior ocean carbon storage estimate corrected for the river-induced natural outgassing flux (2.1 ± 0.4 Pg C yr^{-1}).

Plain Language Summary: The global oceans play a major role in taking up carbon dioxide (CO_2) released by human activity from the atmosphere. Accurate sea surface temperature (SST) measurements and quantification of any upper ocean temperature gradients (e.g., cool skin effect) are critical for ocean CO_2 uptake estimates. We determine a slight warm bias in the SST dataset used for CO_2 flux calculation by utilising a gold standard reference buoy SST dataset. We then derive a physics-based temperature correction for the ubiquitous cool skin effect on the ocean surface. The temperature-revised CO_2 flux bridges the gap between estimates from the surface observation-based air-sea CO_2 fluxes and from the independent ocean carbon inventory.

5.1 Introduction

Since the Industrial Revolution, humans have emitted large amounts of carbon dioxide (CO_2) into the atmosphere, which is the main reason for observed global warming. The oceans are a major CO_2 sink accounting for ~25% (~2.5 Pg C yr^{-1} for the last decade) of the annual anthropogenic CO_2 emissions (Friedlingstein et al., 2022) and ~40% of all anthropogenic CO_2 released since industrialization (Gruber et al., 2019; Sabine et al., 2004).

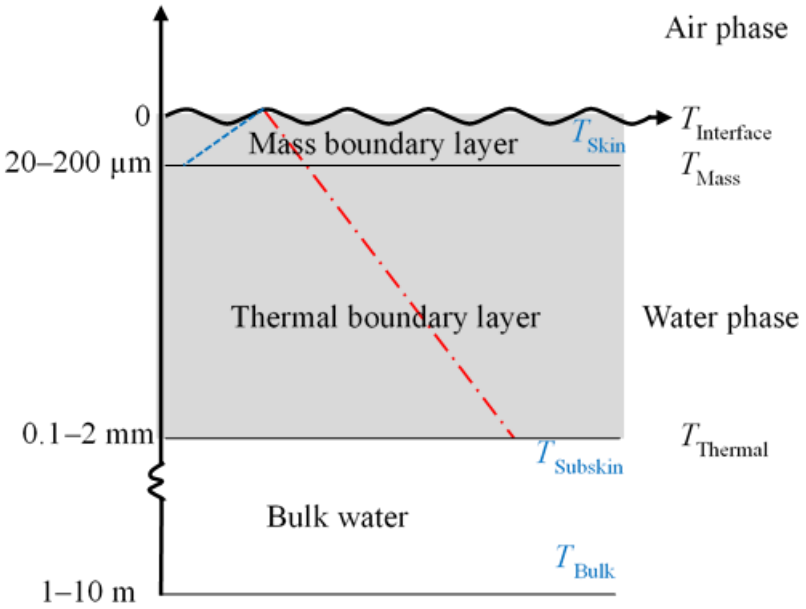

Figure 5.1 A schematic of the upper ocean (0–10 m depth) using an example where temperature is influenced by a positive (ocean heat loss) sensible heat flux and CO_2 is being taken up by the ocean. The grey shaded area represents the thermal boundary layer (TBL), and the red line represents the temperature gradient in the TBL. The mass (in this case, CO_2) boundary layer (MBL) is embedded within the TBL. The blue line corresponds to the CO_2 concentration gradient within the MBL. The TBL is characteristically ten times thicker than the MBL because heat is transferred about an order of magnitude quicker than CO_2 (Jähne, 2009). Sea surface temperature (SST) is a general term for all temperatures mentioned in the figure. $T_{Interface}$: the temperature at the air-sea interface; T_{Skin}: the skin temperature at ~10 µm depth measured by an infrared radiometer; T_{Mass}: the temperature at the base of the MBL (20–200 µm depth); $T_{Thermal}$: the temperature at the base of the TBL (0.1–2 mm depth); $T_{Subskin}$: the temperature of seawater below the TBL at a depth of ~0.1–1 m such as measured by drifting buoys; T_{Bulk}: the temperature at 1–10 m depth as measured at the typical depth of a ship's seawater intake. $T_{Interface}$, T_{Mass}, and $T_{Thermal}$ are conceptual (black text), whereas T_{Skin}, $T_{Subskin}$, and T_{Bulk} are from actual measurements (practical, blue text). Figure developed from Donlon et al. (2007).

The global air-sea CO_2 flux is often estimated by the bulk method combining *in-situ* fCO_{2w} (fugacity of CO_2 in seawater) measurements (e.g., from the Surface Ocean CO_2 Atlas, SOCAT; Bakker et al., 2016) with a wind speed-dependent gas transfer velocity (e.g., Wanninkhof, 2014; see Methods). Thanks to the SOCAT (http://www.socat.info/) community, a key dataset of fCO_{2w} has been available since 2011 (Pfeil et al., 2013; Sabine et al., 2013). The latest SOCAT version, SOCAT v2021, contains 30.6 million quality-controlled fCO_{2w} observations from 1957 to 2020 with an accuracy better than 5 µatm (Bakker et al., 2016, 2021).

Sea surface temperature (SST) is key for bulk air-sea CO_2 flux estimates. Takahashi et al. (2009) reported a 13% increase in ocean CO_2 uptake by correcting for a 0.08 K warm bias in SST. CO_2 is a water-side controlled gas (Liss & Slater, 1974), and thus air-sea CO_2 exchange is mainly limited by transfer within the ~20–200 μm mass boundary layer (MBL, Figure 5.1; Jähne, 2009). The MBL temperature should be used for the CO_2 flux calculation, but it is impractical to measure *in-situ* SST within the very thin MBL. The bulk *in-situ* seawater temperature (T_{Bulk}) measured concurrently with fCO_{2w} (typically at ~5 m depth by ship) in SOCAT is often used for the bulk air-sea CO_2 flux calculation by assuming a well-mixed upper ocean (top ~10 m) without any vertical temperature gradients. However, two temperature issues might generate bias in the CO_2 flux estimates by using the SOCAT SST. The first issue is the ship's intake depth (~5 m instead of micrometres) and the other is the location of the SST sensor (within the warm hull of the ship instead of in the unperturbed seawater).

Firstly, the SOCAT SST represents the bulk seawater temperature, which might not be equal to the temperature at the MBL because many processes can generate vertical temperature gradients in the upper ocean. There is a temperature gradient (red line in Figure 5.1) in the thermal boundary layer (TBL, grey shaded area) relating to air-sea heat exchange. Infrared radiometer measurements indicate that the skin temperature at ~10 μm depth (T_{Skin}) is on average ~0.17 K (Donlon et al., 2002) lower than the subskin temperature ($T_{Subskin}$, at ~0.1–1 m depth) because the ocean surface generally loses heat through longwave radiation, and latent and sensible heat fluxes (the so-called cool skin effect; e.g., Donlon et al., 2007, 2002; Minnett et al., 2011; Robertson & Watson, 1992; Zhang et al., 2020). Another process that might create an upper ocean temperature gradient is the diurnal warm layer effect. Water close to the surface (e.g., at 0.5 m depth) is sometimes warmer than deeper water (e.g., at 5 m depth) due to daytime solar insolation, especially under conditions of clear sky and low wind speed (Gentemann & Minnett, 2008; Prytherch et al., 2013; Ward et al., 2004). The warming leads to the stabilisation of the surface layer and thus helps maintain a layered upper ocean structure. The diurnal warm layer effect is not as ubiquitous as the cool skin effect (Fairall et al., 1996), and the warm layer is complex to characterize. In the absence of the warm layer effect, the bulk seawater temperature (T_{Bulk}) is approximately equal to $T_{Subskin}$, and $T_{Thermal}$ (the temperature at the base of the TBL) because the water below the TBL is well-mixed by turbulence.

The second issue is the potential warm bias in the SOCAT SST. The SST community has identified a warm bias in shipboard SST measurements in the ICOADS (International Comprehensive Ocean-Atmosphere Data Set; Huang et al., 2021; Kennedy et al., 2011, 2019;

Reynolds & Chelton, 2010). This might be because ship SST measurements are affected by engine room warming because the SST sensor is often located in the engine room or somewhere in the ship's interior (Kennedy et al., 2019). The SSTs in SOCAT were almost exclusively measured by shipboard systems (98%), meaning that a warm bias also likely exists in the SOCAT SST dataset. It is worth noting that the percentage of the SST data measured by research vessels in SOCAT is likely higher than in the ICOADS shipboard SST dataset. The SST measured by research ships (typically external to the ship's hull) is expected to have a higher accuracy than the SST measured by commercial ships (often in the ship's interior/ within the engine room), so the warm bias in SOCAT SST may well be different with the warm bias in ICOADS ship SST.

Satellite observation of SST represents a consistent estimate of subskin temperature and avoids the diurnal warm layer effect and any potential warm bias issue. Satellite SST thus has been proposed as an alternative to calculate the bulk air-sea CO_2 flux (Goddijn-Murphy et al., 2015; Shutler et al., 2019; Watson et al., 2020; Woolf et al., 2016). Results, based on a satellite SST dataset suggest a ~25% increase (i.e., warm bias correction; the cool skin correction results in another ~25% increase) in ocean CO_2 uptake compared to the flux estimate based on the SOCAT SST (Watson et al., 2020). However, satellite SST is not measured concurrently with the fCO_{2w}. Co-locating the 1° × 1°, monthly gridded satellite SSTs with individual fCO_{2w} in SOCAT might introduce extra uncertainties. In addition, various issues in satellite SSTs (e.g., cloud masking, the impact of aerosol, diurnal variability, uncertainty estimation, and validation) have not been fully resolved, especially at high latitudes and in coastal and highly dynamic regions (O'Carroll et al., 2019). A comparison of eight global gap-free satellite/blended SST products showed that their global mean ranged from 20.02 °C to 20.17 °C for the period 2003–2018 (Yang et al., 2021). Therefore, the current accuracy of satellite SST means that it probably does not allow an optimal estimate of the global air-sea CO_2 flux.

SST observations from drifting buoys are unaffected by engine room warming, and are expected to provide the best-quality reference temperature to assess bias in the ship SST, and satellite SST retrievals (Huang et al., 2021; Kennedy et al., 2011, 2019; Kent et al., 2017; Merchant et al., 2019; Reynolds & Chelton, 2010). This work utilises drifting buoy SST as the reference temperature to determine the accuracy of the SOCAT SST, and to correct for any bias in the SOCAT SST dataset.

Subskin temperature with a cool skin correction represents the skin temperature, which can be used to calculate air-sea CO_2 flux. Watson et al. (2020) reported a ~25% increase in ocean CO_2 uptake by considering a constant cool skin effect (-0.17 K, Donlon et al., 2002) from 1982 to 2020. In this study, the cool skin effect estimated by a physical model (Fairall et al., 1996) and by an empirical model (Donlon et al., 2002) are compared at a global scale. The updated temperature corrections are then used to estimate their impact on the global air-sea CO_2 flux. The revised global air-sea CO_2 flux based on an ensemble of CO_2 flux products (Fay et al., 2021) is then compared with the ocean carbon inventory (Gruber et al., 2019).

5.2 Methods

5.2.1 Global air-sea CO_2 flux estimates

The bulk air-sea CO_2 flux equation is:

$$F = K_{660}(Sc/660)^{-0.5}(\alpha_w f\mathrm{CO}_{2\mathrm{w}} - \alpha_i f\mathrm{CO}_{2\mathrm{a}}) \quad (5.1)$$

where F (mmol m^{-2} day^{-1}) is the air-sea CO_2 flux and K_{660} (cm h^{-1}) is the gas transfer velocity (e.g., Wanninkhof, 2014) normalised to a Sc (Schmidt number) of 660. The Sc is defined as the ratio of the kinematic viscosity of water (m^2 s^{-1}) and the molecular diffusivity of CO_2 (m^2 s^{-1}). The CO_2 solubility (mol L^{-1} atm^{-1}) at the base of the MBL and at the air-sea interface are represented by α_w and α_i, respectively (Figure 5.1). Sc and α are calculated from seawater temperature and salinity (Wanninkhof et al., 2009; Weiss, 1974). Sc is equal to 660 for CO_2 at 20 °C and 35‰ seawater. The CO_2 fugacity (µatm) at the base of the MBL and just above the air-sea interface are represented by $f\mathrm{CO}_{2\mathrm{w}}$ and $f\mathrm{CO}_{2\mathrm{a}}$, respectively.

To calculate the global air-sea CO_2 flux, $f\mathrm{CO}_{2\mathrm{w}}$ measured at the equilibrator temperature is first corrected to the *in-situ* bulk temperature (SOCAT SST). Seawater at ~5 m depth (ranging from 1–10 m depth depending on the ship or sampling platform) is sampled from the ship's underway water intake and is pumped through an equilibrator. The equilibrated CO_2 mole fraction in the air of the headspace ($\chi\mathrm{CO}_{2\mathrm{w}}$) is measured in a gas analyser. $\chi\mathrm{CO}_{2\mathrm{w}}$ is then converted to equilibrator fugacity ($f\mathrm{CO}_{2\mathrm{w\_equ}}$) (Text S5.1 in Supplement S5). $f\mathrm{CO}_{2\mathrm{w\_equ}}$ is further corrected by the chemical temperature normalisation (Takahashi et al., 1993) to obtain $f\mathrm{CO}_{2\mathrm{w}}$ in the bulk seawater:

$$f\mathrm{CO}_{2\mathrm{w}} = f\mathrm{CO}_{2\mathrm{w\_equ}}\, e^{0.0423\left(T_{\mathrm{w\_bulk}} - T_{\mathrm{equ}}\right)} \quad (5.2)$$

where T_{w_bulk} is the seawater temperature measured concurrently with fCO_{2w} at the ship's water intake at typically 5 m depth. Seawater fCO_{2w} measurements are then interpolated to obtain a global gap-free fCO_{2w} product (at 1° × 1°, monthly resolution, e.g., Landschützer et al., 2013). A global gap-free SST dataset is generally one of the independent input variables for the fCO_{2w} interpolation process. Other variables in Equation 5.1 are calculated using a global gap-free SST product and related datasets (e.g., mole fraction of atmospheric CO_2 for the calculation of fCO_{2a}). Finally, globally mapped fCO_{2w}, fCO_{2a}, Sc, α_w, α_i, and gas transfer velocity (K_{660}, estimated using a global gap-free wind speed dataset) are used for the CO_2 flux calculation via Equation 5.1.

Table 5.1 Variables and relevant sea surface temperature (SST) types for global air-sea CO_2 flux estimates and their relative importance for the flux estimate (after Woolf et al., 2016). The back-of-the-envelope calculation in the last column is for fCO_{2w} of ~380 µatm, fCO_{2a} of ~390 µatm, and ΔfCO_2 of -10 µatm, values typical for the last decade (Landschützer et al., 2020).

Variable (x)	Conceptual SST	Practical SST product	$\frac{\partial \ln(x)}{\partial T}$	$\frac{\partial \ln(flux)}{\partial T}$
$Sc^{-0.5}$	T_{Bulk}	Global gap-free $T_{Subskin}$	2.5% K^{-1}	2.5% K^{-1}
α_i	$T_{Interface}$	T_{Skin} (Global gap-free $T_{Subskin}$ with a cool skin correction)	-2.5% K^{-1}	100% K^{-1}
fCO_{2a}	$T_{Interface}$	T_{Skin} (Global gap-free $T_{Subskin}$ with a cool skin correction)	-0.2% K^{-1}	10% K^{-1}
α_w	$T_{Thermal}$	Global gap-free $T_{Subskin}$	-2.5% K^{-1}	-100% K^{-1}
Individual fCO_{2w}	$T_{Thermal}$	Individual $T_{Subskin}$ (*In-situ* T_{Bulk} with any bias correction)	4.23% K^{-1}	160% K^{-1}
Mapped fCO_{2w}	$T_{Thermal}$	Global gap-free $T_{Subskin}$	< 4.23% K^{-1}*	< 160% K^{-1}*

*The interpolation method (e.g., MPI-SOMFFN neural network technique; Landschützer et al., 2013) can largely dampen the effect of SST on mapped fCO_{2w}.

Table 5.1 summarizes the SST types that should be used to calculate variables in Equation 5.1. Sc should be calculated from the temperature utilised to derive K_{660} (e.g., T_{Bulk} for the K_{660} derived from the dual-tracer method; e.g., Ho et al., 2006; Nightingale et al., 2000). The air-sea interface temperature ($T_{Interface}$) should be used for the calculation of fCO_{2a} and α_i, while the temperature at the base of the MBL (T_{Mass}) should be employed to calculate fCO_{2w} (via

Equation 5.2) and α_w. However, Woolf et al. (2016) suggested that T_{Thermal} might be a better temperature for calculating fCO_{2w} and α_w. The seawater carbonate system creates a unique situation for air-sea CO_2 exchange, which does not exist for other gases. Seawater temperature changes cause chemical repartitioning of the carbonate species (CO_2, carbonic acid, bicarbonate, and carbonate; Zeebe & Wolf-Gladrow, 2001). We find that the timescale of this repartitioning equilibration (e-folding time > 10 s for typical seawater; Johnson, 1982; Zeebe & Wolf-Gladrow, 2001) is much longer than the timescale (~1 s) of water mixing below the MBL but within the TBL, where viscous dissipation dominates the water mixing (Jähne, 2009; Jähne et al., 1987; Woolf et al., 2016). The explanation of the timescales is detailed in Text S5.2 in Supplement S5. Although there is a temperature gradient in the TBL due to the cool skin effect, the carbonate species are not expected to have time to thermally adjust, which suggests that T_{Thermal} is the optimal temperature for calculating fCO_{2w} and α_w.

T_{Thermal}, T_{Mass}, and $T_{\text{Interface}}$ are conceptual temperatures, which can be approximated by practical temperatures (Figure 5.1). Satellite SST, which represents the subskin temperature, is a good approximation for T_{Thermal} (Shutler et al., 2019; Watson et al., 2020; Woolf et al., 2016). A satellite T_{Subskin} product can be used to calculate α_w and Sc, and to map fCO_{2w} for the global ocean. T_{Subskin} with a cool skin correction can then be utilised to calculate global fCO_{2a}, and α_i. *In-situ* T_{Subskin} should ideally be used to correct fCO_{2w} from the equilibrator temperature to the subskin seawater temperature. However, the *in-situ* temperature measured concurrently with the fCO_{2w} in SOCAT is T_{Bulk}, and *in-situ* T_{Subskin} measurements are unavailable to exactly match the SOCAT space and time-stamp. Using *in-situ* T_{Bulk} (i.e., SOCAT SST) to correct fCO_{2w} is reasonable in the absence of a warm layer effect, but it is important to account for the potential warm bias in the SOCAT SST.

Table 5.1 also summarizes the influence of SST and the corresponding importance for the variables used to make air-sea CO_2 flux estimates (after Woolf et al., 2016). The Sc and fCO_{2a} variations due to the bias in the SST product have a small influence on the global air-sea CO_2 flux. However, any bias in the SST data used for the calculation of α_w, α_i, and especially fCO_{2w} can result in a considerable bias in the flux. The temperature influence on the fCO_{2w} mapping should be significantly dampened by the interpolation process. The most significant influence on the CO_2 flux due to temperature bias comes from individual fCO_{2w} (~160% K^{-1}, Table 5.1). An average bias of 0.1 K could result in a bias in fCO_{2w} of ~1.6 µatm, which corresponds to ~16% of the net air-sea CO_2 flux for the last decade (Landschützer et al., 2020).

The skin temperature should be used for the calculation of α_i and fCO_{2a}. The T_{Skin} can be obtained from $T_{Subskin}$ with a cool skin correction. If $T_{Subskin}$ is used rather than T_{Skin} for the calculation of α_i, and fCO_{2a}, the ocean CO_2 uptake is in theory underestimated by ~19% for the last decade with a mean cool skin effect of -0.17 K (Donlon et al., 2002).

5.2.2 Bias assessment

The *in-situ* bulk SST in SOCAT is generally used to correct individual fCO_{2w} observations from the equilibrator temperature to the seawater temperature (e.g., studies in Table S5.1 in Supplement S5). However, a warm bias might exist in the SOCAT SST due to heating in the engine room. Watson et al. (2020) co-located the DOISST v2.0 (NOAA Daily Optimum Interpolation SST dataset; Reynolds et al., 2007; representing the subskin temperature) with individual *in-situ* SST measurements in SOCAT. They found that the SOCAT SST is on average 0.13 ± 0.78 K higher than the co-located DOISST v2.0. However, Huang et al. (2021) pointed out that there might be a cold bias in the DOISST v2.0 and DOISST v2.1 products (the difference between DOISST v2.0 and v2.1 can be seen in Text S5.4 in Supplement S5).

This study uses accurate SST observed by drifting buoys to assess the potential cold bias in the DOISST v2.1 and the warm bias in SOCAT SST. A drifting buoy SST (measured at nominally 10–20 cm depth; representing the subskin temperature) dataset from iQuam (*in situ* SST Quality Monitor v2.10; Xu & Ignatov, 2014) with high accuracy (quality level = 5) is used for the assessment. The buoy SST is first gridded (1° × 1°, monthly) and then compared with the resampled DOISST v2.1 (1/4° × 1/4°, daily data are resampled to 1° × 1°, monthly resolution) and the gridded SST (1° × 1°, monthly) in SOCAT v2021.

5.2.3 Cool skin effect estimate

The cool skin effect is ubiquitous in the ocean (Donlon et al., 2002) and should be considered when estimating air-sea CO_2 fluxes. Watson et al. (2020) used a constant value (-0.17 K) to account for the impact of the cool skin effect on air-sea CO_2 fluxes. However, the cool skin effect is affected by many environmental processes. Donlon et al. (2002) proposed a wind speed-dependent cool skin effect based on skin and bulk temperature measurements (Donlon02, hereafter). A physical model for the cool skin effect proposed by Saunders (1967) and developed by Fairall et al. (1996) considers wind speed, longwave radiation, heat flux, and solar radiation (Fairall96, hereafter). Fairall96 has been included in the COARE 3.5 model (Edson et al., 2013) and recent studies (Alappattu et al., 2017; Embury et al., 2012; Zhang et

al., 2020) suggest that Fairall96 better accounts for the cool skin effect than the parameterisation dependent upon a single variable (wind speed).

We employ the ERA5 wind speed data (Hersbach et al., 2020) to estimate the Donlon02 cool skin effect. The COARE 3.5 model is used to estimate the Fairall96 cool skin effect. The following model inputs are used: CCI SST v2.1 (European Space Agency Climate Change Initiative SST product; Merchant et al., 2019; Merchant & Embury, 2020), NCEP sea level pressure (Kalnay et al., 1996), ERA5 monthly averaged reanalysis datasets (Hersbach et al., 2020) for wind speed, 2 m above mean sea level (AMSL) air temperature, relative humidity (calculated from 2 m AMSL air temperature and dewpoint temperature using the August-Roche-Magnus approximation), downward shortwave radiation, downward longwave radiation, and boundary layer height.

5.2.4 Global air-sea CO_2 flux estimates with the temperature correction

We use two different methods to account for the bias in the SOCAT SST for the global air-sea CO_2 flux estimates. For the first method, we use the buoy SST as the reference temperature to assess the bias in SOCAT SST (bias_buoy, hereafter). We correct the 1° × 1°, monthly fCO_{2w} in SOCAT v2021 via Equation 5.2 (i.e., $fCO_{2w\_corrected} = fCO_{2w}\ e^{-0.0423 * \Delta SST}$) by the temperature difference (ΔSST) between SOCAT SST and buoy SST. The ΔSST varies with latitude (with a 10° latitude running mean, see the orange line in Figure 5.2b) but we do not consider the variation of ΔSST over time. The number of matched data points between SOCAT SST and buoy SST is small in most years, so ΔSST is averaged over 1982 to 2020. In addition, only fCO_{2w} data within 70°S to 70°N are corrected because of the small number of measurements in the polar oceans. For the second method, the co-located DOISST v2.1 replaces SOCAT SST in Equation 5.2 to reanalyse fCO_{2w} (bias_OI, hereafter; Watson et al., 2020). The reanalysed fCO_{2w} is used for the flux calculation (see Goddijn-Murphy et al., 2015 and Holding et al., 2019 for the reanalysis process).

We employ the MPI-SOMFFN neural network technique (Landschützer et al., 2013) to interpolate the $fCO_{2w\_corrected}$ and the reanalysed fCO_{2w} to the global ocean from 1982 through 2020, using a set of input variables. We use the same datasets as Landschützer et al. (2014) for the neural network inputs, except for the SST product. The CCI SST (Merchant et al., 2019) represents the subskin temperature and is independent of *in-situ* SST measurements, so we utilise the 1° × 1°, monthly CCI SST v2.1 for the neural network training process. The CCI

SST v2.1 is also used to calculate *Sc* and α_w, while the CCI SST v2.1 with a cool skin correction is employed to calculate α_i and fCO_{2a}.

We use two models (Fairall96 and Donlon02) to estimate the cool skin effect. Both Fairall96 and Donlon02 cool skin effect estimates are applied to the CCI SST v2.1 to calculate α_i and fCO_{2a}, respectively. The quadratic wind speed-dependent formulation ($K_{660} = a\ U_{10}^2$; Ho et al., 2006; Wanninkhof, 2014) is used to calculate gas transfer velocity. The 1° × 1°, monthly ERA5 wind speed data from 1982 to 2020 is utilised to scale the transfer coefficient *a* to match to a global mean K_{660} of 18.2 cm h^{-1} (equal to 16.5 cm h^{-1} for *K*) from the ^{14}C inventory method (Naegler, 2009). It is worth noting that the cool skin effect and the warm layer effect do not impact the global mean K_{660} calculated from the ^{14}C inventory because the air-sea ^{14}C concentration difference ($\Delta^{14}C$) is very large (Naegler, 2009; Sweeney et al., 2007), and the upper ocean temperature gradients only result in a minor change in $\Delta^{14}C$. In the end, we substitute all variables above into Equation 5.1 to calculate the global air-sea CO_2 flux. This study typically adopts 1 standard deviation (i.e., 1 sigma) as a representation of uncertainty unless specified otherwise.

5.3 Results

5.3.1 Warm bias in the *in-situ* SOCAT SST

The temperature assessment using the buoy SST suggests a cold bias in the DOISST v2.1 (0.09 K on average, standard error 4.7×10^{-4} K) and a small warm bias (0.02 K on average, standard error 4.1×10^{-3} K) in the SOCAT SST, which indicates that while a warm bias exists in the SOCAT SST, using the co-located DOISST would overestimate this bias in SOCAT SST (Figure 5.2a).

Figure 5.2b shows the latitudinal variation of the bias in SOCAT SST. The number of grid cells with both SOCAT and buoy data (green bars in Figure 5.2b) is small and the standard error for the temperature difference (grey shading) is large in the high-latitude oceans. Therefore, we only consider data between 70°S and 70°N. The SOCAT SST minus buoy SST (ΔSST, orange line in Figure 5.2b) shows apparent variation with latitude. ΔSST is on average positive, but is slightly negative at 35°N and 30°S. In the northern hemisphere, ΔSST is +0.04 K near the equator and increases by +0.1 K to a maximum at 25°N and then decreases to -0.05 K at 35°N. ΔSST also increases from 35°N to a maximum of +0.15 K at 50°N and then decreases further

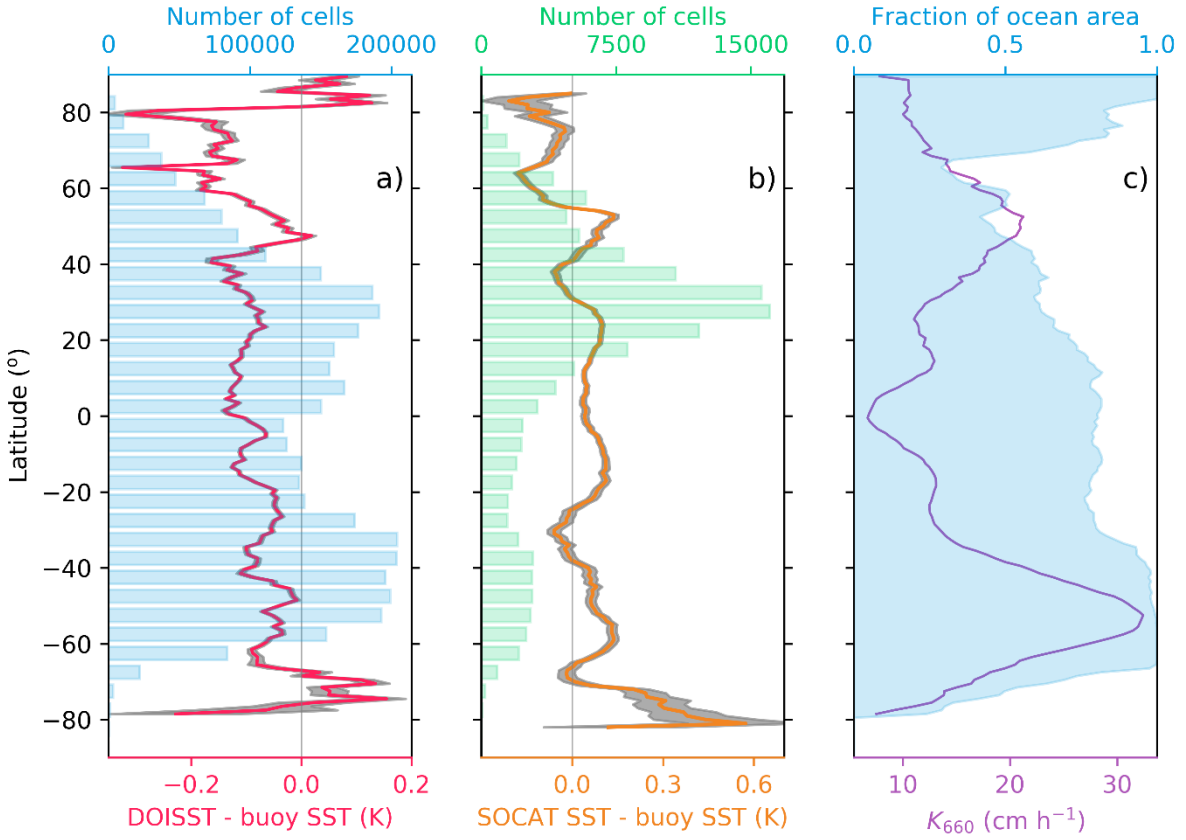

Figure 5.2 Latitudinal variation in SST differences, number of matched grid cells, the gas transfer velocity (K_{660}) and the fraction of the globe's surface area covered by ocean: (a) 1° latitude average temperature difference between DOISST v2.1 and buoy SST (red line) ± 1 standard error (grey shading). The input data are from 1982 to 2020 and have a 1° × 1°, monthly resolution. Blue bars show the number of cells (5° latitude bin) containing both DOISST and buoy SST data; (b) 10° latitude running mean of the temperature difference between SOCAT SST (from SOCATv2021) and buoy SST (orange line, i.e., ΔSST in the main text) ± 1 standard error (grey shading). Green bars correspond to the number of cells (5° latitude bin) containing both gridded SOCAT and buoy SST; (c) 1° latitude average K_{660} (purple line) calculated with a wind speed-dependent parameterization (Ho et al., 2006) using the ERA5 wind speed data (Hersbach et al., 2020) for the global ocean. The blue shaded area corresponds to the fraction of ocean area in different latitudes (1° latitude average).

north. The ΔSST pattern in the southern hemisphere roughly mirrors that in the northern hemisphere with a 5° northward shift.

It is worth noting that under-sampling affects these bias assessments for SOCAT SST. If we consider all paired cells with both buoy and SOCAT SST measurements, the warm bias is on average +0.02 K. If we only consider cells with at least ten buoy SST and ten SOCAT SST

measurements, the warm bias is on average +0.03 K (Figure S5.2a in Supplement S5). The latitudinal variation of the bias is very similar no matter considering how many measurements are within a cell (Figure S5.2b in Supplement S5).

It is important to consider latitudinal variation when correcting for bias in SOCAT SST. For instance, SOCAT SST has a relatively large warm bias (thus a large bias in the fCO_{2w}) in the Southern Ocean (south of 35°S, Figure 5.2b), which coupled with a high K_{660} and a large surface ocean area (Figure 5.2c) results in a substantial bias in Southern Ocean CO_2 flux estimates. This study uses a latitude-varying temperature bias (i.e., the orange line in Figure 5.2b) to correct the air-sea CO_2 flux between 70°S and 70°N (see Section 5.2.4).

5.3.2 The cool skin effect

Figure 5.3 shows the cool skin effect estimated by Donlon02 and Fairall96. The Fairall96 estimate of the cool skin effect is stronger than the Donlon02 estimate for low wind speeds (U_{10} < 9 m s^{-1}) but weaker for high wind speeds (9 m s^{-1} < U_{10} < 16 m s^{-1}) (Figure 5.3a). The monthly wind speed distribution (green bars in Figure 5.3a) shows that wind speeds less than 9 m s^{-1} account for 80% of the wind conditions. Therefore, the cool skin effect estimated by Fairall96 is typically stronger than that estimated by Donlon02. The standard deviation of the Fairall96 cool skin effect is much higher at low wind speeds than at high wind speeds, which reflects that the drivers (longwave radiation, heat flux, and solar radiation) can produce substantial variations in the cool skin effect under relatively calm conditions.

The Donlon02 cool skin effect only has a slight latitudinal variation that is not substantially different from a constant (-0.17 K) value (Figure 5.3b), which was used by a previous study for air-sea CO_2 flux correction (Watson et al., 2020). In contrast, the Fairall96 cool skin estimate shows a clear latitudinal variation with two relatively small cool skin effect regions at around 50°S and 50°N where wind speeds are high. The Fairall96 cool skin effect is stable in the tropical zone and decreases toward both poles to ~50° and then increases at even higher latitudes.

In most ocean regions, the Fairall96 cool skin effect follows variations in wind speed. Intriguingly, the Fairall96 cool skin effect is nearly constant within the tropical and subtropical zones, even though the wind speed is much lower near the equator than in the subtropics.

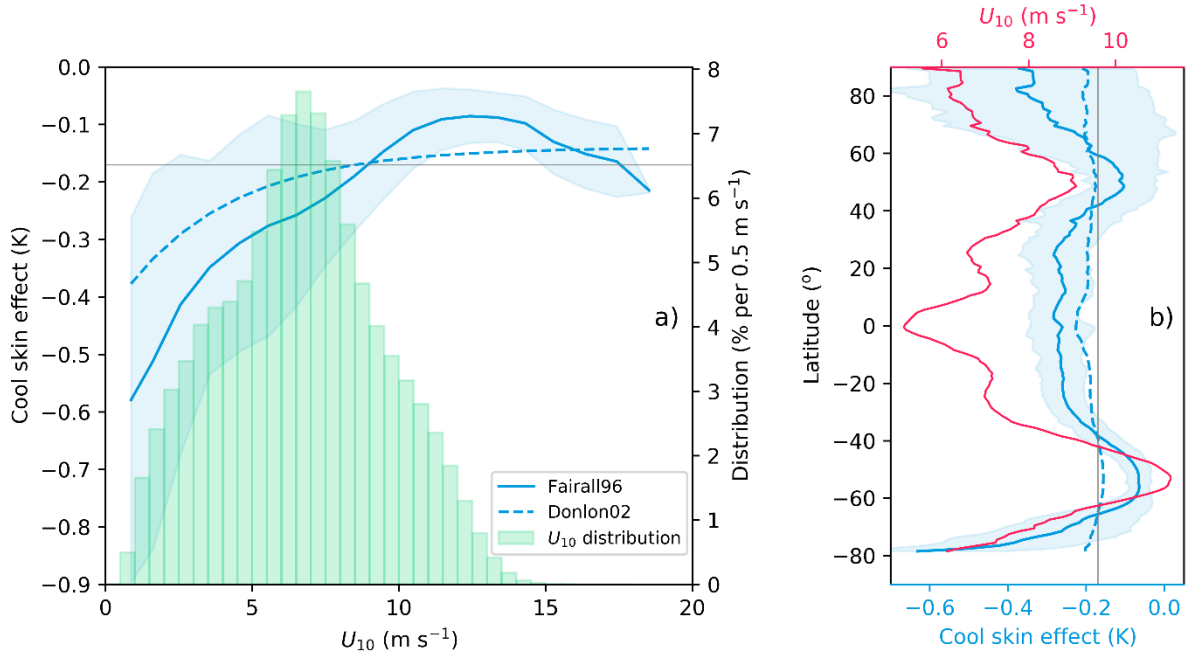

Figure 5.3 (a) Relationship between the cool skin effect and the 10 m wind speed (U_{10}). Green bars represent the frequency distribution of the ERA5 monthly averaged reanalysis wind speeds (1° × 1°) over the global ocean for 1982–2020. (b) Latitudinal variation in U_{10} (red line) and the cool skin effect (1° latitude bins). Both subplots show the average cool skin effect estimated by the Fairall96 physical model (Fairall et al., 1996, solid blue line), the Donlon02 wind speed-dependent empirical model (Donlon et al., 2002, dashed blue line) and a constant value (-0.17 K, grey line; Donlon et al., 2002). The light blue shaded area in both subplots indicates one standard deviation of the bin averages in Fairall96 cool skin estimates. Global ocean 1° × 1°, monthly datasets are used to estimate the cool skin effect (see Section 5.2.3).

Drivers other than wind speed (i.e., latent and sensible heat fluxes, and longwave radiation) might counteract the low wind speed effect in this area.

5.4 Discussion

5.4.1 Variation in the CO_2 flux correction

In this section, we discuss the impact of the warm bias and cool skin effects on global air-sea CO_2 flux estimates. The corrections are applied over time (between 1982 and 2020, Figure 5.4a, b) and by latitude (Figure 5.4c, d).

The bias correction using the buoy SST assessment (bias_buoy) leads to an average increase in ocean CO_2 uptake of 0.19 Pg C yr^{-1}, while the bias correction utilising the co-located DOISST (bias_OI) suggests an average increase of 0.43 Pg C yr^{-1} (Figure 5.4a). Adopting the

cool skin correction from Fairall96 and Donlon02 increases the 1982–2020 average ocean CO_2 uptake by 0.39 Pg C yr^{-1} and 0.43 Pg C yr^{-1}, respectively (Figure 5.4b). A constant cool skin correction of -0.17 K increases the flux by an amount similar to using the Donlon02 correction. Zhang et al. (2020) show that the mean difference between the Fairall96 cool skin effect and the observed cool skin effect (7239 observations) is 0.04 K. If we take this value as the uncertainty of the Fairall96 cool skin estimate, the corresponding relative uncertainty in the Fairall96 flux correction is ~20% (i.e., 0.08 Pg C yr^{-1}). In total, the flux correction using the bias_buoy and Fairall96 is on average ~0.3 Pg C yr^{-1} lower than if the bias_OI and Donlon02 are used for 1982 to 2020. The inter-annual variation in the net air-sea CO_2 flux with different temperature corrections is shown in Figure S5.4 in Supplement S5.

Figure 5.4a and 5.4c show the change in the air-sea CO_2 flux (ΔFlux) generated by correcting for the warm bias in SOCAT SST. The temporal and the latitudinal variation of the two flux corrections (bias_buoy and bias_OI) follow similar patterns, but the magnitude is different. Using bias_OI creates a ΔFlux that is twofold larger (in absolute terms) than that using bias_buoy. The data in Figure 5.2a suggest that using bias_OI may overestimate the bias in SOCAT SST, which would result in a ~0.25 Pg C yr^{-1} overestimation of the air-sea CO_2 flux correction. Therefore, we favour the bias_buoy correction over the bias_OI correction.

While we use the same latitude-varying temperature difference (i.e., bias_buoy) to correct the bias in SOCAT SST for every year, the flux correction shows a clear inter-annual variation (green line in Figure 5.4a). A possible reason is that the number of measurements in each year of SOCAT is different (Figure S5.3 in Supplement S5), and their spatial distribution differs between years. The latitude-dependent bias correction, when applied to the different year-to-year spatial distribution in the SOCAT data, results in a time-varying annual mean bias correction (Figure S5.3 in Supplement S5).

Figures 5.4b and 5.4d show the change in air-sea CO_2 flux when accounting for the cool skin effect using the Fairall96 and Donlon02 models. Figure 5.4b indicates an increase over time in both flux corrections (absolute value), which is driven by the increase in fCO_{2a} (see Equation 5.1 and Table 5.1). The impact of the cool skin effect on the air-sea CO_2 flux is through $\alpha_i * fCO_{2a}$. The ever-rising atmospheric CO_2 concentration and thus fCO_{2a}, result in the growing cool skin flux correction.

The flux correction using Donlon02 exceeds that of by Fairall96 by ~0.05 Pg C yr^{-1} (in absolute terms). The largest difference in flux between the two cool skin corrections occurs in the

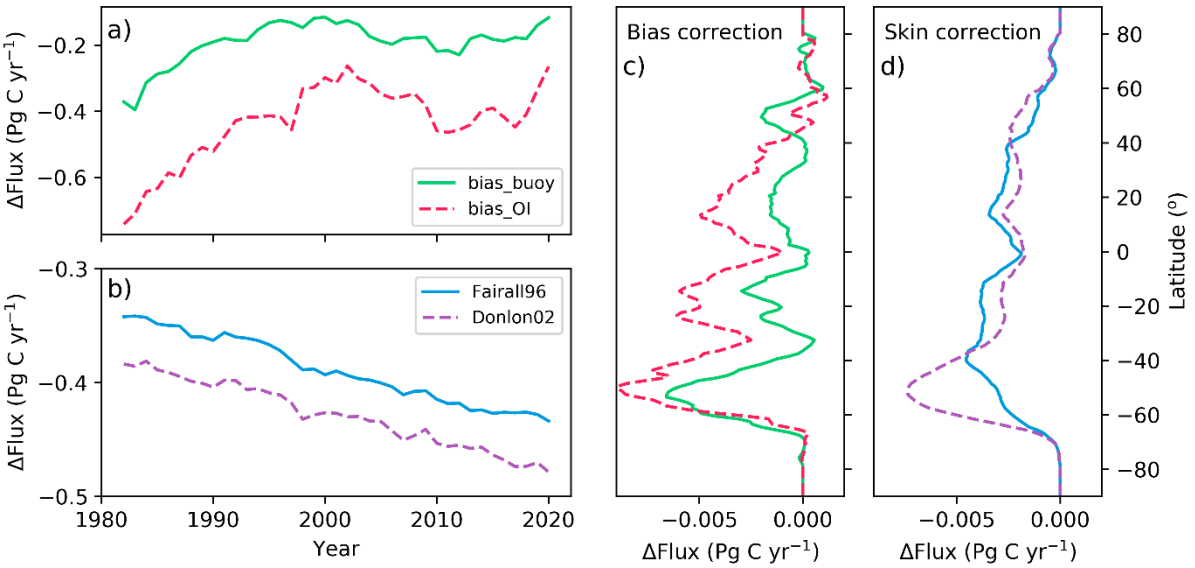

Figure 5.4 SST corrections to the air-sea CO_2 flux (ΔFlux) versus time (a, b) and versus latitude (c, d). SST corrections account for the bias in the SOCAT SST (a, c) and the cool skin effect (b, d). Negative ΔFlux values represent increased ocean CO_2 uptake. Green and red lines represent ΔFlux due to the bias correction assessed by drifting buoy SST (bias_buoy) and by co-located DOISST (bias_OI), respectively. Blue and purple lines represent ΔFlux due to the Fairall96 and the Donlon02 cool skin corrections, respectively. ΔFlux in a) and b) is the global annual mean, while ΔFlux in (c) and (d) is the long-term average (1982–2020) in 1° latitude bins. Results are based on the MPI-SOMFFN fCO_{2w} mapping method (Landschützer et al., 2013) (See Section 5.2). The inter-annual variation of the global air-sea CO_2 flux with different temperature corrections can be seen in Figure S5.4 (Supplement S5). Our preferred corrections are bias_buoy for warm bias in SOCAT SST and Fairall96 for the cool skin effect (see Section 5.4.1).

Southern Ocean (Figure 5.4d). The Donlon02 cool skin effect has minimal latitudinal variation, so the flux correction is largest at ~50°S where the gas transfer velocity is maximum and the ocean area is relatively large (Figure 5.2c). The Fairall96 cool skin effect has an apparent latitudinal variation and a minimum (absolute) value at ~50°S (Figure 5.3). This minimum cool skin effect offsets the maximum wind speed and large ocean area, resulting in a smaller flux correction (in absolute terms) at ~50°S for Fairall96 than for Donlon02. Recent work (Alappattu et al., 2017; Embury et al., 2012; Zhang et al., 2020) has suggested that the Fairall96 cool skin model is better than Donlon02 at capturing the cool skin effect at a global scale and this, coupled with our estimates indicates that using the Donlon02 model may lead to an over-correction of the air-sea CO_2 flux, especially in the Southern Ocean.

5.4.2 Implications for air-sea CO_2 flux estimates

This study deals with the potential bias in the fCO_{2w}-based air-sea CO_2 flux estimates due to upper ocean temperature effects. A large amount of uncertainty in this fCO_{2w}-based flux also comes from the gas transfer velocity (Woolf et al., 2019). The air-sea CO_2 flux estimated from the ocean carbon inventory (Gruber et al., 2019) does not require the gas transfer velocity, is unaffected by upper ocean temperature effects and provides an independent estimate of ocean CO_2 uptake. To compare the fCO_{2w}-based net air-sea CO_2 flux with the anthropogenic air-sea CO_2 flux of the ocean carbon inventory, we need to adjust for river-induced CO_2 outgassing. The riverine carbon flux has been estimated as 0.23 Pg C yr^{-1} (Lacroix et al., 2020), 0.45 Pg C yr^{-1} (Jacobson et al., 2007), 0.65 Pg C yr^{-1} (Regnier et al., 2022) and 0.78 Pg C yr^{-1} (Resplandy et al., 2018). Here we adopt the mean of these values (0.53 ± 0.21 Pg C yr^{-1}).

The net air-sea CO_2 flux derived from the ocean carbon inventory for 1994 to 2007 is -2.1 ± 0.4 Pg C yr^{-1} (i.e., -2.6 Pg C yr^{-1} anthropogenic flux plus 0.53 Pg C yr^{-1} river carbon flux; see the footnote of Table 5.2 for the propagated uncertainty) (Gruber et al., 2019), which is shown in Table 5.2 along with the ensemble mean of eighteen fCO_{2w}-based fluxes (Fay et al., 2021). Fluxes from six fCO_{2w} products and three wind speed products (three wind products are used for each fCO_{2w} product) are utilised to generate the ensemble mean flux, where missing fCO_{2w} has been filled with a scaled climatology and gas transfer velocity (K_{660}) has been calibrated to a global average of 18.2 cm hr^{-1} over the ice-free ocean based on ^{14}C-bomb flux estimates (Fay et al., 2021). All six fCO_{2w} products (which include the MPI SOMFFN method) have been developed from the SOCAT v2021 dataset. So the corrections of the ensemble mean flux for the temperature effects should be similar to the corrections in this study based on the MPI-SOMFFN fCO_{2w} mapping method (Landschützer et al., 2013). Furthermore, an ensemble of different data interpolation methods and different wind products provides a more robust flux estimate than a single interpolation method based on a single wind product. The flux corrections estimated in this study are applied to the ensemble mean flux.

The ensemble mean air-sea CO_2 flux without any bias and cool skin corrections (-1.7 ± 0.4 Pg C yr^{-1}) is 0.4 Pg C yr^{-1} lower than the net flux estimate from the ocean carbon inventory. The ensemble mean CO_2 flux with bias_buoy and Fairall96 cool skin corrections is -2.2 ± 0.4 Pg C yr^{-1}, similar to the ocean carbon inventory derived net ocean CO_2 uptake. The corrections using the bias_OI and the Donlon02 suggested by a previous study (Watson et al., 2020) push the ensemble mean air-sea CO_2 flux (-2.4 ± 0.4 Pg C yr^{-1}) towards the lower limit of the ocean

carbon inventory flux estimate (Table 5.2). However, these comparisons depend on the choice of the riverine carbon flux correction. The riverine flux is still an unresolved issue and the flux estimates span from 0.23 Pg C yr^{-1} to 0.78 Pg C yr^{-1} (Jacobson et al., 2007; Lacroix et al., 2020; Regnier et al., 2022; Resplandy et al., 2018). Without knowing which of the riverine flux estimates is most accurate, an average is simply taken here. Therefore, an accurate estimate of the river flux is required to increase our confidence for the comparison above.

Table 5.2 Global mean net air-sea CO_2 fluxes for 1994 to 2007 (numbers in the text are generally the mean for 1982 to 2020 unless specified otherwise). Here bias_buoy and bias_OI represent the bias correction (to SOCAT SST) using the assessment from buoy SST and co-located DOISST, respectively. Fairall96 (Fairall et al., 1996) and Donlon02 (Donlon et al., 2002) correspond to the cool skin effect estimated by the physical and empirical models, respectively. We favour the bias_buoy and Fairall96 corrections (see Section 5.4.1).

Net air-sea CO_2 flux estimates (Pg C yr^{-1})	**Flux without a temperature correction**	**Flux with warm bias correction**		**Flux with warm bias and cool skin correction**	
		bias_buoy	bias_OI	bias_buoy + Fairall96	bias_OI + Donlon02
Ensemble mean of fCO_{2w}-based fluxes*	-1.7 ± 0.4	-1.8 ± 0.4	-2.0 ± 0.4	-2.2 ± 0.4	-2.4 ± 0.4
Ocean carbon inventory**	-2.1 ± 0.4				

*The ensemble mean of the fluxes from six fCO_2 products and three wind speed products (Fay et al., 2021).

**From Gruber et al. (2019) (-2.6 ± 0.3 Pg C yr^{-1}) with a riverine-derived carbon flux adjustment (0.53 ± 0.21 Pg C yr^{-1}). The uncertainty (i.e., ± 0.4 Pg C yr^{-1}) is calculated as $\sqrt{0.30^2 + 0.21^2}$ Pg C yr^{-1}.

Another question is whether the warm bias and cool skin flux corrections conflict with our understanding of air-sea CO_2 fluxes. One might argue that the preindustrial ocean and atmosphere would have been in a natural equilibrium (i.e., the global total of a steady state of natural air-sea CO_2 fluxes would have been zero; see Hauck et al., 2020 for details), but the temperature corrections would create a preindustrial ocean carbon sink. However, the warm bias in SOCAT SST is not a natural phenomenon and should not affect the preindustrial flux estimate. Furthermore, while cool skin is a natural phenomenon, the flux correction due to the cool skin effect includes both natural and anthropogenic contributions. Figure 5.4b shows that

the cool skin flux correction decreased almost linearly by ~0.1 Pg C yr^{-1} (from -0.34 to -0.43 Pg C yr^{-1}) due to the increase in atmospheric CO_2 (~70 ppm or μmol mol^{-1}, from 341 to 414 ppm) from 1982 to 2020 (Dlugokencky & Tans, 2018). Preindustrial atmospheric CO_2 was ~260–280 ppm (Wigley, 1983), which is ~70 ppm lower than atmospheric CO_2 in 1982. Thus, the preindustrial natural air-sea CO_2 flux correction due to the cool skin effect could be ~-0.25 Pg C yr^{-1}, with the remaining correction (~-0.2 Pg C yr^{-1} in 2020) due to the increase in atmospheric CO_2 by anthropogenic emissions.

A flux correction for the cool skin effect is only related to the fCO_{2w} observation-based flux estimate, which is available from the 1980s onwards (Friedlingstein et al., 2022). There were no fCO_{2w} measurements in preindustrial times, so the total preindustrial air-sea CO_2 flux (the sum of steady-state natural flux and river flux) is based on model studies, theory, and lateral transport constraints (Hauck et al., 2020). Although the cool skin effect might result in an ~-0.25 Pg C yr^{-1} flux, we can still assume that ocean and atmosphere were in a natural equilibrium in preindustrial times. Specifically, the cool skin effect has been implicitly included in the preindustrial natural equilibrium assumption. Therefore, this study improves our understanding by suggesting an increasing anthropogenic contribution to the air-sea CO_2 flux, while there is no contradiction between the temperature correction and the preindustrial natural equilibrium assumption.

The cool skin effect and its impact on the air-sea CO_2 flux have been discussed for decades. While the cool skin effect itself has been well observed and modelled, its impact on the air-sea CO_2 flux is mainly based on theoretical arguments. We still lack strong observational evidence to confirm the need to include the cool skin effect on estimates of air-sea CO_2 flux – an important topic we urge the community to demonstrate experimentally. The eddy covariance method (e.g., Dong et al., 2021a) provides direct flux measurements, that could be used as a reference CO_2 flux to assess the accuracy of the bulk CO_2 flux. Long-term eddy covariance measurements at a place with $|\Delta fCO_2|$ ~0 would be insightful because the relative effect of cool skin on the bulk CO_2 flux is in theory more prominent for regions of low $|\Delta fCO_2|$. Appropriate laboratory experiments may yield further insight.

In summary, this work updates the temperature corrections to fCO_{2w}-based air-sea CO_2 flux estimates. It shows that there is a slight warm bias in SOCAT SST and a latitude-varying cool skin effect, resulting in ~0.6 Pg C yr^{-1} additional ocean CO_2 uptake from 1982 to 2020. The corrected air-sea CO_2 flux for an ensemble of six gap-filled air-sea CO_2 flux products agrees

well with the ocean carbon inventory-derived net flux. The extreme sensitivity of the air-sea CO_2 flux to the accuracy of SST means that we should carefully choose the reference temperature to assess any bias in the SOCAT SST. The importance of the Southern Ocean for atmospheric CO_2 uptake, and the strong winds encountered there mean that large-scale assessments need a suitable model for the cool skin correction to the air-sea CO_2 flux.

Chapter 6

6 Conclusions and future research

> "Don't think too much about the results, just do it. No matter whether you can make it, you will learn something and benefit from the process."
>
> (Thomas G. Bell, April 2022)

Abstract: This concluding chapter draws together the findings of the preceding chapters, provides a general discussion of the topic I focus on, and identifies the areas that I and the scientific community should make efforts to address in the future.

6.1 General discussions and conclusions

The global ocean is a major CO_2 sink and thus plays a critical role in climate change. However, the global and regional air-sea CO_2 flux estimates include large uncertainties. The main objective of this PhD thesis is to improve the air-sea CO_2 flux estimates in different ways.

First, the uncertainty in the gas transfer velocity (K_{660}) dominates the uncertainty in surface observation-based global air-sea CO_2 flux estimates (Woolf et al., 2019), indicating a lack of mechanistic understanding of air-sea gas exchange. The air-sea gas exchange community has employed the eddy covariance (EC) technique and has made significant progress in the parametrisation of K_{660} (e.g., Yang et al., 2022) in the last decade. However, the uncertainties in the ship-based EC air-sea CO_2 flux measurements are not well quantified. I employed the EC CO_2 flux measurements from four cruises to thoroughly analyse the flux uncertainties and made conclusions:

- The inherent random uncertainty accounts for the majority of the uncertainty in the hourly EC air-sea CO_2 flux, while the bias (systematic error) is small. The low flux bias indicates that the EC flux measurements are well-suited as a reference to validate the indirect flux estimates and the EC technique is powerful in the study of K_{660}.

- The mean relative uncertainty in hourly EC air-sea CO_2 flux is estimated to be ~20% in high flux regions and ~50% in low flux areas. The total random uncertainty of two state-of-the-art gas analysers (Picarro G2311-f and LI-7200) is similar and both are suitable for air-sea CO_2 flux measurements.

- The random uncertainty in the EC CO_2 flux contributes directly to scatter in the EC-derived K_{660}. Applying an appropriate averaging timescale (1–3 hours) substantially reduces the random uncertainty in both EC CO_2 flux and the EC-derived K_{660}. A minimum $|\Delta fCO_2|$ threshold of 20 µatm enables an optimal analysis of hourly K_{660} derived from EC air-sea CO_2 flux measurements because the relative flux uncertainty is low for high flux signal observations. See Chapter 2 and also Dong et al. (2021a).

Second, the polar oceans may be responsible for ~50% of the global ocean uptake of anthropogenic CO_2 although these regions only cover ~25% of the world's ocean's surface (Gruber et al., 2019; Yasunaka et al., 2018). In addition, the polar oceans are a major driver of the variation in the global ocean CO_2 sink and are sensitive to climate change (Gruber et al., 2019; Turner & Marshall, 2011). Thus, the accurate quantification of the CO_2 flux in polar oceans is important. However, uncertainties in CO_2 flux estimates of both the Arctic Ocean and the Southern Ocean are larger compared to those for other ocean basins (Bates & Mathis, 2009; Gloege et al., 2021). Shallow stratification generated by the seasonal sea ice melt in the Arctic Ocean is a major challenge for bulk air-sea CO_2 flux estimates in this area. The seawater CO_2 fugacity (fCO_{2w}) measurements made at ~5 m depth probably do not represent fCO_{2w} in the microlayer where the air-sea gas exchange occurs (Liss & Slater, 1974; Miller et al., 2019). Therefore, the summertime sea-ice melt-induced shallow stratification could bias bulk air-sea CO_2 flux estimates based on the fCO_{2w} measurements at ~5 m depth. The direct air-sea CO_2 flux measurements by EC are free of this stratification issue, and are thus employed on two Arctic cruises (JR18006 and JR18007) to assess the effect of sea-ice melt on Arctic Ocean CO_2 flux estimates.

- The results indicate that the implied surface fCO_{2w} (using the EC air-sea CO_2 flux measurements) is substantially lower than the subsurface fCO_{2w} (~6.5 m depth) in regions with near-surface stratification due to sea-ice melt. Cooling and freshening due to sea-ice melt account for half of the difference between surface and subsurface fCO_{2w} during the Arctic cruise JR18007.

- A back-of-the-envelope calculation suggests that near-surface stratification due to sea-ice melt could lead to a ~10 Tg C yr^{-1} underestimation of the Arctic Ocean CO_2 uptake. See Chapter 3 and also Dong et al. (2021b).

Furthermore, in comparison to the Arctic Ocean, the ocean carbon community recently paid more attention to Southern Ocean CO_2 flux estimates. The sparsity of the high-quality shipboard fCO_{2w} observations is a major challenge for the Southern Ocean CO_2 flux estimates. The Southern Ocean CO_2 uptake estimates based on the shipboard fCO_{2w} measurements (SOCAT) and novel float pH observations (SOCCOM) suggest large disagreements (Bushinsky et al., 2019). An independent CO_2 flux dataset from EC measurements in the Southern Ocean is employed to compare with the SOCAT-based and SOCCOM-based flux estimates.

- The comparison suggests that the independent EC CO_2 flux dataset supports air-sea CO_2 flux estimates based on shipboard observations (SOCAT) after considering two temperature corrections, but indicates much stronger (by the factor of 1.6) CO_2 uptake than the estimates based on the float data (SOCCOM).

- A new gas transfer velocity–wind speed relationship is proposed based on the EC-derived K_{660} observations in the Southern Ocean, which is in good agreement with the widely used K_{660} parameterisations (e.g., Wanninkhof, 2014).

Although the shallow stratification issue and the sparsity of observation are important issues for regional ocean flux estimates, they might be insignificant for estimating the annual mean air-sea CO_2 flux globally. An unresolved but important question is if the cool skin effect and the warm bias in the SST dataset influence global air-sea CO_2 flux estimates (Woolf et al., 2016). A recent study suggested a substantial increase (~50% or ~0.9 Pg C yr^{-1}) in the global ocean CO_2 uptake by considering a warm bias in the ship SST dataset in SOCAT (assessed by a satellite SST product, DOISST v2.0) and a constant cool skin effect (-0.17 K) (Watson et al., 2020).

- The re-assessment of these two temperature effects presented in Chapter 5 demonstrates that there is a small warm bias (assessed by the buoy SST dataset) in the ship SST in SOCAT and that the physics-based cool skin effect has a latitudinal variation. Applying these two updated temperature effects increases the average ocean CO_2 uptake by ~35% (0.6 Pg C yr^{-1}), substantially lower than the previous correction (Watson et al., 2020).

- The warm bias flux correction and the cool skin flux correction are not constant and have clear inter-annual and latitudinal variabilities. The temperature-revised CO_2 flux bridges the gap between estimates from the surface observation-based air-sea CO_2 fluxes and from the independent ocean carbon inventory (Gruber et al., 2019) from 1994 to 2007. See Chapter 5 and also Dong et al. (2022).

In summary, this PhD study attempts to improve the high-latitude ocean CO_2 flux estimates by employing the EC technique and to improve global ocean CO_2 flux estimates by re-assessing the two temperature effects. A better understanding of the uncertainties in EC air-sea CO_2 flux measurements builds our confidence in using the EC technique to study gas transfer processes. A well-constrained K_{660} is key to reducing uncertainties in global and regional air-sea CO_2 flux estimates.

6.2 Future research

Several conclusions from this thesis deserve further investigation:

- **Make use of the measurements with $|\Delta fCO_2|$ less than 20 µatm.** The uncertainty analysis in Chapter 2 suggests ruling out the K_{660} data derived from the measurements with low flux signals ($|\Delta fCO_2| < 20$ µatm) because of the high relative random uncertainty. However, these low-flux data are highly valuable. First, the cool skin effect is in theory important for global air-sea CO_2 flux estimates (see Chapter 5), but there is a lack of strong observational evidence. The EC technique can be used to measure air-sea CO_2 fluxes in regions with a low flux signal situation (i.e., $|\Delta fCO_2| \sim 0$) but with a strong cool skin effect (low wind speed). The comparison between the long-term averaged EC flux measurements and the bulk flux estimates with and without considering the cool skin effect can provide direct evidence on whether the cool skin effect does impact the air-sea CO_2 flux in line with the prediction of the theory. Second, bubble-mediated transfer is expected to play a first-order role in air-sea CO_2 exchange (Woolf, 1997). Bubble-mediated transfer is asymmetric and favours the invasion process more. This means we may need to use different parameterisation schemes of K_{660} to estimate the air-sea CO_2 flux in outgassing regions and in uptake areas. This asymmetry effect is more evident in regions with low CO_2 flux signals (Woolf, 1997). Therefore, the difference in K_{660} between that derived from small but positive ΔfCO_2 observations and from small but negative ΔfCO_2 measurements can be used to quantify the asymmetry effect. However, the challenge of using these low flux signal measurements is the high relative uncertainty, which might require long-term observations (to average and reduce the uncertainty) or new data analysis techniques (to weaken the effect of the high relative uncertainty on the data analysis).

- **Systematic observations of the upper ocean gradient.** The impact of shallow stratification on the entire Arctic Ocean CO_2 flux has been simply estimated with crude assumptions in Chapter 3. Detailed measurements of upper ocean gradients in fCO_{2w}, temperature, salinity, DIC, and biology variables are required to better understand the impact of sea-ice melt-induced shallow stratification on air-sea gas fluxes in the polar oceans.

- **Producing SOCCOM products with different interpolation methods.** The SOCCOM product used for the comparison with the EC air-sea CO_2 flux measurements in Chapter 4 is only based on a neural network technique (MPI-SOMFFN, Landschützer et al., 2013).

However, not only MPI-SOMFFN, but some other interpolation methods such as Jena-MLS (Rödenbeck et al., 2014) and CSIR-ML6 (Gregor et al., 2019) are also available and have been used for reconstructing the global ocean CO_2 flux based on the SOCAT data. Different interpolation methods contain different uncertainty sources, and using several different products for the comparison in Chapter 4 will make the results more robust. Therefore, it is meaningful to employ other interpolation methods to produce different SOCCOM-based flux products from 2015 to 2022.

- **Impact of the warm layer effect on the air-sea CO_2 flux.** In Chapter 5, I discuss the impact of the cool skin effect on air-sea CO_2 flux estimates, but there is another upper ocean temperature effect – the warm layer effect, that I did not consider in Chapter 5. The warm layer effect is not as prevalent as the cool skin effect, but may have a stronger impact on the air-sea CO_2 flux than the cool skin effect in regions with a clean sky (without clouds) and low wind speed. Quantification of the impact of the warm layer effect on the air-sea CO_2 flux can improve regional CO_2 flux estimates, which is the main aim of the REgional Carbon Cycle Assessment and Processes project (https://www.globalcarbonproject.org/reccap/). In addition, the gas transfer velocity (derived from the EC CO_2 flux and fCO_2 measurements) in tropical oceans with low CO_2 flux signals may be substantially affected by the warm layer effect. The impact of surface warming on gas exchange was investigated in a large wind tunnel (Liss et al., 1981), but needs further observational evidence in the open ocean. Simultaneous observations of the upper ocean temperature gradients are necessary for the K_{660} analysis.

These additional topics also deserve urgent attention.

- **The role of bubbles in air-sea CO_2 exchange.** As shown in Figure 1.7, the standard deviation of the EC-derived K_{660} measurements from different environments is high at high wind speed, which is very possibly due to the underrepresentation of the bubble-mediated transfer in the K_{660}-wind speed relationship. The existing evidence in different environments shows a wide range of the importance of bubbles in air-sea CO_2 exchange (e.g., Bell et al., 2017; Blomquist et al., 2017; Krall et al., 2019; Zavarsky et al., 2018), which indicates a lack of mechanistic understanding of bubble-mediated transfer. A better understanding of the bubble-mediated transfer processes is key to reducing the uncertainties in the parameterisation of K_{660} and to improving the global air-sea CO_2 flux estimates.

- **The riverine flux.** The air-sea CO_2 flux estimates based on surface observations represent the contemporary ocean CO_2 flux, including the anthropogenic perturbation flux and the natural ocean CO_2 flux. The natural flux indicates the air-sea CO_2 flux in the pre-industrial period (without anthropogenic perturbation). The pre-industrial ocean and atmosphere are argued to have been in natural equilibrium, and the total air-sea CO_2 flux globally in the pre-industrial period is characterised by the outgassing of CO_2 due to the land-to-ocean riverine carbon transport (Hauck et al., 2020). Quantification of the riverine CO_2 flux and its distribution are essential to separate the anthropogenic flux component from the contemporary ocean CO_2 flux estimates, and compare them with the anthropogenic CO_2 uptake estimates based on independent estimates of the ocean carbon inventory. However, current estimates of the riverine flux span from 0.23 to 0.78 Pg C yr^{-1} (Jacobson et al., 2007; Lacroix et al., 2020; Regnier et al., 2022; Resplandy et al., 2018) with large uncertainties. In Chapter 5, to compare the global ocean CO_2 flux estimates based on the surface observations and based on the ocean carbon inventory, an average of the existing four riverine CO_2 flux estimates is used. To increase the confidence of the comparison, a better quantified riverine carbon flux is required.

- **The large disagreement between the model and observation-based CO_2 flux estimates.** A more general but important and urgent scientific question is why the disagreement between the global biogeochemical model-based estimates of the anthropogenic CO_2 uptake and the surface observation-based flux estimates has been increasing in recent years. Since 2002, the increasing rate of the surface observation-based ocean CO_2 sink is higher than the model-based ocean CO_2 uptake by a factor of three (Friedlingstein et al., 2022). The ocean uptake of the anthropogenic CO_2 is estimated as the average of the model flux ensemble mean and the observation flux product ensemble mean from 1990 onwards in the Global Carbon Budget 2022 (Friedlingstein et al., 2022). Therefore, the divergence of these two independent flux estimates reduces our confidence in the quantification of the ocean CO_2 sink. It is to be expected that in the future much effort will be expended improving the models' capability and increasing the density of observations, especially in the Southern Ocean.

Appendix

A2 Cruise tracks of JR18006 and JR18007

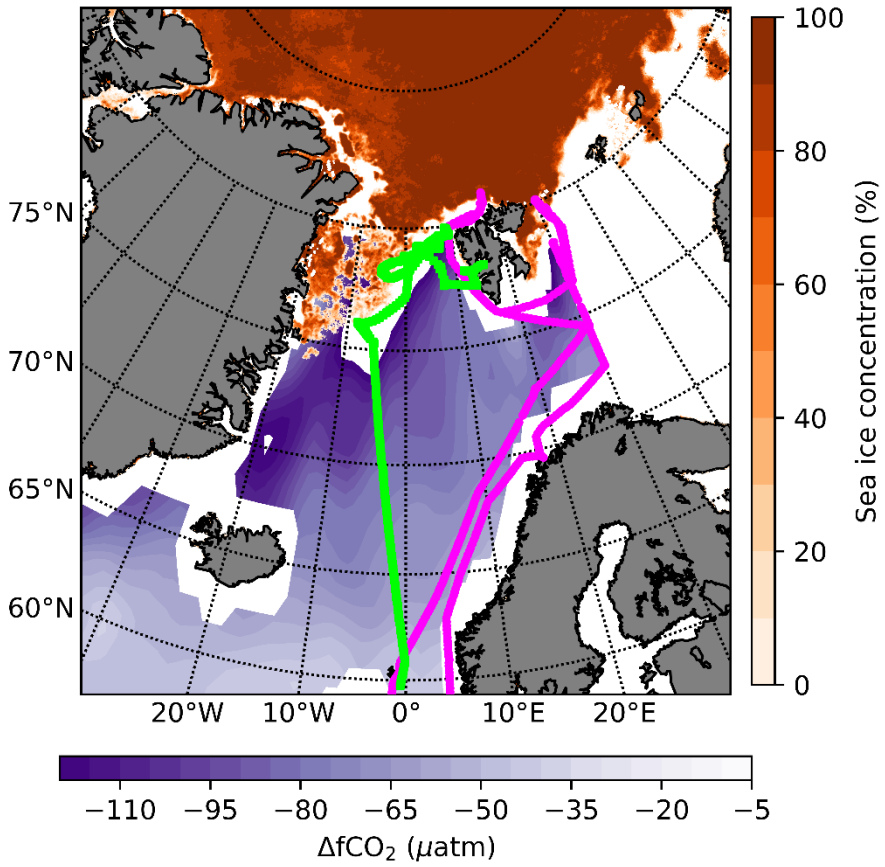

Figure A2.1 Cruise tracks of JR18006 (magenta) and JR18007 (green). The bottom colour bar indicates the CO_2 fugacity difference (ΔfCO_2) of August 2019 (Bakker et al., 2016; Landschützer et al., 2020), while the right colour bar shows the Arctic sea ice concentrations of 1st August 2019 measured by Advanced Microwave Scanning Radiometer - Earth Observing System Sensor (AMSR-E, Spreen et al., 2008).

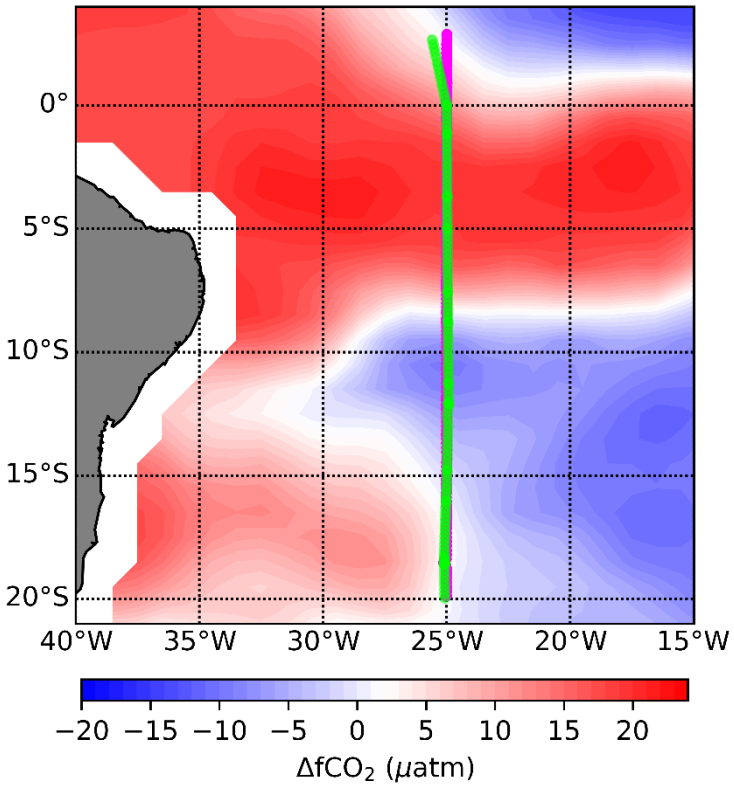

Figure A2.2 Cruise tracks of AMT28 (magenta) and AMT29 (green). The ocean is coloured with the ΔfCO_2 for October 2018 (Bakker et al., 2016; Landschützer et al., 2020).

B2 Integral time scale and variance spectra of CO_2 and vertical wind velocity

An integral time scale is used in the flux uncertainty calculation (Equations 2.5 and 2.7). The definition of integral time scale τ_x of variable *x* is:

$$\tau_x = \frac{1}{\sigma_x^2}\int_0^\infty r_{xx}(t)dt \tag{B2.1}$$

where σ_x^2 is the variance of *x* and r_{xx} is the auto-covariance function of *x*. *t* is the shifting time of auto-covariance (which is different from the lag time between *w* and CO_2 in the EC flux calculation). We can use Equation B2.1 to estimate the integral time scale of *w* and CO_2 directly. However, integration up to infinity is not practical. Instead, we can numerically estimate the time scale by determining the time corresponding to the auto-covariance coefficient function (r_{xx}/σ_x^2) value decaying to 1/e (1/e decaying method) or by integrating the auto-covariance function up to the first zero crossing of the function (zero crossing method) (Rannik et al., 2009).

One can also use similarity theory to estimate the integral time scale theoretically (Blomquist et al., 2010):

$$\tau_w = 2.8\frac{z}{\overline{u_r}}f_\tau(z/L) \tag{B2.2}$$

Here, $\overline{u_r}$ is the relative wind speed. The similarity function $f_\tau(z/L)$ is described by the stability parameter z/L where z is the observation height (m) and L is the Obukhov length (m) (Blomquist et al., 2010).

Yet another method to estimate the integral time scale is from the peak frequency ($f_{\max}$) in the *w* variance spectrum (Kaimal & Finnigan, 1994):

$$\tau_w = \frac{1}{2\pi f_{\max}} \tag{B2.3}$$

The integral time scales of *w* estimated by these four methods for cruise JR18007 are shown in Figure B2.1. The integral time scale estimated by the zero crossing method agrees well with the peak frequency estimates using Equation B2.3. The 1/e decaying method tends to underestimate the integral time scale, which is generally observed for turbulent signals (Rannik et al., 2009), whereas the similarity method (Equation B2.2) considerably overestimates the integral time scale. Based on the recent analysis (as yet unpublished) of the entire NOAA PSL flux database, the Equation B2.2 formulation is now thought to be an overestimate (review comment for this paper from Blomquist, 2021). In this study, we use the integral time scale of

w from the zero crossing method to estimate the theoretical flux uncertainty (Equations 2.5 and 2.7). The theoretical systematic error estimates (Equation 2.5) also require the integral time scale of CO_2. The integral time scale of CO_2 is difficult to evaluate from the above four methods due to instrument noise. Instead, we estimate it by directly integrating the auto-covariance function (Equation B2.1) to a shift time of 200 s (we found no significant difference in the integral time scale when integrating the CO_2 auto-covariance function for shift times ranging from 150 s to 250 s).

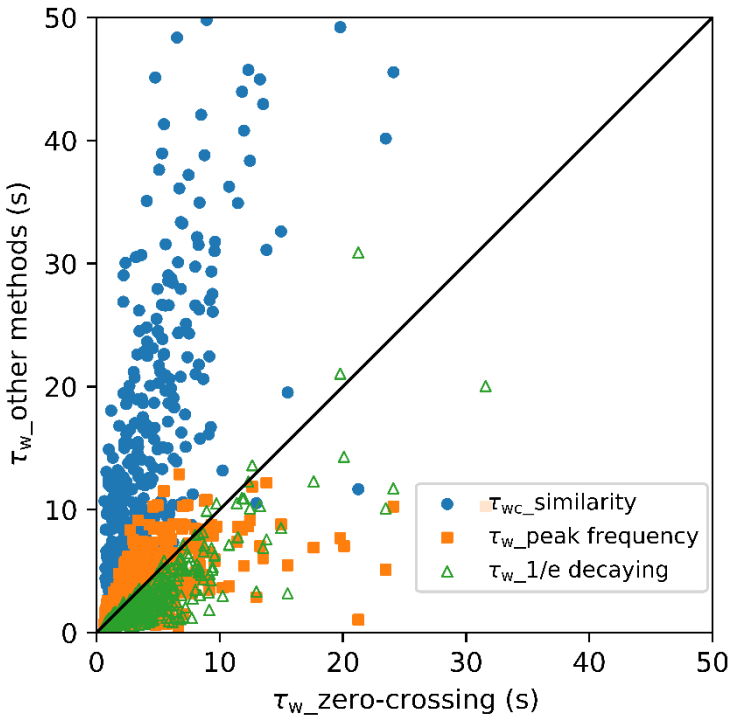

Figure B2.1 Comparison of integral time scales of *w* estimated by four different methods. Estimated integral time scales from the zero crossing method (integrating the auto-covariance function up to the first zero crossing the function) agree well with the estimation of the peak frequency method (Equation B2.3). However, the similarity method (Equation B2.2) overestimates the integral time scale whereas the 1/e decaying method (determining the time needed for the auto-covariance coefficient function value to decay to 1/e) tends to underestimate the integral time scale.

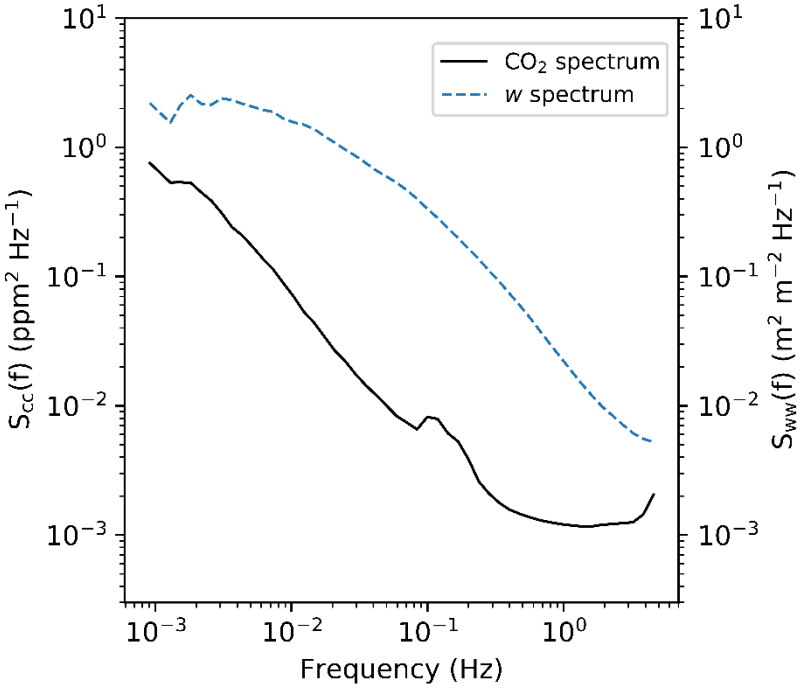

Figure B2.2 Mean-variance spectra for CO_2 and *w* for one Arctic cruise JR18007. The near constant CO_2 variance at high frequency (1–5 Hz) indicates the band-limited noise in the CO_2 signal. In contrast, the *w* spectrum does not show a similar band-limited noise at < 10 Hz.

C2 Comparison of the uncertainty estimates by different methods

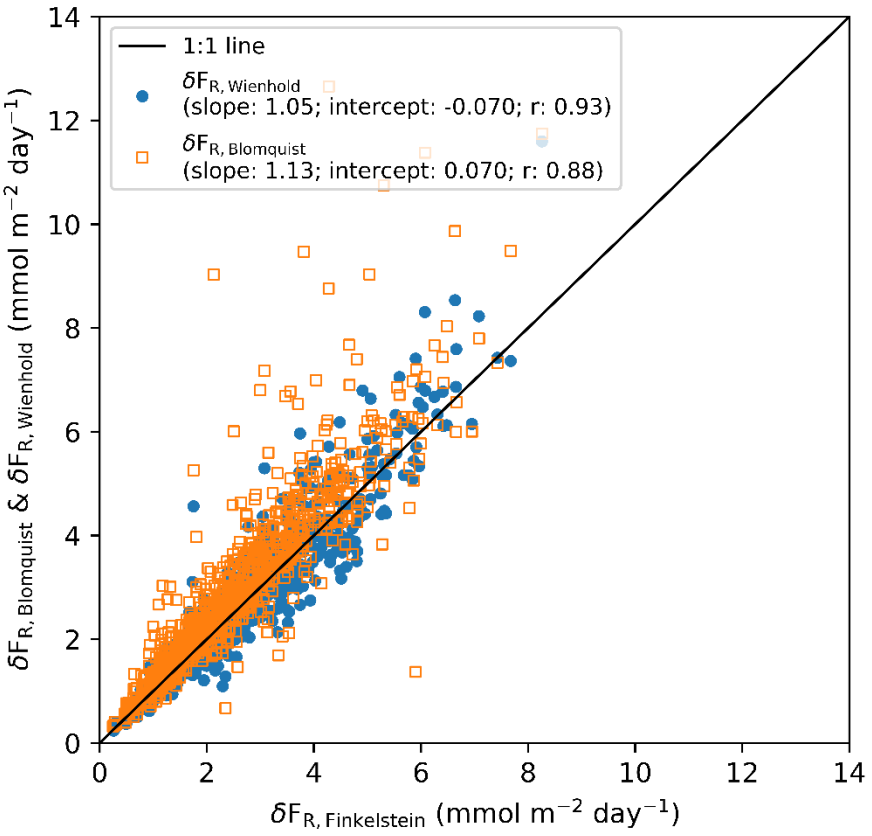

Figure C2.1 Comparison of total random uncertainties in hourly flux estimated by three different methods for the Arctic cruises. The empirical estimates $F_{R,\,\mathrm{Wienhold}}$ agree well with one of the theoretical estimates $\Delta F_{R,\,\mathrm{Finkelstein}}$ (r = 0.93). The other theoretical estimate $\Delta F_{R,\mathrm{Blomquist}}$ is slightly higher than the random uncertainties $\Delta F_{R,\,\mathrm{Finkelstein}}$ (slope = 1.13) if the constant in Equation 2.8 is set equal to $\sqrt{2}$.

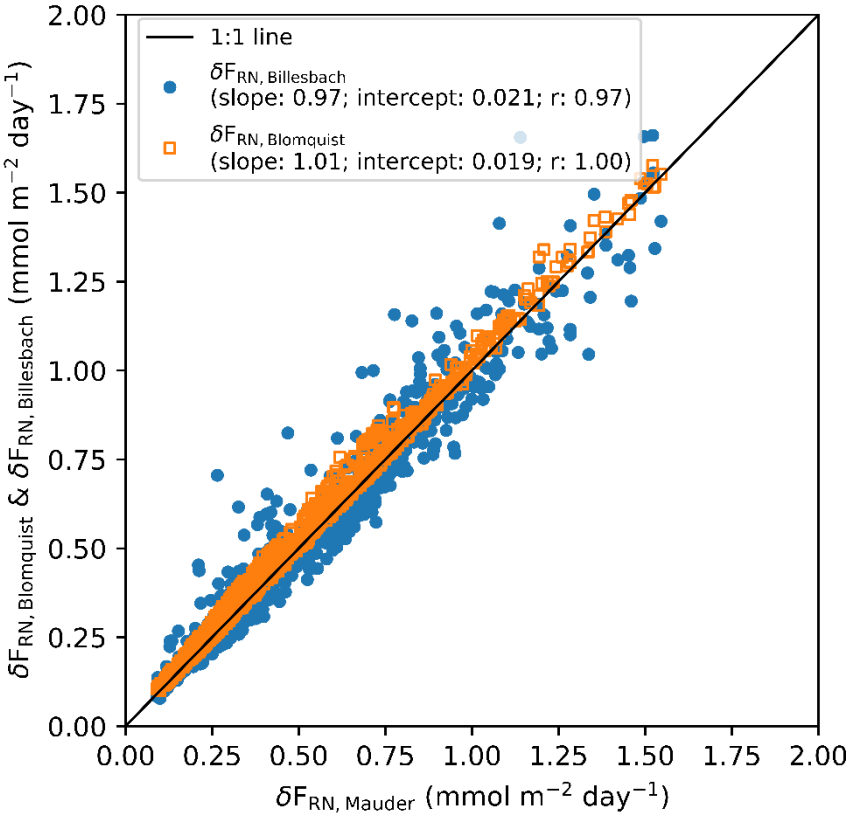

Figure C2.2 Comparison of random error in hourly flux due to instrument white noise, estimated by three different methods for the Arctic cruises. The three uncertainty estimations agree well. The correlation coefficient (r) between $\delta F_{RN,\ Mauder}$ and $\delta F_{RN,\ Blomquist}$ is 1 if the constant in Equation 2.7 (a) is set to $\sqrt{2}$.

D2 Performance of two gas analysers

Figure D2.1 shows a comparison between the performance of the Picarro 2311-f and the LI-7200 gas analysers. We estimated that the noise of the LI-7200 is on average 3 times higher than that of the Picarro 2311-f (Table 2.3). Indeed, random error in the CO_2 flux due to the white noise is much higher for the LI-7200 than for the Picarro 2311-f, but the total flux uncertainty of the EC system with the LI-7200 on AMT29 is only slightly higher than that of the EC system with the Picarro 2311-f on AMT28 (Table 2.4). Again, this is because, for both EC systems, sampling error dominates the total random uncertainty, while the contribution of instrument noise (< 30%) to the total uncertainty is relatively small (Billesbach, 2011; Langford et al., 2015; Mauder et al., 2013; Rannik et al., 2016). Another often used CRDS gas analyser in EC measurements is the Los Gatos Research (LGR) Fast Greenhouse Gas Analyser (FGGA) (Prytherch et al., 2017). Yang et al. (2016a) showed that LGR FGGA is ca. 10 times noisier than the Picarro G2311-f, and as a result, the total CO_2 flux uncertainty measured by the LGR is 4 times higher than that by the Picarro. From the perspective of measurement noise, Picarro and LI-7200 gas analysers are better suited for air-sea CO_2 flux measurements than the LGR FGGA.

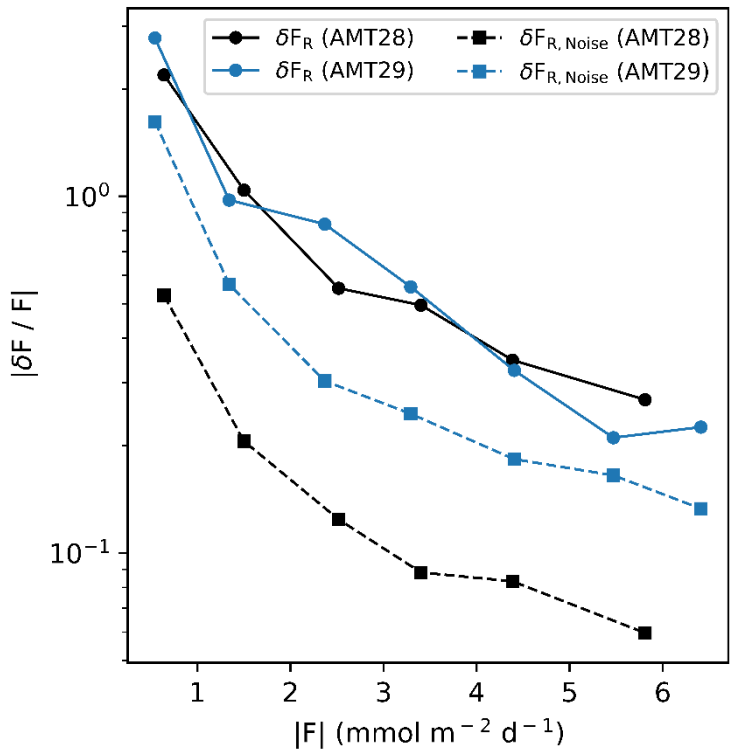

Figure D2.1 Comparison of the relative total random uncertainty and the relative random error component due to white noise for different gas analysers. A Picarro G2311-f gas analyser was used on AMT28 and a LI-7200 infrared gas analyser on AMT29.

Supplement

S1 Summary of eddy covariance observations from 1996 to 2022

The progress in *K* derivations from EC CO_2 and dimethylsulfide (DMS) flux measurements over the last quarter of a century is assessed here. EC CO_2 flux measurements in the early period produced unreasonable fluxes in both magnitude and variability (e.g., Edson et al., 2011; Else et al., 2011; Jacobs et al., 2002; Kondo & Tsukamoto, 2007; Lauvset et al., 2011; Prytherch et al., 2010a). This is now generally attributed to be a measurement artefact due to water vapour (H_2O) cross-sensitivity in the CO_2 measurement in a salty marine atmosphere (Blomquist et al., 2014; Kohsiek, 2000; Landwehr et al., 2014; Nilsson et al., 2018; this study, see Section 2.2.1). With advances in: 1) instrumentation (CO_2 and DMS analysers); 2) EC system setup (drying, choice of location to minimise flow distortion); and 3): motion correction procedures, the EC technique has improved substantially and is now largely mature for air-sea CO_2 and DMS flux measurements (Blomquist et al., 2010, 2014; Dong et al., 2021a; Landwehr et al., 2014; Miller et al., 2010). Now that EC CO_2 flux measurements and EC-derived K_{660} are reasonable, the maturation of the technique has enabled a shift in emphasis toward uncovering the mechanisms that influence air-sea gas exchange. Examples of using EC to study exchange processes in the open ocean include: evidence of the impact of surfactants (Yang et al., 2021) and chemical enhancement (Fairall et al., 2022) at low to moderate wind speeds, ocean waves (Brumer et al., 2017; Yang et al., 2022) and bubble-mediated transfer (Bell et al., 2017; Blomquist et al., 2017; Zavarsky et al., 2018) at high wind speeds, the impact of sea ice on the air-sea CO_2 transfer velocity (Butterworth & Miller, 2016; Prytherch & Yelland, 2021), and the effect of near-surface stratification in the Arctic (Dong et al., 2021b). See Table S1.1 for a summary of EC-based studies of *K* for CO_2 and DMS.

Table S1.1 Summary of eddy covariance (EC)-based CO_2 and DMS transfer velocity studies from 1996 to 2022. The reasonable (unreasonable) K_{660} derived from EC fluxes largely agree (disagree) with the predicted K_{660} (e.g., Ho et al., 2006; Nightingale et al., 2000; Wanninkhof, 2014) constrained by the dual-tracer measurements or bomb-^{14}C inventory in both magnitude and variability.

Project	Region, Time, Platform	Gas analyser, Measured gas, Sample air dried?	Notes
ASGAMAGE	• North Sea (coastal ocean) • Fall 1996 • Tower, Meetpost Noordwijk	• Two open path gas analysers • CO_2 • N	• Unreasonable K_{660} (higher than expected by a factor of 2.5) • (Jacobs et al., 2002)
GasEx-98	• North Atlantic (open ocean) • May–June 1998 • Ship, *Ronald H. Brown*	• Closed path gas analyser: LI-6262 • CO_2 • N	• The first largely reasonable EC-derived K_{660} from field EC CO_2 measurements • Informs the cubic parametrization between K_{660} and wind speed • (McGillis et al., 2001)
GasEx-01	• Equatorial Pacific (open ocean) • Feb. 2001 • Ship, *Ronald H. Brown*	• Closed path gas analyser: LI-6262 and/or LI-7000 • CO_2 • N	• Largely reasonable K_{660} in magnitude with a weak wind speed dependence • Focused on low wind speeds, strong solar insolation region • (McGillis et al., 2004)
TAO	• Equatorial Pacific (open ocean) • Nov. 2003 • Ship, *Ronald H. Brown*	• Atmospheric pressure ionization mass spectrometer (APIMS) • DMS • Y	• First measurements of DMS K_{660} from a ship, which showed a strong, near-linear relationship with wind speed • (Huebert et al., 2004)
ArKona Spar	• Baltic Sea (coastal ocean) • March 2003–Oct. 2004 • Tower	• Open path gas analyser: LI-7500 • CO_2 • N	• Reasonable K_{660} in the mean but highly scattered • Low salinity (7–9‰) • (Weiss et al., 2007)
PHASE I	• North Pacific (open ocean) • May–Jul. 2004 • Ship, Wecoma	• APIMS • DMS • Y	• Similar results to Huebert et al. (2004), showing a strong, near-linear relationship with wind speed • (Marandino et al., 2007)
BIO	• Sargasso Sea (coastal ocean) • summer 2004 • Ship, *Seward Johnson*	• APIMS • DMS • Y	• Together with Huebert et al. (2004) provided the data for tuning the NOAA/COARE gas transfer model • (Blomquist et al., 2006)

Knorr06	• South-east Pacific Ocean (open ocean) • Jan. 2006 • Ship, *Knorr*	• APIMS • DMS • Y	• Generally showed a strong wind speed dependence, unlike McGillis et al. (2004) (CO_2) in a similar region • (Marandino et al., 2009)
58GS20060721	• North Atlantic (open ocean) • July–Aug. 2006 • Ship, *G.O. Sars*	• Open path gas analyser: LI-7500 • CO_2 • N	• Unreasonable K_{660} (factor of 10 higher than expected) • K_{660} not unreasonable in magnitude after applying the 'PKT' (see Prytherch et al., 2010a) correction • (Lauvset et al., 2011)
HiWASE	• North Atlantic (open ocean) • Sep. 2006 –Sep. 2007 • Ship, *Polarfront*	• Open path gas analyser: LI-7500 • CO_2 • N	• Unreasonable K_{660} (factor of 10 higher than expected) • Proposed the 'PKT' correction to make K_{660} more reasonable • (Prytherch et al., 2010a, 2010b)
Knorr07	• North Atlantic (open ocean) • May–July 2007 • Ship, *Knorr*	• Closed path gas analyser: Modified LI-7500 • CO_2, DMS • Y	• First use of a dryer for CO_2 flux measurements • Reasonable CO_2 K_{660} in both magnitude and variability • Some very high DMS K_{660} possibly due to environmental or measurement complications related to seawater DMS gradients • First time when K of CO_2 and DMS were both measured, but concurrently for only a brief period • (Miller et al., 2009, 2010; Marandino et al., 2008)
SO GasEx	• Southern Ocean (open ocean) • Feb.–April 2008 • Ship, *Ronald H. Brown*	• Open path gas analyser: LI-7500 • CO_2, DMS • N	• Unreasonable K_{660} from EC CO_2 measurements (factor of 10 higher than expected) • K_{660} less unreasonable in magnitude after applying a numerical correction but the corrected K_{660} remain scattered • Low DMS K_{660} at high wind speeds during a single storm event • (Blomquist et al., 2017; Edson et al., 2011; Yang et al., 2011)
DOGEE	• North Atlantic (open ocean) • June–July 2007 • Ship, *Discovery*	• APIMS • DMS • Y	• Showed that DMS K_{660} is at least as well correlated with the friction velocity (obtained from inertial dissipation method) as with wind speed • Artificial surfactant deployment is shown to reduce gas transfer • (Huebert et al., 2010; Salter et al., 2011)
VOCALS	• Southeast Pacific (open ocean) • Oct.–Nov. 2008	• APIMS • DMS • Y	• Similar results to Huebert et al. (2004), showing a strong, near-linear relationship with wind speed • (Yang et al., 2009)

	• Ship, *Ronald H. Brown*		
DMS synthesis	• Global oceans (open oceans) • 5 research cruises with 3 different ships	• APIMS • DMS • Y	• Synthesized DMS K_{660} measurements from five cruises, including SO GasEx • Showed that bubble-mediated exchange of DMS has a different temperature dependence compared to interfacial transfer and needs to be normalised separately • (Yang et al., 2011)
FINO-2	• Western Baltic (coastal ocean) • Nov. 2011–Aug. 2013 • Tower, FINO-2	• Open path gas analyser: LI-7500 • CO_2 • N	• Reasonable K_{660} in magnitude but scattered • Low salinity (surface, 7–9‰) • (Ghobadian and Stammer, 2019)
Knorr-11	• North Atlantic (open ocean) • June–July 2011 • Ship, *Knorr*	• Closed path gas analyser (CO2): Modified LI-7500 • APIMS (DMS) • CO2, DMS • Y	• Reasonable K_{660} in both magnitude and variability, with CO_2 transfer much faster than DMS transfer at high winds • First field evidence of bubble-mediated transfer indicated by simultaneous EC CO_2 and DMS measurements • Low DMS K_{660} during a single storm event at high wind speeds • (Bell et al., 2013, 2017)
DYNAMO	• Tropical Indian (open ocean) • Aug. 2011–Feb. 2012 • Ship, *Roger Revelle*	• Open path gas analyser: LI-7500; Two closed path gas analysers: LI-7200 (one with a dryer and another without a dryer) • CO_2 • Y/N	• Direct comparison between CO_2 fluxes measured with open and closed path analysers • Reasonable fluxes from a closed path gas analyser with a dryer, and unreasonable results from an open path gas analyser and from a closed path gas analyser without a dryer • Similar data collected on SOAP cruise (Landwehr et al., 2014). Together, these papers confirmed the water vapour cross-sensitivity issue and recommended a closed path gas analyser with a Nafion dryer for open ocean EC CO_2 measurements • (Blomquist et al., 2014)
SOAP	Southern Ocean (open ocean) Feb.–March 2012 Ship, *Tangaroa*	• APIMS (DMS) and closed path gas analyser (CO_2): Modified LI-7500 • CO_2, DMS • Y	• Reasonable K_{660} in both magnitude and variability, with CO_2 transfer much faster than DMS transfer at high winds • (Bell et al., 2015; Landwehr et al., 2018)
NBP-1210/ 1402	• Southern Ocean (polar ocean)	• Closed path gas analysers: LI-7200	• Reasonable K_{660} in both magnitude and variability

	• Jan.–Feb. 2013 and Feb.–March 2014 • Ship, *Palmer*	• CO_2 • Y	• Quantified the K_{660}–U_{10N} relationship at different sea-ice concentrations • (Butterworth & Miller, 2016)
HiWinGS	• North Atlantic (open ocean) • Oct.–Nov. 2013 • Ship, *Knorr*	• Two closed path gas analysers: Picarro G1301-f and LI-7200 • CO_2, DMS • Y	• Reasonable K_{660} in both magnitude and variability, with CO_2 transfer much faster than DMS transfer at high winds • The first field EC measurements with wind speed spanning from very low wind speed to very high wind speed (24 m s^{-1}) • Quantified the contribution of bubbles to the air-sea CO_2 exchange • (Blomquist et al., 2017)
Arctic fjords	• Arctic fjords (coastal ocean) • 14–30 March 2013 • Tower	• Open path gas analysers: LI-7500 • CO_2 • N	• K_{660} derived from EC were significantly higher than K_{660} estimated from the (Wanninkhof et al., 2009) parameterisation. • High salinity environment (34.8‰) • (Andersson et al., 2017)
ACSE (SWERUSC3)	• Arctic ocean (both open ocean and seawater with sea ice) • July–Oct. 2014 • Ship, *Oden*	• Closed path gas analyser: Los Gatos Fast Greenhouse Gas Analyser (LGR FGGA) • CO_2 • N	• Reasonable K_{660} in the mean but with large variability • Quantified the K_{660}–U_{10N} relationship at different sea-ice concentrations • (Prytherch et al., 2017)
Penlee Point Atmospheric Observatory	• South-west coast of the United Kingdom (coastal ocean) • Sep. 2015–Aug. 2016 • Tower	• Two closed path gas analysers: Picarro G2311-f (dried); LGR FGGA (undried) • CO_2 • Y/N	• Similar K_{660} in the mean compared to previous open ocean observations • Showed that CO_2 flux from dried Picarro and undried FGGA are similar in magnitude • Implied complex and dynamic drivers for the air-sea gas exchange in this coastal environment • (Yang et al., 2016a, 2019)
S234-2/235	• Tropical Indian (open ocean) • July–Aug. 2014 • Ship, *Sonne*	• Closed path gas analyser, LI-7200 • CO_2, DMS • Y	• Reasonable K_{660} in magnitude • DMS and CO_2 transfer similar, implying insignificant role of bubble-mediated CO_2 transfer (U_{10N} up to ~16 m s^{-1}) • EC CO_2 fluxes were measured in both invasion and evasion environments, but flux signal was relatively low • (Zavarsky et al., 2018)
Östergarnsholm station	• Baltic Sea (coastal ocean) • 2013 and 2021 • Tower	• Open path gas analyser: LI-7500 • CO_2 • N	• Largely reasonable K_{660} in magnitude, but with a large scatter • Low salinity environment (6.5–7.5‰) • (Gutiérrez-Loza et al., 2022; Rutgersson and Smedman, 2010)

Ice camp Arctic Ocean 2018	• Arctic ocean (lead) • 2018–2019 • Ship, *Oden*	• Closed path gas analyser: LI-7200 • CO_2 • Y	• Reasonable K_{660} in both magnitude and variability • Quantified the K_{660}–U_{10N} relationship in sea-ice lead water • (Prytherch & Yelland, 2021)
ANDREXII	• Southern Ocean (open ocean) • Feb.–April 2019 • Ship, *James Clark Ross*	• Closed path gas analyser: Picarro G2311-f • CO_2 • Y	• Reasonable K_{660} in both magnitude and variability • Gas transfer efficiency was measured coincidently with EC K_{660} and appears to indicate the impact of natural surfactants on gas exchange • (Yang et al., 2021)
JR18007	• Arctic Ocean (open ocean) • Aug. 2019 • Ship, *James Clark Ross*	• Closed path gas analyser: Picarro G2311-f • CO_2 • Y	• Reasonable K_{660} in both magnitude and variability • K_{660} were measured in very high flux signal regions ($fCO_{2w} - fCO_{2a}$) between -181 and -71 µatm), which means the relative flux uncertainty is low. • Identifies the impact of sea-ice-induced shallow stratification on Arctic CO_2 flux estimates. • (Dong et al., 2021a, 2021b)
EC CO_2 synthesis	• Global oceans • 11 research cruises with 5 different ships	• Closed path gas analyser • CO_2 • Y	• Synthesis of high-quality K_{660} datasets derived from ship-based EC CO_2 measurements using closed path gas analysers with a dryer • The grand average of EC-derived K_{660} is similar to dual-tracer-based K_{660} parameterisations at moderate to high winds, but is greater at low winds. • (Yang et al., 2022)

S2 Eddy covariance data processing and quality control

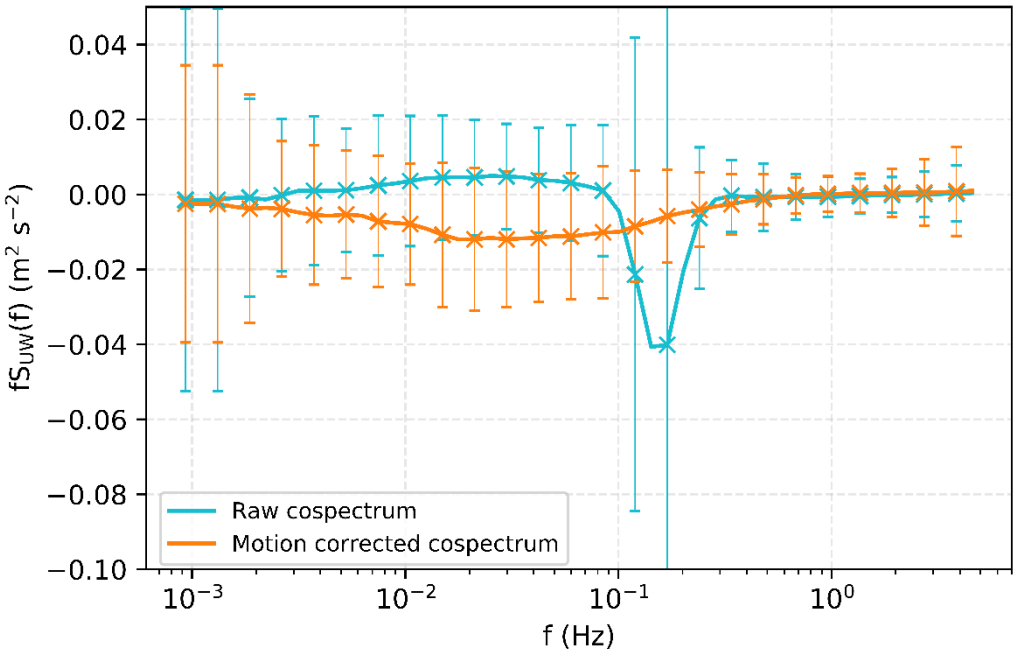

Figure S2.1 Mean momentum cospectrum $S_{UW}(f)$ before (cyan line) and after (orange line) motion correction for cruise JR18007. Error bars represent the standard deviation of $S_{UW}(f)$. For the raw cospectrum, there is a spectral peak in the frequency of 0.1–0.3 Hz which is the typical frequency of the ocean waves (swell) and ship motion.

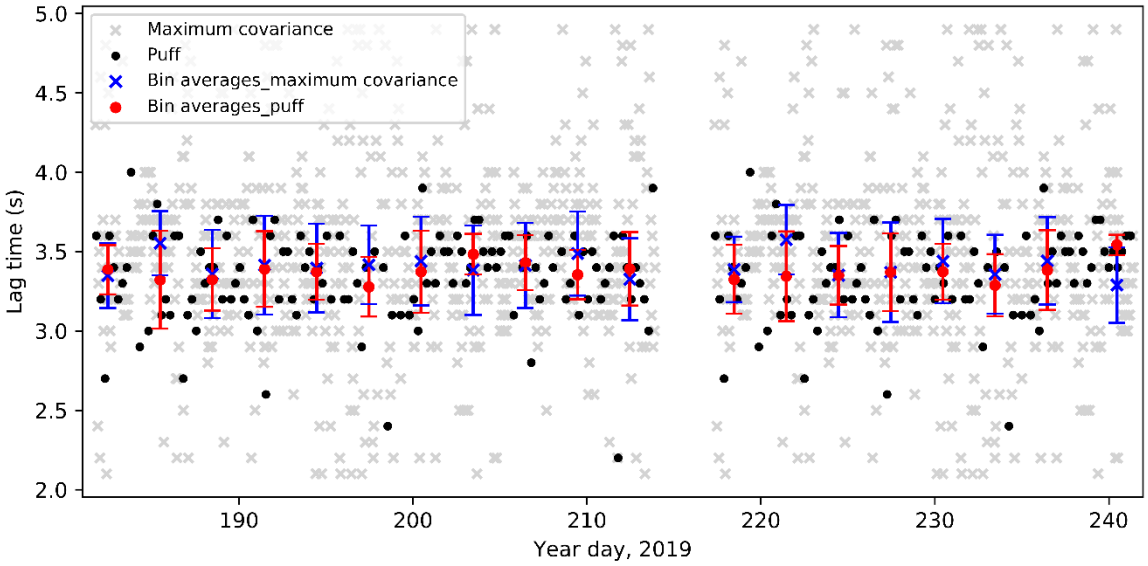

Figure S2.2 Time series of time lags for two Arctic cruises. Grey crosses represent the lag time estimated by the maximum covariance method and the blue crosses represent 3-day (72 hours) bin averages with error bars representing the standard deviation. Black-filled circles represent the lag time estimated by the nitrogen puff method and red circles represent 3 days bin averages with error bars representing the standard deviation. The gap in data between year days 213 and 217 is due to the break between cruise JR18006 and JR18007.

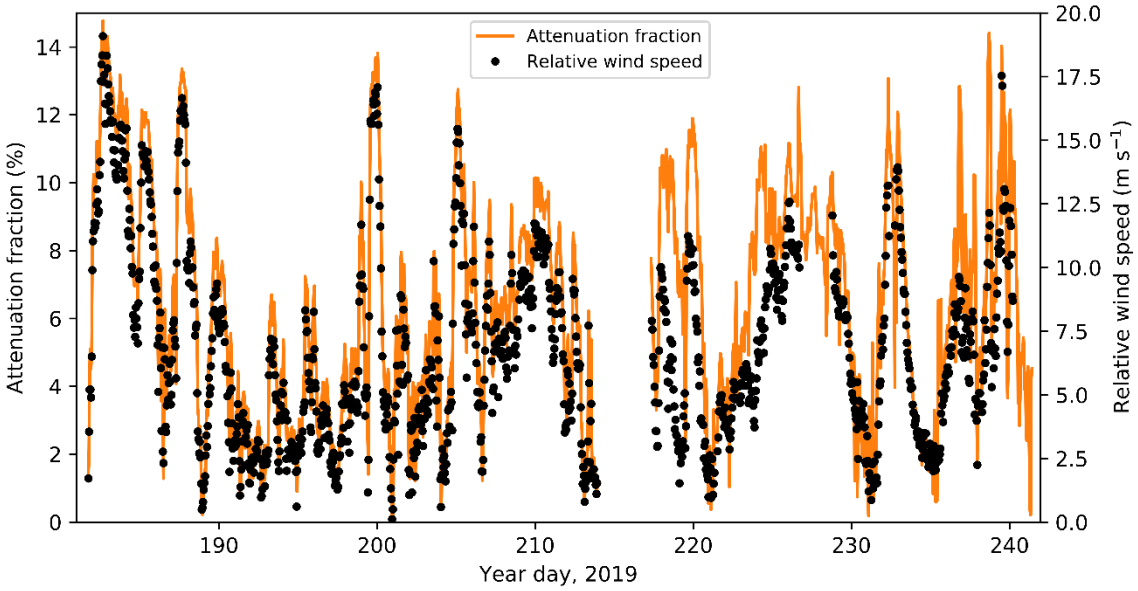

Figure S2.3 Time series of flux attenuation fraction and relative wind speed for two Arctic cruises. The gap in data between year days 213 and 217 is due to the break between cruise JR18006 and JR18007.

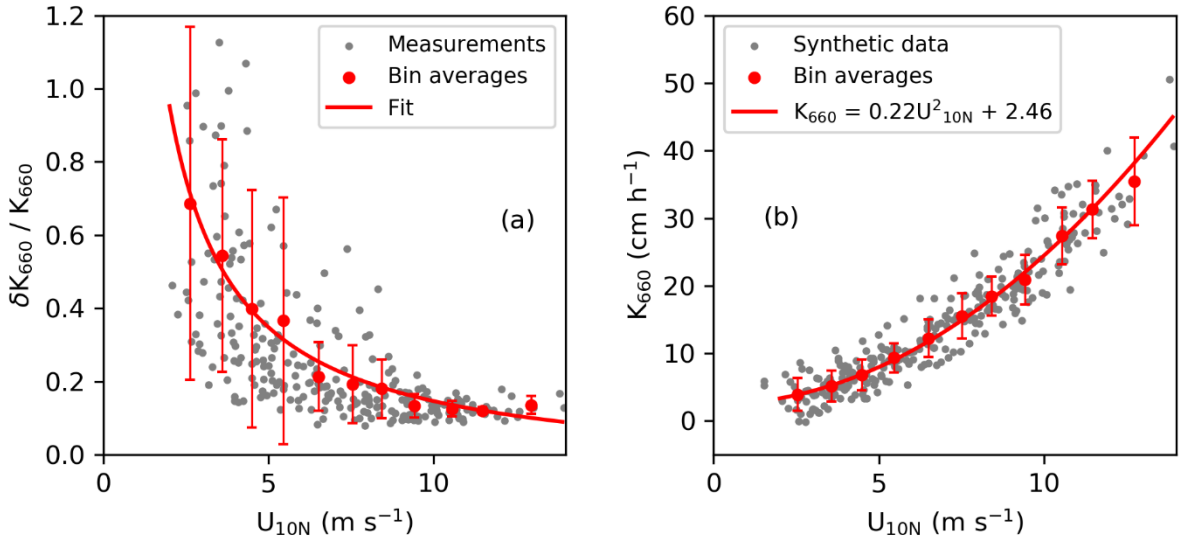

Figure S2.4 (a) Relative uncertainty in the gas transfer velocity (K_{660}) due to the uncertainty in the EC flux, and (b) the synthetic K_{660} data versus wind speed. Red circles in panel (a) represent the 1 m s^{-1} bin averages of the relative uncertainty data with error bars representing standard deviation. The red curve in panel (a) represents a least square fit: $\frac{\delta K_{660}}{K_{660}} = 1.83 \times U_{10N}^{-1} - 0.036$ (R^2 = 0.36). Red circles in panel (b) represent the 1 m s^{-1} bin averages of the synthetic K_{660} with error bars representing standard deviation. The red curve in panel b represents the quadratic fit of the K_{660} from the cruise JR18007.

EC CO_2 flux data quality control: The overall aim of the quality control process is to remove data during periods when conditions were clearly unfavourable for EC measurements. These include excessive ship manoeuvres (invalidating motion correction of winds), winds from the stern sector (large flow distortion and contamination in CO_2 signal from ship exhaust), and large variability in winds and CO_2 (non-stationary). We do not attempt to filter spectrally for poorly resolved irregularities at low frequencies because the CO_2 cospectra tend to be very noisy. Given a large enough dataset, such low-frequency variability should mostly average out. The specific filtering criteria are similar to Blomquist et al., 2014 and Blomquist et al., 2017, and are listed in Table S2.1.

Table S2.1 Filtering criteria (within 20 minutes averaging intervals) of EC fluxes for two Arctic cruises (the criteria for AMT cruises are similar to Arctic cruises). The right column points out the number of segments (percentage) of valid flux data which satisfy the filtering criteria at each stage of the quality control sequence.

	Criteria	Segments (percentage) passed	
		JR18006	JR18007
Wind	Standard deviation in ship heading < 40° Range in ship heading < 60° Change in ship heading between two adjacent segments < 60° Standard deviation in ship speed < 1 m s^{-1} Change in ship speed between two adjacent segments < 1.5 m s^{-1}	1923 (83.0)	1356 (78.6)
	| Relative wind direction | < 140°	1813 (78.3)	1318 (76.4)
	Standard deviation in Relative wind direction < 40°	1802 (77.8)	1300 (75.4)
	Tilt in wind speed < 10°	1741 (75.2)	1283 (74.4)
CO_2	Range in CO_2 mixing ratio < 2 ppm | Trend in CO_2 mixing ratio | < 2 ppm h^{-1}	1419 (61.3)	1224 (71.0)
CO_2 flux	Valid wind and CO_2	1741 (75.2)	1283 (74.4)
	| Horizontal flux | < 0.08 ppm m s^{-1}	1375 (59.4)	1199 (69.5)

S3 Eddy covariance observations in the Arctic

Text S3.1 Bulk sensible heat flux

The air-sea sensible heat flux (F_S, W m^{-2}) is usually estimated by the bulk equation:

$$F_S = \rho_a c_{pa} K_H (T_w - T_a) \quad \text{(S3.1)}$$

where ρ_a (kg m^{-3}) is the density of dry air, c_{pa} (J kg^{-1} K^{-1}) is the heat capacity of air, K_H (cm h^{-1}) is the sensible heat transfer velocity, T_w (K) is the sea surface temperature and T_a (K) is the air temperature. Air-sea heat exchange is controlled on the airside of the interface (Yang et al., 2016c). T_w thus corresponds to the ocean skin temperature ($T_{w\_surface}$), which is generally lower than the subskin and the bulk water temperature by a few tenths of a degree (Donlon et al., 2002). This cool skin effect (dT), due mostly to longwave and latent heat loss to the atmosphere, can be estimated using the COARE 3.5 model (Edson et al., 2013; Fairall et al., 1996). In practice, T_w is generally derived from bulk seawater measurements either from the ship's underway system or from sensors mounted at the underway inlet at ~6 m depth. The upper several meters of the ocean (beneath the cool skin) is usually assumed to be homogeneous in bulk flux calculations (i.e., $T_w = T_{w\_surface} = T_{w\_bulk}$ - dT).

Text S3.2 Eddy covariance

The EC air-sea CO_2 flux calculation equation is:

$$F_{CO_2\_EC} = \rho_a \overline{w'c'} \quad \text{(S3.2)}$$

where c is the dry CO_2 mixing ratio (ppm); and w is the vertical wind velocity (m s^{-1}). The prime denotes fluctuations from the mean, while the overbar indicates a time average.

The EC air-sea sensible heat flux calculation equation is:

$$F_{S\_EC} = \rho_a c_{pa} \overline{w'T_s'} + F_{L\_C} \quad \text{(S3.3)}$$

where T_s is the sonic temperature (K). F_{L_C} is the latent heat correction accounting for the difference between the air temperature (T_a) and T_s.

$$F_{L\_C} = \frac{-0.51\, T_a\, F_L\, c_{pa}}{10^6[2.501 - 0.00237(T_a - 273.15)]} \quad \text{(S3.4)}$$

where T_a (K) is the air temperature, and F_L (in W m^{-2}) is the latent heat flux estimated by the COARE 3.5 model (Edson et al., 2013). The denominator is the latent heat of evaporation. For the sea ice stations, the water temperature (T_w) and thus the latent heat flux was unavailable.

Therefore, in regions with sea ice, the (small) latent heat correction is not applied in the derivation of EC sensible heat flux.

Text S3.3 Instrumental setup

A high-precision closed-path gas analyser (Picarro G2311-f) with a Nafion dryer was used to determine the dry CO_2 mixing ratio. A Metek sonic anemometer was used to measure the wind velocity (u, v, w) and sonic temperature (Ts). Ship motion was characterized by three-dimensional rotational rates and acceleration rates using a motion sensor. The CO_2, wind, and motion measurements were all made at a frequency of 10 Hz. The EC system was installed on the foremast at 20 m above mean sea level (AMSL) to minimise airflow distortion. A complementary filtering method (Edson et al., 1998) was used to remove apparent winds generated by ship movements. Further decorrelation against ship motion and double rotation were used to yield the vertical wind velocity required in the EC flux calculation. The CO_2 mixing ratio data were further decorrelated against analyser cavity pressure and temperature, ship's heave and acceleration to remove spurious CO_2 sensitivity to ship motion. The CO_2 sampling delay and high-frequency CO_2 flux attenuation due to the use of a closed-path instrument with an inlet and dryer were estimated by a nitrogen (N_2) 'injection' system on JCR every six hours. Fluxes were initially calculated in 20 min averaging intervals, and the flux was filtered for non-ideal ship manoeuvers and violations of the homogeneity/stationary requirement of EC. The quality controlled 20 min fluxes were further averaged to 1 h fluxes to reduce random uncertainty. For a more detailed description of all of the above, please see (Dong et al., 2021a).

Underway seawater measurements on the JCR include temperature (T_{w_bulk}) and salinity (Seabird, SBE48), at ~6 m depth. Underway CO_2 mole fraction (xCO_{2w_eq}) was measured on JR18007 by a non-dispersive infrared detector (LI-COR, LI-840) following 'vented-showerhead' equilibration of the seawater from the same depth (PML-Dartcom live pCO_2 system; Kitidis et al., 2017). The CO_2 mole fraction was then converted into CO_2 fugacity (fCO_{2w_equ}) using the water temperature (T_{eq}), salinity and air pressure in the equilibrator. The equilibrator CO_2 fugacity was then corrected to the bulk seawater temperature (fCO_{2w_bulk}) via the empirical temperature relationship of Takahashi et al. (1993):

$$fCO_{2w\_bulk} = fCO_{2w\_eq}\exp\left[0.0423\left(T_{w\_bulk} - T_{eq}\right)\right] \quad \text{(S3.5)}$$

The system performed an hourly cycle of measurements through equilibrated seawater, three non-zero CO_2 standards and atmospheric measurements (xCO_{2a}, from an air intake on the

bridge wing at 16 m above mean sea level, AMSL). Atmospheric measurements, including air temperature (T_a), pressure (P) and relative humidity (RH), were taken from the JCR meteorological platform (20 m AMSL).

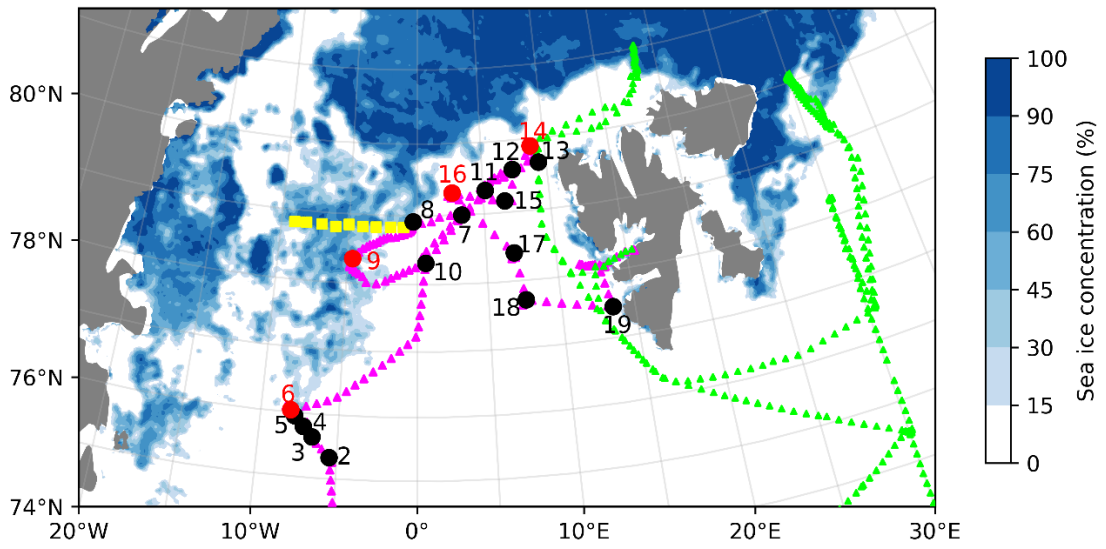

Figure S3.1 Cruise tracks of JR18006 (green, from and to Aberdeen, UK) and JR18007 (magenta, from Harwich, UK to Svalbard). The red points represent CTD stations with near-surface stratification while the black points indicate non-stratified stations during cruise JR18007. Yellow squares represent fCO_{2w} data calculated from DIC and TA measurements in the upper 10 meters from the FS2019 cruise. The background indicates the daily sea ice concentrations from the Advanced Microwave Scanning Radiometer-Earth Observing System (AMSR-E, Spreen et al., 2008) on 1 August 2019.

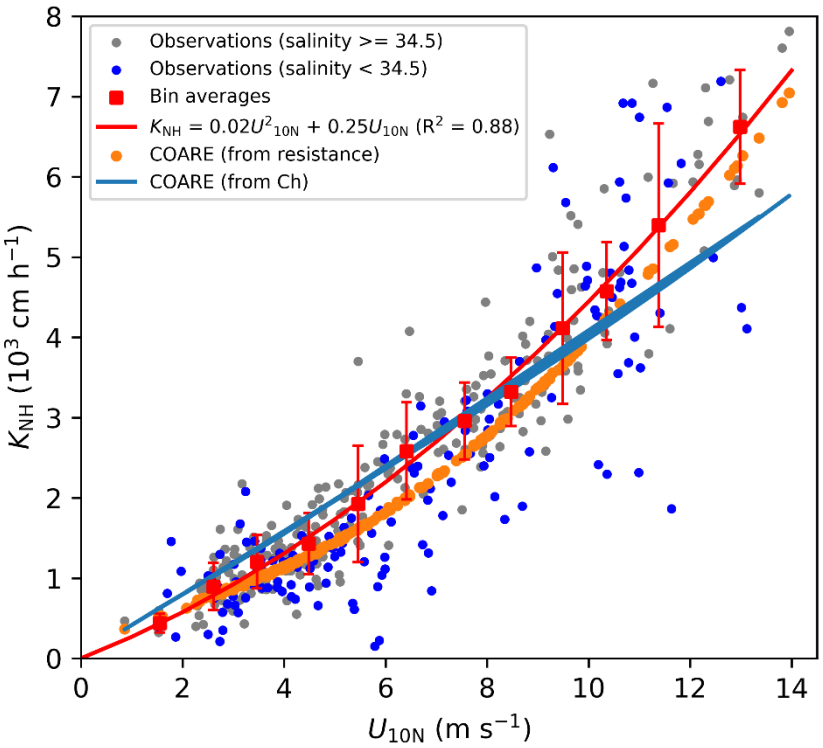

Figure S3.2 Relationship between heat transfer velocity under neutral conditions (K_{NH}) derived from EC measurements and wind speeds during JR18006 and JR18007. To ensure a sufficient signal-to-noise ratio, only values for $|T_w - T_a| > 1$ K are shown. Grey points represent the K_{NH} at high salinity (≥ 34.5‰), and blue points represent K_{NH} at low salinity (< 34.5‰). Red squares indicate 1 m s^{-1} bin averages of the grey points with error bars representing 1 standard deviation. The red curve corresponds to a quadratic fit using the bin averages (10^3 cm h^{-1}). Two different parameterisations of K_{NH} from the COARE3.5 model (Edson et al., 2013) are also shown, from the sensible heat transfer coefficient Ch and based on atmospheric resistance. The observed K_{NH} from JR18006 and JR18007 show a wind speed dependence that is more similar to the resistance-based parameterisation from COARE3.5.

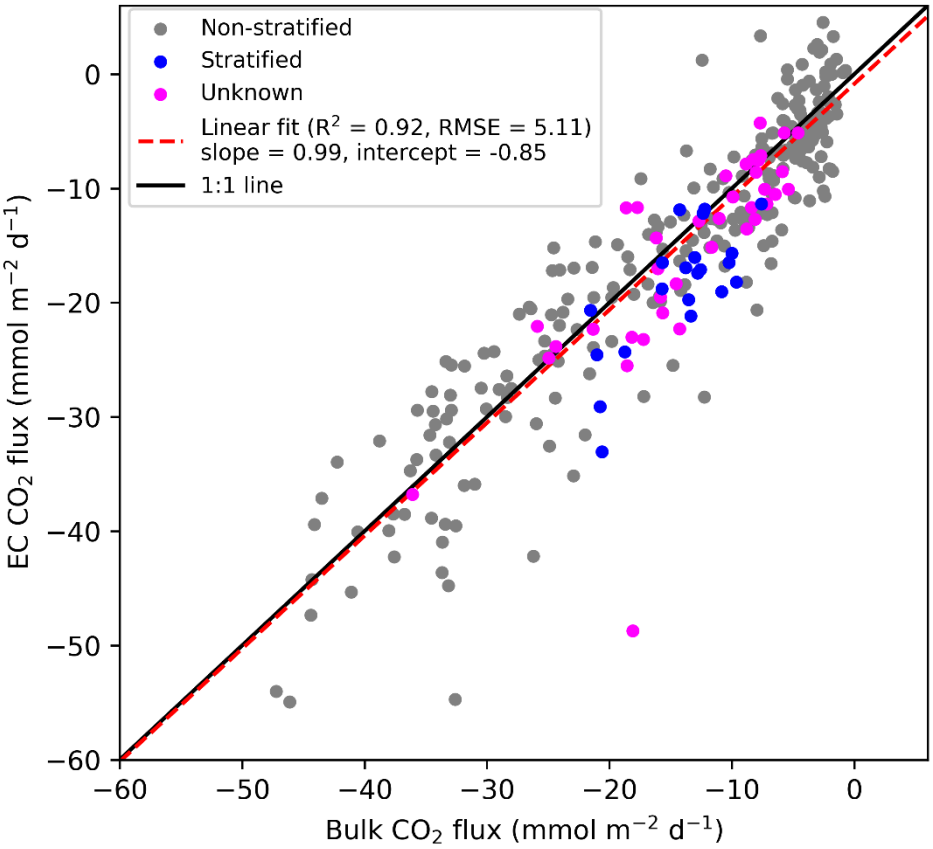

Figure S3.3 Comparison between eddy covariance air-sea CO_2 flux and bulk CO_2 flux. The Nightingale et al. (2000) gas transfer velocity parameterisation is used for the bulk CO_2 flux calculation. The grey, blue and magenta points represent flux measurements in non-stratified waters, stratified waters, and waters with 'unknown' stratification status, respectively. The dashed line corresponds to the linear fit using non-stratified points. The average of the difference between the bulk CO_2 flux (-15.3 mmol m^{-2} d^{-1}) and the EC CO_2 flux (-16.0 mmol m^{-2} d^{-1}) is 0.7 ± 2.0 mmol m^{-2} d^{-1} (i.e., bulk flux – EC flux) and the relative difference is 4% (0.7 mmol m^{-2} d^{-1} / 16 mmol m^{-2} d^{-1} *100%). For the stratified waters, the average of the difference between the bulk CO_2 flux (-14.3 mmol m^{-2} d^{-1}) and the EC CO_2 flux (-18.4 mmol m^{-2} d^{-1}) is 4.1 ± 3.5 mmol m^{-2} d^{-1} with 22% relative difference.

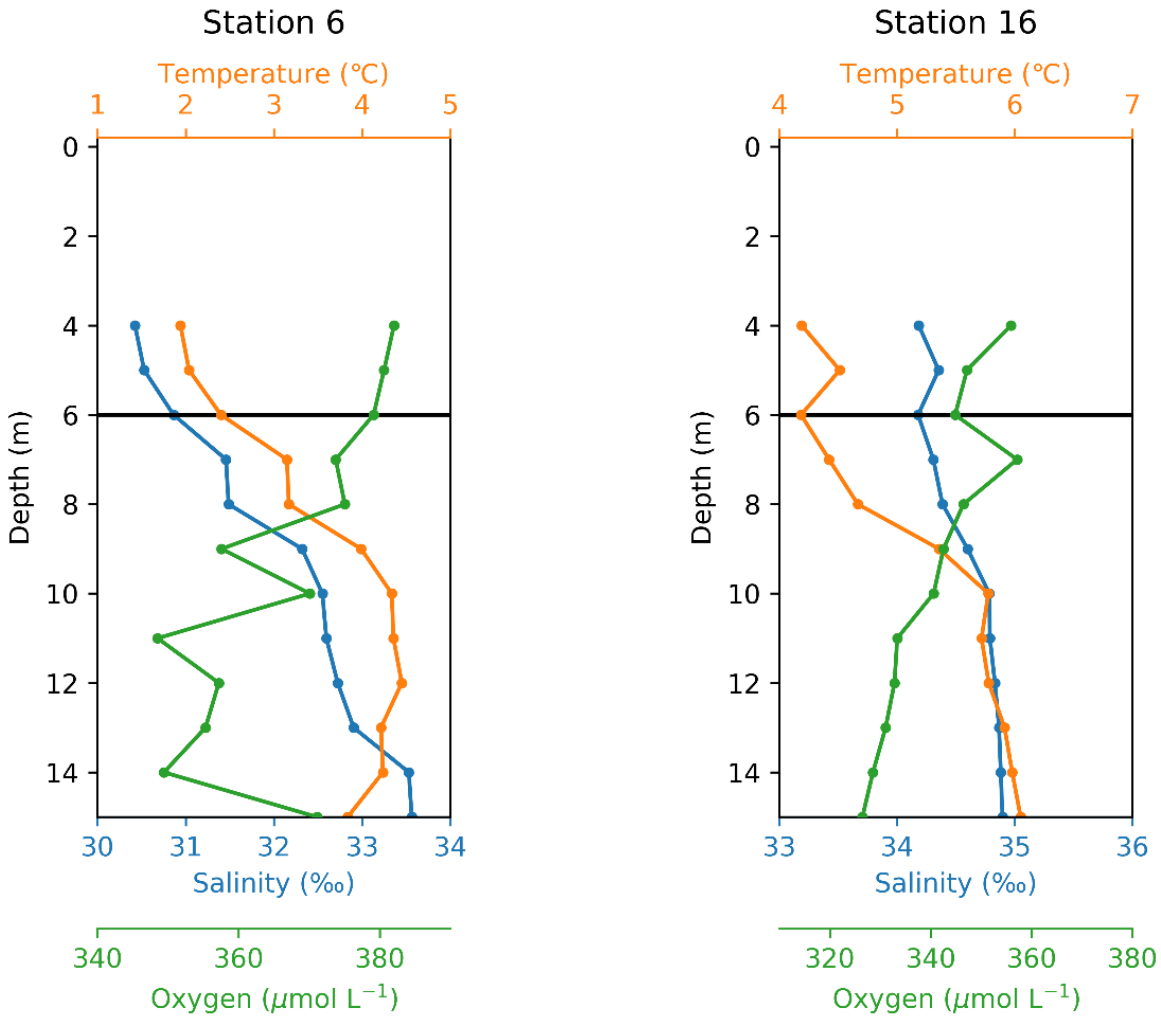

Figure S3.4 Salinity (blue line), temperature (orange line), and oxygen (green line) profiles of stations 6 and 16 (see Figure S3.1) from CTD down casts during cruise JR18007. Temperature and salinity tend to decrease close to the surface while the oxygen concentration increases near the surface.

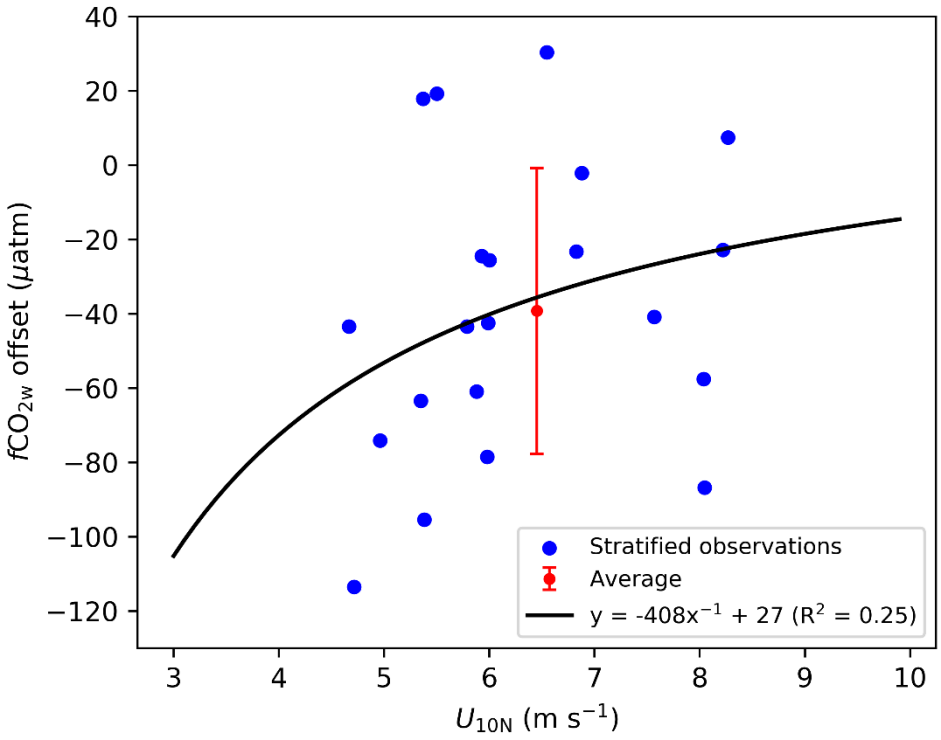

Figure S3.5 fCO_{2w} offset (EC implied $fCO_{2w\_surface}$ minus fCO_{2w_bulk}) versus neutral wind speed (U_{10N}) for stratified waters. The black line represents a power function fit using the stratified observations (blue points). We assume that this power function works when the wind speed is higher than 3 m s^{-1} and that the fCO_{2w} offset is constant (-109 µatm) when the wind speed is less than 3 m s^{-1}. The red point corresponds to the average of the fCO_{2w} offset in the stratified regions with the error bar representing 1 standard deviation. The wind speed-dependent fCO_{2w} offset and the constant fCO_{2w} offset (-39 µatm) is applied in Section 3.3.4.

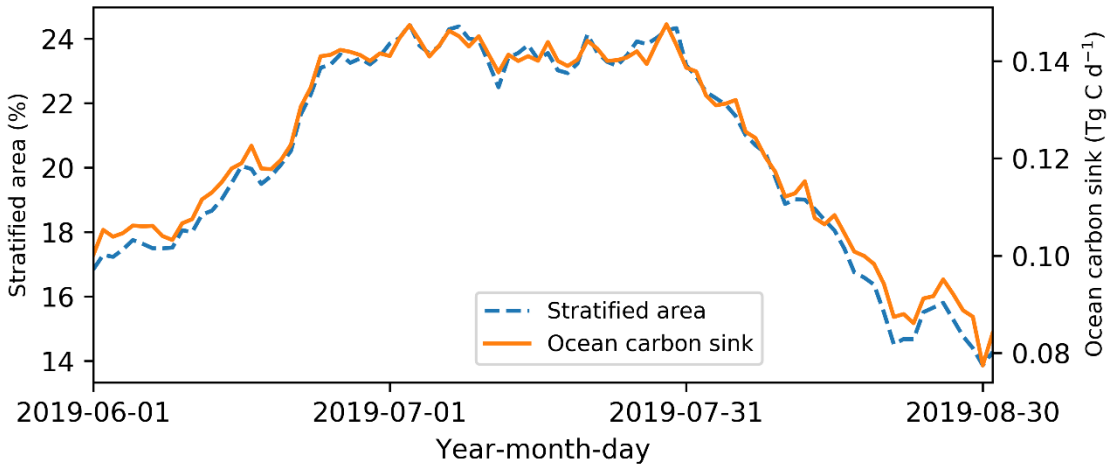

Figure S3.6 Time series of Arctic summer near-surface stratification and estimated impact on carbon uptake by the ocean. Blue dashed line: estimated stratified area due to sea ice melt expressed as a percent of the entire Arctic Ocean (1.4×10^7 km^2). Orange solid line: potential underestimation of Arctic Ocean carbon uptake resulting from sea ice melt and the resultant near- surface fCO_{2w} gradient.

Table S3.1 Quadratic fits between wind speed (U_{10N}) and K_{660} derived from EC CO_2 flux and ΔfCO_2 ($fCO_{2w\_bulk} - fCO_{2a}$) observations during JR18007. K_{660} and U_{10N} are grouped into 1 m s^{-1} bin. The bin averages are used to make the quadratic fit for all three data types in the table. R^2 is the determination coefficient for fits of hourly K_{660} data. Numbers in parentheses indicate the total number of hourly K_{660} data within each category.

Data category	Quadratic fit	R^2
All data (298)	$K_{660} = 0.219\ U_{10N}^2 + 2.549$	0.777
Non-stratified data (239)	$K_{660} = 0.220\ U_{10N}^2 + 2.213$	0.801
Stratified data and those with unknown stratification status (59)	$K_{660} = 0.242\ U_{10N}^2 + 2.734$	0.581

Table S3.2 DIC and TA measurements during cruise FS2019 from 2 to 5 September 2019 nearby Fram Strait (Figure S3.1).

Latitude	Longitude	Depth [m]	salinity	TA [µmol kg^{-1}]	DIC [µmol kg^{-1}]
78.83	-1.00	5	31.28	2098	1940
78.83	-1.96	6	31.21	2124	1982
78.83	-3.01	6	30.82	2123	2001
78.83	-4.01	5	30.98	2114	1981
78.85	-5.02	5	30.25	2102	1985
78.81	-6.00	5	29.64	2054	1949
78.83	-7.00	5	29.86	2079	1970
78.84	-8.15	5	30.72	2109	1986
78.83	-9.02	5	30.59	2096	1973

S4 Eddy covariance observations in the Southern Ocean

The basic information of the seven cruises with eddy covariance (EC) observations is summarized in Table S1. The seven cruises took place from 2019 to 2021 on the research vessel RRS *James Clark Ross* (JCR; JR18004, JR18005, JR19001, JR19002, and JR30001) and RRS *Discovery* in the Pacific sector (DY111, DY113). The setup of the EC systems on both ships can be found in Dong et al. (2021a) and Yang et al. (2021). Detailed information for these seven cruises can be found in the cruise reports available by searching the cruise name on the website of the British Oceanographic Data Centre (https://www.bodc.ac.uk/). JR30001 is a long cruise which includes several successive short cruises in the Southern Ocean. The cruise report of JR30001 is not yet available, but the EC system and the underway system are the same and have the same configuration as the systems used on other cruises on the JCR.

The three-dimensional (3D) sonic anemometer plus a motion sensor (IMU – Systron Donner MotionPak II or LPMS) were deployed on the top of the bow mast. The motion sensor is used to detect ship motions and a motion correction is applied to the 3D wind signals to obtain the true wind velocity following the principles of Edson et al. (1998). All of these cruises used a closed-path gas analyser plus a dryer (to remove water vapour fluctuations) to measure the EC flux, which is recommended for having reliable EC air-sea CO_2 flux measurements (Blomquist et al., 2014; Landwehr et al., 2014; Miller et al., 2010; Nilsson et al., 2018). The EC systems on JCR used a Picarro G2311-f cavity ring-down spectrometer (Picarro Inc., Santa Clara, California, USA) as the gas analyser, while the EC system based on *Discovery* used a LI-7200 (LICOR Biosciences, Lincoln, Nebraska, USA) infrared gas analyser. Dong et al. (2021a) confirmed that both G2311-f and LI-7200 are reliable for EC air-sea CO_2 flux observations.

In addition, underway seawater measurements (sea surface temperature, salinity, and seawater CO_2 fugacity) and atmospheric measurements (air temperature, pressure, relative humidity, and atmospheric CO_2 fugacity) were also made during all of these cruises.

Table S4.1. Basic information for the seven Southern Ocean cruises on which air-sea EC CO_2 fluxes were measured.

Cruise names		Platform	Sonic anemometer	Gas analyser	Date and time (hours with at least 40 minutes, days with at least 4 hours)	Reference
JR	18004	RRS *James Clark Ross* (JCR)	Metek uSonic-3 Scientific + motion sensor	G2311-f + dryer	11 Jan.–15 Feb. 2019 (531, 31)	(Dong et al., 2021a; Yang et al., 2021)
	18005				24 Feb.–14 Apr. 2019 (884, 48)	
	19001				6 Nov.–26 Dec. 2019 (552, 36)	
	19002				27 Dec. 2019–7 Mar. 2020 (372, 29)	
	30001				1 Dec. 2020–4 Apr. 2021 (313, 17)	
DY	111	RRS *Discovery*	Gill R3-50	LI-7200 + dryer	2 Dec. 2019–2 Jan. 2020 (297, 23)	(Dong et al., 2021a)
	113				5 Feb.–12 Mar. 2020 (250, 24)	
In total	3370 hours with at least 40 min in one hour, 221 days with at least 4 hours. After removing measurements in regions with sea-ice coverage and coastal oceans, 2567 hours (175 days) EC CO_2 flux observations are used for further analysis.					

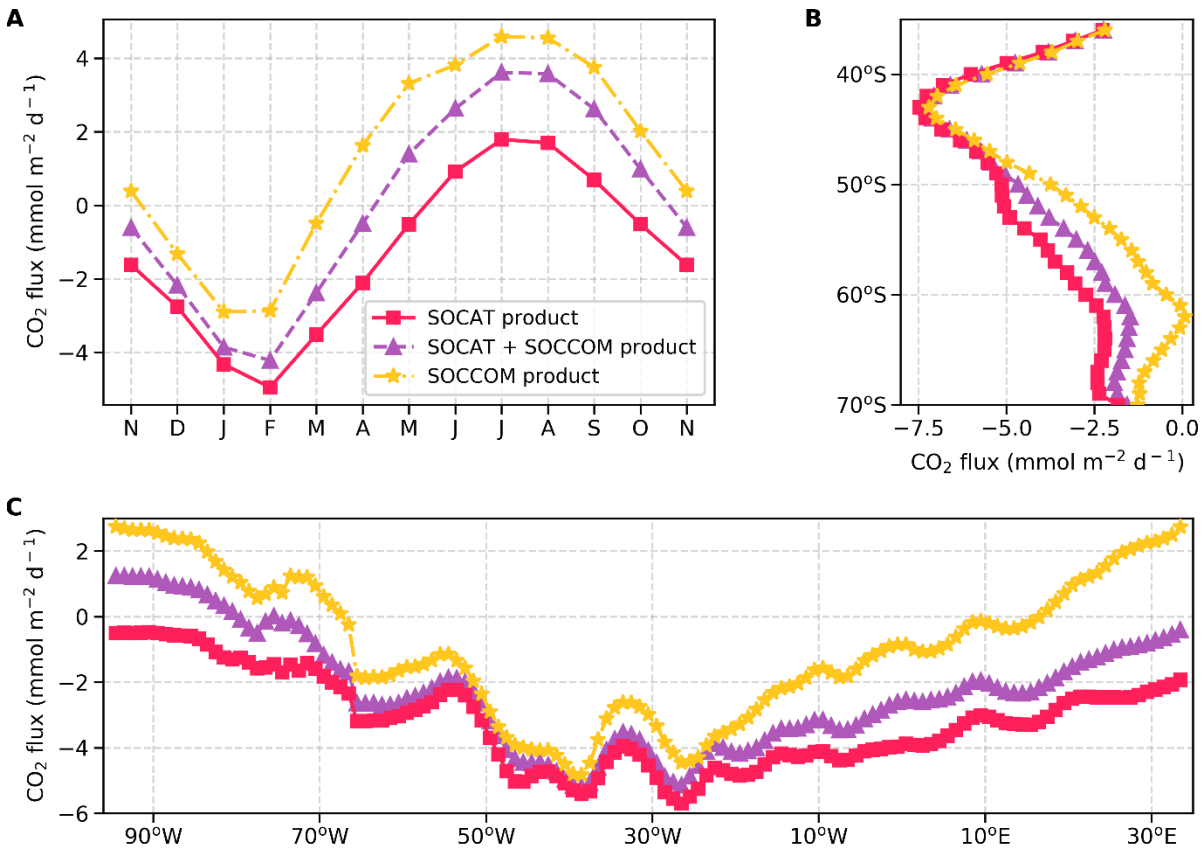

Figure S4.1 Monthly, latitudinal, and longitudinal variations of the Southern Ocean CO_2 flux from three neural network-based flux products (Landschützer et al., 2016; Bushinsky et al., 2019) on average from 2015 to 2020. The red, purple, and yellow lines represent SOCAT-based, SOCAT plus SOCCOM-based, and SOCCOM-based flux products, respectively. (A) Monthly averaged CO_2 flux from three products of a Southern Ocean region (longitude between 95°W and 35°E and latitude < 35°S). (B) Latitudinal variation of the CO_2 flux from three products in the summertime Southern Ocean (longitude between 95°W and 35°E). (C) Longitudinal variation of the CO_2 flux from three products in the summertime Southern Ocean (latitude < 35°S).

S5 Temperature corrections for global ocean CO_2 flux estimates

Text S5.1 Conversion of CO_2 concentration

The mole fraction of the equilibrated CO_2 (χCO_{2w}) in the equilibrator is measured by a gas analyser and is then converted into CO_2 partial pressure (pCO_{2w_equ}) using the equilibrator temperature (T_{equ}, K) and pressure (P_{equ}, atm):

$$pCO_{2w\_equ} = \chi CO_{2w}\left(P_{equ} - pH_2O\right) \quad \text{(S5.1)}$$

where pH_2O (atm) is the water vapour pressure and can be calculated from T_{equ} and the seawater salinity (Pierrot et al., 2009). The pCO_{2w_equ} is then converted into fCO_{2w_equ} to correct for the non-ideal behaviour of the gas (Weiss, 1974):

$$fCO_{2w\_equ} = \gamma\, pCO_{2w\_equ} \quad \text{(S5.2)}$$

where the fugacity coefficient γ is ~0.996 (Bakker et al., 2014).

Text S5.2 The Timescale of chemical repartitioning and water mass transport

The seawater carbonate system creates unique properties for air-sea CO_2 exchange. The seawater carbonate system includes several different carbonate species, i.e., CO_2, carbonic acid, bicarbonate, and carbonate. Among these species, only CO_2 is directly involved in the air-sea CO_2 exchange. There is a dynamic equilibrium between these carbonate species. When the seawater temperature varies, these carbonate species repartition and gradually approach a new equilibrium. The relaxation time (the time after which a perturbation has reached e^{-1} of its initial value) for this equilibration depends on pH and temperature. For typical seawater (pH ~8.2, total dissolved inorganic carbon ~2000 μmol kg^{-1}, and salinity ~35) at ~25°C, the relaxation time is ~13 s (Johnson, 1982; Zeebe & Wolf-Gladrow, 2001). For warmer seawater (e.g., ~30°C), the relaxation time is shorter (~11 s) (Johnson, 1982; Zeebe & Wolf-Gladrow, 2001), while for colder seawater, the relaxation time is longer. Therefore, the timescale of the chemical repartitioning of the CO_2 system is at least 10 s. i.e., if the seawater temperature varies, more than 10 s is required for the carbonate species to approach equilibrium.

There is a temperature gradient in the thermal boundary layer (TBL), and the temperature at the top of the TBL is lower than that at the bottom of the TBL due to the cool skin effect. The typical thickness of the TBL (L) is 1 mm (Jähne, 2009). The mass boundary layer (MBL) is at the top of the TBL with a typical thickness of 0.1 mm (Jähne, 2009). Molecular diffusion dominates water mass transport within MBL. There is a viscous boundary layer (VBL) below

the MBL and the VBL has a similar thickness as the TBL (i.e., L ~1 mm) (Jähne, 2009). Viscous dissipation dominates water mass transport in the VBL (Jähne, 2009). The kinematic viscosity (v) is ~1 $mm^2\ s^{-1}$ at 25°C seawater (v is larger at colder seawater). So, the timescale of water mixing in the TBL (below the MBL) is ~1 s (L^2 / v).

Text S5.3 SST dataset for air-sea CO_2 flux estimates

The SST data used for flux estimates differ between studies. Table S5.1 lists SST datasets used in eight global observation-based (i.e., fCO_2-based) air-sea CO_2 flux estimates. Within a specific study, the same global gap-free SST dataset is typically used for the calculation of Schmidt number, Sc, solubility at the base of the MBL, α_w, and at the air-sea interface, α_i, CO_2 fugacity in the atmosphere, fCO_{2a}, and for the fCO_{2w} mapping, while the *in-situ* bulk water temperature (T_{Bulk}) measured concurrently with fCO_{2w} is used for correcting individual fCO_{2w} from the equilibrator temperature to the seawater temperature.

An exception to the above is Watson et al. (2020), which co-located the DOISST v2.0 (1° × 1°, monthly data) (Reynolds et al., 2007) to the individual fCO_{2w} measurements in SOCAT (Goddijn-Murphy et al., 2015). The co-located DOISST v2.0 was used to re-calculate fCO_{2w} (via Equation 5.2 in the main text). Watson et al. (2020) showed that SOCAT SST is on average 0.13 ± 0.78 K higher than the co-located DOISST v2.0, and the SOCAT fCO_{2w} is on average 1.65 ± 11.98 µatm higher than the re-calculated fCO_{2w}. Watson et al. (2020) and this study are the only two studies that considered the cool skin effect. Watson et al. (2020) applied a constant cool skin correction (0.17 K) to the satellite subskin SST product (i.e., DOISST v2.0 minus 0.17 K) for the calculation of α_i and fCO_{2a}. In addition, Watson et al. (2020) used HadISST for the mapping process instead of the SST product used to calculate the other variables (i.e., DOISST v2.0).

As discussed in the main text, a global gap-free $T_{Subskin}$ product is an important practical SST for air-sea CO_2 flux calculation. However, only some of the global gap-free SST products in Table S5.1 (MOISST v2, DOISST v2.0, OAFlux, and CCI SST v2.1) represent the subskin temperature, while the others (ASMD, ARMOR3D, MGDSST, HadISST) correspond to the temperature of bulk seawater.

Text S5.4 Comparison of three satellite SST products

The satellite SST product is expected to provide a consistent subskin temperature which can be used for calculating global Sc, α_w, α_i, and fCO_{2a}, and for mapping fCO_{2w}. Recent research

compared eight global gap-free satellite/blend SST products (ESA CCI SST v2.0, ERA5, HadISST1, DOISST v2.1, MUR25 v4.2, MGDSST, BoM Monthly SST, OSITASST) and showed that the global mean of these eight SST products ranges from 20.02 °C to 20.17 °C (for the period 2003-2018 with 95% confidence level) (Yang et al., 2021). So, a bias potentially exists in some or all of these satellite SST products. In addition, among these eight satellite SST products, only the CCI SST (Merchant et al., 2019; Merchant & Embury, 2020) and the DOISST (Huang et al., 2021; Reynolds et al., 2007) represent the subskin temperature (Yang et al., 2021). The other SST products provide a bulk temperature for a depth below the subskin. So, hereafter, only the CCI SST and the OISST (DOISST and MOISST) are assessed.

There are two types of OISST products: 1) 1° × 1°, monthly OI.V2 SST (MOISST), which is derived by linear interpolation of the 1° × 1°, weekly OI.v2 SST fields to daily fields which are then averaged over a month (Reynolds et al., 2002); 2) 1/4° × 1/4°, daily OISST v2 (Reynolds et al., 2007) which has been replaced by DOISST v2.1 (Huang et al., 2021) with some quality improvements for data from January 1, 2016, onwards. DOISST data are constructed differently than the MOISST, although both use satellite-derived SST data with a calibration based on *in-situ* measurements (including both ICOADS ship and drifting buoy SST) (Freeman et al., 2017; Xu & Ignatov, 2014). With the warm bias in the ICOADS ship SST well-recognized by the SST community (Huang et al., 2017; Kennedy et al., 2011, 2019), a constant (0.14 K) is subtracted from the ICOADS ship SST to compensate for the large scale (global mean) ship-buoy SST difference (Reynolds & Chelton, 2010) before it is used to calibrate the DOISST v2.0. In addition, the latest research shows that the bias in the ICOADS ship SST has substantially reduced since 2006 (Kennedy et al., 2019). So for the DOISST v2.1 dataset, the ship-buoy SST difference has been set to 0.14 K from 1981 to 2015 and to 0.01 K from 2016 onwards (Huang et al., 2021). However, the warm bias in the ICOADS ship SST is not corrected for when it is used for the calibration of the MOISST. So the DOISST tends to be lower than the monthly MOISST, particularly in the 1980s and 1990s when ship SST data were dominant (Banzon et al., 2016).

Here we test the agreement between the gridded drifting buoy SST (as a reference SST; Xu & Ignatov, 2014) and three satellite SST products: CCI SST v2.1, MOISST v2, DOISST v2.1. Figure S5.1a shows a comparison between different SST products. The DOISST v2.1 is on average 0.09 K lower than the buoy SST (red curve), while the MOISST v2 is on average 0.01 K lower than the buoy SST (blue curve). The orange curve shows that the CCI SST v2.1 is on average 0.05 K lower than the buoy SST.

Although MOISST v2 has the smallest bias, it is an old SST product and has not been updated for a long time. The standard deviation (SD) of MOISST minus the buoy SST (blue line in Figure S5.1b) is larger than that of DOISST v2.1 (or CCI SST v2.1) minus buoy SST (red and orange lines in Figure S5.1b). Therefore, we suggest that the MOISST should better not be used for air-sea CO_2 flux estimates.

The SD of DOISST v2.1 minus the buoy SST is similar to the SD of CCI SST v2.1 minus the buoy SST (red and orange lines in Figure S5.1b). Therefore, both DOISST v2.1 and CCI SST v2.1 can be used for the air-sea CO_2 flux estimates (i.e., calculating global Sc, α_w, α_i, fCO_{2a}, and mapping fCO_{2w}). However, as the *in-situ* SST measurements were employed for the validation process, DOISST and MOISST are not fully independent from the *in-situ* SSTs. The CCI SST is independent of the *in-situ* SST dataset because the CCI SST is not calibrated against *in-situ* SST measurements as a reduced-state-vector optimal estimation algorithm (Merchant et al., 2019) is used instead.

The purple line in Figure S5.1b shows that the SD of CCI SST v2.1 minus DOISST v2.1 is ~0.5 K and decreasing to ~0.4 K in recent years, which suggests that there is a discrepancy between these two satellite SST products. the SD of DOISST v2.0 minus SOCAT SST is ~0.8 K. The large SDs suggest that using any co-located satellite SST products to calculate fCO_{2w} could significantly increase the uncertainty in fCO_{2w} and thus the uncertainty in the estimated air-sea CO_2 flux.

Text S5.5 Under-sampling and inter-annual variation of the bias correction

Due to the limited measurements in SOCAT and buoy SST datasets, especially during the 1980s, many grid cells only have a small number of SOCAT and buoy SST measurements. The number of measurements in grid cells might influence the comparison between the SOCAT SST and the buoy SST. Figure S5.2a shows the under-sampling issue and its influence on the average of SOCAT SST minus buoy SST. If we consider all matched grid cells, the average of SOCAT SST minus buoy SST is ~0.02 K. But if we consider cells with at least 10 measurements, the average of SOCAT SST minus buoy SST is ~0.03 K. However, Figure S5.2b suggests that under-sampling does not significantly influence the latitudinal variation of SOCAT SST minus buoy SST.

Figure S5.3 shows the inter-annual variation of the number of cells with SOCAT measurements and the bias correction for the SOCAT SST. We apply the latitudinal-varying bias correction (red curve in Figure S5.2b) to account for the bias in the SOCAT SST (use buoy SST as the

reference). However, as the number of SOCAT measurements varies with the year, and the measurements in years before 1990 are limited (blue bars in Figure S5.3), we do not consider the inter-annual variation of the latitudinal-varying bias correction. Thus, the same bias correction value is applied to a specific latitude for every year (every month) between 1982 and 2020. However, as the spatial distribution of the SOCAT measurements is different in different years, the annual mean bias correction varies with year (red line in Figure S5.3)

.

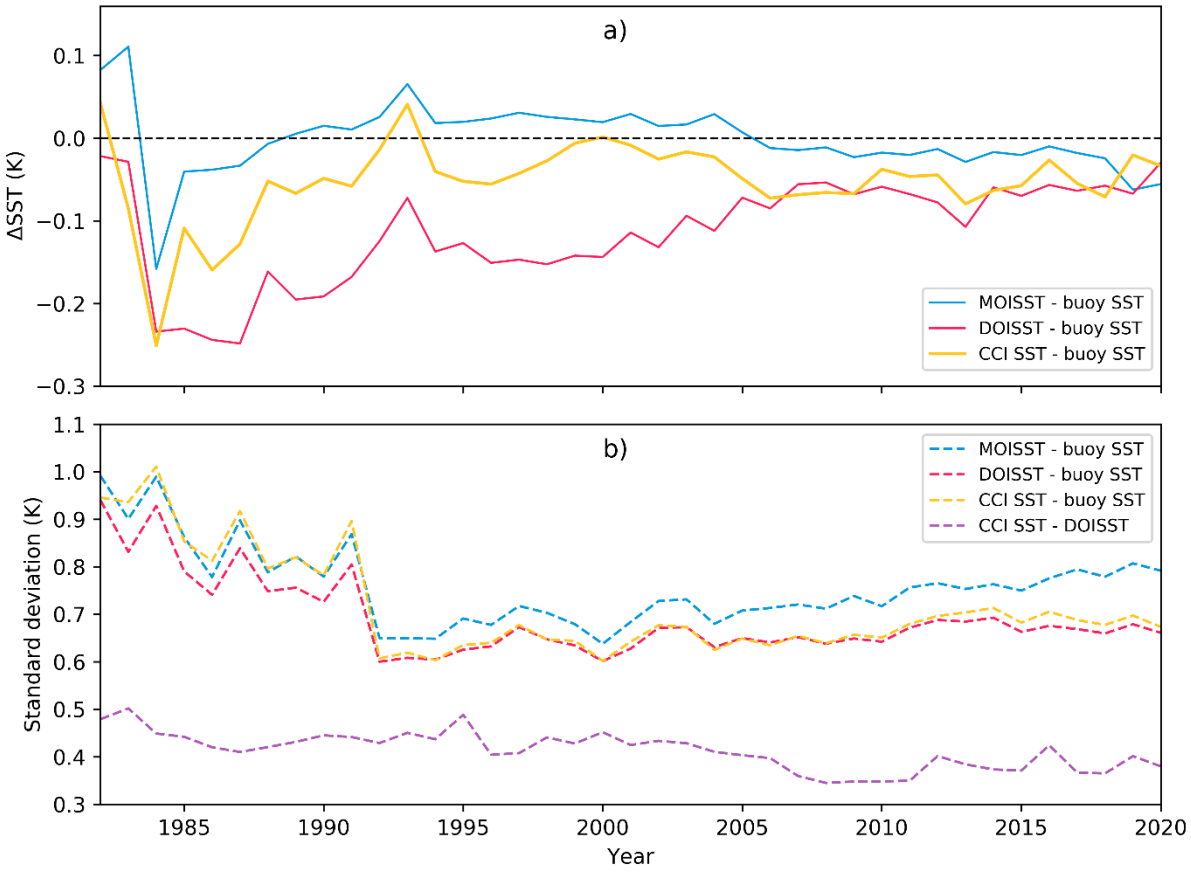

Figure S5.1 Time series of the global annual mean SST difference and its standard deviation between SST products. (a) The blue, red and orange lines represent the MOISST v2 (MOISST) minus drifting buoy SST, DOISST v2.1 (DOISST) minus buoy SST, and ESA CCI SST v2.1 (CCI SST) minus buoy SST, respectively. (b) The blue, red, orange, and purple dashed lines correspond to the standard deviation of MOISST minus buoy SST, DOISST minus buoy SST, CCI SST and buoy SST, and CCI SST minus DOISST, respectively.

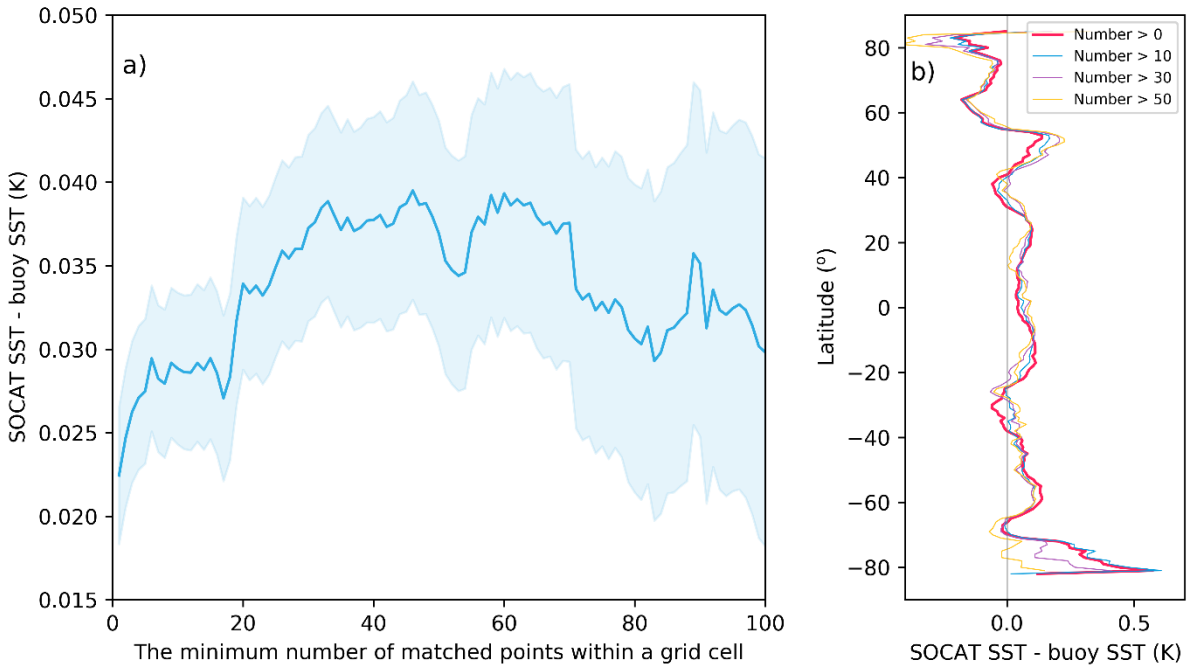

Figure S5.2 (a) Average of SOCAT SST minus buoy SST (from 1982 to 2020) versus the minimum number of matched points within a grid cell, and (b) the latitudinal variation of SOCAT SST minus buoy SST. The first (second) point in (a) represents the average temperature difference considering all grid cells with at least one (two) SOCAT and one (two) buoy measurement (s). The blue shading indicates one standard deviation. The red, blue, purple, and orange lines in (b) correspond to the average temperature difference for grid cells with at least one, eleven, thirty-one, and fifty-one matched SOCAT and buoy measurements, respectively.

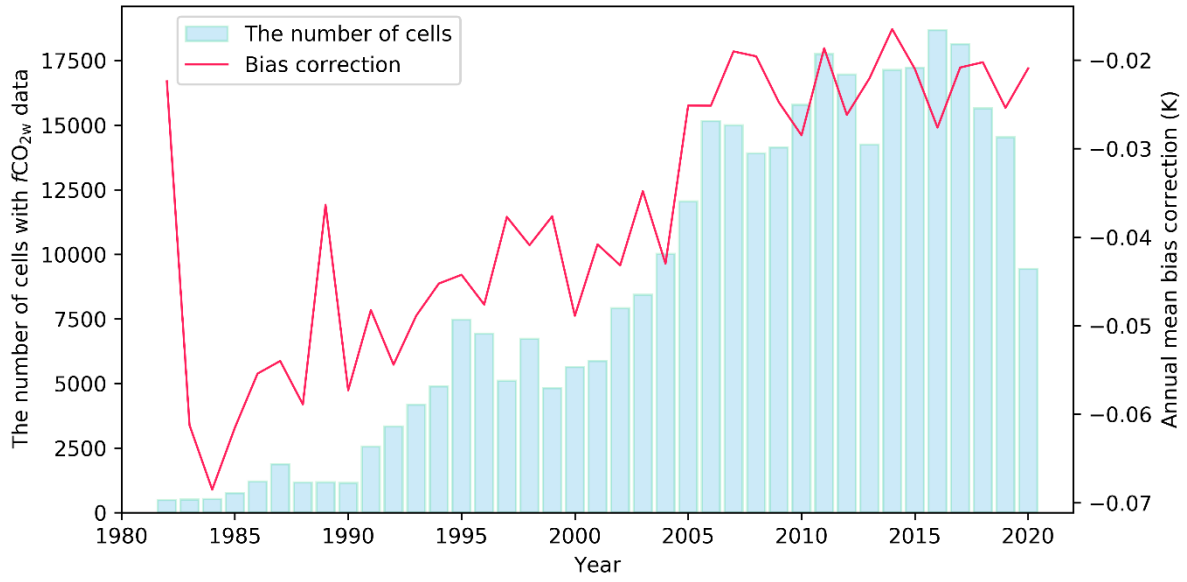

Figure S5.3 The number of grid cells (per year) with measurements in the 1° × 1°, monthly gridded SOCAT data (blue bars) and the inter-annual mean bias correction for the SOCAT SST (red line) assessed by the buoy SST.

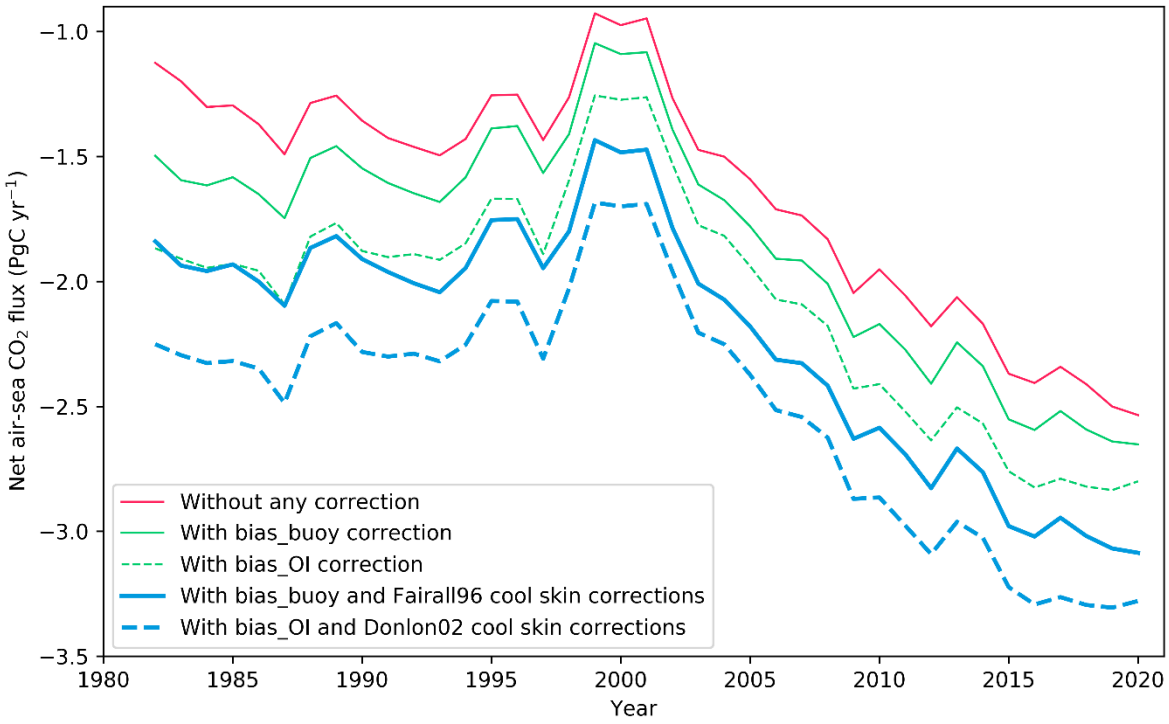

Figure S5.4 Time series of the annual mean global net air-sea CO_2 flux calculated by interpolating the sea surface CO_2 fugacity (fCO_{2w}) data in SOCATv2021 using a neural network-based method (Landschützer et al., 2013). Negative values represent ocean CO_2 uptake. The red, green, and blue solid lines represent the uncorrected flux, the flux with bias_buoy correction (bias assessed by buoy SST), and the flux with bias_buoy and Fairall96 cool skin corrections, respectively (this study). The green and blue dashed curves correspond to the flux with the bias_OI (using co-located DOISST v2.1 to account for the bias in SOCAT SST) and Donlon02 cool skin corrections (Watson et al., 2020). The same datasets, the interpolation method (Landschützer et al., 2013), and the Arctic and the coastal flux compensation method (Fay et al., 2021) are used for the flux calculations in the figure.

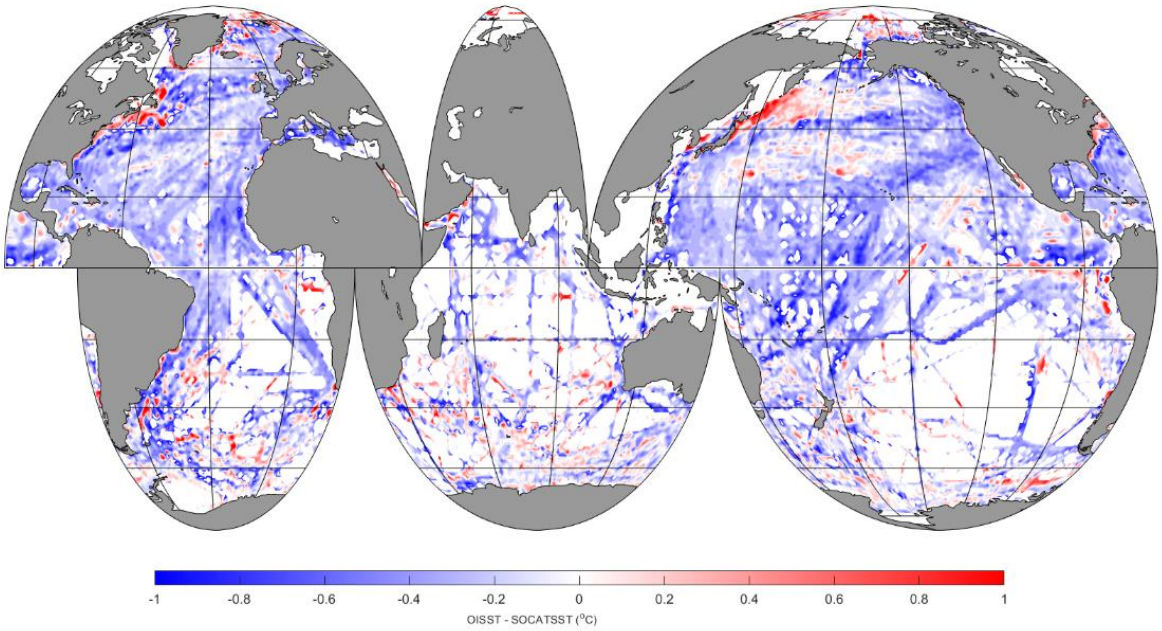

Figure S5.5 Mean difference between the OISST and the gridded SOCAT SST for 1982 to 2020. The positive (negative) value represents the OISST is higher (lower) than the SOCAT SST.

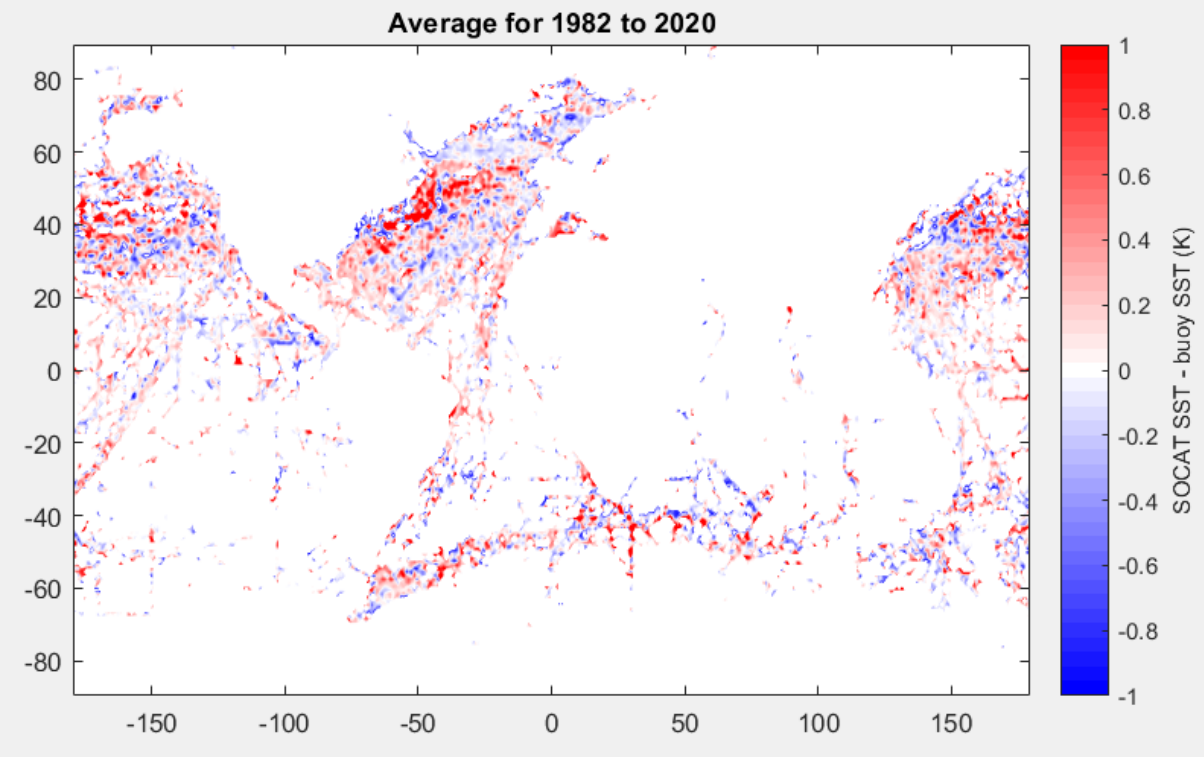

Figure S5.6 Mean difference between the gridded SOCAT SST and the gridded buoy SST for 1982 to 2020. The positive (negative) value represents the SOCAT is higher (lower) than the buoy SST.

Table S5.1 Summary of the SST datasets used in global air-sea CO_2 flux estimates by the bulk flux method (Equation 5.1 in the main text). Acronyms of SST products and related references are in the footnotes.

Studies	***Sc* and α_w**	**α_i and fCO_{2a}**	**Individual fCO_{2w}**	**fCO_{2w} mapping**
Takahashi et al. (2009)	ASMD	ASMD	*In-situ* T_{Bulk}	Interpolated T_{Bulk}
Rödenbeck et al. (2013)	OAFlux	OAFlux	*In-situ* T_{Bulk}	OAFlux
Zeng et al. (2014) and Landschützer et al. (2016)	MOISST v2	MOISST v2	*In-situ* T_{Bulk}	MOISST v2
Denvil-Sommer et al. (2019)	ARMOR3D	ARMOR3D	*In-situ* T_{Bulk}	ARMOR3D
Gregor et al. (2019)	DOISST v2.0	DOISST v2.0	*In-situ* T_{Bulk}	DOISST v2.0
Watson et al. (2020)	DOISST v2.0	DOISST v2.0 – 0.17 K	Co-located DOISST v2.0	HadISST
Iida et al. (2021)	MGDSST	MGDSST	*In-situ* T_{Bulk}	MGDSST
This study	CCI SST v2.1	CCI SST v2.1 with a Fairall96 cool skin correction	*In-situ* T_{Bulk} with a bias correction assessed by buoy SST	CCI SST v2.1

ASMD: surface water temperature from the NOAA Atlas of Surface Marine Data (1994, as cited in Takahashi et al., 2009). OAFlux: SST from the Objectively Analysed Air-Sea Fluxes for the global oceans dataset (Yu & Weller, 2007). MOISST v2: NOAA Monthly Optimum Interpolation SST dataset version 2, also known as OI.V2 SST (Reynolds et al., 2002). ARMOR3D: SST from monthly global reprocessed products of physical variables from the ARMOR3D L4 dataset (Guinehut et al., 2012). DOISST v2.0: NOAA Daily Optimum Interpolation SST dataset version 2 (Banzon et al., 2016; Reynolds et al., 2007). HadISST: Hadley Centre Sea Ice and Sea Surface Temperature dataset (Rayner et al., 2003). MGDSST: Merged satellite and *in-situ* data global daily SST analysis dataset (Sakurai et al., 2005). CCI SST v2.1: European Space Agency Climate Change Initiative SST product (Merchant et al., 2019; Merchant & Embury, 2020). *In-situ* T_{Bulk} represents the *in-situ* bulk SST measurements in the LDEO and SOCAT datasets. The study of Takahashi et al. (Takahashi et al., 2009) used the LDEO (Lamont-Doherty Earth Observatory) fCO_{2w} dataset (Takahashi et al., 2008) while the other studies employed the SOCAT fCO_{2w} dataset (Bakker et al., 2016). Co-located DOISST v2.0: the 0.25° × 0.25°, daily DOISST v2.0 is resampled to 1° × 1°, monthly data and then co-located with the individual fCO_{2w} measurements in SOCAT (Goddijn-Murphy et al., 2015).

References

Ahmed, M. M. M., Else, B. G. T., Capelle, D., Miller, L. A., & Papakyriakou, T. (2020). Underestimation of surface pCO_2 and air-sea CO_2 fluxes due to freshwater stratification in an Arctic shelf sea, Hudson Bay. *Elementa: Science of the Anthropocene*, 8(1): 084. https://doi.org/10.1525/elementa.084

Alappattu, D. P., Wang, Q., Yamaguchi, R., Lind, R. J., Reynolds, M., & Christman, A. J. (2017). Warm layer and cool skin corrections for bulk water temperature measurements for air-sea interaction studies. *Journal of Geophysical Research: Oceans*, *122*(8), 6470–6481. https://doi.org/10.1002/2017JC012688

Anderson, L. G., Olsson, K., & Chierici, M. (1998). A carbon budget for the Arctic Ocean. *Global Biogeochemical Cycles*, *12*(3), 455–465. https://doi.org/10.1029/98GB01372

Andersson, A., Falck, E., Sjöblom, A., Kljun, N., Sahlée, E., Omar, A. M., & Rutgersson, A. (2017). Air-sea gas transfer in high Arctic fjords. *Geophysical Research Letters*, *44*(5), 2519–2526. https://doi.org/10.1002/2016GL072373

Arrigo, K. R., & van Dijken, G. L. (2015). Continued increases in Arctic Ocean primary production. *Progress in Oceanography*, 136, 60–70. https://doi.org/10.1016/j.pocean.2015.05.002

Asher, W. E., Karle, L. M., Higgins, B. J., Farley, P. J., Monahan, E. C., & Leifer, I. S. (1996). The influence of bubble plumes on air-seawater gas transfer velocities. *Journal of Geophysical Research: Oceans*, *101*(C5), 12027–12041. https://doi.org/10.1029/96JC00121

Assmy, P., Fernández-Méndez, M., Duarte, P., Meyer, A., Randelhoff, A., Mundy, C. J., et al. (2017). Leads in Arctic pack ice enable early phytoplankton blooms below snow-covered sea ice. *Scientific Reports*, *7* (40850 2017), 1–9. https://doi.org/10.1038/srep40850

Atlas, R., Hoffman, R. N., Ardizzone, J., Leidner, S. M., Jusem, J. C., Smith, D. K., & Gombos, D. (2011). A cross-calibrated, multiplatform ocean surface wind velocity product for meteorological and oceanographic applications. *Bulletin of the American Meteorological Society*, *92*(2), 157–174. https://doi.org/10.1175/2010BAMS2946.1

Bakker, D. C. E., Alin, S., Castaño-Primo, R., Cronin, M., Gkrizalis, T., Kozyr, A., et al. (2021). SOCAT version 2021 for quantification of ocean CO_2 uptake. Available at https://www.socat.info/index.php/data-access/. Released 15 June 2021.

Bakker, D. C. E., Bange, H. W., Gruber, N., Johannessen, T., Upstill-Goddard, R. C., Borges, A. V, et al. (2014). Air-sea interactions of natural long-lived greenhouse gases (CO_2, N_2O, CH_4) in a changing climate. In P. S. Liss & M. T. Johnson (Eds.), *Ocean-atmosphere interactions of gases and particles* (pp. 113–169). Berlin, Heidelberg: Springer Berlin Heidelberg. https://doi.org/10.1007/978-3-642-25643-1_3

Bakker, D. C. E., Pfeil, B., Landa, C. S., Metzl, N., O'Brien, K. M., Olsen, A., et al. (2016). A multi-decade record of high-quality *f*CO_2 data in version 3 of the Surface Ocean CO_2 Atlas (SOCAT). *Earth System Science Data*, *8*(2), 383–413. https://doi.org/10.5194/essd-8-383-2016

Baldocchi, D., Falge, E., Gu, L., Olson, R., Hollinger, D., Running, S., Anthoni, P., Bernhofer, C., Davis, K. and Evans, R.: FLUXNET: A new tool to study the temporal and spatial variability of ecosystem-scale carbon dioxide, water vapor, and energy flux densities, Bull. Am. Meteorol. Soc., 82(11), 2415–2434, 2001. https://doi.org/10.1175/1520-0477(2001)082<2415:FANTTS>2.3.CO;2

Banzon, V., Smith, T. M., Mike Chin, T., Liu, C., & Hankins, W. (2016). A long-term record of blended satellite and in situ sea-surface temperature for climate monitoring, modeling and environmental studies. *Earth System Science Data*, *8*(1), 165–176. https://doi.org/10.5194/essd-8-165-2016

Bariteau, L., Helmig, D., Fairall, C. W., Hare, J. E., Hueber, J., & Lang, E. K. (2010). Determination of oceanic ozone deposition by ship-borne eddy covariance flux measurements. *Atmospheric Measurement Techniques*, *3*(2), 441–455. https://doi.org/10.5194/amt-3-441-2010

Bates, N. R., & Mathis, J. T. (2009). The Arctic Ocean marine carbon cycle: evaluation of air-sea CO_2 exchanges, ocean acidification impacts and potential feedbacks.

Biogeosciences, *6*(11). https://doi.org/10.5194/bg-6-2433-2009

Bell, T. G., Landwehr, S., Miller, S. D., De Bruyn, W. J., Callaghan, A. H., Scanlon, B., et al. (2017). Estimation of bubble-mediated air-sea gas exchange from concurrent DMS and CO_2 transfer velocities at intermediate-high wind speeds. *Atmospheric Chemistry and Physics*, *17*(14), 9019–9033. https://doi.org/10.5194/acp-17-9019-2017

Bell, T. G., De Bruyn, W., Marandino, C. A., Miller, S. D., Law, C. S., Smith, M. J., & Saltzman, E. S. (2015). Dimethylsulfide gas transfer coefficients from algal blooms in the Southern Ocean. *Atmospheric Chemistry and Physics*, *15*(4), 1783–1794. https://doi.org/10.5194/acp-15-1783-2015

Bell, T. G., De Bruyn, W., Miller, S. D., Ward, B., Christensen, K., & Saltzman, E. S. (2013). Air-sea dimethylsulfide (DMS) gas transfer in the North Atlantic: Evidence for limited interfacial gas exchange at high wind speed. *Atmospheric Chemistry and Physics*, *13*(21), 11073–11087. https://doi.org/10.5194/acp-13-11073-2013

Billesbach, D. P. (2011). Estimating uncertainties in individual eddy covariance flux measurements: A comparison of methods and a proposed new method. *Agricultural and Forest Meteorology*, *151*(3), 394–405. https://doi.org/10.1016/j.agrformet.2010.12.001

Blomquist, B. W., Fairall, C. W., Huebert, B. J., & Wilson, S. T. (2012). Direct measurement of the oceanic carbon monoxide flux by eddy correlation. *Atmospheric Measurement Techniques*, *5*(12), 3069–3075. https://doi.org/10.5194/amt-5-3069-2012

Blomquist, B. W., Brumer, S. E., Fairall, C. W., Huebert, B. J., Zappa, C. J., Brooks, I. M., et al. (2017). Wind speed and sea state dependencies of air-sea gas transfer: Results from the High Wind Speed Gas Exchange Study (HiWinGS). *Journal of Geophysical Research: Oceans*, *122*(10), 8034–8062. https://doi.org/10.1002/2017JC013181

Blomquist, B. W., Huebert, B. J., Fairall, C. W., & Faloona, I. C. (2010). Determining the sea-air flux of dimethylsulfide by eddy correlation using mass spectrometry. *Atmospheric Measurement Techniques*, *3*(1), 1–20. https://doi.org/10.5194/amt-3-1-2010

Blomquist, B. W., Huebert, B. J., Fairall, C. W., Bariteau, L., Edson, J. B., Hare, J. E., & McGillis, W. R. (2014). Advances in air-sea CO_2 flux measurement by eddy correlation. *Boundary-Layer Meteorology*, *152*(3), 245–276. https://doi.org/10.1007/s10546-014-

9926-2

Blomquist, B. W., Fairall, C. W., Huebert, B. J., Kieber, D. J., & Westby, G. R. (2006). DMS sea-air transfer velocity: Direct measurements by eddy covariance and parameterizarion based on the NOAA/COARE gas transfer model. Geophysical Research Letters, *33*(7), 2–5. https://doi.org/10.1029/2006GL025735

Boutin, J., Etcheto, J., & Ciais, P. (1999). Possible consequences of the chemical enhancement effect for air-sea CO_2 flux estimates. *Physics and Chemistry of the Earth, Part B: Hydrology, Oceans and Atmosphere*, *24*(5), 411–416. https://doi.org/10.1016/S1464-1909(99)00021-0

Broecker, W. S., & Peng, T. H. (1993). *Greenhouse puzzles.* Columbia University: Eldigio. https://www.ldeo.columbia.edu/~broecker/Home_files/GreenhousePuzzles.pdf

Broecker, W. S, Peng, T., Ostlund, G., & Stuiver, M. (1985). The distribution of bomb radiocarbon in the ocean. *Journal of Geophysical Research: Oceans*, *90*(C4), 6953–6970. https://doi.org/10.1029/JC090iC04p06953

Broecker, W. S, Ledwell, J. R., Takahashi, T., Weiss, R., Merlivat, L., Memery, L., et al. (1986). Isotopic versus micrometeorologic ocean CO_2 fluxes: A serious conflict. *Journal of Geophysical Research: Oceans*, *91*(C9), 10517–10527. https://doi.org/10.1029/JC091iC09p10517

Brumer, S. E., Zappa, C. J., Blomquist, B. W., Fairall, C. W., Cifuentes-Lorenzen, A., Edson, J. B., et al. (2017). Wave-related Reynolds number parameterizations of CO_2 and DMS transfer velocities. *Geophysical Research Letters*, *44*(19), 9865–9875. https://doi.org/10.1002/2017GL074979

Bushinsky, S. M., Landschützer, P., Rödenbeck, C., Gray, A. R., Baker, D., Mazloff, M. R., et al. (2019). Reassessing Southern Ocean air-sea CO_2 flux estimates with the addition of biogeochemical float observations. *Global Biogeochemical Cycles*, *33*(11), 1370–1388. https://doi.org/10.1029/2019GB006176

Businger, J. (1986). Evaluation of the accuracy with which dry deposition can be measured with current micrometeorological techniques. *Journal of Climate and Applied Meteorology*, *25*(8), 1100–1124. https://doi.org/10.1175/1520-0450(1986)025<1100:EOTAWW>2.0.CO;2

Butterworth, B. J., & Miller, S. D. (2016). Air-sea exchange of carbon dioxide in the Southern Ocean and Antarctic marginal ice zone. *Geophysical Research Letters*, *43*(13), 7223–7230. https://doi.org/10.1002/2016GL069581

Butterworth, B. J., & Else, B. G. T. (2018). Dried, closed-path eddy covariance method for measuring carbon dioxide flux over sea ice. *Atmospheric Measurement Techniques*, *11*(11), 6075–6090. https://doi.org/10.5194/amt-11-6075-2018

Cai, W.-J., Chen, L., Chen, B., Gao, Z., Lee, S. H., Chen, J., et al. (2010). Decrease in the CO_2 uptake capacity in an ice-free Arctic Ocean basin. *Science*, *329*(5991), 556–559. https://doi.org/10.1126/science.1189338

Calleja, M. L., Duarte, C. M., Álvarez, M., Vaquer-Sunyer, R., Agustí, S., & Herndl, G. J. (2013). Prevalence of strong vertical CO_2 and O_2 variability in the top meters of the ocean. *Global Biogeochemical Cycles*, *27*(3), 941–949. https://doi.org/10.1002/gbc.20081

Chierici, M., Vernet, M., Fransson, A., & Børsheim, K. Y. (2019). Net community production and carbon exchange from winter to summer in the Atlantic water inflow to the Arctic Ocean. *Frontiers in Marine Science*, *6*(9), 1–24. https://doi.org/10.3389/fmars.2019.00528

Danckwerts, P. V. (1951). Significance of liquid-film coefficients in gas absorption. *Industrial & Engineering Chemistry*, *43*(6), 1460–1467. https://pubs.acs.org/doi/pdf/10.1021/ie50498a055

Denvil-Sommer, A., Gehlen, M., Vrac, M., & Mejia, C. (2019). LSCE-FFNN-v1: a two-step neural network model for the reconstruction of surface ocean pCO_2 over the global ocean. *Geoscientific Model Development*, *12*(5), 2091–2105. https://doi.org/10.5194/gmd-12-2091-2019

DeVries, T. (2014). The oceanic anthropogenic CO_2 sink: Storage, air-sea fluxes, and transports over the industrial era. *Global Biogeochemical Cycles*, *28*(7), 631–647. https://doi.org/10.1002/2013GB004739

Dlugokencky, E., & Tans, P. (2023). Trends in atmospheric carbon dioxide, National Oceanic & Atmospheric Administration, Earth System Research Laboratory (NOAA/ESRL). last access: 17 March 2023. https://gml.noaa.gov/ccgg/trends/

Dong, Y., Yang, M., Bakker, D. C. E., Kitidis, V., & Bell, T. G. (2021a). Uncertainties in eddy covariance air-sea CO_2 flux measurements and implications for gas transfer velocity parameterisations. *Atmospheric Chemistry and Physics*, *21*(10), 8089–8110. https://doi.org/10.5194/acp-21-8089-2021

Dong, Y., Yang, M., Bakker, D. C. E., Liss, P. S., Kitidis, V., Brown, I., et al. (2021b). Near-surface stratification due to ice melt biases Arctic air-sea CO_2 flux estimates. *Geophysical Research Letters*, *48*(22), 1–10. https://doi.org/10.1029/2021GL095266

Dong, Y., Bakker, D. C. E., Bell, T. G., Huang, B., Landschützer, P., Liss, P. S., & Yang, M. (2022). Update on the temperature corrections of global air-sea CO_2 flux estimates . *Global Biogeochemical Cycles*, *36*(9). https://doi.org/10.1029/2022gb007360

Donlon, C. J., Robinson, I., Casey, K. S., Vazquez-Cuervo, J., Armstrong, E., Arino, O., et al. (2007). The global ocean data assimilation experiment high-resolution sea surface temperature pilot project. *Bulletin of the American Meteorological Society*, *88*(8), 1197–1214. https://doi.org/10.1175/BAMS-88-8-1197

Donlon, C. J., Minnett, P. J., Gentemann, C., Nightingale, T. J., Barton, I. J., Ward, B., & Murray, M. J. (2002). Toward improved validation of satellite sea surface skin temperature measurements for climate research. *Journal of Climate*, *15*(4), 353–369. https://doi.org/10.1175/1520-0442(2002)015<0353:TIVOSS>2.0.CO;2

Edson, J. B., Hinton, A. A., Prada, K. E., Hare, J. E., & Fairall, C. W. (1998). Direct covariance flux estimates from mobile platforms at sea. *Journal of Atmospheric and Oceanic Technology*, *15*(2), 547–562. https://doi.org/10.1175/1520-0426(1998)015<0547:DCFEFM>2.0.CO;2

Edson, J. B., Fairall, C. W., Bariteau, L., Zappa, C. J., Cifuentes-Lorenzen, A., McGillis, W. R., et al. (2011). Direct covariance measurement of CO_2 gas transfer velocity during the 2008 Southern Ocean Gas Exchange Experiment: Wind speed dependency. *Journal of Geophysical Research: Oceans*, *116*(C4), C00F10. https://doi.org/10.1029/2011JC007022

Edson, James B, Jampana, V., Weller, R. A., Bigorre, S. P., Plueddemann, A. J., Fairall, C. W., et al. (2013). On the exchange of momentum over the open ocean. *Journal of Physical Oceanography*, *43*(8), 1589–1610. https://doi.org/10.1175/JPO-D-12-0173.1

Else, B. G. T., Papakyriakou, T. N., Galley, R. J., Drennan, W. M., Miller, L. A., & Thomas, H. (2011). Wintertime CO_2 fluxes in an Arctic polynya using eddy covariance: Evidence for enhanced air-sea gas transfer during ice formation. *Journal of Geophysical Research: Oceans*, *116(C9)*, *C00G03*. https://doi.org/10.1029/2010JC006760

Else, B. G. T., Galley, R. J., Lansard, B., Barber, D. G., Brown, K., Miller, L. A., et al. (2013). Further observations of a decreasing atmospheric CO_2 uptake capacity in the Canada Basin (Arctic Ocean) due to sea ice loss. *Geophysical Research Letters*, *40*(6), 1132–1137. https://doi.org/10.1002/grl.50268

Embury, O., Merchant, C. J., & Corlett, G. K. (2012). A reprocessing for climate of sea surface temperature from the along-track scanning radiometers: Initial validation, accounting for skin and diurnal variability effects. *Remote Sensing of Environment*, *116*, 62–78. https://doi.org/10.1016/j.rse.2011.02.028

Fairall, C. W., Bradley, E. F., Godfrey, J. S., Wick, G. A., Edson, J. B., & Young, G. S. (1996). Cool-skin and warm-layer effects on sea surface temperature. *Journal of Geophysical Research: Oceans*, *101*(C1), 1295–1308. https://doi.org/10.1029/95JC03190

Fairall, C. W., Hare, J. E., Edson, J. B., & McGillis, W. (2000). Parameterization and micrometeorological measurement of air-sea gas transfer. *Boundary-Layer Meteorology*, *96*(1–2), 63–105. https://doi.org/10.1023/a:1002662826020

Fairall, C. W., Yang, M., Brumer, S. E., Blomquist, B. W., Edson, J. B., Zappa, C. J., et al. (2022). Air-sea trace gas fluxes: Direct and indirect measurements. *Frontiers in Marine Science*, *9*(7), 1–16. https://doi.org/10.3389/fmars.2022.826606

Fay, A. R., & McKinley, G. A. (2021). Observed regional fluxes to constrain modeled estimates of the ocean carbon sink. *Geophysical Research Letters*, *48*(20), 1–11. https://doi.org/10.1029/2021GL095325

Fay, A. R., Gregor, L., Landschützer, P., McKinley, G. A., Gruber, N., Gehlen, M., et al. (2021). SeaFlux: Harmonization of air-sea CO_2 fluxes from surface pCO_2 data products using a standardized approach. *Earth System Science Data*, *13*(10), 4693–4710. https://doi.org/10.5194/essd-13-4693-2021

Fick, A. (1855). V. On liquid diffusion. *The London, Edinburgh, and Dublin Philosophical Magazine and Journal of Science*, *10*(63), 30–39.

https://doi.org/10.1080/14786445508641925

Finkelstein, P. L., & Sims, P. F. (2001). Sampling error in eddy correlation flux measurements. *Journal of Geophysical Research: Atmospheres*, *106*(D4), 3503–3509. https://doi.org/10.1029/2000JD900731

Fischer, T., Kock, A., Arévalo-Martínez, D. L., Dengler, M., Brandt, P., & Bange, H. W. (2019). Gas exchange estimates in the Peruvian upwelling regime biased by multi-day near-surface stratification. *Biogeosciences*, *16*(11), 2307–2328. https://doi.org/10.5194/bg-16-2307-2019

Flügge, M., Paskyabi, M. B., Reuder, J., Edson, J. B., & Plueddemann, A. J. (2016). Comparison of direct covariance flux measurements from an offshore tower and a buoy. *Journal of Atmospheric and Oceanic Technology*, *33*(5), 873–890. https://doi.org/10.1175/JTECH-D-15-0109.1

Fransson, A., Chierici, M., & Nojiri, Y. (2009). New insights into the spatial variability of the surface water carbon dioxide in varying sea ice conditions in the Arctic Ocean. *Continental Shelf Research*, *29*(10), 1317–1328. https://doi.org/10.1016/j.csr.2009.03.008

Fransson, A., Chierici, M., Miller, L. A., Carnat, G., Shadwick, E., Thomas, H., et al. (2013). Impact of sea-ice processes on the carbonate system and ocean acidification at the ice-water interface of the Amundsen Gulf, Arctic Ocean. *Journal of Geophysical Research: Oceans*, *118*(12), 7001–7023. https://doi.org/10.1002/2013JC009164

Fransson, A., Chierici, M., Skjelvan, I., Olsen, A., Assmy, P., Peterson, A. K., et al. (2017). Effects of sea-ice and biogeochemical processes and storms on under-ice water fCO_2 during the winter-spring transition in the high Arctic Ocean: Implications for sea-air CO_2 fluxes. *Journal of Geophysical Research: Oceans*, *122*(7), 5566–5587. https://doi.org/10.1002/2016JC012478

Freeman, E., Woodruff, S. D., Worley, S. J., Lubker, S. J., Kent, E. C., Angel, W. E., et al. (2017). ICOADS Release 3.0: a major update to the historical marine climate record. *International Journal of Climatology*, *37*(5), 2211–2232. https://doi.org/10.1002/joc.4775

Frew, N. M., Goldman, J. C., Dennett, M. R., & Johnson, A. S. (1990). Impact of

phytoplankton-generated surfactants on air-sea gas exchange. *Journal of Geophysical Research: Oceans, 95*(C3), 3337-3352. https://doi.org/10.1029/JC095iC03p03337

Friedlingstein, P., O'Sullivan, M., Jones, M. W., Andrew, R. M., Hauck, J., Olsen, A., et al. (2020). Global Carbon Budget 2020. *Earth System Science Data, 12*(4), 3269–3340. https://doi.org/10.5194/essd-12-3269-2020

Friedlingstein, P., Jones, M. W., O'Sullivan, M., Andrew, R. M., Bakker, D. C. E., Hauck, J., et al. (2022). Global carbon budget 2021. *Earth System Science Data, 14*(4), 1917–2005. https://doi.org/10.5194/essd-14-1917-2022

Friedlingstein, P., O'Sullivan, M., Jones, M. W., Andrew, R. M., Gregor, L., Hauck, J., et al. (2022). Global Carbon Budget 2022. *Earth System Science Data, 14*(11), 4811–4900. https://doi.org/10.5194/essd-14-4811-2022

Garbe, C. S., Rutgersson, A., Boutin, J., De Leeuw, G., Delille, B., Fairall, C. W., et al. (2014). Transfer across the air-sea interface. In P. S. Liss & M. T. Johnson (Eds.), *Ocean-atmosphere interactions of gases and particles* (pp. 55–112). Berlin, Heidelberg: Springer Berlin Heidelberg.. http://dx.doi.org/10.1007/978-3-642-25643-1_2

Gentemann, C. L., & Minnett, P. J. (2008). Radiometric measurements of ocean surface thermal variability. *Journal of Geophysical Research: Oceans, 113*(C8). https://doi.org/10.1029/2007JC004540

Ghobadian, M., & Stammer, D. (2019). Inferring air-sea carbon dioxide transfer velocities from sea surface scatterometer measurements. *Journal of Geophysical Research: Oceans, 124*(11), 7974–7988. https://doi.org/10.1029/2019JC014982

Gloege, L., McKinley, G. A., Landschützer, P., Fay, A. R., Frölicher, T. L., Fyfe, J. C., et al. (2021). Quantifying errors in observationally based estimates of ocean carbon sink variability. *Global Biogeochemical Cycles, 35*(4), e2020GB006788. https://doi.org/10.1029/2020GB006788

Goddijn-Murphy, L. M., Woolf, D. K., Land, P. E., Shutler, J. D., & Donlon, C. (2015). The OceanFlux Greenhouse Gases methodology for deriving a sea surface climatology of CO_2 fugacity in support of air-sea gas flux studies. *Ocean Science, 11*(4), 519–541. https://doi.org/10.5194/os-11-519-2015

Gray, A. R., Johnson, K. S., Bushinsky, S. M., Riser, S. C., Russell, J. L., Talley, L. D., et al.

(2018). Autonomous biogeochemical floats detect significant carbon dioxide outgassing in the high-latitude Southern Ocean. *Geophysical Research Letters*, *45*(17), 9049–9057. https://doi.org/10.1029/2018GL078013

Gregor, L., Lebehot, A. D., Kok, S., & Scheel Monteiro, P. M. (2019). A comparative assessment of the uncertainties of global surface ocean CO_2 estimates using a machine-learning ensemble (CSIR-ML6 version 2019a)-Have we hit the wall? *Geoscientific Model Development*, *12*(12), 5113–5136. https://doi.org/10.5194/gmd-12-5113-2019

Gruber, N., Clement, D., Carter, B. R., Feely, R. A., van Heuven, S., Hoppema, M., et al. (2019). The oceanic sink for anthropogenic CO_2 from 1994 to 2007. *Science*, *363*(6432), 1193–1199. https://doi.org/10.1126/science.aau5153

Gruber, N., Landschützer, P., & Lovenduski, N. S. (2019). The variable Southern Ocean carbon sink. *Annual Review of Marine Science*, *11*, 159–186. https://doi.org/10.1146/annurev-marine-121916-063407

Guinehut, S., Dhomps, A. L., Larnicol, G., & Le Traon, P. Y. (2012). High resolution 3-D temperature and salinity fields derived from in situ and satellite observations. *Ocean Science*, *8*(5), 845–857. https://doi.org/10.5194/os-8-845-2012

Gulev, S. K., Thorne, P. W., Ahn, J., Dentener, F. J., Domingues, C. M., Gerland, S., Gong, D., et al. (2021). Climate change 2021: The physical science basis. Contribution of Working Group I to the sixth assessment report of the intergovern-mental panel on climate change. Cambridge: Cambridge University. https://www.ipcc.ch/report/sixth-assessment-report-working-group-i/

Gutiérrez-Loza, L., Nilsson, E., Wallin, M. B., Sahlée, E., & Rutgersson, A. (2022). On physical mechanisms controlling air-sea CO_2 exchange. *Biogeosciences*, *19*(24), 5645-5665. https://doi.org/10.5194/bg-19-5645-2022

Hauck, J., Zeising, M., Le Quéré, C., Gruber, N., Bakker, D. C. E., Bopp, L., et al. (2020). Consistency and challenges in the ocean carbon sink estimate for the global carbon budget. *Frontiers in Marine Science*, *7*(October), 1–22. https://doi.org/10.3389/fmars.2020.571720

Hersbach, H., Bell, B., Berrisford, P., Hirahara, S., Horányi, A., Muñoz-Sabater, J., et al. (2020). The ERA5 global reanalysis. *Quarterly Journal of the Royal Meteorological*

Society, *146*(730), 1999–2049. https://doi.org/10.1002/qj.3803

Van Heuven, S., Pierrot, D., Rae, J. W. B., Lewis, E., & Wallace, D. W. R. (2011). MATLAB program developed for CO_2 system calculations. *ORNL/CDIAC-105b*, *530*. https://www.ncei.noaa.gov/access/ocean-carbon-acidification-data-system/oceans/CO2SYS/co2rprt.html

Ho, D. T., Law, C. S., Smith, M. J., Schlosser, P., Harvey, M., & Hill, P. (2006). Measurements of air-sea gas exchange at high wind speeds in the Southern Ocean: Implications for global parameterizations. *Geophysical Research Letters*, *33*(16), L16611. https://doi.org/10.1029/2006GL026817

Ho, D. T., Wanninkhof, R., Schlosser, P., Ullman, D. S., Hebert, D., & Sullivan, K. F. (2011). Toward a universal relationship between wind speed and gas exchange: Gas transfer velocities measured with $^3He/SF_6$ during the Southern Ocean Gas Exchange Experiment. *Journal of Geophysical Research: Oceans*, *116*(7), 1–13. https://doi.org/10.1029/2010JC006854

Holding, T., Ashton, I. G., Shutler, J. D., Land, P. E., Nightingale, P. D., Rees, A. P., et al. (2019). The fluxengine air-sea gas flux toolbox: Simplified interface and extensions for in situ analyses and multiple sparingly soluble gases. *Ocean Science*, *15*(6), 1707–1728. https://doi.org/10.5194/os-15-1707-2019

Huang, B., Thorne, P. W., Banzon, V. F., Boyer, T., Chepurin, G., Lawrimore, J. H., et al. (2017). Extended reconstructed sea surface temperature, version 5 (ERSSTv5): Upgrades, validations, and intercomparisons. *Journal of Climate*, *30*(20), 8179–8205. https://doi.org/10.1175/JCLI-D-16-0836.1

Huang, B., Liu, C., Banzon, V., Freeman, E., Graham, G., Hankins, B., et al. (2021). Improvements of the daily optimum interpolation sea surface temperature (DOISST) version 2.1. *Journal of Climate*, *34*(8), 2923–2939. https://doi.org/10.1175/JCLI-D-20-0166.1

Huebert, B. J, Blomquist, B. W., Yang, M. X., Archer, S. D., Nightingale, P. D., Yelland, M. J., et al. (2010). Linearity of DMS transfer coefficient with both friction velocity and wind speed in the moderate wind speed range. *Geophysical Research Letters*, *37*(1), L01605. https://doi.org/10.1029/2009GL041203

Huebert, B. J., Blomquist, B. W., Hare, J. E., Fairall, C. W., Johnson, J. E., & Bates, T. S.

(2004). Measurement of the sea-air DMS flux and transfer velocity using eddy correlation. *Geophysical Research Letters*, *31*(23), 1–4. https://doi.org/10.1029/2004GL021567

Iida, Y., Takatani, Y., Kojima, A., & Ishii, M. (2021). Global trends of ocean CO_2 sink and ocean acidification: an observation-based reconstruction of surface ocean inorganic carbon variables. *Journal of Oceanography*, *77*(2), 323–358. https://doi.org/10.1007/s10872-020-00571-5

Ikawa, H., Faloona, I., Kochendorfer, J., Paw U, K. T., & Oechel, W. C. (2013). Air-sea exchange of CO_2 at a Northern California coastal site along the California Current upwelling system. *Biogeosciences*. *10*(7), 4419–4432. https://doi.org/10.5194/bg-10-4419-2013

Jacobs, C., Friis Kjeld, J., Nightingale, P., Upstill-Goddard, R., Larsen, S., & Oost, W. (2002). Possible errors in CO_2 air-sea transfer velocity from deliberate tracer releases and eddy covariance measurements due to near-surface concentration gradients. *Journal of Geophysical Research: Oceans*, *107*(C9), 11. https://doi.org/10.1029/2001JC000983

Jacobson, A. R., Mikaloff Fletcher, S. E., Gruber, N., Sarmiento, J. L., & Gloor, M. (2007). A joint atmosphere-ocean inversion for surface fluxes of carbon dioxide: 1. Methods and global-scale fluxes. *Global Biogeochemical Cycles*, *21*, GB1019. https://doi.org/10.1029/2005GB002556

Jähne, B., Münnich, K. O. M., Bösinger, R., Dutzi, A., Huber, W., & Libner, P. (1987). On the parameters influencing air-water gas exchange. *Journal of Geophysical Research: Oceans*, *92*(C2), 1937–1949. https://doi.org/10.1029/JC092iC02p01937

Jähne, B. (2009). Air-sea gas exchange. *Elements of Physical Oceanography: A Derivative of the Encyclopedia of Ocean Sciences*, 160–169. https://doi.org/10.1016/B978-0-12-409548-9.11613-6

Jähne, B. (2019). Air-sea gas exchange. In J. K. Cochran, et al. (Eds.), *Encyclopedia of ocean Sciences* (Third Edition) (pp. 1–13). Oxford: Academic Press. https://doi.org/https://doi.org/10.1016/B978-0-12-409548-9.11613-6

JCGM. (2008). Evaluation of measurement data—guide to theexpression of uncertainty in measurement. GUM: Guideto the expression of uncertainty in measurement, International Organization for Standardization. Online:

http://www.bipm.org/en/publications/guides/gum.html.

Johnson, K. S. (1982). Carbon dioxide hydration and dehydration kinetics in seawater. *Limnology and Oceanography*, *27*(5), 849–855. https://doi.org/10.4319/lo.1982.27.5.0849

Jones, E. P., & Smith, S. D. (1977). A first measurement of sea-air CO_2 flux by eddy correlation. *Journal of Geophysical Research*, *82*(37), 5990–5992. https://doi.org/10.1029/JC082i037p05990

Kaimal, J. C., & Finnigan, J. J. (1994). *Atmospheric boundary layer flows: their structure and measurement*. New York: Oxford university press. https://doi.org/10.1002/qj.49712152512

Kaimal, J., Wyngaard, J., Izumi, Y., & Cote, O. (1972). Spectral characteristics of surface-layer turbulence. *Quarterly Journal of the Royal Meteorological Society*, *098*(417), 563–589. https://doi.org/10.1256/smsqj.41706

Kalnay, E., Kanamitsu, M., Kistler, R., Collins, W., Deaven, D., Gandin, L., et al. (1996). The NCEP/NCAR 40-year reanalysis project. *Bulletin of the American Meteorological Society*, *77*(3), 437–472. https://doi.org/10.1175/1520-0477(1996)077<0437:TNYRP>2.0.CO;2

Keeling, C. D. (1960). The concentration and isotopic abundances of carbon dioxide in the atmosphere. *Tellus*, *12*(2), 200–203. https://doi.org/10.3402/tellusa.v12i2.9366

Kennedy, J. J., Rayner, N. A., Smith, R. O., Parker, D. E., & Saunby, M. (2011). Reassessing biases and other uncertainties in sea surface temperature observations measured in situ since 1850: 2. Biases and homogenization. *Journal of Geophysical Research*, *116*(D14), 1–22. https://doi.org/10.1029/2010jd015220

Kennedy, J. J., Rayner, N. A., Atkinson, C. P., & Killick, R. E. (2019). An ensemble data set of sea surface temperature change from 1850: The Met Office Hadley Centre HadSST.4.0.0.0 data set. *Journal of Geophysical Research: Atmospheres*, *124*(14), 7719–7763. https://doi.org/10.1029/2018JD029867

Kent, E. C., Kennedy, J. J., Smith, T. M., Hirahara, S., Huang, B., Kaplan, A., et al. (2017). A call for new approaches to quantifying biases in observations of sea surface temperature. *Bulletin of the American Meteorological Society*, *98*(8), 1601–1616.

https://doi.org/10.1175/BAMS-D-15-00251.1

Kitaigorodskii, S. (2011). The calculation of the gas transfer between the ocean and atmosphere. In Komori S & McGillis W. R. (Eds), *Gas transfer at water surfaces* 2010 (pp. 13–28). Kyoto: *Kyoto University Press*.

Kitidis, V., Brown, I., Hardman-Mountford, N., & Lefèvre, N. (2017). Surface ocean carbon dioxide during the Atlantic Meridional Transect (1995–2013); evidence of ocean acidification. *Progress in Oceanography*, *158*, 65–75. https://doi.org/10.1016/j.pocean.2016.08.005

Kohsiek, W. (2000). Water vapor cross-sensitivity of open path H_2O/CO_2 sensors. *Journal of Atmospheric and Oceanic Technology*, *17*(3), 299–311. https://doi.org/10.1175/1520-0426(2000)017<0299:WVCSOO>2.0.CO;2

Kondo, F., & Tsukamoto, O. (2007). Air-sea CO_2 flux by eddy covariance technique in the equatorial Indian Ocean. *Journal of Oceanography*, *63*(3), 449–456. https://doi.org/10.1007/s10872-007-0040-7

Krall, K. E., Smith, A. W., Takagaki, N., & Jähne, B. (2019). Air-sea gas exchange at wind speeds up to 85 m s^{-1}. *Ocean Science*, *15*(6), 1783–1799. https://doi.org/10.5194/os-15-1783-2019

Lacroix, F., Ilyina, T., & Hartmann, J. (2020). Oceanic CO_2 outgassing and biological production hotspots induced by pre-industrial river loads of nutrients and carbon in a global modeling approach. *Biogeosciences*, *17*(1), 55–88. https://doi.org/10.5194/bg-17-55-2020

Landschützer, P., Gruber, N., Bakker, D. C. E., Schuster, U., Nakaoka, S., Payne, M. R., et al. (2013). A neural network-based estimate of the seasonal to inter-annual variability of the Atlantic Ocean carbon sink. *Biogeosciences*, *10*(11), 7793–7815. https://doi.org/10.5194/bg-10-7793-2013

Landschützer, P., Gruber, N., Bakker, D. C. E., & Schuster, U. (2014). Recent variability of the global ocean carbon sink. *Global Biogeochemical Cycles*, *28*(9), 927–949. https://doi.org/10.1002/2014GB004853

Landschützer, P., Gruber, N., Haumann, F. A., Rödenbeck, C., Bakker, D. C. E., Van Heuven, S., et al. (2015). The reinvigoration of the Southern Ocean carbon sink.

Science, *349*(6253), 1221–1224. https://doi.org/10.1126/science.aab26

Landschützer, P., Gruber, N., & Bakker, D. C. E. (2016). Decadal variations and trends of the global ocean carbon sink. *Global Biogeochemical Cycles*, *30*(10), 1396–1417. https://doi.org/10.1002/2015GB005359

Landschützer, P., Gruber, N., & Bakker, D. C. E. (2020). An observation-based global monthly gridded sea surface pCO_2 and air-sea CO_2 flux product from 1982 onward and its monthly climatology. *NCEI Accession, 160558*. https://doi.org/10.7289/V5Z899N6

Landschützer, P., Gruber, N., & Bakker, D. C. E. (2021). An observation-based global monthly gridded sea surface pCO_2 and air-sea CO_2 flux product from 1982 onward and its monthly climatology. *NCEI Accession, 160558*. https://doi.org/10.7289/V5Z899N6

Landwehr, S., Miller, S. D., Smith, M. J., Saltzman, E. S., & Ward, B. (2014). Analysis of the PKT correction for direct CO_2 flux measurements over the ocean. *Atmospheric Chemistry and Physics*, *14*(7), 3361-3372. https://doi.org/10.5194/acp-14-3361-2014

Landwehr, S., O'Sullivan, N., & Ward, B. (2015). Direct flux measurements from mobile platforms at sea: Motion and airflow distortion corrections revisited. *Journal of Atmospheric and Oceanic Technology*, *32*(6), 1163–1178. https://doi.org/10.1175/JTECH-D-14-00137.1

Landwehr, S., Miller, S. D., Smith, M. J., Bell, T. G., Saltzman, E. S., & Ward, B. (2018). Using eddy covariance to measure the dependence of air-sea CO_2 exchange rate on friction velocity. *Atmospheric Chemistry and Physics*, *18*(6), 4297–4315. https://doi.org/10.5194/acp-18-4297-2018

Langford, B., Acton, W., Ammann, C., Valach, A., & Nemitz, E. (2015). Eddy-covariance data with low signal-to-noise ratio: Time-lag determination, uncertainties and limit of detection. *Atmospheric Measurement Techniques*, *8*(10), 4197–4213. https://doi.org/10.5194/amt-8-4197-2015

Lashof, D. A., & Ahuja, D. R. (1990). Relative contributions of greenhouse gas emissions to global warming. *Nature*, *344*(6266), 529-531. https://doi.org/10.1038/344529a0

Lauvset, S. K., McGillis, W. R., Bariteau, L., Fairall, C. W., Johannessen, T., Olsen, A., & Zappa, C. J. (2011). Direct measurements of CO_2 flux in the Greenland Sea. *Geophysical Research Letters*, *38*(12), L12603. https://doi.org/10.1029/2011GL047722

Lenschow, D. H., Mann, J., & Kristensen, L. (1994). How long is long enough when measuring fluxes and other turbulence statistics? *Journal of Atmospheric & Oceanic Technology*, *11*(3), 661–673. https://doi.org/10.1175/1520-0426(1994)011<0661:HLILEW>2.0.CO;2

Lenschow, D. H, & Kristensen, L. (1985). Uncorrelated noise in turbulence measurements. *Journal of Atmospheric and Oceanic Technology*, *2*(1), 68–81. https://doi.org/10.1175/1520-0426(1985)002<0068:UNITM>2.0.CO;2

Lenschow, D. H., Wulfmeyer, V., & Senff, C. (2000). Measuring second- through fourth-order moments in noisy data. *Journal of Atmospheric and Oceanic Technology*, *17*(10), 1330–1347. https://doi.org/10.1175/1520-0426(2000)017<1330:MSTFOM>2.0.CO;2

Lenschow, D. H, Mann, J., & Kristensen, L. (1993). *How long is long enough when measuring fluxes and other turbulence statistics, NCAR Tech. Note*. NCAR/TN-389, 53 Natl. Cent. for Atmos. Res., Boulder, Colo. http://dx.doi.org/10.5065/D6PG1PPK

Lenton, A., Tilbrook, B., Law, R. M., Bakker, D., Doney, S. C., Gruber, N., et al. (2013). Sea-air CO_2 fluxes in the Southern Ocean for the period 1990–2009. *Biogeosciences*, *10*(6), 4037–4054. https://doi.org/10.5194/bg-10-4037-2013

Lewis, E. R., & Wallace, D. W. R. (1998). *Program developed for CO_2 system calculations*. Environmental System Science Data Infrastructure for a Virtual Ecosystem. https://doi.org/10.15485/1464255

Li, W. K. W., McLaughlin, F. A., Lovejoy, C., & Carmack, E. C. (2009). Smallest algae thrive as the Arctic Ocean freshens. *Science*, *326*(5952), 539–539. https://doi.org/10.1126/science.1179798

Liss, P. S., & Slater, P. G. (1974). Flux of gases across the air-sea interface. *Nature*, *247*(5438), 181–184. https://doi.org/10.1038/247181a0

Liss, P S, Balls, P. W., Martinelli, F. N., & Coantic, M. (1981). The effect of evaporation and condensation on gas transfer across an air-water-interface. *Oceanologica Acta*, *4*(2), 129–138. https://archimer.ifremer.fr/doc/00121/23202/21047.pdf

Liss, P. S., & Merlivat, L. (1986). Air-sea gas exchange rates: Introduction and synthesis. In Buat-Ménard P. (Eds.), *The role of air-sea exchange in geochemical cycling* (pp. 113–127). Dordrecht: *Springer*. https://doi.org/10.1007/978-94-009-4738-2_5

Loescher, H. W., Law, B. E., Mahrt, L., Hollinger, D. Y., Campbell, J., & Wofsy, S. C. (2006). Uncertainties in, and interpretation of, carbon flux estimates using the eddy covariance technique. *Journal of Geophysical Research Atmospheres*, *111*(21), 1–19. https://doi.org/10.1029/2005JD006932

Long, M. C., Stephens, B. B., McKain, K., Sweeney, C., Keeling, R. F., Kort, E. A., et al. (2021). Strong Southern Ocean carbon uptake evident in airborne observations. *Science*, *374*(6572), 1275–1280. https://doi.org/10.1126/science.abi43

Loose, B., Kelly, R. P., Bigdeli, A., Williams, W., Krishfield, R., Rutgers van der Loeff, M., & Moran, S. B. (2017). How well does wind speed predict air-sea gas transfer in the sea ice zone? A synthesis of radon deficit profiles in the upper water column of the Arctic Ocean. *Journal of Geophysical Research: Oceans*, *122*(5), 3696-3714. https://doi.org/10.1002/2016JC012460

Loose, B., McGillis, W. R., Schlosser, P., Perovich, D., & Takahashi, T. (2009). Effects of freezing, growth, and ice cover on gas transport processes in laboratory seawater experiments. *Geophysical Research Letters*, *36*(5), L05603. https://doi.org/10.1029/2008GL036318

Mackay, N., Watson, A. J., Suntharalingam, P., Chen, Z., & Landschützer, P. (2022). Improved winter data coverage of the Southern Ocean CO_2 sink from extrapolation of summertime observations. *Communications Earth and Environment*, *3*(1), 1–9. https://doi.org/10.1038/s43247-022-00592-6

Mahrt, L. (1998). Flux sampling errors for aircraft and towers. *Journal of Atmospheric and Oceanic Technology*, *15*(2), 416–429. https://doi.org/10.1175/1520-0426(1998)015<0416:FSEFAA>2.0.CO;2

Marandino, C. A., De Bruyn, W. J., Miller, S. D., & Saltzman, E. S. (2009). Open ocean DMS air/sea fluxes over the eastern South Pacific Ocean. *Atmospheric Chemistry and Physics*, *9*(2), 345–356. https://doi.org/10.5194/acp-9-345-2009

Marandino, C. A., De Bruyn, W. J., Miller, S. D., & Saltzman, E. S. (2007). Eddy correlation measurements of the air/sea flux of dimethylsulfide over the North Pacific Ocean. *Journal of Geophysical Research: Atmospheres*, *112*(D3), D03301. https://doi.org/10.1029/2006JD007293

Matthews, B. J. H. (1999). The rate of air-sea CO_2 exchange: chemical enhancement and catalysis by marine microalgae. Doctoral dissertation, University of East Anglia, Norwic, UK. https://benmatthews.eu/benphd/welcome.html

Mauder, M., Cuntz, M., Drüe, C., Graf, A., Rebmann, C., Schmid, H. P., et al. (2013). A strategy for quality and uncertainty assessment of long-term eddy-covariance measurements. *Agricultural and Forest Meteorology*, *169*, 122–135. https://doi.org/10.1016/j.agrformet.2012.09.006

McGillis, W. R., Edson, J. B., Ware, J. D., Dacey, J. W. H., Hare, J. E., Fairall, C. W., & Wanninkhof, R. (2001). Carbon dioxide flux techniques performed during GasEx-98. *Marine Chemistry*, *75*(4), 267–280. https://doi.org/10.1016/S0304-4203(01)00042-1

McGillis, W. R., Edson, J. B., Zappa, C. J., Ware, J. D., McKenna, S. P., Terray, E. A., et al. (2004). Air-sea CO_2 exchange in the equatorial Pacific. *Journal of Geophysical Research: Oceans*, *109*(C8). https://doi.org/10.1029/2003JC002256

McKinley, G. A., Fay, A. R., Lovenduski, N. S., & Pilcher, D. J. (2017). Natural variability and anthropogenic trends in the ocean carbon sink. *Annual Review of Marine Science*, *9*(1), 125–150. https://doi.org/10.1146/annurev-marine-010816-060529

McPhee, M. G., Proshutinsky, A., Morison, J. H., Steele, M., & Alkire, M. B. (2009). Rapid change in freshwater content of the Arctic Ocean. *Geophysical Research Letters*, *36*(10). https://doi.org/10.1029/2009GL037525

Memery, L., & Merlivat, L. (1985). Modelling of gas flux through bubbles at the air-water interface. *Tellus B: Chemical and Physical Meteorology*, *37*(4–5), 272–285. https://doi.org/10.3402/tellusb.v37i4-5.15030

Merchant, C. J., & Embury, O. (2020). Adjusting for desert-dust-related biases in a climate data record of sea surface temperature. *Remote Sensing*, *12*(16), 1–15. https://doi.org/10.3390/RS12162554

Merchant, C. J., Embury, O., Bulgin, C. E., Block, T., Corlett, G. K., Fiedler, E., et al. (2019). Satellite-based time-series of sea-surface temperature since 1981 for climate applications. *Scientific Data*, *6*(1), 1–18. https://doi.org/10.1038/s41597-019-0236-x

Merlivat, L., Boutin, J., & Antoine, D. (2015). Roles of biological and physical processes in driving seasonal air-sea CO_2 flux in the Southern Ocean: New insights from CARIOCA

pCO_2. *Journal of Marine Systems*, *147*, 9–20. https://doi.org/10.1016/j.jmarsys.2014.04.015

Miller, L. A., Burgers, T. M., Burt, W. J., Granskog, M. A., & Papakyriakou, T. N. (2019). Air-sea CO_2 flux estimates in stratified arctic coastal waters: how wrong can we be? *Geophysical Research Letters*, *46*(1), 235–243. https://doi.org/10.1029/2018GL080099

Miller, S. D., Marandino, C., De Bruyn, W., & Saltzman, E. S. (2009). Air-sea gas exchange of CO_2 and DMS in the North Atlantic by eddy covariance. *Geophysical Research Letters*, *36*(15), 1–5. https://doi.org/10.1029/2009GL038907

Miller, S. D., Marandino, C., & Saltzman, E. S. (2010). Ship-based measurement of air-sea CO_2 exchange by eddy covariance. *Journal of Geophysical Research Atmospheres*, *115*(D2), 1–14. https://doi.org/10.1029/2009JD012193

Moat, B. I., & Yelland, M. J. (2015). *Airflow distortion at instrument sites on the RRS James Clark Ross during the WAGES project*. https://nora.nerc.ac.uk/id/eprint/509304

Moat, B. I., Yelland, M. J., & Cooper, E. B. (2006). The airflow distortion at instruments sites on the RRS" James Cook". http://eprints.soton.ac.uk/id/eprint/41147

Minnett, P. J., Smith, M., & Ward, B. (2011). Measurements of the oceanic thermal skin effect. *Deep-Sea Research Part II: Topical Studies in Oceanography*, *58*(6), 861–868. https://doi.org/10.1016/j.dsr2.2010.10.024

Monahan, E. C., & Spillane, M. C. (1984). The role of oceanic whitecaps in air-sea gas exchange. In Brutsaert W., Jirka G. H. (Eds.), *Gas Transfer at Water Surfaces. Water Science and Technology Library* (pp. 495–503). Dordrecht: *Springer*. https://doi.org/10.1007/978-94-017-1660-4_45

Monteiro, P. M. S., Gregor, L., Lévy, M., Maenner, S., Sabine, C. L., & Swart, S. (2015). Intraseasonal variability linked to sampling alias in air-sea CO_2 fluxes in the Southern Ocean. *Geophysical Research Letters*, *42*(20), 8507–8514. https://doi.org/10.1002/2015GL066009

Mustaffa, N. I. H., Striebel, M., & Wurl, O. (2017). Enrichment of extracellular carbonic anhydrase in the sea surface microlayer and its effect on air-sea CO_2 exchange. *Geophysical Research Letters*, 44(24), 12,324-12,330. https://doi.org/10.1002/2017GL075797

Naegler, T. (2009). Reconciliation of excess ^{14}C-constrained global CO_2 piston velocity estimates. *Tellus, Series B: Chemical and Physical Meteorology*, *61* (2), 372–384. https://doi.org/10.1111/j.1600-0889.2008.00408.x

Nightingale, P. D., Malin, G., Law, C. S., Watson, A. J., Liss, P. S., Liddicoat, M. I., et al. (2000). In situ evaluation of air-sea gas exchange parameterizations using novel conservative and volatile tracers. *Global Biogeochemical Cycles*, 14(1), 373–387. https://doi.org/10.1029/1999GB900091

Nilsson, E., Bergström, H., Rutgersson, A., Podgrajsek, E., Wallin, M. B., Bergström, G., et al. (2018). Evaluating humidity and sea salt disturbances on CO_2 flux measurements. *Journal of Atmospheric and Oceanic Technology*, *35*(4), 859–875. https://doi.org/10.1175/JTECH-D-17-0072.1

O'Carroll, A. G., Armstrong, E. M., Beggs, H., Bouali, M., Casey, K. S., Corlett, G. K., et al. (2019). Observational needs of sea surface temperature. *Frontiers in Marine Science*, *7*:571720. https://doi.org/10.3389/fmars.2019.00420

Park, Y., Park, T., Kim, T., Lee, S., Hong, C., Lee, J., et al. (2019). Observations of the Antarctic Circumpolar Current over the Udintsev Fracture Zone, the narrowest choke point in the Southern Ocean. *Journal of Geophysical Research: Oceans*, *124*(7), 4511–4528. https://doi.org/10.1029/2019JC015024

Pereira, R., Ashton, I., Sabbaghzadeh, B., Shutler, J. D., & Upstill-Goddard, R. C. (2018). Reduced air-sea CO_2 exchange in the Atlantic Ocean due to biological surfactants. *Nature Geoscience*, *11*(7), 492–496. https://doi.org/10.1038/s41561-018-0136-2

Perovich, D., Meier, W., Tschudi, M., Hendricks, S., Petty, A. A., Divine, D., et al. (2020). Sea Ice. https://doi.org/10.25923/n170-9h57

Perovich, D. K., Light, B., Eicken, H., Jones, K. F., Runciman, K., & Nghiem, S. V. (2007). Increasing solar heating of the Arctic Ocean and adjacent seas, 1979–2005: Attribution and role in the ice-albedo feedback. *Geophysical Research Letters*, *34*(19), L19505. https://doi.org/10.1029/2007GL031480

Pfeil, B., Olsen, A., Bakker, D. C. E., Hankin, S., Koyuk, H., Kozyr, A., et al. (2013). A uniform, quality controlled Surface Ocean CO_2 Atlas (SOCAT). *Earth System Science Data*, *5*(1), 125–143. https://doi.org/10.5194/essd-5-125-2013

Pierrot, D., Neill, C., Sullivan, K., Castle, R., Wanninkhof, R., Lüger, H., et al. (2009). Recommendations for autonomous underway pCO_2 measuring systems and data-reduction routines. *Deep-Sea Research Part II: Topical Studies in Oceanography*, *56*(8–10), 512–522. https://doi.org/10.1016/j.dsr2.2008.12.005

Post, H., Hendricks Franssen, H. J., Graf, A., Schmidt, M., & Vereecken, H. (2015). Uncertainty analysis of eddy covariance CO_2 flux measurements for different EC tower distances using an extended two-tower approach. *Biogeosciences*, *12*(4), 1205–1221. https://doi.org/10.5194/bg-12-1205-2015

Prytherch, J, Yelland, M. J., Pascal, R. W., Moat, B. I., Skjelvan, I., & Neill, C. C. (2010a). Direct measurements of the CO_2 flux over the ocean: Development of a novel method. *Geophysical Research Letters*, *37*(3), L03607. https://doi.org/10.1029/2009GL041482

Prytherch, J, Yelland, M., Pascal, R., Moat, B., Skjelvan, I., & Srokosz, M. (2010b). Open ocean gas transfer velocity derived from long-term direct measurements of the CO_2 flux. *Geophysical Research Letters*, *37*(23), L23607. https://doi.org/10.1029/2010GL045597

Prytherch, J., Farrar, J. T., & Weller, R. A. (2013). Moored surface buoy observations of the diurnal warm layer. *Journal of Geophysical Research: Oceans*, *118*(9), 4553–4569. https://doi.org/10.1002/jgrc.20360

Prytherch, J, Brooks, I. M., Crill, P. M., Thornton, B. F., Salisbury, D. J., Tjernström, M., et al. (2017). Direct determination of the air-sea CO_2 gas transfer velocity in Arctic sea ice regions. *Geophysical Research Letters*, *44*(8), 3770–3778. https://doi.org/10.1002/2017GL073593

Prytherch, J., & Yelland, M. J. (2021). Wind, convection and fetch dependence of gas transfer velocity in an Arctic sea-ice lead determined from eddy covariance CO_2 flux measurements. *Global Biogeochemical Cycles*, *35*, e2020GB006633. https://doi.org/10.1029/2020GB006633

Rannik, Ü, Mammarella, I., Aalto, P., Keronen, P., Vesala, T., & Kulmala, M. (2009). Long-term aerosol particle flux observations part I: Uncertainties and time-average statistics. *Atmospheric Environment*, *43*(21), 3431–3439. https://doi.org/10.1016/j.atmosenv.2009.02.049

Rannik, Ü., Peltola, O., & Mammarella, I. (2016). Random uncertainties of flux

measurements by the eddy covariance technique. *Atmospheric Measurement Techniques*, *9*(10), 5163–5181. https://doi.org/10.5194/amt-9-5163-2016

Rayner, N. A., Parker, D. E., Horton, E. B., Folland, C. K., Alexander, L. V., Rowell, D. P., et al. (2003). Global analyses of sea surface temperature, sea ice, and night marine air temperature since the late nineteenth century. *Journal of Geophysical Research: Atmospheres*, *108*(14). https://doi.org/10.1029/2002jd002670

Regnier, P., Resplandy, L., Najjar, R. G., & Ciais, P. (2022). The land-to-ocean loops of the global carbon cycle. *Nature*, *603*(7901), 401–410. https://doi.org/10.1038/s41586-021-04339-9

Resplandy, L., Keeling, R. F., Rödenbeck, C., Stephens, B. B., Khatiwala, S., Rodgers, K. B., et al. (2018). Revision of global carbon fluxes based on a reassessment of oceanic and riverine carbon transport. *Nature Geoscience*, *11*(7), 504–509. https://doi.org/10.1038/s41561-018-0151-3

Reynolds, R. W., & Chelton, D. B. (2010). Comparisons of daily sea surface temperature analyses for 2007-08. *Journal of Climate*, *23*(13), 3545–3562. https://doi.org/10.1175/2010JCLI3294.1

Reynolds, R. W., Rayner, N. A., Smith, T. M., Stokes, D. C., & Wang, W. (2002). An improved in situ and satellite SST analysis for climate. *Journal of Climate*, *15*(13), 1609–1625. https://doi.org/10.1175/1520-0442(2002)015<1609:AIISAS>2.0.CO;2

Reynolds, R. W., Smith, T. M., Liu, C., Chelton, D. B., Casey, K. S., & Schlax, M. G. (2007). Daily high-resolution-blended analyses for sea surface temperature. *Journal of Climate*, *20*(22), 5473–5496. https://doi.org/10.1175/2007JCLI1824.1

Robertson, J. E., & Watson, A. J. (1992). Thermal skin effect of the surface ocean and its implications for CO_2 uptake. *Nature*, *358*(6389), 738–740. https://doi.org/10.1038/358738a0

Rödenbeck, C., Keeling, R. F., Bakker, D. C. E., Metzl, N., Olsen, A., Sabine, C., & Heimann, M. (2013). Global surface-ocean pCO_2 and sea-air CO_2 flux variability from an observation-driven ocean mixed-layer scheme. *Ocean Science*, *9*(2), 193–216. https://doi.org/10.5194/os-9-193-2013

Rödenbeck, Christian, Bakker, D. C. E., Metzl, N., Olsen, A., Sabine, C., Cassar, N., et al.

(2014). Interannual sea-air CO_2 flux variability from an observation-driven ocean mixed-layer scheme. *Biogeosciences*, *11*(17), 4599–4613. https://doi.org/10.5194/bg-11-4599-2014

Rödenbeck, C., Bakker, D. C. E., Gruber, N., Iida, Y., Jacobson, A. R., Jones, S., et al. (2015). Data-based estimates of the ocean carbon sink variability - First results of the Surface Ocean *p*CO_2 Mapping intercomparison (SOCOM). *Biogeosciences*, *12*(23), 7251–7278. https://doi.org/10.5194/bg-12-7251-2015

Romanovsky, V., Isaksen, K., D, D., Anisimov, O., A, I., Leibman, M., et al. (2017). Changing permafrost and its impacts. In: *Snow, Water, Ice and Permafrost in the Arctic (SWIPA) 2017* (pp. 65–102). http://hdl.handle.net/11374/1931

Rudels, B., Björk, G., Nilsson, J., Winsor, P., Lake, I., & Nohr, C. (2005). The interaction between waters from the Arctic Ocean and the Nordic Seas north of Fram Strait and along the East Greenland Current: Results from the Arctic Ocean-02 Oden expedition. *Journal of Marine Systems*, *55*(1–2), 1–30. https://doi.org/10.1016/j.jmarsys.2004.06.008

Rutgersson, A., & Smedman, A. (2010). Enhanced air-sea CO_2 transfer due to water-side convection. *Journal of Marine Systems*, *80*(1–2), 125–134. https://doi.org/10.1016/j.jmarsys.2009.11.004

Rysgaard, S., Glud, R. N., Sejr, M. K., Bendtsen, J., & Christensen, P. B. (2007). Inorganic carbon transport during sea ice growth and decay: A carbon pump in polar seas. *Journal of Geophysical Research: Oceans*, *112*(3), 1–8. https://doi.org/10.1029/2006JC003572

Sabine, C. L., Feely, R. A., Gruber, N., Key, R. M., Lee, K., Bullister, J. L., et al. (2004). The oceanic sink for anthropogenic CO_2. *Science*, *305*(5682), 367–371. https://doi.org/10.1126/science.1097403

Sabine, C. L., Hankin, S., Koyuk, H., Bakker, D. C. E., Pfeil, B., Olsen, A., et al. (2013). Surface Ocean CO_2 Atlas (SOCAT) gridded data products. *Earth System Science Data*, *5*(1), 145–153. https://doi.org/10.5194/essd-5-145-2013

Sakurai, T., Yukio, K., & Kuragano, T. (2005). Merged satellite and in-situ data global daily SST. In *Proceedings. 2005 IEEE International Geoscience and Remote Sensing Symposium, 2005. IGARSS'05.* (Vol. 4, pp. 2606–2608). IEEE.

https://doi.org/10.1109/IGARSS.2005.1525519

Salter, M. E., Upstill-Goddard, R. C., Nightingale, P. D., Archer, S. D., Blomquist, B., Ho, D. T., et al. (2011). Impact of an artificial surfactant release on air-sea gas fluxes during Deep Ocean Gas Exchange Experiment II. *Journal of Geophysical Research: Oceans*, *116*(C11), C11016. https://doi.org/10.1029/2011JC007023

Saunders, P. M. (1967). The temperature at the ocean-air interface. *Journal of Atmospheric Sciences*, *24*(3), 269–273. https://doi.org/10.1175/1520-0469(1967)024<0269:TTATOA>2.0.CO;2

Shutler, J. D., Wanninkhof, R., Nightingale, P. D., Woolf, D. K., Bakker, D. C. E., Watson, A., et al. (2019). Satellites will address critical science priorities for quantifying ocean carbon. *Frontiers in Ecology and the Environment*, *18*(1): 27– 35. https://doi.org/10.1002/fee.2129

Smith, S. D., & Jones, E. P. (1985). Evidence for wind-pumping of air-sea gas exchange based on direct measurements of CO_2 fluxes. *Journal of Geophysical Research: Oceans*, *90*(C1), 869–875. https://doi.org/10.1029/JC090iC01p00869

Spreen, G., Kaleschke, L., & Heygster, G. (2008). Sea ice remote sensing using AMSR-E 89-GHz channels. *Journal of Geophysical Research: Oceans*, 113, C02S03. https://doi.org/10.1029/2005JC003384

Sutton, A. J., Williams, N. L., & Tilbrook, B. (2021). Constraining Southern Ocean CO_2 flux uncertainty using Uncrewed Surface Vehicle observations. *Geophysical Research Letters*, *48*(3), 1–9. https://doi.org/10.1029/2020GL091748

Sweeney, C., Gloor, E., Jacobson, A. R., Key, R. M., McKinley, G., Sarmiento, J. L., & Wanninkhof, R. (2007). Constraining global air-sea gas exchange for CO_2 with recent bomb ^{14}C measurements. *Global Biogeochemical Cycles*, *21*, GB2015. https://doi.org/10.1029/2006GB002784

Takahashi, T., Olafsson, J., Goddard, J., Chipman, D. W., Sutherland, S. C. (1993). Seasonal variation of CO_2 and nutrients in the high-latitude surface oceans: a comparative study. *Global Biogeochemical Cycles*, *7*(4), 843–878. https://doi.org/10.1029/93GB02263

Takahashi, T., Feely, R. A., Weiss, R. F., Wanninkhof, R. H., Chipman, D. W., Sutherland, S. C., & Takahashi, T. T. (1997). Global air-sea flux of CO_2: An estimate based on

measurements of sea-air pCO_2 difference. *Proceedings of the National Academy of Sciences of the United States of America*, *94*(16), 8292–8299. https://doi.org/10.1073/pnas.94.16.8292

Takahashi, T., Sutherland, S. C., Sweeney, C., Poisson, A., Metzl, N., Tilbrook, B., et al. (2002). Global sea-air CO_2 flux based on climatological surface ocean pCO_2, and seasonal biological and temperature effects. *Deep Sea Research Part II: Topical Studies in Oceanography*, *49*(9–10), 1601–1622. https://doi.org/10.1016/S0967-0645(02)00003-6

Takahashi, T., Sutherland, S. C., & Kozyr, A. (2008). Global ocean surface water partial pressure of CO_2 database: Measurements performed during 1968-2006 (Version 1.0). *ORNL/CDIAC-152, NDP-088. Carbon Dioxide Information Analysis Center, Oak Ridge National Laboratory, US Department of Energy, Oak Ridge, TN*, *37831*, 20.

Takahashi, T., Sutherland, S. C., Wanninkhof, R., Sweeney, C., Feely, R. A., Chipman, D. W., et al. (2009). Climatological mean and decadal change in surface ocean pCO_2, and net sea-air CO_2 flux over the global oceans. *Deep Sea Research Part II: Topical Studies in Oceanography*, *56*(8–10), 554–577. https://doi.org/10.1016/J.DSR2.2008.12.009

Tsukamoto, O., Kondo, F., & Kamei, Y. (2014). Overestimation of downward air-sea eddy CO_2 flux due to optical window contamination of open-path gas analyzer. *SOLA*, *10*, 117–121. https://doi.org/10.2151/sola.2014-024

Turner, J., & Marshall, G. J. (2011). *Climate change in the polar regions*. Cambridge: Cambridge University Press. https://doi.org/10.1017/CBO9780511975431

Wanninkhof, R. H., & Bliven, L. F. (1991). Relationship between gas exchange, wind speed, and radar backscatter in a large wind-wave tank. *Journal of Geophysical Research: Oceans*, *96*(C2), 2785–2796. https://doi.org/10.1029/90JC02368

Wanninkhof, R. (1992). Relationship between wind speed and gas exchange over the ocean. *Journal of Geophysical Research*, *97*(C5), 7373–7382. https://doi.org/10.1029/92JC00188

Wanninkhof, R. (2014). Relationship between wind speed and gas exchange over the ocean revisited. *Limnology and Oceanography: Methods*, *12*(6), 351–362. https://doi.org/10.4319/lom.2014.12.351

Wanninkhof, R., & Knox, M. (1996). Chemical enhancement of CO_2 exchange in natural waters. *Limnology and Oceanography*, *41*(4), 689–697. https://doi.org/10.4319/lo.1996.41.4.0689

Wanninkhof, R., & McGillis, W. R. (1999). A cubic relationship between air-sea CO_2 exchange and wind speed. *Geophysical Research Letters*, *26*(13), 1889–1892. https://doi.org/10.1029/1999GL900363

Wanninkhof, R., Ledwell, J. R., & Broecker, W. S. (1985). Gas exchange-wind speed relation measured with sulfur hexafluoride on a lake. *Science*, *227*(4691), 1224–1226. https://doi.org/10.1126/science.227.4691.1224

Wanninkhof, R., Asher, W. E., Ho, D. T., Sweeney, C., & McGillis, W. R. (2009). Advances in quantifying air-sea gas exchange and environmental forcing. *Annual Review of Marine Science*, *1*(1), 213–244. https://doi.org/10.1146/annurev.marine.010908.163742

Ward, B., Wanninkhof, R., McGillis, W. R., Jessup, A. T., DeGrandpre, M. D., Hare, J. E., & Edson, J. B. (2004). Biases in the air-sea flux of CO_2 resulting from ocean surface temperature gradients. *Journal of Geophysical Research C: Oceans*, *109*(8), 1–14. https://doi.org/10.1029/2003JC001800

Watson, A. J., Upstill-Goddard, R. C., & Liss, P. S. (1991). Air-sea gas exchange in rough and stormy seas measured by a dual-tracer technique. *Nature*, *349*(6305), 145–147. https://doi.org/10.1038/349145a0

Watson, A. J., Schuster, U., Shutler, J. D., Holding, T., Ashton, I. G. C., Landschützer, P., et al. (2020). Revised estimates of ocean-atmosphere CO_2 flux are consistent with ocean carbon inventory. *Nature Communications*, *11*(1), 1–6. https://doi.org/10.1038/s41467-020-18203-3

Weiss, A., Kuss, J., Peters, G., & Schneider, B. (2007). Evaluating transfer velocity-wind speed relationship using a long-term series of direct eddy correlation CO_2 flux measurements. *Journal of Marine Systems*, *66*(1–4), 130–139. https://doi.org/10.1016/j.jmarsys.2006.04.011

Weiss, R. F. (1974). Carbon dioxide in water and seawater: the solubility of a non-ideal gas. *Marine Chemistry*, *2*(3), 203–215. https://doi.org/10.1016/0304-4203(74)90015-2

Wesely, M. L., Cook, D. R., Hart, R. L., & Williams, R. M. (1982). Air-sea exchange of CO_2

and evidence for enhanced upward fluxes. *Journal of Geophysical Research: Oceans*, *87*(C11), 8827–8832. https://doi.org/10.1029/JC087iC11p08827

Wienhold, F. G., Welling, M., & Harris, G. W. (1995). Micrometeorological measurement and source region analysis of nitrous oxide fluxes from an agricultural soil. *Atmospheric Environment*, *29*(17), 2219–2227. https://doi.org/10.1016/1352-2310(95)00165-U

Wigley, T. M. L. (1983). The pre-industrial carbon dioxide level. *Climatic Change*, *5*(4), 315–320. https://doi.org/10.1007/BF02423528

Williams, N. L., Juranek, L. W., Feely, R. A., Johnson, K. S., Sarmiento, J. L., Talley, L. D., et al. (2017). Calculating surface ocean pCO_2 from biogeochemical Argo floats equipped with pH: An uncertainty analysis. *Global Biogeochemical Cycles*, *31*(3), 591–604. https://doi.org/10.1002/2016GB005541

Woolf, D. K., Land, P. E., Shutler, J. D., Goddijn-Murphy, L. M., & Donlon, C. J. (2016). On the calculation of air-sea fluxes of CO_2 in the presence of temperature and salinity gradients. *Journal of Geophysical Research: Oceans*, *121*(2), 1229–1248. https://doi.org/10.1002/2015JC011427

Woolf, D. K., Shutler, J. D., Goddijn-Murphy, L., Watson, A. J., Chapron, B., Nightingale, P. D., et al. (2019). Key uncertainties in the recent air-sea flux of CO_2. *Global Biogeochemical Cycles*, *33*(12), 1548–1563. https://doi.org/10.1029/2018GB006041

Woolf, D. K. (1997). Bubbles and their role in gas exchange. In Duce R. A. & Liss P. S. (Eds.), *The Sea Surface and Global Change* (pp. 173–205). UK: Cambridge University Press. https://doi.org/10.1017/CBO9780511525025.007

Wyngaard, J. C. (2010). Getting to know turbulence, Part I, Chapt. 2, in *Turbulence in the Atmosphere* (pp. 27–54), UK: Cambridge University Press. https://doi.org/10.1017/CBO9780511840524

Xu, F., & Ignatov, A. (2014). In situ SST quality monitor (i Quam). *Journal of Atmospheric and Oceanic Technology*, *31*(1), 164–180. https://doi.org/10.1175/JTECH-D-13-00121.1

Yamamoto-Kawai, M., McLaughlin, F. A., Carmack, E. C., Nishino, S., & Shimada, K. (2009). Aragonite undersaturation in the Arctic Ocean: effects of ocean acidification and sea ice melt. *Science*, *326*(5956), 1098–1100. https://doi.org/10.1126/science.1174190

Yang, C., Leonelli, F. E., Marullo, S., Artale, V., Beggs, H., Nardelli, B. B., et al. (2021). Sea

surface temperature intercomparison in the framework of the copernicus climate change service (C3S). *Journal of Climate*, *34*(13), 5257–5283. https://doi.org/10.1175/JCLI-D-20-0793.1

Yang, M., Blomquist, B. W., & Huebert, B. J. (2009). Constraining the concentration of the hydroxyl radical in a stratocumulus-topped marine boundary layer from sea-to-air eddy covariance flux measurements of dimethylsulfide. *Atmospheric Chemistry and Physics*, *9*(23), 9225–9236. https://doi.org/10.5194/acp-9-9225-2009

Yang, M., Blomquist, B. W., Fairall, C. W., Archer, S. D., & Huebert, B. J. (2011). Air-sea exchange of dimethylsulfide in the Southern Ocean: Measurements from so GasEx compared to temperate and tropical regions. *Journal of Geophysical Research: Oceans*, *116*(8), 1–17. https://doi.org/10.1029/2010JC006526

Yang, M., Beale, R., Liss, P., Johnson, M., Blomquist, B., & Nightingale, P. (2014). Air-sea fluxes of oxygenated volatile organic compounds across the Atlantic Ocean. *Atmospheric Chemistry and Physics*, *14*(14), 7499–7517. https://doi.org/10.5194/acp-14-7499-2014

Yang, M., Blomquist, B. W., Fairall, C. W., Archer, S. D., & Huebert, B. J. (2011). Air-sea exchange of dimethylsulfide in the Southern Ocean: Measurements from SO GasEx compared to temperate and tropical regions. *Journal of Geophysical Research: Oceans*, *116*(C4), C00F05. https://doi.org/10.1029/2010JC006526

Yang, M., Nightingale, P. D., Beale, R., Liss, P. S., Blomquist, B., & Fairall, C. (2013). Atmospheric deposition of methanol over the Atlantic Ocean. *Proceedings of the National Academy of Sciences of the United States of America*, *110*(50), 20034–20039. https://doi.org/10.1073/pnas.1317840110

Yang, M., Prytherch, J., Kozlova, E., Yelland, M. J., Parenkat Mony, D., & Bell, T. G. (2016a). Comparison of two closed-path cavity-based spectrometers for measuring air-water CO_2 and CH_4 fluxes by eddy covariance. *Atmospheric Measurement Techniques*, *9*(11), 5509–5522. https://doi.org/10.5194/amt-9-5509-2016

Yang, M., Bell, T. G., Hopkins, F. E., Kitidis, V., Cazenave, P. W., Nightingale, P. D., et al. (2016b). Air-sea fluxes of CO_2 and CH_4 from the penlee point atmospheric observatory on the south-west coast of the UK. *Atmospheric Chemistry and Physics*, *16*(9), 5745–5761. https://doi.org/10.5194/acp-16-5745-2016

Yang, M., Bell, T. G., Blomquist, B. W., Fairall, C. W., Brooks, I. M., & Nightingale, P. D. (2016c). Air-sea transfer of gas phase controlled compounds. *IOP Conference Series: Earth and Environmental Science*, *35*(1), 0–8. https://doi.org/10.1088/1755-1315/35/1/012011

Yang, M., Bell, T. G., Brown, I. J., Fishwick, J. R., Kitidis, V., Nightingale, P. D., et al. (2019). Insights from year-long measurements of air-water CH_4 and CO_2 exchange in a coastal environment. *Biogeosciences*, *16*(5), 961–978. https://doi.org/10.5194/bg-16-961-2019

Yang, M., Smyth, T. J., Kitidis, V., Brown, I. J., Wohl, C., Yelland, M. J., & Bell, T. G. (2021). Natural variability in air-sea gas transfer efficiency of CO_2. *Scientific Reports*, *11*(1), 1–9. https://doi.org/10.1038/s41598-021-92947-w

Yang, M., Bell, T. G., Bidlot, J. R., Blomquist, B. W., Butterworth, B. J., Dong, Y., et al. (2022). Global synthesis of air-sea CO_2 transfer velocity estimates from ship-based eddy covariance measurements. *Frontiers in Marine Science*, *9*(6), 1–15. https://doi.org/10.3389/fmars.2022.826421

Yasunaka, S., Siswanto, E., Olsen, A., Hoppema, M., Watanabe, E., Fransson, A., et al. (2018). Arctic Ocean CO_2 uptake: an improved multiyear estimate of the air-sea CO_2 flux incorporating chlorophyll *a* concentrations. *Biogeosciences*, *15*(6), 1643–1661. https://doi.org/10.5194/bg-15-1643-2018

Yelland, M. J., Moat, B. I., Taylor, P. K., Pascal, R. W., Hutchings, J., & Cornell, V. C. (1998). Wind stress measurements from the open ocean corrected for airflow distortion by the ship. *Journal of Physical Oceanography*, *28*(7), 1511–1526. https://doi.org/10.1175/1520-0485(1998)028<1511:WSMFTO>2.0.CO;2

Yelland, M. J., Moat, B. I., Pascal, R. W., & Berry, D. I. (2002). CFD model estimates of the airflow distortion over research ships and the impact on momentum flux measurements. *Journal of Atmospheric and Oceanic Technology*, *19*(10), 1477–1499. https://doi.org/10.1175/1520-0426(2002)019<1477:CMEOTA>2.0.CO;2

Yu, L., & Weller, R. A. (2007). Objectively analyzed air-sea heat fluxes for the global ice-free oceans (1981–2005). *Bulletin of the American Meteorological Society*, *88*(4), 527–540. https://doi.org/10.1175/BAMS-88-4-527

Zavarsky, A., Goddijn-Murphy, L., Steinhoff, T., & Marandino, C. A. (2018). Bubble-mediated gas transfer and gas transfer suppression of DMS and CO_2. *Journal of Geophysical Research: Atmospheres*, *123*(12), 6624–6647. https://doi.org/10.1029/2017JD028071

Zeebe, R. E., & Wolf-Gladrow, D. (2001). *CO_2 in seawater: equilibrium, kinetics, isotopes*. Elsevier Oceanography Series, vol. 65, the Netherlands: Elsevier. http://geosci.uchicago.edu/~kite/doc/Zeebe_CO2_In_Seawater_Ch_1.pdf

Zeng, J., Nojiri, Y., Landschützer, P., Telszewski, M., & Nakaoka, S. (2014). A global surface ocean fCO_2 climatology based on a feed-forward neural network. *Journal of Atmospheric and Oceanic Technology*, *31*(8), 1838–1849. https://doi.org/10.1175/JTECH-D-13-00137.1

Zhang, H., Beggs, H., Ignatov, A., & Babanin, A. V. (2020). Nighttime cool skin effect observed from infrared SST autonomous radiometer (ISAR) and depth temperatures. *Journal of Atmospheric and Oceanic Technology*, *37*(1), 33–46. https://doi.org/10.1175/JTECH-D-19-0161.1

Zhao, D., Toba, Y., Suzuki, Y., & Komori, S. (2003). Effect of wind waves on air-sea gas exchange: proposal of an overall CO_2 transfer velocity formula as a function of breaking-wave parameter. *Tellus B: Chemical and Physical Meteorology, 55*(2), 478–487. https://doi.org/10.3402/tellusb.v55i2.16747